DEPARTMENT OF PHYSICS
UNIVERSITY OF JYVÄSKYLÄ
RESEARCH REPORT No. 14/2018

NUMERICAL STUDIES ON NEUTRINO OSCILLATION PHYSICS IN LONG BASELINE EXPERIMENTS

BY
SAMPSA VIHONEN

Academic Dissertation
for the Degree of
Doctor of Philosophy

To be presented, by permission of the
Faculty of Mathematics and Science
of the University of Jyväskylä,
for public examination in Auditorium FYS1 of the
University of Jyväskylä on December 5, 2018
at 12 o'clock

Jyväskylä, Finland
December 2018

Author Sampsa Vihonen
Department of Physics
University of Jyväskylä
Finland

Supervisor Professor Jukka Maalampi
Department of Physics
University of Jyväskylä
Finland

Reviewers Dr. Iiro Vilja
Laboratory of Theoretical Physics
University of Turku
Finland

Dr. Martti Raidal
National Institute of Chemical Physics and Biophysics
Estonia

Opponent Professor Mattias Blennow
KTH Royal Institute of Technology
Sweden

Vihonen, Sampsa
Numerical studies on neutrino oscillation physics in long baseline experiments
Jyväskylä: University of Jyväskylä, 2018, 162 p.
(Research report/Department of Physics, University of Jyväskylä,
ISSN 0075-465X; 14/2018)
ISBN 978-951-39-7627-9 (paper version)
ISBN 978-951-39-7628-6 (electronic version)
Dissertation

Abstract

This thesis examines the prospects of future long baseline neutrino oscillation experiments. Using computer simulation techniques, we calculate the experimental sensitivities for two experimental configurations in a set of important questions which are all relevant for modern day neutrino physics. First, we set focus on the determination of the θ_{23} octant, where the aim is to find whether the atmospheric neutrino mixing angle θ_{23} lies in the high octant, $\theta_{23} > 45^\circ$, or in the low octant, $\theta_{23} < 45^\circ$. On the other hand, we study how well the long baseline experiments could test the limits of the Standard Model by seeking deviations from the oscillation patterns that follow from the standard three-neutrino paradigm. As an example, we study so called triplet Higgs bosons, which play a central role in the Type II seesaw mechanism, and calculate their effect on neutrino oscillations in the next generation long baseline experiment DUNE.

Keywords Neutrino physics, neutrino telescopes

Preface

The work reviewed in this thesis has been carried out in 2014-2018 at the Department of Physics in the University of Jyväskylä.

This thesis is dedicated to my loved ones, that is, my family and all my friends around the world. You remind me that science is not just about hard work, drinking coffee and frequent traveling, but it is also about the joy of exploring and going beyond.

I express my gratitude to my supervisor, professor Jukka Maalampi, for guiding me through the doctoral studies in the Graduate School of Particle and Nuclear Physics at the University of Jyväskylä. Working under his supervision taught me not only what it takes to be a researcher, but it also taught me about such important skills as patience, perseverance, pro-activeness and self-belief.

This thesis would not have been possible without the intensive teamwork and international collaboration. During my doctoral studies I worked in several collaborations, some of them larger than others, but they were all equally important to the success of this work. For this reason I would like to express my deepest gratitude to my collaborators Prof. João Pulido and Dr. Chitta Ranjan Das for the work that was done on the question of the octant degeneracy, and Prof. Katri Huitu and Dr. Timo Kärkkäinen with whom we studied long baseline physics beyond the Standard Model interactions. I also present thanks to Dr. Wladeslaw Trzaska for inviting me to join the WA105 experiment at CERN, which gave me an opportunity to learn about the dual phase liquid argon time projection chamber technology.

Of my friends, I cannot find the words to show my appreciation for the friendship I have been blessed with over the course of my doctoral studies. I would like to present special thanks to Mr. Pedro Pasquini, Ms. Gabriela Vitti Stenico, Dr. Kosti Tapio, Dr. Armen Julukian, Dr. Paavo Nieminen, Dr. Marko Käyhkö, Mr. Teemu Parviainen, and many others who helped me get through the graduate school.

Last but not least, I acknowledge Department of Physics, University of Jyväskylä and Centro de Física Teórica de Partículas, University of Lisbon, for the support they have given me throughout my doctoral studies.

Jyväskylä, November 2018
Sampsa Vihonen

List of Publications

The main results of this thesis have been reported in the following publications:

I C.R. DAS, J. MAALAMPI, J. PULIDO AND S. VIHONEN, *Determination of the θ_{23} octant in LBNO*, JHEP **02** (2015) 048 [arXiv:1411.2829 [hep-ph]].

II C.R. DAS, J. MAALAMPI, J. PULIDO AND S. VIHONEN, *On the determination of the θ_{23} octant in long baseline neutrino experiments*, Submitted to Int. J. Mod. Phys. **A** [arXiv:1606.02504 [hep-ph]].

III C.R. DAS, J. MAALAMPI, J. PULIDO AND S. VIHONEN, *Determination of the θ_{23} octant in long baseline neutrino experiments within and beyond the Standard Model*, Phys. Rev. **D97** (2018) no.3, 035023 [arXiv:1708.05182 [hep-ph]].

IV K. HUITU, T. J. KÄRKKÄINEN, J. MAALAMPI AND S. VIHONEN, *Constraining the nonstandard interaction parameters in long baseline neutrino experiments*, Phys.Rev. **D93** (2016) no.5, 053016 [arXiv:1601.07730 [hep-ph]].

V K. HUITU, T. J. KÄRKKÄINEN, J. MAALAMPI AND S. VIHONEN, *The effects of triplet Higgs boson in long baseline neutrino experiments*, Phys. Rev. **D97** (2018) no.9, 095037 [arXiv:1711.02971 [hep-ph]].

The author contributed to the planning and writing of all of the five publications, and performed the numerical analysis completely in publications I, II and III, and in collaboration with Dr. Timo Kärkkäinen in publications IV and V.

Contents

Chapter 1

Introduction

Neutrinos are elementary particles which have tiny masses, no electric charge, and interactions only via the weak nuclear force. Neutrinos are some of the most abundant particles in the visible universe, yet they are so elusive that one needs large detectors to find any trace of their existence. Neutrinos can be found in various types of nuclear reactions, and they play a crucial role in many of the important astrophysical and cosmogenic phenomena that have shaped the universe into what we see today. For example, neutrinos are involved in the fusion cycle that powers the Sun and participate in the complex star explosion mechanisms that drive the evolution of the supernovae. Neutrinos also contributed to the evolution of the young universe during its first moments after the Big Bang [1].

Neutrinos are born in three flavours (electron, muon and tau) and they are known to interact only via the exchange of heavy $W^{\pm}$ and Z^0 bosons. Because of this weak-only-interaction character, neutrinos interact so rarely that a typical neutrino originating from the Sun can easily pass through the Earth without interacting with its matter content. At the same time neutrinos are so common that the number of solar neutrinos reaching the surface of the Earth alone exceeds 60×10^9 cm^{-1}s^{-1}.

Perhaps the most striking property of neutrinos is their ability to change flavour (type) in flight. This means that a neutrino that is born in one flavour state (e.g. as an electron neutrino) can be found in a different flavour state (such as a muon or tau neutrino) after propagating some distance in space. This quantum mechanical phenomenon is known as the neutrino oscillation. Its discovery in early 2000s was a major milestone as its existence indicates that neutrinos have mass [2]. This is in contrast with the predictions of the Standard Model, and hence the existence of neutrino oscillations shows that there must be physics beyond the Standard Model. Neutrino oscillations were first predicted by Bruno Pontecorvo in 1957 [3] and they were finally discovered in Super-Kamiokande [4] and Sudbury Neutrino Observatory [5] in 1998 and 2002, a feat which was later recognized with the 2015 Nobel prize.

The oscillation of neutrinos, their abundance in astrophysical sources and their ability to travel through space nearly unhindered are the properties that make neutrinos very useful for contemporary astronomy, as they can be used to probe the phe-

nomena that are difficult to access with the conventional methods. Future prospects in neutrino oscillation physics could provide information about the supernova explosion mechanisms, illuminate the internal structure of the Earth and the Sun, and hint us whether neutrinos had a role in the disappearance of the antimatter in the early moments of the Universe [6,7]. A careful study of neutrino oscillations could also give us hints on the mechanism that gives rise to the neutrino masses. But before neutrinos can be harnessed to their full potential, one must first solve the remaining open questions in the physics of neutrino oscillations by determining the mixing between the neutrino flavours and masses at high precision.

Neutrino oscillations are in the three-flavour case described in terms of six physical parameters: the three mixing angles θ_{12}, θ_{13} and θ_{23}, two square-mass differences $\Delta m^2_{21} = m^2_2 - m^2_1$ and $\Delta m^2_{31} = m^2_3 - m^2_1$, and a Dirac CP phase δ_{CP}. Whereas the mixing angles describe the entanglement of the three neutrino mass states with a given flavour state, the square-mass differences define the oscillation frequencies and the CP phase determines the fundamental difference between neutrino and antineutrino oscillations. Many of these six oscillation parameters have been successfully determined in the past and ongoing experiments, which have studied the oscillations of solar, atmospheric, accelerator and reactor neutrinos. The only remaining questions are the ordering of the three mass eigenstates m_1, m_2 and m_3, the value of the Dirac CP phase parameter δ_{CP} and the octant of the mixing angle θ_{23}, that is, whether the atmospheric mixing angle θ_{23} lies in the low octant, $\theta_{23} < 45^\circ$, or the high octant, $\theta_{23} > 45^\circ$ [8,9]. Answers to these questions are sought in the present and future neutrino oscillation experiments (see e.g. Ref. [10] for a comprehensive list).

There are currently a number of notable neutrino oscillation experiments set in place around the world, either in operation or under construction. Whereas the long baseline experiments T2K [11] and NOνA [12] in Japan and the USA study the neutrino mixing through the $\nu_\mu \to \nu_e$ and $\bar{\nu}_\mu \to \bar{\nu}_e$ conversion using accelerator neutrinos, the experiments Double Chooz in France [13], RENO in South Korea [14] and Daya Bay in China [15] probe the $\bar{\nu}_e \to \bar{\nu}_\mu$ oscillations utilizing neutrinos from nuclear reactors, and the giant neutrino telescopes IceCube near the South Pole [16] and ANTARES at the bottom of the Mediterranean sea [17] look for neutrinos of atmospheric and astrophysical origin. In Japan, SuperKamiokande keeps observing solar and atmospheric neutrino oscillations to this day [18], and Borexino searches for low energy solar and geo-neutrinos in Italy [19]. Currently under construction are the next generation long baseline experiment DUNE [20], the very large scale deep-sea telescope KM3NeT [21], and the India-based neutrino observatory INO [22]. Moreover, the next generation reactor neutrino experiment JUNO [23] is being built in China and the plan to build the HyperKamiokande detector [24] is under consideration in Japan.

In addition to finding answers to the mass hierarchy, CP violation and θ_{23} oc-

tant questions, the next generation of neutrino oscillation experiments are going to look for hints of physics beyond the Standard Model. There is both experimental and theoretical motivation to investigate whether there are non-standard physics influencing the neutrino oscillations. Over the last few decades, there have been several reports of anomalies where the experimental data could not be fully explained with the usual three neutrino oscillations. This includes the so called short baseline anomaly, an excess of $\nu_\mu \to \nu_e$ and $\bar{\nu}_\mu \to \bar{\nu}_e$ events, which was first observed in the LSND experiment [25, 26] and was recently confirmed in the MiniBooNE experiment [27]. On the other hand, the existence of neutrino oscillations indicates that there must be a mechanism that allows neutrinos to acquire mass, and this requires elements beyond the Standard Model fields and interactions. A popular method to explain the smallness of the neutrino masses is to employ the so called seesaw mechanism [28–30], where the smallness of the neutrino masses is balanced with very massive new particle fields. In neutrino oscillations, these anomalies and neutrino mass models could mean various new physics effects, including the non-unitarity of the neutrino mixing matrix [31], non-standard neutrino interactions [32], and active–sterile neutrino oscillations [33].

In this thesis the focus is set on the prospects of the future long baseline neutrino oscillation experiments. Long baseline neutrino experiments are accelerator-driven facilities, where intense beams of muon neutrinos and antineutrinos are set to traverse very long distances underground. As the neutrinos propagate in a dense medium, the oscillation to the electron flavour state is enhanced by the so called Mikheyev-Smirnov-Wolfenstein effect [34, 35], which arises from the neutrino interactions with the matter. This matter effect allows the search for the experimental conditions which are optimal for studying neutrino oscillations.

The main question of this thesis is to calculate the expected sensitivities for the experimental configurations we have simulated in Refs. [36–38] and determine their prospects in determining the θ_{23} octant. Resolving the octancy of this mixing angle will not only significantly improve the precision on θ_{23} but could also provide valuable insight for constructing a model that explains the origin of the neutrino masses and mixing. Furthermore, we investigate the impact of potential new physics effects on neutrino oscillations [39, 40], and discuss how the future experiments can be used to probe the parameters of the new physics that gives rise to the small neutrino masses. As an example, we study the effects of the triplet Higgs bosons in the Type II seesaw model and check their testability in the future neutrino oscillation experiments.

This thesis is organized as follows: We begin in Chapter 2 by presenting the theoretical framework for neutrino oscillations and derive the neutrino oscillation probabilities in the standard three neutrino paradigm. We further discuss the topics of neutrino oscillations in vacuum and in the presence of matter, and make a brief detour to the status of the neutrino oscillation parameters and the questions therein.

In Chapter 3, we consider the typical low energy effects that could arise from the existence of neutrino masses and discuss their realization in the neutrino oscillation framework. In this context, the common parametrization methods are presented for the active-sterile neutrino mixing, non-unitarity of the neutrino mixing matrix and non-standard neutrino interactions. In Chapter 4, a brief overview is given of the experimental configurations we simulated in Publications I – IV [36–39], and the principles of the numerical methods used are disclosed. We discuss the main results of Publications I – III [36–38] in Chapter 5 and of IV and V [39, 40] in Chapter 6. Finally, we summarize the findings of this thesis and the future outlook in Chapter 7.

Chapter 2

Theory of neutrino oscillations

The concept of neutrino oscillations boils down to the mass of the neutrinos. Neutrino oscillations are made possible by the fact that the neutrinos are mixed when they get their masses, and each neutrino flavour state is in fact a superposition of the various mass eigenstates. The propagation of the neutrinos is well understood in the mass eigenstate basis, but since neutrinos can only be studied by their interactions, which are different for each flavour state, it requires the use of the flavour eigenstates to properly model the neutrino oscillations between a source and a detector. In this Chapter, we discuss the theory of neutrino oscillations and derive the neutrino oscillation probabilities in both vacuum and matter. We start in Section 2.1 by discussing the neutrino propagation in vacuum and continue in Section 2.2 by introducing the concept of matter effects to the oscillation probabilities. In Section 2.3 we revisit the status of the neutrino oscillation parameters and list the open questions therein.

2.1 Neutrino mixing and oscillations in vacuum

Each of the neutrino flavour states is a superposition of the neutrino mass eigenstates. The flavour basis and the mass basis are related through a unitary transformation [1]:

$$|\nu_l\rangle = \sum_k U_{lk}|\nu_k\rangle, \tag{2.1}$$

where l stands for the flavour and k for mass eigenstates. In a similar manner, the relation between the antineutrino flavour and mass states is given by

$$|\bar{\nu}_{l'}\rangle = \sum_k U^{\dagger}_{l'k}|\bar{\nu}_k\rangle, \tag{2.2}$$

where l' stands for another lepton flavour.

In the case of the three-neutrino oscillations, there are three flavour eigenstates (ν_e, ν_μ, ν_τ) and three mass eigenstates (ν_1, ν_2, ν_3), which are related by a unitary 3×3

matrix:

$$\begin{pmatrix} |\nu_e\rangle \\ |\nu_\mu\rangle \\ |\nu_\tau\rangle \end{pmatrix} = \begin{pmatrix} U_{e1} & U_{e2} & U_{e3} \\ U_{\mu 1} & U_{\mu 2} & U_{\mu 3} \\ U_{\tau 1} & U_{\tau 2} & U_{\tau 3} \end{pmatrix} \begin{pmatrix} |\nu_1\rangle \\ |\nu_2\rangle \\ |\nu_3\rangle \end{pmatrix}. \tag{2.3}$$

The matrix U is called the Pontecorvo-Maki-Nakagawa-Sakata (PMNS) matrix [41]. It can be parametrized in terms of three mixing angles θ_{12}, θ_{13} and θ_{23}, and a phase δ_{CP}:

$$U = \begin{pmatrix} 1 & 0 & 0 \\ 0 & c_{23} & s_{23} \\ 0 & -s_{23} & c_{23} \end{pmatrix} \begin{pmatrix} c_{13} & 0 & s_{13}e^{-i\delta_{\text{CP}}} \\ 0 & 1 & 0 \\ -s_{13}e^{i\delta_{\text{CP}}} & 0 & c_{13} \end{pmatrix} \begin{pmatrix} c_{12} & s_{12} & 0 \\ -s_{12} & c_{12} & 0 \\ 0 & 0 & 1 \end{pmatrix}, \tag{2.4}$$

where $s_{ij} = \sin\theta_{ij}$ and $c_{ij} = \cos\theta_{ij}$ for i, $j = 1, 2, 3$. The phase δ_{CP} is called the Dirac CP phase. In a general case, there are two other phases, called the Majorana phases [42–44], but they are irrelevant for the oscillation phenomena and are not presented here.

The three mixing angles θ_{12}, θ_{13} and θ_{23} are often referred to as the solar, reactor and atmospheric mixing angles, respectively, named after the origin of neutrinos in the experiments where their values were first determined. The δ_{CP} parameter, on the other hand, is called the CP violation parameter, as it defines the difference between the oscillation of neutrinos and antineutrinos. The intriguing violation of CP, the combined symmetry under the charge conjugation and parity, has been previously observed among quarks but never among leptons.

The time evolution of the neutrino fields can be determined from the Schödinger equation of the mass states in vacuum. For example, the mass state $|\nu_k\rangle$ with energy E_k ($k = 1, 2, 3$) evolves as

$$i\frac{\mathrm{d}}{\mathrm{d}\,t}|\nu_k\rangle = H|\nu_k\rangle = E_k|\nu_k\rangle, \tag{2.5}$$

where H refers to the Hamiltonian. This equation has the solution

$$|\nu_k(t)\rangle = e^{-i\,E_k\,t}|\nu_k\rangle, \tag{2.6}$$

which yields, together with equation (2.1), the time evolution of the flavour state $|\nu_l\rangle$:

$$|\nu_l(t)\rangle = \sum_k U_{lk}|\nu_k\rangle = \sum_k U_{lk}e^{-iE_k t}|\nu_k\rangle, \tag{2.7}$$

where $l = e, \mu, \tau$.

In this work we are interested in the neutrino oscillations probed in the long baseline neutrino experiments. In these experiments, neutrinos traverse the distances of the order of $L \sim \mathcal{O}(1000$ km) at energies of the order of $E \sim \mathcal{O}(1$ GeV). At such high energies, the neutrinos are relativistic and their masses are negligible

with respect to their momenta ($m_k \ll p_k$) and they traverse nearly at the speed of light (implying $t \simeq L$). One may therefore use the following approximation for the energies:

$$E_k = \sqrt{p_k^2 + m_k^2} \simeq p_k + \frac{m_k^2}{2p_k}. \tag{2.8}$$

Equation (2.8) suggests the following expression for the energy difference between the two mass states m_j and m_k:

$$E_j - E_k \simeq \frac{\Delta m_{jk}^2}{2E}, \tag{2.9}$$

where E_j, $E_k \simeq E + \mathcal{O}\left(\Delta m_{jk}^2/E\right)$ and $\Delta m_{jk}^2 = m_j^2 - m_k^2$ is the aforementioned square-mass difference.

The probability of a neutrino in the flavour state ν_l to oscillate into the flavour state $\nu_{l'}$ is obtained from equations (2.7) and (2.9):

$$\begin{aligned} P_{\nu_l \to \nu_{l'}} &= |\langle \nu_{l'}(t) | \nu_l(t) \rangle|^2 \\ &= |(\sum_j U_{l'k}^* \langle \nu_k | e^{i\,E_k k})(\sum_j U_{lj}\, e^{-i\,E_j t} | \nu_j \rangle)|^2 \\ &= \sum_{j,k} U_{lj}^* U_{l'j} U_{lk} U_{l'k}^* e^{-iL\Delta m_{jk}^2/2E}. \end{aligned} \tag{2.10}$$

This expression can be simplified further into the following form:

$$P_{\nu_l \to \nu_{l'}} = \delta_{ll'} - \sum_{j,k;j>k} \left[4 \sin^2 \Delta_{kj}\, \mathrm{Re}\, W_{ll'}^{jk} - 2 \sin 2\Delta_{kj}\, \mathrm{Im}\, W_{ll'}^{jk} \right], \tag{2.11}$$

where $W_{ll'}^{jk} = U_{lj}^* U_{l'j} U_{lk} U_{l'k}^*$ and $\Delta_{kj} = \Delta m_{kj}^2 L/4E$.

In a neutrino oscillation experiment, one is usually restricted to studying the oscillation between two neutrino flavour states. In accelerator-based experiments, for instance, the measured probabilities are mainly related to the channels $\nu_\mu \to \nu_e$ and $\nu_\mu \to \nu_\mu$, where the first is often called as the conversion or disappearance probability and the latter as the survival or appearance probability. It is evident from equation (2.11) that the conversion probability peaks when either $\sin^2 \Delta_{kj}$ or $\sin 2\Delta_{kj}$ acquires its maximum value, meaning that the sensitivity of a neutrino oscillation experiment is largely dependent on the value of the Δ_{kj} parameter.

In the special case of two-neutrino oscillations, the analytical form of the oscillation probability in equation (2.11) can be simplified into one that depends on one mixing angle θ and one square-mass difference Δm^2, in addition to the neutrino energy E and the traversed distance L. In this limit, the conversion probability is

given as

$$P_{\nu_l \to \nu_{l'}} \simeq \sin^2 2\theta \sin^2 \left(\frac{\Delta m^2 L}{4 E} \right), \tag{2.12}$$

where $l \neq l'$. Conversely, the survival probability $P_{\nu_l \to \nu_l}$ can be obtained as a complement of the conversion probability, i.e. $P_{\nu_l \to \nu_l} \simeq 1 - P_{\nu_l \to \nu_{l'}}$.

2.2 The MSW effect and oscillations in matter

When neutrinos traverse through a dense matter medium, such as the interior of the Sun, neutrinos interact with the particles in that medium by exchanging $W^{\pm}$ and Z^0 bosons. The coherent forward scattering of the neutrinos off the protons, electrons and neutrons of the medium can alter the neutrino oscillation probabilities substantially and change the propagation of neutrinos in dense environments such as the Sun, the Earth and the developing supernovae [45–48]. This is the so called Mikheyev-Smirnov-Wolfenstein effect (the MSW effect) [34, 35].

The matter may influence the neutrino propagation via the charged current (CC) and neutral current (NC) interactions, as it is illustrated in Figure (2.1). Whereas the CC interactions can only involve electron neutrinos, the NC interactions affect all three neutrino flavours the same way. This means that the matter effects have different contribution to the propagation of electron neutrinos from what they have on the propagation of muon or tau neutrinos. The MSW effect changes the effective masses of neutrinos due to the potential energy associated with the interactions of neutrinos with the particles in the matter.

In a given neutrino oscillation experiment one is mainly interested in the oscillation between two neutrino flavour states, e.g. $\nu_\mu \leftrightarrow \nu_e$, which dominates over the other oscillation channels. In the two-neutrino oscillations, the effective square-mass difference Δm^2_m, which defines the oscillation frequency in matter, is given by [1]:

$$\Delta m^2_m = \sqrt{(\Delta m^2 \cos 2\theta - A)^2 + (\Delta m^2 \sin 2\theta)^2}, \tag{2.13}$$

where $A = \pm 2\sqrt{2} G_F N_e E / \Delta m^2$, G_F is the Fermi coupling constant, N_e the electron number density, E the neutrino energy, and Δm^2 the square-mass difference in vacuum. The sign of the parameter A is set to be positive for neutrinos and negative for antineutrinos.

The matter effects also alter the mixing angle θ:

$$\sin^2 2\theta_m = \frac{\Delta m^2}{\Delta m^2_m} \sin^2 2\theta, \tag{2.14}$$

where Δm^2_m is given by equation (2.13), and θ_m is the effective mixing angle in the matter.

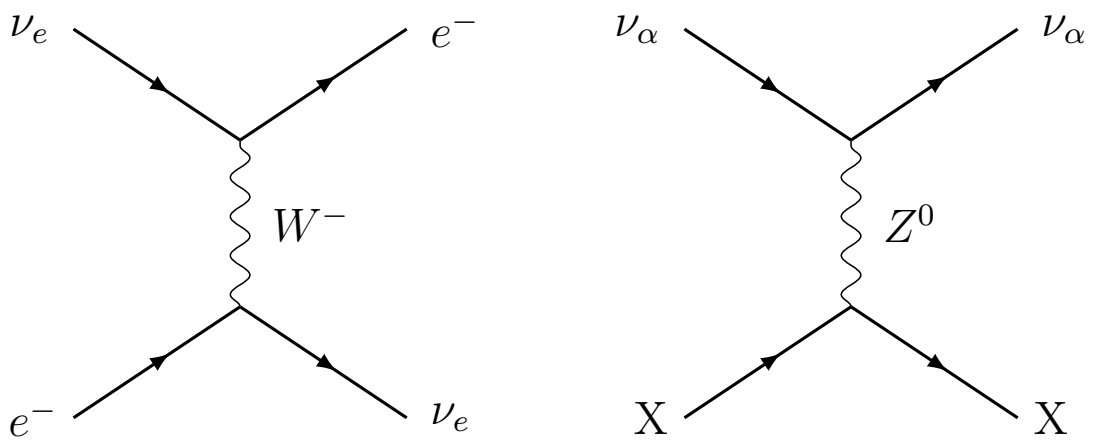

FIGURE 2.1 The Feynman diagrams of the charged current (left) and neutral current (right) processes that contribute to the neutrino–matter interactions. Here, ν_α stands for ν_e, ν_μ, ν_τ, and X for p^+, n^0, e^-.

With the effective mixing angle and square-mass difference taken into account, the neutrino oscillation probability can be written in the form

$$P_{\nu_\mu \to \nu_e} \simeq \sin^2 2\theta_m \sin^2 \left(\frac{\Delta m^2_m \, L}{4 \, E} \right), \tag{2.15}$$

which is analogous to the vacuum probability we defined in equation (2.12).

One notable consequence of the matter effects is so called MSW resonance [35, 49, 50]. The conversion probability in equation (2.15) exhibits resonant behaviour when the effective square-mass difference Δm^2_m in equation (2.13) approaches zero. The resonance takes place when $A \to \Delta m^2 \cos 2\theta$, which prompts the effective mixing angle θ_m in equation (2.14) and therefore also the oscillation probability in equation (2.15) to increase rapidly. The matter effects may therefore significantly enhance the oscillation probabilities when the neutrino energy E and baseline length L meet the resonance condition $A = \Delta m^2 \cos 2\theta$.

In the case of the three-neutrino oscillations, the probability becomes more cumbersome to express in terms of analytical functions. At $L \simeq 1300$ km, for instance, the probability for the $\nu_\mu \to \nu_e$ conversion is given by [51]:

$$\begin{aligned} P_{\nu_\mu \to \nu_e} \simeq & \sin^2 \theta_{23} \sin^2 2\theta_{13} \frac{\sin^2 (\Delta_{31} - a \, L)}{(\Delta_{31} - a \, L)^2} \Delta^2_{31} \\ & + \sin 2\theta_{23} \sin 2\theta_{13} \sin 2\theta_{12} \frac{\sin (\Delta_{31} - a \, L)}{(\Delta_{31} - a \, L)} \Delta_{31} \frac{\sin (a \, L)}{(a \, L)} \Delta_{21} \cos (\Delta_{31} + \delta_{\text{CP}}) \\ & + \cos^2 \theta_{23} \sin^2 2\theta_{12} \frac{\sin^2 (a \, L)}{(a \, L)^2} \Delta^2_{21}, \end{aligned} \tag{2.16}$$

where $\Delta_{kj} = \Delta m^2_{kj} L/4E$, $a = G_F N_e/\sqrt{2}$ and $\theta_{13} \ll 1$.

In a more accurate treatment of the three-neutrino oscillations, the oscillation probabilities are calculated by using the effective Hamiltonian H:

$$P_{\nu_l \to \nu_{l'}} = \left| \langle \nu_{l'} | e^{-iHt} | \nu_l \rangle \right|^2 . \tag{2.17}$$

When the neutrinos are subjected to the matter effects, the Hamiltonian acquires the matter potential term $2\,EV$ and is given by:

$$H = \frac{1}{2E} \left[U \begin{pmatrix} 0 & 0 & 0 \\ 0 & \Delta m^2_{21} & 0 \\ 0 & 0 & \Delta m^2_{31} \end{pmatrix} U^\dagger + 2\,EV \right], \tag{2.18}$$

where U is the PMNS matrix, E is the neutrino energy and V is a 3×3 matrix which contains the matter potential energies V_{CC} and V_{NC}, associated with the CC and NC interactions, respectively:

$$V = \begin{pmatrix} V_{\text{CC}} + V_{\text{NC}} & 0 & 0 \\ 0 & V_{\text{NC}} & 0 \\ 0 & 0 & V_{\text{NC}} \end{pmatrix}, \tag{2.19}$$

where $V_{\text{CC}} = \sqrt{2}\, G_F\, N_e$ and $V_{\text{NC}} = -G_F\, N_e/\sqrt{2}$.

In the standard three-neutrino oscillation case, the diagonal entries V_{NC} can be subtracted from equation (2.19) as they will appear as an overall phase in the transition amplitude and therefore do not affect the oscillation probabilities. Hence, in the case of the three standard neutrinos the oscillations in matter are only influenced by the CC potential V_{CC}, whereas the NC potential V_{NC} has no effect. Note, however, that in the presence of sterile neutrinos, which do not interact with the matter at all, the NC potential does have an effect as it makes the difference between the active and sterile flavours.

2.3 Status of the neutrino oscillation parameters

Since the neutrinos were first discovered by C. Cowan and F. Reines in 1956 [52], the knowledge on neutrino physics has improved significantly as the various neutrino experiments have studied neutrinos originating in the Sun, the atmosphere, nuclear reactors and particle accelerators (see e.g. Ref. [53] for a complete review). On the one hand, the mixing angle θ_{12} and the square-mass difference Δm^2_{21} were successfully determined in the various solar neutrino experiments (incl. Homestake [54], Kamiokande [55], GNO [56] and SAGE [57]), where the flux of the neutrinos born in the Sun were measured and compared with the predictions of the standard solar model. In a similar manner, the neutrino oscillation parameters θ_{23} and Δm^2_{32} have

TABLE 2.1 The experimental best-fit values and standard deviations for the standard neutrino oscillation parameters. These values are shown for both mass hierarchies and are taken from a recent global analysis [64]. Note that Δm^2_{3l} stands for Δm^2_{31} in normal hierarchy (NH) and Δm^2_{32} in inverted hierarchy (IH).

Parameter	Central value $\pm$ error (NH)	Central value $\pm$ error (IH)
$\sin^2\theta_{12}$	$0.320^{+0.020}_{-0.016}$	$0.320^{+0.020}_{-0.016}$
$\sin^2\theta_{13}$	$0.02160^{+0.00083}_{-0.00069}$	$0.02220^{+0.00074}_{-0.00076}$
$\sin^2\theta_{23}$	$0.547^{+0.020}_{-0.030}$	$0.551^{+0.018}_{-0.030}$
$\delta_{\rm CP}$ (°)	$237.6^{+37.8}_{-27.0}$	$280.8^{+23.4}_{-27.0}$
Δm^2_{21} (10^{-5} eV^2)	$7.55^{+0.20}_{-0.16}$	$7.55^{+0.20}_{-0.16}$
Δm^2_{3l} (10^{-3} eV^2)	$2.50^{+0.03}_{-0.03}$	$-2.42^{+0.04}_{-0.03}$

been determined in the atmospheric neutrino experiments (SuperKamiokande [58], ANTARES [59] and IceCube [60]), where the muon neutrinos born in the Earth's atmosphere from cosmic ray interactions were observed. More recently, the reactor mixing angle θ_{13} has been measured in the reactor neutrino experiments (Daya Bay [61], RENO [62] and Double Chooz [63]), where neutrino oscillations have been studied using the neutrinos from nuclear reactors.

The recent years of neutrino oscillation studies have brought the determination of the oscillation parameters to an era of high precision measurements. The solar, atmospheric and reactor mixing angles and the solar and atmospheric square-mass differences have been determined with an unprecedented precision in a host of neutrino oscillation experiments of various types [9, 64, 65]. The only remaining questions concerning the neutrino oscillation parameters are the relative order of the neutrino masses m_1, m_2 and m_3, the value of the CP violation parameter $\delta_{\rm CP}$ and the octant of the atmospheric mixing angle θ_{23}. The results of the recent experiments are summarized in Table 2.1.

2.3.1 The order of neutrino masses

Just as each neutrino flavour is a superposition of the three mass states, it can be said that each mass state is a mixture of the three flavour states. The first neutrino mass, m_1, is defined by convention as the mass that has the largest electron flavour component, and the second neutrino mass m_2 is the one that follows it, i.e. $m_1 < m_2$. According to the neutrino oscillation experiments, the square-mass differences $\Delta m^2_{\rm sol}$ and $\Delta m^2_{\rm atm}$ have the values of the order of 10^{-5}eV^2 and 10^{-3}eV^2, respectively, which implies that the third neutrino mass, m_3, is either much larger or much smaller than the other two masses (see Figure 2.2).

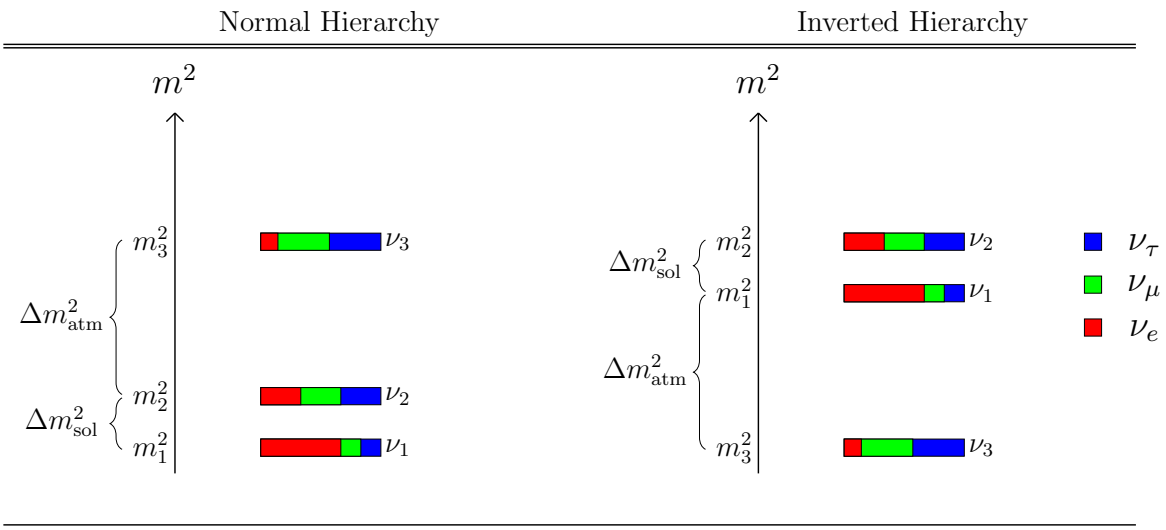

FIGURE 2.2 An illustrative chart of the ordering and flavour compositions of the neutrino masses m_1, m_2 and m_3 , arranged according to their hierarchy. In the normal hierarchy, the masses are ordered as $m_1 < m_2 \ll m_3$, whereas in the inverted hierarchy the ordering is $m_3 \ll m_1 < m_2$. The image is not drawn to the exact scale.

What remains unsolved is whether the correct mass ordering is $m_1 < m_2 \ll m_3$ or $m_3 \ll m_1 < m_2$. It is said that if m_3 is much larger than m_1 and m_2, that is, if $\Delta m^2_{31} = m_3^2 - m_1^2 > 0$, the neutrino masses follow the normal hierarchy (NH). Conversely, if m_3 is much smaller than m_1 and m_2, or $\Delta m^2_{31} < 0$, the masses are said to follow the inverted hierarchy (IH). At the moment there is no decisive evidence of whether the hierarchy is normal or inverted, though there is a mild preference for the hierarchy being NH [64]. This is the so called neutrino mass hierarchy or ordering problem.

The mass hierarchy can be probed in neutrino oscillation experiments, but it is made challenging by the fact that the neutrino oscillation probabilities are typically independent of the sign of the dominating square-mass difference, as is seen e.g. from equations (2.12) and (2.15). The determination of the mass hierarchy requires very high precision, and it is the main experimental goal of the next generation experiment JUNO, for example, which seeks to determine the mass hierarchy by at least a $3\,\sigma$ confidence level [23].

2.3.2 The search for CP violation

Another important issue to study in neutrino oscillation experiments is whether the neutrinos and antineutrinos interact with other particles in the same way. Weak interactions are known to violate the charge conjugation (C) and parity (P) symmetries, but it is yet not known whether they violate the CP symmetry. In neutrino oscillations, the violation of the CP symmetry leads to a difference between the os-

cillation probabilities of neutrinos and antineutrinos. The presence of the matter effects may also create an effect that resembles CP violation in neutrino oscillations, which must be properly taken into account in neutrino oscillation experiments (see e.g. [66]). In the three-neutrino oscillations, the amount of CP violation is effectively controlled by the Dirac CP phase parameter δ_{CP}, which may be either CP conserving, $\sin\delta_{\mathrm{CP}} = 0$, or CP violating, $\sin\delta_{\mathrm{CP}} \neq 0$.

The question of CP violation is important, as it is believed that a sufficient CP violation among neutrinos could explain, through the so called leptogenesis mechanism [7], why there is so little antimatter in the universe. The latter is the so called baryon asymmetry problem [1], which has turned out to be impossible to explain in terms of the CP violation taking place in the quark sector [67].

Finding the answer to the CP violation question requires experimental data from both neutrino and antineutrino oscillations. There are experiments that can probe both oscillation modes, as is the case in the accelerator-based experiments like T2K and NOνA. So far there is very little knowledge of the true value of the δ_{CP} parameter, though a mild hint of it being $\delta_{\mathrm{CP}} \sim 270^\circ$ (see Table 2.1) has been provided by T2K [68].

Finding an evidence of CP violation will be one of the main goals of the next generation long baseline experiment DUNE, which is predicted to attain a $3\,\sigma$ confidence level for the majority of the available δ_{CP} values after seven years of running [51].

2.3.3 The problem of θ_{23} octant

The third, and often overlooked, open question in the neutrino oscillation physics pertains to the true value of the atmospheric mixing angle θ_{23} [8]. At $3\,\sigma$ confidence level, the measured value of the mixing angle θ_{23} has a significantly higher uncertainty and dependence on the mass hierarchy than the solar and reactor mixing angles [64]. More importantly, it is unclear whether the true value of θ_{23} lies in the high octant, $\theta_{23} > 45^\circ$, or the low octant, $\theta_{23} < 45^\circ$. It could also be that the atmospheric mixing angle corresponds to the maximal mixing, i.e. $\sin^2 2\theta_{23} = 1$.

The difficulty to pinpoint the true value of the atmospheric mixing angle θ_{23} accurately derives from the probability of the $\nu_\mu \to \nu_\mu$ oscillations, which plays a significant role in the measuring of the muon neutrino deficit in atmospheric neutrino experiments. In the two-neutrino approximation, the survival probability can be written as

$$P_{\nu_\mu \to \nu_\mu} \simeq 1 - \sin^2 2\theta_{23} \sin^2\left(\frac{\Delta m^2_{32} L}{4\,E_\nu}\right). \tag{2.20}$$

The leading θ_{23}–dependent term in the survival probability in equation (2.20) is symmetric with respect to the maximal mixing value $\theta_{23} = 45^\circ$, meaning that the values

in the both octants can yield similar probabilities:

$$P_{\nu_\mu \to \nu_\mu}(90^\circ - \theta_{23}) = P_{\nu_\mu \to \nu_\mu}(\theta_{23}). \tag{2.21}$$

The problem of the θ_{23} deters the precise determination of the θ_{23} mixing angle, and exacerbate the challenge of discovering the mass hierarchy and CP violation, as the three oscillation parameters are often severely entangled. Determination of the θ_{23} octant will therefore not only improve the θ_{23} value estimate significantly, but it will also likely improve the precision of the other unknown oscillation parameters. Furthermore, the knowledge of whether θ_{23} resides in the high or low octant or corresponds to the maximal mixing could also hint of a potential flavour symmetry in the neutrino mixing matrix U [69].

The determination of the θ_{23} octant in the next generation long baseline neutrino experiments is the main research question of this thesis, and it is studied in Publications I–III. The results of these publications are covered in Chapter 5.

Chapter 3

Low energy effects of the neutrino mass

The discovery of neutrino oscillations established that neutrinos have mass, which is in contrast to the Standard Model (SM) premise. Not only that, but the cosmological surveys and beta decay experiments have also shown that the neutrino masses must be tiny in comparison with those of the other particles. The models that accommodate the neutrino masses often introduce new particle fields or symmetries, with implications on many of the SM observables that can be tested, such as the masses of the intermediate vector bosons $W^{\pm}$ and Z^0. Some of these models indicate considerable effects on the neutrino oscillation probabilities, which could make it possible to study them in the future neutrino oscillation experiments.

In this Chapter, we discuss the potential low energy effects arising from the existence of the neutrino masses, from active–sterile neutrino oscillations to non-standard neutrino interactions, and evaluate their impact on the neutrino oscillation probabilities. We begin in Section 3.1 by describing the role of the neutrinos in the SM and explain why the neutrinos cannot gain the mass with the SM–Higgs field the same way as the other known particles do. In Section 3.2, we describe the most popular mechanism to generate and explain the lightness of the neutrino masses, the so called seesaw mechanism, and discuss its potential effects on neutrino oscillations. We conclude the Chapter in Section 3.3 by presenting some of the most popular methods to parametrize the implications of these mass models.

3.1 The origin of neutrino mass

The Standard Model of particle physics is a gauge quantum field theory which describes the properties and interactions of the elementary particles. The SM characterizes the elementary particles in the three generations of quarks (up u and down d, charm c and strange s, and top t and bottom b), three generations of leptons (electron e, muon μ, tau τ, and the corresponding neutrinos ν_e , ν_μ and ν_τ), three types of force

carriers (photon γ, gluon g, and the weak bosons $W^{\pm}$ and Z^0), and the Higgs boson H. Whereas the quarks and leptons are spin–$\frac{1}{2}$ fermions which constitute all of the known matter, the force carriers γ, g, and $W^{\pm}$, Z^0 are spin–1 bosons which mediate the electromagnetic, strong and weak interactions, respectively. The Higgs boson, on the other hand, is a spin–0 particle, and it enables the quarks, charged leptons and the weak bosons to have mass.

The SM is based on the gauge symmetry group $\mathrm{SU(3)_C}\times\mathrm{SU(2)_L}\times\mathrm{U(1)_Y}$, where L stands for the left-handedness and Y for the hyper charge. The theory of weak and electromagnetic interactions is described in the so called electroweak theory, which is based on the $\mathrm{SU(2)_L}\times\mathrm{U(1)_Y}$ symmetry group. The SM Higgs mechanism breaks spontaneously the $\mathrm{SU(2)_L}\times\mathrm{U(1)_Y}$ symmetry into $\mathrm{U(1)}_{EM}$, separating the weak and electromagnetic forces and giving rise to the massive weak bosons $W^{\pm}$ and Z^0 and the massless photon γ. The Higgs mechanism also gives masses to the electrically charged fermions, which all have both left and right-handed chiral components.

In the SM, neutrinos are electrically chargeless particles that consist of only left-handed chiral fields and have only weak interactions. Because of the absence of the right-handed fields, neutrinos cannot gain the mass from the same mechanism as the other fermions, and hence the SM neutrinos are massless particles in the original SM theory.

If one introduces also the right-handed neutrino fields, the neutrino mass could be generated via the SM Higgs mechanism through the Yukawa coupling

$$\mathcal{L}_{\nu} = -Y_{\alpha\beta}\,\overline{L}_{\alpha\mathrm{L}}\,\tilde{\phi}\,\nu_{\beta\mathrm{R}} + \mathrm{h.c.} \tag{3.1}$$

where $Y_{\alpha\beta}$ is the Yukawa coupling constant ($\alpha, \beta = e, \mu, \tau$), L_{L} is the $\mathrm{SU(2)_L}$ doublet containing the left-handed neutrino and charged lepton fields, ν_{R} is the right-handed neutrino field, $\tilde{\phi} = i\sigma_2\phi^*$ is the SU(2) conjugate of the SM Higgs doublet ϕ. The Lagrangian in equation (3.1) would give rise to the Dirac mass of the neutrino fields.

The first problem with generating the neutrino masses from the SM Higgs mechanism and equation (3.1) comes from the observation that the individual neutrino masses are very tiny. Neutrino masses have been probed in several cosmological surveys and tritium beta decay experiments [70,71], establishing upper bounds for the neutrino masses, e.g. $\sum m_{\nu} \lesssim 0.12$ eV, which is only a fraction of that of the lightest elementary particle, the electron. The smallness of the neutrino masses therefore makes it unlikely that neutrinos could have acquired their masses from the SM Higgs mechanism as it would require extremely weak Yukawa couplings.

3.2 The seesaw mechanism

An alternative to the Dirac mass arising from the Yukawa coupling would be the so called Majorana mass, where the right-handed chiral components of neutrino fields are conceived from the left-handed fields ν_{L} via the charge conjugation ($\nu_{\mathrm{R}} = (\nu_{\mathrm{L}})^{\mathrm{C}}$) by making neutrinos their own antiparticles. This type of a particle is called a Majorana particle. There are multiple ways to construct a theory where neutrinos are Majorana particles and have at the same time naturally small masses, and many of them involve the so called seesaw mechanism [28–30].

The seesaw mechanism tackles the problem of the small neutrino masses by introducing an entirely new particle field, which is not described in the SM, and entails a mass much larger than the electroweak scale 246 GeV. In the seesaw mechanism, the tiny neutrino masses result naturally from the tree-level exchange of the heavy particle, which may be either a fermion or a scalar boson. Whereas a singlet fermion gives rise to the so called Type I version of the seesaw mechanism, a scalar triplet results in the Type II and a fermionic triplet in the Type III realization of the seesaw mechanism. The tree-level Feynman diagrams of these three versions of the seesaw mechanism are presented in Figure 3.1.

The phenomenological consequences of the heavy fields of the seesaw mechanism can be analyzed at the low energies with the so called effective field theory approach, where the SM Lagrangian $\mathcal{L}_{\mathrm{SM}}$ is augmented with a chain of non-renormalizable higher dimension operators [72,73]:

$$\mathcal{L}_{\mathrm{eff}} = \mathcal{L}_{\mathrm{SM}} + \delta\mathcal{L}^{d=5} + \delta\mathcal{L}^{d=6} + \dots, \tag{3.2}$$

where $\delta\mathcal{L}^{d=5}$, $\delta\mathcal{L}^{d=6}$, ... are operators of dimensions 5, 6 etc. These operators are invariant under the SM gauge group and consist of the SM fields, weighted by the inverse of the mass of the new heavy fields.

For the seesaw mechanism, there is only one way to write the dimension $d = 5$ operator:

$$\delta\mathcal{L}^{d=5} = \frac{1}{2} c_{\alpha\beta}^{d=5} \left(\overline{L}_{\alpha\mathrm{L}}^{\mathrm{C}} \tilde{\phi}^{*}\right) \left(\tilde{\phi}^{\dagger} L_{\beta\mathrm{L}}\right) + \mathrm{h.c.} \tag{3.3}$$

where the coefficients $c_{\alpha\beta}^{d=5}$ are inversely proportional to the mass of the heavy fields N_{R}, Δ or Σ_{R} (see Figure 3.1).

Upon the electroweak symmetry breaking, the neutrinos acquire the Majorana masses from the following mass matrix:

$$m_{\nu} = -\frac{v^2}{2}\, c^{d=5}, \tag{3.4}$$

where $v/\sqrt{2} \simeq 174$ GeV is the vacuum expectation value of the SM Higgs field ϕ. The neutrino masses, obtained by diagonalizing the matrix in equation (3.4), are naturally light, as the $c_{\alpha\beta}^{d=5}$ coefficients are inversely proportional to the mass of the

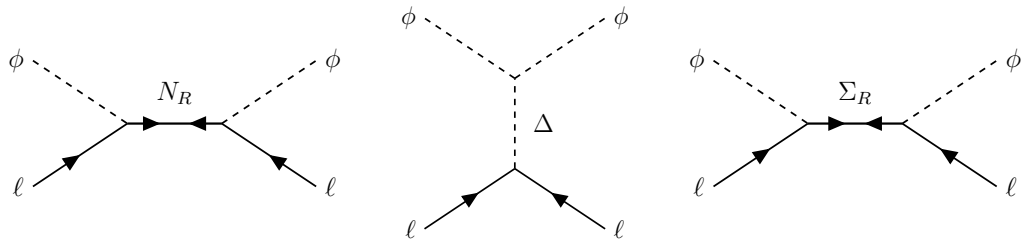

(a) Type I **(b)** Type II **(c)** Type III

FIGURE 3.1 The tree-level Feynman diagrams for the mass-generating processes in the (a) Type I, (b) Type II, and (c) Type III realizations of the seesaw mechanism. Whilst Type I generates the neutrino masses from a fermionic singlet $N_{\rm R}$, Type II attains them with a scalar triplet Δ and Type III with a fermionic triplet $\Sigma_{\rm R}$.

heavy particle field, $c_{\alpha\beta}^{d=5} \sim \frac{1}{M}$.

The seesaw mechanism is involved in a large number of neutrino mass models, either at the tree-level or as some kind of a derivative, as is the case with the radiative neutrino mass models [74], where the seesaw mechanism is realized at the loop level. The seesaw mechanism emerges naturally in the left-right symmetric models, such as the Pati-Salam theory [75–80] for example, and it is one of the most popular method to incorporate the small neutrino masses.

In this thesis, we are interested in the low energy effects of the seesaw mechanism and their implications in the neutrino oscillations. We discuss the details of the Type I models in Section 3.2.1 and of the Type II models in Section 3.2.2, respectively.

3.2.1 Type I: Fermionic singlets

In the Type I version of the seesaw mechanism, the neutrino masses are explained by the presence of neutral heavy fermions, which are singlets under the electroweak symmetry group $\mathrm{SU(2)_L}\times\mathrm{U(1)_Y}$. This is easily achieved by adding the right-handed neutrino fields to the SM particle content, as they are already allowed by the SM symmetry group. This realization of the seesaw mechanism is often called as the economic or the minimal seesaw model.

The Type I seesaw model is based on the following Lagrangian terms:

$$\mathcal{L} = -Y_{\alpha\beta}^{\ell}\overline{L}_{\alpha\mathrm{L}}\phi\ell_{\beta\mathrm{R}} - Y_{\alpha\beta}^{N}\overline{L}_{\alpha\mathrm{L}}\tilde{\phi}\nu_{\beta\mathrm{R}} - \frac{1}{2}M_{\alpha\beta}^{N}\overline{\nu}_{\alpha\mathrm{R}}\left(\nu_{\beta\mathrm{R}}\right)^{\mathrm{C}} + \mathrm{h.c.} \tag{3.5}$$

where α, $\beta = e$, μ, τ, ϕ is the Higgs doublet, $\tilde{\phi} = i\sigma_2\phi^*$, $L_\alpha^{\mathrm{T}} = (\nu_\alpha, \ell_\alpha)$, $Y_{\alpha\beta}^{\ell}$ and $Y_{\alpha\beta}^{N}$ are the Majorana mass terms of the right-handed neutrinos. As a result of the spontaneous breaking of the $\mathrm{SU(2)_L}\times\mathrm{U(1)_Y}$ gauge symmetry, this yields the following

mass Lagrangian for neutrinos:

$$\mathcal{L}_m = -\overline{\nu}_{\mathrm{L}} \frac{v\, Y^N}{\sqrt{2}} \nu_{\mathrm{R}} - \frac{1}{2} \overline{\nu}_{\mathrm{R}} M^N (\nu_{\mathrm{R}})^{\mathrm{C}} + \mathrm{h.c.} \tag{3.6}$$

where $\nu_{\mathrm{L}}^{\mathrm{T}} = (\nu_{e\mathrm{L}}, \nu_{\mu\mathrm{L}}, \nu_{\tau\mathrm{L}})$, $\nu_{\mathrm{R}}^{\mathrm{T}} = (\nu_{e\mathrm{R}}, \nu_{\mu\mathrm{R}}, \nu_{\tau\mathrm{R}})$, Y^N is the 3×3 Yukawa matrix and M^N is the 3×3 Majorana mass matrix.

The diagonalization of the Lagrangian in equation (3.6) results in three light Majorana neutrinos (ν_1, ν_2, ν_3) with a mass of the order

$$m_\nu \sim \frac{v^2}{M}, \tag{3.7}$$

where M is the scale of the elements of the Majorana mass matrix M^N. The mass M is assumed to be much larger than the symmetry breaking scale v, which explains the lightness of the neutrinos compared with the charged leptons and quarks.

In addition to the three light Majorana neutrinos, there exist three heavy Majorana neutrinos (N_1, N_2, N_3) in this model, with masses of the order of M.

Given that $v \sim \mathcal{O}(100$ GeV), and assuming the light neutrino masses to be $m_\nu \lesssim \mathcal{O}(1$ eV), the mass scale of the heavy neutrinos is to be $M \gtrsim \mathcal{O}(10^{13}$ GeV). The heavy neutrinos will thus play no role in the low energy phenomena.

In neutrino oscillation experiments, the right-handed neutrinos of the Type I seesaw models are relevant as they may give rise to the non-unitarity of the 3×3 mixing matrix U, which describes the mixing among the light neutrinos. The non-unitarity arises through the higher dimensional operators in the Lagrangian expansion (3.3), particularly in the dimension–6 operator [73], which could also have notable effects on the other electroweak observables, for example on the determination of the value of the Fermi coupling constant G_F through the muon decay rate.

The the non-unitarity of the mixing matrix U and its constraints from the electroweak and neutrino oscillation experiments are studied in e.g. Refs. [81, 82]. The effect of the non-unitarity in the determination of the θ_{23} octant is studied in the long baseline neutrino experiment DUNE in Publication III of this thesis. The main results of the publication are presented in Chapter 5.

3.2.2 Type II: Scalar triplets

The Type II version of the seesaw mechanism generates the small neutrino masses by adding a new type of Higgs bosons into the SM particle content. This is done by including the set of scalar fields $\Delta = (\Delta^0, \Delta^+, \Delta^{++})$, which has hypercharge $\mathrm{Y} = 2$ and transforms as a triplet under the $\mathrm{SU(2)_L}$ gauge group. The neutrinos ν_e, ν_μ and ν_τ then gain their masses from the vacuum expectation value of the triplet Higgs as Majorana masses.

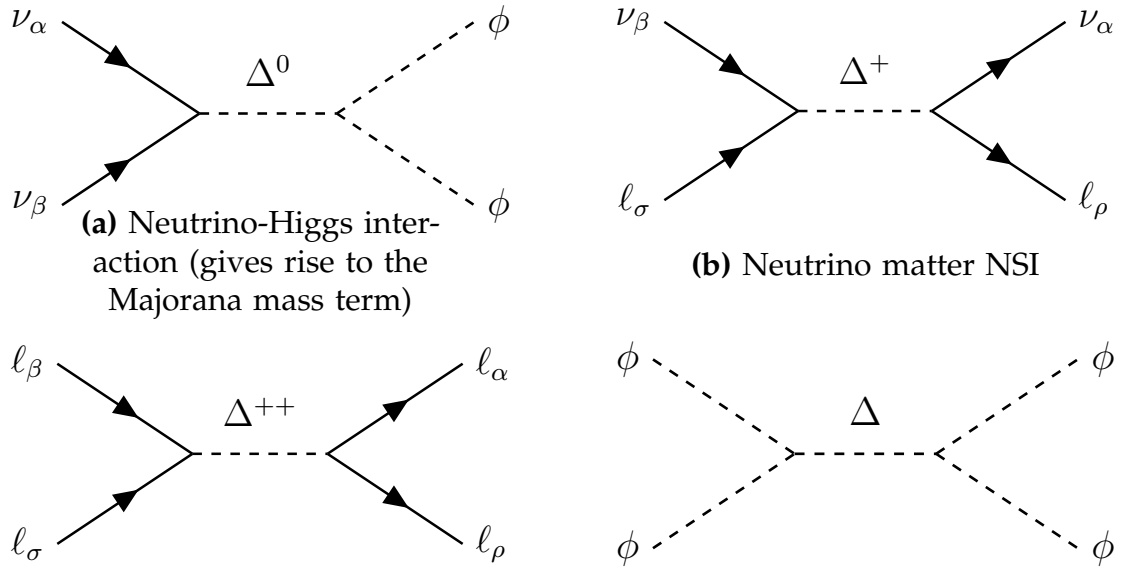

(a) Neutrino-Higgs interaction (gives rise to the Majorana mass term)

(b) Neutrino matter NSI

(c) Four-lepton NSI

(d) SM Higgs self-coupling

FIGURE 3.2 The tree-level Feynman diagrams for the interactions of the scalar triplet Δ in the Type II seesaw mechanism. The triplet fields interact with the neutrinos ν, leptons ℓ, and the SM Higgs scalar ϕ. The diagrams correspond to the processes responsible for the (a) Majorana mass term, (b) non-standard neutrino interactions in matter, (c) non-standard four-lepton interactions, and (d) SM Higgs self-coupling.

The interactions of the triplet $\Delta = (\Delta_1, \Delta_2, \Delta_3) \sim (\mathbf{3}, 2)$ are defined by the Lagrangian [83]

$$\mathcal{L}_\Delta = Y_{\alpha\beta}\, L_{\alpha L}^T\, C\, i\sigma_2\, \Delta\, L_{\beta L} + \lambda_\phi\, \phi^T\, i\sigma_2\, \Delta^\dagger \phi + \text{h.c.}, \tag{3.8}$$

where $Y_{\alpha\beta}$ (α, $\beta = e$, μ, τ) are the Yukawa coupling constants, λ_ϕ is a dimensionful coupling constant, C is the charge conjugation operator, and the triplet Δ is presented in the 2×2 matrix form as

$$\Delta = \frac{1}{\sqrt{2}}\sigma_i \Delta_i = \begin{pmatrix} \frac{\Delta^+}{\sqrt{2}} & \Delta^{++} \\ \Delta^0 & -\frac{\Delta^+}{\sqrt{2}} \end{pmatrix}, \tag{3.9}$$

where σ_i is the Pauli matrix for $i = 1, 2, 3$. The tree-level interactions of the leptons and the scalar triplet Δ are presented in Figure 3.2. Note that the triplet scalar Δ does not couple with quarks.

Upon the electroweak symmetry breaking, the neutrino masses are generated at the tree-level through the coupling presented in Figure 3.2a, which leads to an

effective dimension–5 operator $LL\phi\phi$ and yields a Majorana mass [73]

$$(m_\nu)_{\alpha\beta} = -2\, Y_{\alpha\beta}\, v^2\, \frac{\lambda_\phi}{M_\Delta^2}, \tag{3.10}$$

where $v/\sqrt{2} \simeq 174$ GeV is the vacuum expectation value of the SM Higgs field ϕ and M_Δ is the mass of the triplet Δ.

In addition to the neutrino masses, the scalar triplet Δ also influences various electroweak parameters, some of which can be measured to a great precision. An example of these parameters is the mass of the weak boson $\mathrm{W}^\pm$, which gets a shift from the dimension–6 operators as follows [73]:

$$\delta M_\mathrm{W}^2 = -\frac{M_\mathrm{W}^2}{2M_\mathrm{W}^2 - M_\mathrm{Z}^2}\left(\frac{|\lambda_\phi|^2}{M_\Delta^4}\frac{M_\mathrm{W}^2}{G_F\sqrt{2}} - \frac{M_\mathrm{W}^2 - M_\mathrm{Z}^2}{\sqrt{2}G_F M_\Delta^2} Y_{e\mu} Y_{e\mu}^\dagger\right), \tag{3.11}$$

where M_W is the SM prediction for the $\mathrm{W}^\pm$ mass, λ_ϕ is the dimensionful strength of the trilinear $\Delta\phi\phi$ coupling, $Y_{e\mu}$ is the Yukawa coupling constant, and δM_W is the correction to the $\mathrm{W}^\pm$ mass induced by the scalar triplet Δ. In this scheme, M_Z and G_F are the experimental values of the renormalized Z^0 mass and the Fermi coupling constant. Comparing the SM prediction $M_\mathrm{W} \simeq (80.47887 \pm 0.0515)$ GeV and the experimentally measured value, it has been shown that the parameters λ_ϕ and M_Δ^2 can be constrained to $|\lambda_\phi|/M_\Delta^2 < 8.7\times10^{-2}$ TeV^{-1} [73].

The other notable signatures of the scalar triplet are the possibility of the lepton flavour violating (LFV) processes, e.g. the $\mu^- \to e^- e^+ e^-$ decay, and the so called non-standard neutrino interactions (NSI) that affect neutrino oscillations in matter (see Figure 3.2).

The effects of the triplet Higgs bosons are investigated in neutrino oscillations as well as in the LFV processes in Publication V. The main results of the publication are discussed in Chapter 6.

3.3 Parametrizing new physics at low energies

Many of the new physics signatures that emerge from the various SM extensions have also implications at the GeV energy scale, where they can affect neutrino oscillations. In this Section, we discuss the parametrization methods that can be used to study these new physics effects in long baseline neutrino experiments. Whereas Section 3.3.1 concerns the active–sterile neutrino mixing, the non-unitarity of the neutrino mixing matrix is discussed in Section 3.3.2, and the non-standard neutrino interactions in Section 3.3.3.

3.3.1 Active–sterile neutrino mixing

The possibility that the active neutrinos ν_e, ν_μ and ν_τ could mix with the sterile neutrinos, resulting in a new neutrino mass state with a mass in the $m_{\text{sterile}} \sim \mathcal{O}(\text{eV})$ scale and predominantly sterile in its interactions, has been a subject of active discussion in neutrino physics already for a long time. Though the eV–scale sterile neutrinos are too light to be consistent with the Type I seesaw mechanism in its simplest form, there have been several observations of anomalous neutrino oscillation in the solar, reactor and short baseline neutrino data, where the experimental data could not be thoroughly explained with the three-neutrino oscillations, but seem to indicate the existence of a fourth, relatively light neutrino species. A well-known example of these anomalies is the anomaly seen in the short baseline LSND experiment [25, 26] (see Figure 3.3), where the $3.8\,\sigma$ CL excess of the electron-like events in $\bar{\nu}_\mu \to \bar{\nu}_e$ oscillations has been interpreted as a potential signal of active–sterile neutrino oscillations with $\Delta m^2_{41} = m^2_4 - m^2_1 \sim \mathcal{O}(\text{eV}^2)$, where m_4 is the mass of the new mass eigenstate arising from the active–sterile mixing (see Figure 3.4). This excess was recently confirmed in the MiniBooNE experiment [27] with a similar excess in the $\nu_\mu \to \nu_e$ channel, building up a combined $6.1\,\sigma$ CL significance. There have been similar reports of anomalous patterns in the reactor neutrino experiments like Daya Bay and Double Chooz [84], however, it has been recently disputed whether the observed excess is indeed a hint of a light, predominantly sterile neutrino (see Ref. [85] for a detailed review). It will be investigated in the presently running MicroBooNE experiment [86] whether the excess in MiniBooNE is due to the electrons or photons, and in the upcoming SBND experiment [87] whether it is due to active–sterile oscillations in the $\Delta m^2_{\text{sterile}} \sim \text{eV}^2$ regime. The reactor neutrino anomaly, on the other hand, will be cross-checked in the PROSPECT experiment [88], which recently started taking data.

If the active–sterile neutrino oscillations are confirmed in the mass regime where $\Delta m^2_{41} \simeq 0.1.....10$ eV^2, it could also affect the neutrino oscillations studied in the long baseline neutrino experiments.

Perhaps the most commonly used method to parametrize the active–sterile neutrino oscillations is to use the so called Okubo notation [90], which is also used to construct the CKM matrix for the quark mixing and the PMNS for the three-neutrino oscillations. For example, in the so called 3+1 model, where a single sterile neutrino mixes with the three active neutrinos, the full neutrino mixing matrix is a 4×4 unitary matrix that comprises of six discreet rotations:

$$U = \tilde{R}(\theta_{34})\, R(\theta_{24})\, \tilde{R}(\theta_{14})\, R(\theta_{23})\, \tilde{R}(\theta_{13})\, R(\theta_{12}), \tag{3.12}$$

where the rotation matrices $R(\theta_{12})$, $\tilde{R}(\theta_{13})$ and $R(\theta_{23})$ are the usual solar, reactor and

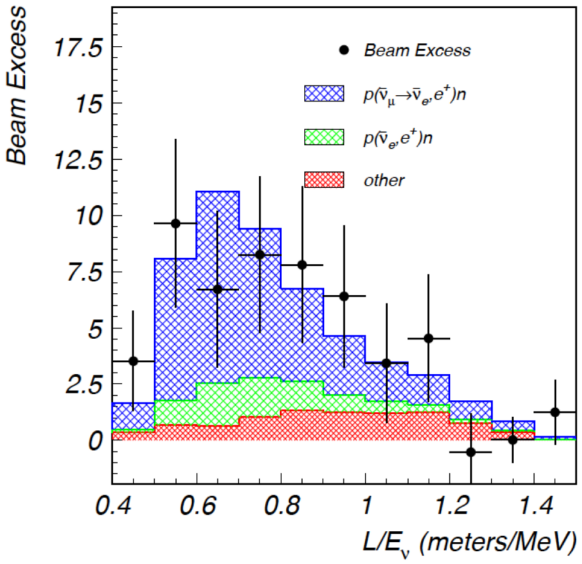

FIGURE 3.3 The observed beam excess in the LSND experiment, indicating the possible $\bar{\nu}_\mu \to \bar{\nu}_e$ appearance. The black dots corresponds to the measured data points, whereas the red and green histograms illustrate the experimental background. The blue histogram presents an example of what a $\bar{\nu}_\mu \to \bar{\nu}_e$ signal could look like in the case of $\Delta m^2 \simeq 1$ eV^2. This image is taken from Ref. [89].

atmospheric matrices of the PMNS matrix, but embedded in 4×4 matrices, e.g.

$$R(\theta_{12}) = \begin{pmatrix} c_{12} & s_{12} & 0 & 0 \\ -s_{12} & c_{12} & 0 & 0 \\ 0 & 0 & 1 & 0 \\ 0 & 0 & 0 & 1 \end{pmatrix}. \tag{3.13}$$

The rotation matrices $\tilde{R}(\theta_{13})$ and $R(\theta_{23})$ are defined in a similar manner. The active–sterile neutrino mixing is brought upon with the three new rotation matrices, of which $\tilde{R}(\theta_{14})$ and $\tilde{R}(\theta_{34})$ are complex and $R(\theta_{24})$ is not. For example, $\tilde{R}(\theta_{14})$ is given by:

$$\tilde{R}(\theta_{14}) = \begin{pmatrix} c_{14} & 0 & 0 & e^{-i\phi_{14}} s_{14} \\ 0 & 1 & 0 & 0 \\ 0 & 0 & 1 & 0 \\ -e^{i\phi_{14}} s_{14} & 0 & 0 & c_{14} \end{pmatrix}, \tag{3.14}$$

where $c_{14} = \cos\theta_{14}$ and $s_{14} = \sin\theta_{14}$, and ϕ_{14} is a new CP phase parameter. The other oscillation parameters related to the sterile neutrino are θ_{24}, θ_{34} and ϕ_{34}. One can easily obtain the standard three-neutrino oscillation scheme from equations (3.12)–(3.14) when the parameters associated with the sterile neutrino are set to zero, i.e.

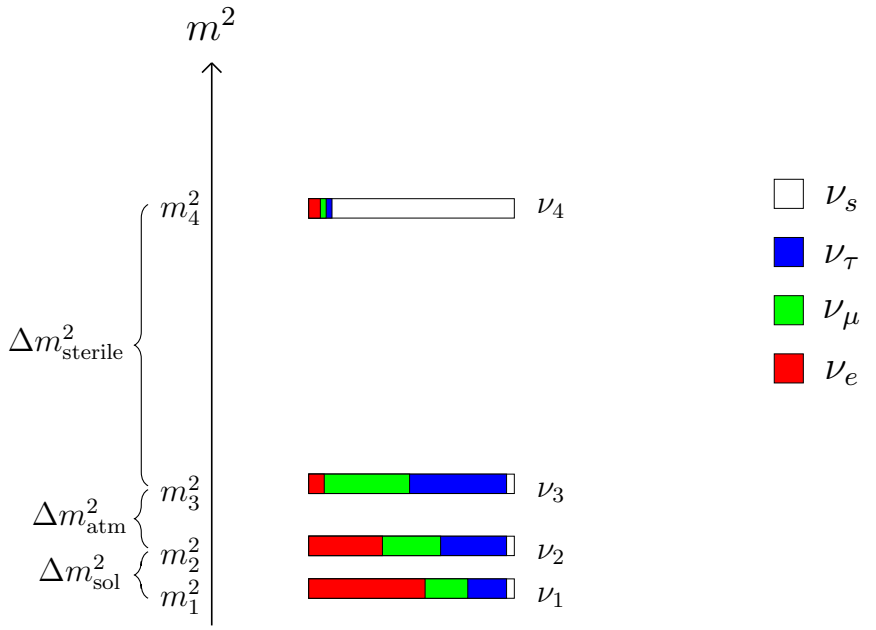

FIGURE 3.4 An illustrative chart of the neutrino masses and their compositions in presence of a sterile neutrino. The mixing between the active neutrinos ν_e, ν_μ, ν_τ and the sterile neutrino ν_s is typically small due to the relatively large value of $\Delta m^2_{\text{sterile}}$. The image is not drawn to the exact scale.

when $\theta_{14} = \theta_{24} = \theta_{34} = 0$.

In the 3+1 model, the probability for the neutrino of flavour $l = e, \mu, \tau$ oscillating into a neutrino of flavour $l' = e, \mu, \tau$ can be written as [89]

$$P_{\nu_l \to \nu_{l'}} \simeq 4 \left|U_{l4}\right|^2 \left|U_{l'4}\right|^2 \sin^2 \left(1.27 \frac{\Delta m^2_{41} L}{E}\right), \tag{3.15}$$

where $l \neq l'$, L is the baseline length in m, E is the energy of the neutrino in MeV, and U_{l4} and $U_{l'4}$ are elements of the mixing matrix U of the equation (3.12). The active–sterile oscillations that would match the LSND anomaly, where $\Delta m^2_{41} \simeq 1\,\text{eV}^2$ can typically be studied in oscillation experiments with a short baseline, where e.g. $\nu_\mu \to \nu_e$ oscillations are probed with $L \sim 100$ m and $E \lesssim 1$ GeV.

3.3.2 Non-unitarity of the mixing matrix

If the sterile neutrinos are so heavy that the active–sterile neutrino oscillations could not develop in the neutrino oscillation experiment, the only traceable signature of the sterile neutrinos would be the non-unitarity of the neutrino mixing matrix. This is typically the case in the models employing the Type I seesaw mechanism, where the sterile neutrino mass is typically close to the Grand Unification scale 10^{14} GeV.

The non-unitarity of the neutrino mixing matrix stems from the fact that in the

presence of one or more sterile neutrinos, the 3×3 matrix that governs the ordinary three-neutrino oscillations becomes a sub-matrix of the larger unitary matrix $\mathcal{U}$, that is,

$$\mathcal{U} = \begin{pmatrix} N & S \\ T & V \end{pmatrix}, \tag{3.16}$$

where the oscillations between the three flavour states ν_e, ν_μ and ν_τ is dictated by the 3×3 sub-matrix N, whereas the oscillations between the active–sterile, sterile–active, and sterile–sterile states are defined by S, T and V, respectively [31]. The dimensions of these matrices depend on the number of sterile neutrinos.

As usual, the propagation of the active neutrinos in matter is determined by the effective Hamiltonian, which is now dependent on the non-unitary matrix N [91]:

$$H = \frac{1}{2E} \begin{pmatrix} 0 & 0 & 0 \\ 0 & \Delta m^2_{21} & 0 \\ 0 & 0 & \Delta m^2_{31} \end{pmatrix} + N^\dagger \begin{pmatrix} V_{\rm CC} + V_{\rm NC} & 0 & 0 \\ 0 & V_{\rm NC} & 0 \\ 0 & 0 & V_{\rm NC} \end{pmatrix} N. \tag{3.17}$$

Since the mixing matrix N is not unitary, the NC matter potential $V_{\rm NC}$ can no longer be ignored in the Hamiltonian in equation (3.17), in contrast with the ordinary three-neutrino case.

There are multiple ways to define the non-unitary mixing matrix N. In this work, we focus on the method presented in Ref. [92], where the non-unitarity nature is absorbed into the triangle matrix

$$N^{\rm NP} = \begin{pmatrix} \alpha_{11} & 0 & 0 \\ \alpha_{21} & \alpha_{22} & 0 \\ \alpha_{31} & \alpha_{32} & \alpha_{33} \end{pmatrix}, \tag{3.18}$$

where the diagonal elements α_{11}, α_{22} and α_{33} are real and close to unity, and the off-diagonal elements α_{21}, α_{31} and α_{32} are complex and small compared with the diagonal ones. It has been shown in Ref. [93] that of the off-diagonal parameters α_{21} has the most significant effect on the $\nu_\mu \leftrightarrow \nu_e$ oscillation probabilities, whereas the parameters α_{31} and α_{32} are less significant.

The non-unitary mixing matrix controlling the active neutrino oscillations in equation (3.17) is obtained from the PMNS matrix $U_{\rm PMNS}$ and the non-unitary part $N^{\rm NP}$ as $N = N^{\rm NP} U_{\rm PMNS}$.

The non-unitarity part of the mixing matrix N can be defined in different ways. In this work, we also adopt the notation that is used in Refs. [94–96]:

$$N^{\rm NP} = \begin{pmatrix} 1 - \alpha_{ee} & 0 & 0 \\ \alpha_{\mu e} & 1 - \alpha_{\mu\mu} & 0 \\ \alpha_{\tau e} & \alpha_{\tau\mu} & 1 - \alpha_{\tau\tau} \end{pmatrix}, \tag{3.19}$$

where all of the parameters $\alpha_{ll'}$ (l, $l' = e$, μ, τ) are small, $\alpha_{ll'} \ll 1$.

When the non-standard effects related to the production and detection of the neutrino are taken into account, the probability of the conversion $\nu_l \to \nu_{l'}$ can be written as follows:

$$P_{\nu_l \to \nu_{l'}} = \frac{\left|\langle \nu_{l'}|e^{-iHL}|\nu_l\rangle\right|^2}{\left|\langle \nu_l|\nu_l\rangle\right|^2} = \frac{\left|\langle \nu_{l'}|e^{-iHL}|\nu_l\rangle\right|^2}{((N^\dagger N)_{ll})^2}. \tag{3.20}$$

The denominator $\langle \nu_l|\nu_l\rangle$ comes from the fact that in long baseline experiments the probability is inferred from the comparison of the neutrino rates in the far and near detectors [94]. In the standard three-neutrino scheme the denominator $\langle \nu_l|\nu_l\rangle$ attains unity, but in the case of non-unitary mixing matrix it can also be different from unity. However, this effect is typically small and it can be safely neglected in the $\nu_l \to \nu_{l'}$ conversion when $\alpha_{ll} \ll 1$ ($l = e, \mu, \tau$), or equivalently $1-\alpha_{ii} \ll 1$ (i =1, 2, 3). For larger values, though, the normalization factor $(N^\dagger N)_{ll}$ must be taken into account.

The non-unitarity parametrizations in equations (3.18) and (3.19) can always be related with the rotation based parametrization we have used in the case of active–sterile neutrino mixing in Section 3.3.1. For instance, the oscillation parameters of the 3+1 mixing case can be related with the matrix containing the non-unitarity part $N^{\rm NP}$ as follows:

$$\begin{pmatrix} N^{\rm NP}U_{\rm PMNS} & S \\ T & V \end{pmatrix} = \tilde{R}(\theta_{34})\, R(\theta_{24})\, \tilde{R}(\theta_{14})\, R(\theta_{23})\, \tilde{R}(\theta_{13})\, R(\theta_{12}), \tag{3.21}$$

where S, T and V are matrices of dimensions 3×1, 1×3 and 1×1, respectively. When one chooses the alpha parametrization shown in equation (3.18), the alpha parameters can be expressed in terms of the active–sterile mixing angles θ_{14}, θ_{24}, θ_{34} and the CP phases ϕ_{14} and ϕ_{34} as follows:

$$\begin{aligned} \alpha_{11} &= c_{14} & \alpha_{21} &= s_{14}s_{24}e^{-i\phi_{14}} \\ \alpha_{22} &= c_{24} & \alpha_{31} &= s_{14}s_{34}e^{-i(\phi_{14}-\phi_{34})} \\ \alpha_{33} &= c_{34} & \alpha_{32} &= s_{24}s_{34}e^{-i\phi_{34}} \end{aligned} \tag{3.22}$$

Similar relations can be derived for also the 3+2 and 3+3 neutrino models, though the expressions become rather complicated, and they are not presented here. See Ref. [92] for the generalized equations.

3.3.3 Non-standard neutrino interactions

The new physics beyond the SM operative in the generation of the neutrino masses generally contains new neutrino interactions, and it therefore influences the production, detection and the neutrino propagation in matter. This kind of neutrino interactions are known as the non-standard neutrino interactions (NSI) [32, 97, 98]. A good example of a particle that generates NSI effects in the neutrino propagation

is the triplet Higgs bosons of the Type II seesaw mechanism [83], which we discussed in Section 3.2.2. These scalars couple to the left-handed neutrino fields and the right-handed antineutrino fields, but have no couplings with the quarks. The interactions they mediate are in general much weaker than the ordinary weak interactions mediated by the $\mathrm{W}^{\pm}$ and Z^{0} bosons, but may still be relevant for the neutrino oscillations in matter, as well as for some rare processes.

When the new particles are sufficiently heavy with respect to the neutrino energies, the interaction lengths become so short that interactions can be approximated as point-like. In such a case, it is convenient to use the effective field theory approach, where NSI are parametrized by the following CC and NC Lagrangians [99]:

$$\begin{aligned} \mathcal{L}_{\mathrm{NSI}}^{\mathrm{CC}} &= -2\sqrt{2}G_F\varepsilon_{\alpha\beta}^{ff',\mathrm{C}}(\overline{\nu}_{\alpha\mathrm{L}}\gamma^{\mu}P_{\mathrm{L}}\nu_{\beta})(\overline{f}\gamma^{\mu}P_{\mathrm{C}}f'), \\ \mathcal{L}_{\mathrm{NSI}}^{\mathrm{NC}} &= -2\sqrt{2}G_F\varepsilon_{\alpha\beta}^{f,\mathrm{C}}(\overline{\nu}_{\alpha\mathrm{L}}\gamma^{\mu}P_{\mathrm{L}}\nu_{\beta})(\overline{f}\gamma^{\mu}P_{\mathrm{C}}f), \end{aligned} \tag{3.23}$$

where P_{L} and P_{C} are the chiral projection operators ($\mathrm{C} = \mathrm{L}, \mathrm{R}$), G_F is the Fermi coupling constant, f and f' stand for charged fermions (f, $f' = e$, μ, τ), and α, $\beta = e$, μ, τ label the neutrino flavours in the interaction. The NSI parameters $\varepsilon_{\alpha\beta}^{ff',\mathrm{C}}$ and $\varepsilon_{\alpha\beta}^{f,\mathrm{C}}$ are dimensionless numbers which parametrize the strength of the NSI couplings.

The CC and NC–like interactions presented in equation (3.23) are assumed to have the V–A Lorentz structure for neutrinos, but allowing both V–A and V+A couplings for the charged fermions. Whilst the CC Lagrangian $\mathcal{L}_{\mathrm{NSI}}^{\mathrm{CC}}$ contributes to the production and detection of the neutrinos, the NC Lagrangian $\mathcal{L}_{\mathrm{NSI}}^{\mathrm{NC}}$ has importance in the neutrino propagation. One can obtain one Lagrangian from the other using the so called Fierz transformation, though, as is done in the case of the triplet interactions below.

The NSI–Lagrangian for the CC interactions alters the neutrino production so that the neutrinos are no longer produced as pure flavour states, but they also have small components of other flavours. Similarly, the interaction that is utilized in the detection is no longer obliged to involve only one neutrino flavour [98]:

$$\begin{aligned} |\nu_{\alpha}^{s}\rangle &= |\nu_{\alpha}\rangle + \varepsilon_{\alpha\beta}^{s}|\nu_{\beta}\rangle \\ \langle\nu_{\beta}^{d}| &= \langle\nu_{\beta}| + \varepsilon_{\alpha\beta}^{d}\langle\nu_{\alpha}| \end{aligned} \tag{3.24}$$

where ε^{s} and ε^{d} are the matrices that contain the NSI parameters involved in the neutrino source and detector, respectively. The NSI parameters associated with the source and detection are dimensionless and complex, and if the production and detection methods are based on the same interaction, $\varepsilon_{\alpha\beta}^{d} = (\varepsilon_{\alpha\beta}^{s})^{*}$.

The NSI–Lagrangian associated with the NC interactions modifies the neutrino

propagation by adding a new term to the matter potential part of the Hamiltonian:

$$H = \frac{1}{2E}\left[U\,\mathrm{diag}(m_1^2, m_2^2, m_3^2)U^\dagger + \mathrm{diag}(\hat{A}, 0, 0) + \hat{A}\varepsilon^m\right], \tag{3.25}$$

where U is the PMNS matrix, $\hat{A} = 2\sqrt{2}EG_FN_e$ and ε^m is the matrix that contains the so called matter–NSI parameters $\varepsilon^m_{\alpha\beta}$ (α, $\beta = e$, μ, τ):

$$\varepsilon^m_{\alpha\beta} = \sum_{f,\mathrm{C}} \varepsilon^{f,\mathrm{C}}_{\alpha\beta}\frac{N_f}{N_e}, \tag{3.26}$$

where $\varepsilon^{f,\mathrm{C}}_{\alpha\beta}$ are the NSI parameters associated with the low energy NC Lagrangian shown in equation (3.24), and N_f is the number density of the fermions of flavour f in the medium which the neutrinos traverse.

The matrix ε^m that is shown in equation (3.25) is defined as

$$\varepsilon^m = \begin{pmatrix} \varepsilon^m_{ee} & \varepsilon^m_{e\mu} & \varepsilon^m_{e\tau} \\ \varepsilon^{m*}_{e\mu} & \varepsilon^m_{\mu\mu} & \varepsilon^m_{\mu\tau} \\ \varepsilon^{m*}_{e\tau} & \varepsilon^{m*}_{\mu\tau} & \varepsilon^m_{\tau\tau} \end{pmatrix}. \tag{3.27}$$

Whereas the diagonal elements of the NSI matrix must be real, the non-diagonal elements can be complex.

The probability of a neutrino oscillating from ν_α to ν_β can now be written as

$$P_{\nu_\alpha\to\nu_\beta} = \left|\langle\nu^d_\beta|e^{-iHL}|\nu^s_\alpha\rangle\right|^2, \tag{3.28}$$

where the initial and final states $|\nu^s_\alpha\rangle$ and $\langle\nu^d_\beta|$ are given by equation (3.24), and the effective Hamiltonian H by equations (3.25)–(3.26), respectively.

The NSI parameters can also be related to the parameters associated with the active–sterile neutrino oscillations and the non-unitarity of the neutrino mixing matrix, see e.g. equation (3.22). Neglecting the higher order terms of $\alpha_{ll'}$ (l, $l' = e$, μ, τ), one may write the following correspondence between the non-unitarity and NSI parameters [94]:

$$\begin{aligned} &\varepsilon^m_{ee} = -\alpha_{ee} && \varepsilon^m_{\mu\mu} = \alpha_{\mu\mu} && \varepsilon^m_{\tau\tau} = \alpha_{\tau\tau} \\ &\varepsilon^m_{e\mu} = \frac{1}{2}\alpha^*_{\mu e} && \varepsilon^m_{e\tau} = \frac{1}{2}\alpha^*_{\tau e} && \varepsilon^m_{\mu\tau} = \frac{1}{2}\alpha^*_{\tau\mu}. \end{aligned} \tag{3.29}$$

As it is the case with the non-unitarity, the probability in long baseline neutrino experiments is often inferred from the ratio of the neutrino rates measured in the far and near detector, and hence it must be normalized:

$$P_{\nu_\alpha\to\nu_\beta} = \frac{\left|\langle\nu^d_\beta|e^{-iHL}|\nu^s_\alpha\rangle\right|^2}{\left|\langle\nu^s_\alpha|\nu^s_\alpha\rangle\right|^2}, \tag{3.30}$$

where the normalization factor $|\langle\nu^s_\alpha|\nu^s_\alpha\rangle|^2$ arises from the CC–like NSI effects and is close to unity. This factor can be replaced with unity when $\left|\varepsilon^s_{\beta\beta}\right|^2 \ll 1$.

One of the possible sources of the NSI effects are the interactions mediated by the scalar triplet $\Delta = (\Delta^0, \Delta^+, \Delta^{++})$ of the Type II seesaw mechanism, which is described in Section 3.2.2. Beginning from the effective Lagrangian that defines the triplet interactions (cf. equation (3.8)) relevant for neutrino oscillations, the Yukawa couplings of Δ's and leptons are given by the Lagrangian [83]:

$$\mathcal{L}_Y = Y_{\alpha\beta}\,\left[\Delta^0\,\overline{\nu^C_{\alpha\mathrm{R}}}\,\nu_{\beta\mathrm{L}} - \frac{1}{\sqrt{2}}\Delta^+\,\left(\overline{\ell^C_{\alpha\mathrm{R}}}\,\nu_{\beta\mathrm{L}} + \overline{\nu^C_{\alpha\mathrm{R}}}\,\ell_{\beta\mathrm{L}}\right) - \Delta^{++}\,\overline{\ell^C_{\alpha\mathrm{R}}}\,\ell_{\beta\mathrm{L}}\right] + \text{h.c.} \tag{3.31}$$

where $Y_{\alpha\beta}$ (α, $\beta = e$, μ, τ) are the coupling constants. In the second order of perturbation theory, these interactions lead to the neutrino-matter NSI, the NSI of four charged leptons, and the Majorana mass term of the active neutrino flavours (see Figure 3.2 for the tree-level Feynman diagrams).

In the limit where the presupposedly degenerate mass of the scalar triplet, M_Δ, is sufficiently large compared with the transferred momenta, the amplitudes of the triplet interactions that give rise to the Majorana mass term and the neutrino matter NSI can be described with the following Lagrangians:

$$\mathcal{L}^m_\nu = \frac{Y_{\alpha\beta}\,\lambda_\phi\,v^2}{M^2_\Delta}\,\left(\overline{\nu^C_{\alpha\mathrm{R}}}\,\nu_{\beta\mathrm{L}}\right) = -\frac{1}{2}\,(m_\nu)_{\alpha\beta}\,\overline{\nu^C_{\alpha\mathrm{R}}}\,\nu_{\beta\mathrm{L}}, \tag{3.32}$$

$$\mathcal{L}_{\mathrm{NSI}} = \frac{Y_{\sigma\beta}\,Y^\dagger_{\alpha\rho}}{M^2_\Delta}\,\left(\overline{\nu_{\alpha L}}\,\gamma_\mu\,\nu_{\beta\mathrm{L}}\right)\,\left(\overline{\ell_{\rho\mathrm{L}}}\,\gamma^\mu\,\ell_{\sigma\mathrm{L}}\right), \tag{3.33}$$

where m_ν is the mass matrix of the active neutrinos, defined in the flavour basis.

The NSI parameters describing the triplet interactions can be obtained by comparing the effective Lagrangians in equations (3.32) and (3.33) with the effective CC Lagrangian $\mathcal{L}^{\mathrm{CC}}_{\mathrm{NSI}}$ from equation (3.23). The result is [83]

$$\varepsilon^{\rho\sigma}_{\alpha\beta} = -\frac{M^2_\Delta}{8\sqrt{2}\,G_F\,\hat{v}^4\,\lambda^2_\phi}\,(m_\nu)_{\sigma\beta}\,(m^\dagger_\nu)_{\alpha\rho}, \tag{3.34}$$

where we denote $\hat{v} = v/\sqrt{2}$. The indices β, σ label the lepton flavours in the initial state, and α, ρ in the final state. The matter–NSI parameters, which alter the neutrino propagation in matter, are obtained from equation (3.34) as $\varepsilon^m_{\alpha\beta} \equiv \varepsilon^{ee}_{\alpha\beta}$.

The neutrino propagation is not the only observable process which is changed by the interactions with the scalar triplet. The amplitude for the four-lepton NSI is described by the effective Lagrangian

$$\mathcal{L}_{4\ell} = \frac{Y_{\sigma\beta}\,Y^\dagger_{\alpha\rho}}{M^2_\Delta}\,\left(\overline{\ell_{\alpha\mathrm{L}}}\,\gamma_\mu\,\ell_{\beta\mathrm{L}}\right)\,\left(\overline{\ell_{\rho\mathrm{L}}}\,\gamma^\mu\,\ell_{\sigma\mathrm{L}}\right), \tag{3.35}$$

which leads to an analogue of equation (3.34) but for processes where the particles in the initial and final states are all charged leptons. This type of NSI contributes to the lepton flavour violating processes where the lepton family number is violated. For instance, the muon decay into an electron and a positronium, $\mu^- \to e^- e^+ e^-$, gains the following decay width [73, 83]:

$$\Gamma(\mu^- \to e^- e^+ e^-) = \frac{m_\mu^5}{24\,\pi^3} G_F \left|\varepsilon_{ee}^{e\mu}\right|^2 , \tag{3.36}$$

where m_μ is the muon mass and $\varepsilon_{ee}^{e\mu}$ is obtained from equation (3.34). Similar equations for the decay widths can be derived for any arbitrary LFV decay $\ell_\sigma \to \ell_\rho\, \ell_\alpha\, \ell_\beta$. The non-observation of these processes sets stringent limits on the parameters $\varepsilon_{\alpha\beta}^{\rho\sigma}$.

Chapter 4

Simulation of the long baseline neutrino experiments

In this thesis, we determine the experimental sensitivities for the determination of the θ_{23} octant and the non-standard neutrino interaction parameters $\varepsilon^m_{ll'}$ (l, $l' = e$, μ, τ) in long baseline neutrino oscillation experiments. An important part of the methodology of this work is the simulation of long baseline experiments, where the sensitivities of the experimental configurations are estimated using the General Long-Baseline Experiment Simulator (GLoBES) [100, 101]. The software discussed in this work is based on the standard compilation of GLoBES, which is appropriately modified to simulate the new physics effects arising from the SM extensions. This Chapter provides a general overview to the experimental configurations and numerical methods featured in the work that is presented in this thesis. The experimental configurations of two setups are described in Section 4.1. Section 4.2 details the main principles of the numerical methods, and Section 4.3 summarizes the relevant simulation parameters.

4.1 Overview of the simulated experiments

The work presented in this thesis focuses on two particular experimental configurations. On the one hand, we review the the long baseline neutrino oscillation part of the LAGUNA–LBNO project [102, 103], which was a design study about a long baseline neutrino experiment featuring the 2300-km-long baseline between CERN, Switzerland, and Pyhäsalmi, Finland. The experiment proposed in this design study was named as the Long Baseline Neutrino Observatory (LBNO) [104]. The other experiment that is discussed in this work is the Deep Underground Neutrino Experiment (DUNE) [20], which will provide an analogous experimental configuration with a 1300-km-long baseline between Fermi National Accelerator Laboratory (Fermilab), IL, and Lead, SD, in the United States. The construction for DUNE started in July 2017, and the experiment is projected to begin operations in 2027. Though the

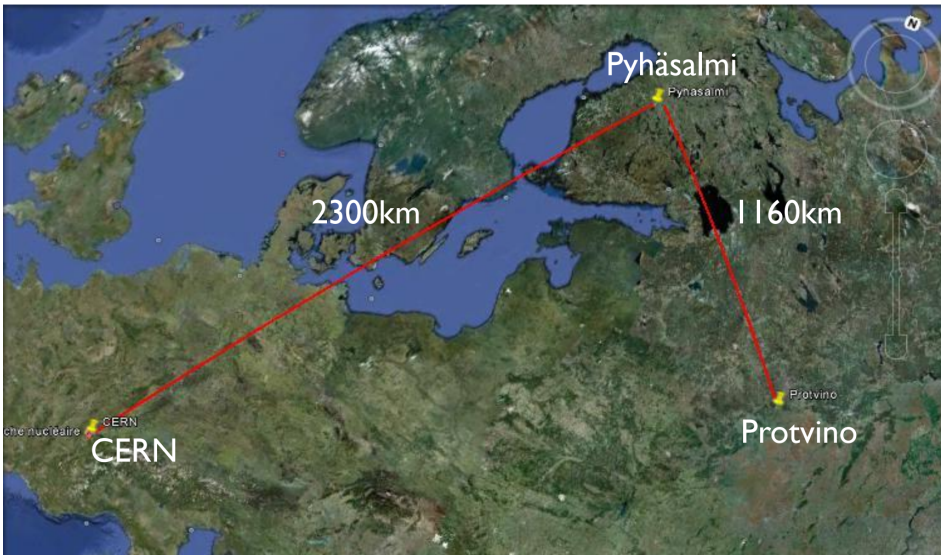

FIGURE 4.1 Schematics of the available baselines in the LBNO configuration [106]. In the plan to build LBNO, it was proposed that a neutrino beam is generated at CERN, Switzerland, whilst the detector, a large-scale liquid argon time projection chamber, would have been placed in a mine in Pyhäsalmi, Finland. An option to send a second, geometrically orthogonal neutrino beam from Protvino, Russia, was also proposed.

LAGUNA–LBNO project never led to the construction of a long baseline neutrino experiment [105], the detector technology that was developed in the design study has been adopted in the designing of DUNE.

4.1.1 LBNO

LBNO is the long baseline neutrino experiment project that was proposed after the LAGUNA and LAGUNA–LBNO design studies. The LBNO configuration features a 2300-km-long baseline, where the neutrino beam was supposed to be delivered using the SPS accelerator at CERN, Switzerland, and studied at an underground detector facility in Pyhäsalmi, Finland. The design studies also considered the opportunity of sending another neutrino beam from Protvino, Russia [106]. An illustration of the two baseline options is presented in Figure 4.1.

According to the proposal [104], the experiment runs at first with the SPS accelerator, which is able to deliver 400 GeV protons at roughly 750 kW and 10^{20} protons-on-target (POT) per year. The accelerated proton beam hits a graphite target at the accelerator facility, creating an intense beam of positive and negative pions. The generated pions decay subsequently into muon neutrinos and antineutrinos. The beam can be switched between muon neutrinos and antineutrinos by separating the positive and negative pions with magnetic horns before the decay. In the second phase the neutrino beam would be produced with the so called High-Power Proton Synchrotron (HPPS) instead, increasing the beam power to 2 MW at 50 GeV proton

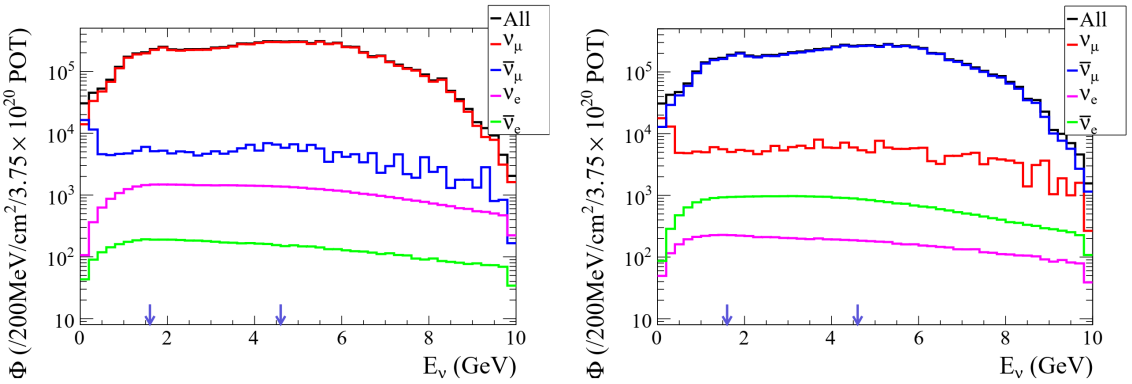

FIGURE 4.2 The spectrum of the neutrino fluxes that are generated in SPS for LBNO [106]. The fluxes are given as function of the neutrino energy E_ν, binned evenly into 200 MeV energy bins and assuming an annual yield of 3.75×10^{20} protons-on-target (POT). Whereas the left panel shows the flux for the neutrino mode, the right panel shows the flux for the antineutrino mode. The locations of the first and second oscillation maximum are indicated with the blue arrows.

energy and 3×10^{21} POT $\cdot$ year^{-1}. The proposal envisioned the experiment to run five years in the muon neutrino mode and five years in the muon antineutrino mode.

The fluxes for the neutrino and antineutrino beams are shown in Figure 4.2. The proposed beam facility configuration would have been able to produce a neutrino flux which has a high yield of muon neutrinos and antineutrinos near the first and second oscillation maxima, where the probabilities for the $\nu_\mu \to \nu_e$ and $\bar{\nu}_\mu \to \bar{\nu}_e$ oscillations are at their local maximum. In LBNO, the first and second oscillation maxima are located between 4...5 GeV and 1...2 GeV, respectively. The large numbers of ν_μ and $\bar{\nu}_\mu$ near the oscillation maximum energies ensures the sufficient oscillation to the ν_e and $\bar{\nu}_e$ states. Both of the beams contain impurities (e.g. the ν_μ beam has small components of $\bar{\nu}_\mu$, ν_e and $\bar{\nu}_e$), which are irreducible and contribute to the background.

The neutrino detector in LBNO was planned to be based on the so called dual phase liquid argon time projection chamber (LArTPC) technology. The LArTPC technology is founded on the idea of detecting neutrinos with liquidized argon, which is subjected to a strong electric field. When an energetic electron or muon neutrino interacts with an argon nuclei, a charged lepton of the same flavour is created. The charged lepton then traverses inside the detector, ionizing the argon atoms on its way. The ionized electrons are drawn by the electric field towards the plane of anodes. In the dual phase version, the anode is encased in a layer of gaseous argon at the top of the detector, which is augmented with a stronger electric field. Once in the gas, the electrons encounter micro-pattern gas detectors, the so called large electron multipliers (LEM), which amplify the drifted charges in the electron avalanche effect before they are collected to the anode wires. The LEM-based amplification used

in the dual phase method is estimated to enhance the signal to roughly 20-fold with respect to the conventional LArTPC design, which has the anode plane immersed in the liquid phase.

Apart from the free electrons, a charged particle crossing the liquid argon produce scintillation light through by exciting the argon atoms. This ultraviolet light is picked up in the photomultiplier tubes deployed at the bottom of the detector. The properties of the event are reconstructed using the information collected from the drift charges and the light, giving information about the energy and the flavour of the incident neutrino.

The detector proposal also includes the addition of a small detector that is based on the magnetized iron calorimeter design, which acts as a tail catcher and collects an independent sample of neutrinos and antineutrinos. This configuration is beneficial in the high energy end of the neutrino spectrum, as the more energetic neutrino events often lead to the longer electron tails.

LArTPC detectors benefit from the relatively high detection efficiency and low energy thresholds. LBNO primarily was planned to study neutrino events taking place between 0.1 GeV and 10 GeV, achieving a 90% efficiency in the electron identification. In the first phase, the far detector of LBNO was planned to contain 20 kton of liquid argon, whereas in the second phase the detector would have been upgraded into 70 kton of fiducial mass.

According to the design study, LBNO would have been able to determine the mass hierarchy at $5\,\sigma$ CL or better for all possible values of δ_{CP}, after running 5+5 years in the neutrino and antineutrino modes. Moreover, it was expected to yield approximately a $3\,\sigma$ CL sensitivity or better for establishing the CP violation for 36.....45% of δ_{CP} values, depending on the true value of θ_{23}.

4.1.2 DUNE

DUNE is a next generation long baseline neutrino experiment that is currently being built in the United States. DUNE comprises of the beam facility at Fermilab and the far detector site at the Sanford Underground Neutrino Facility (SURF), which are located approximately 1300 km apart. The physics program and technical details of DUNE have been described in detail in the Conceptual Design Report (CDR) [51, 107–109], and the status of the development has been recently reviewed in the Interim Design Report [110–112]. The schematics of the DUNE configuration are shown in Figure 4.3.

DUNE bears many similarities with the previously proposed LBNO configuration. On the one hand, the neutrino beam will be generated in DUNE using a 80 GeV and 1.07 MW proton beam, which will be obtained after the PIP-II upgrade at Fermilab. The desired protons-on-target number will be 1.47×10^{21} POT $\cdot$ year^{-1}. In the other end of the baseline, the far detector of DUNE comprises of four LArTPC modules, each hosting 10 kton of liquid argon in fiducial mass. At least one of the

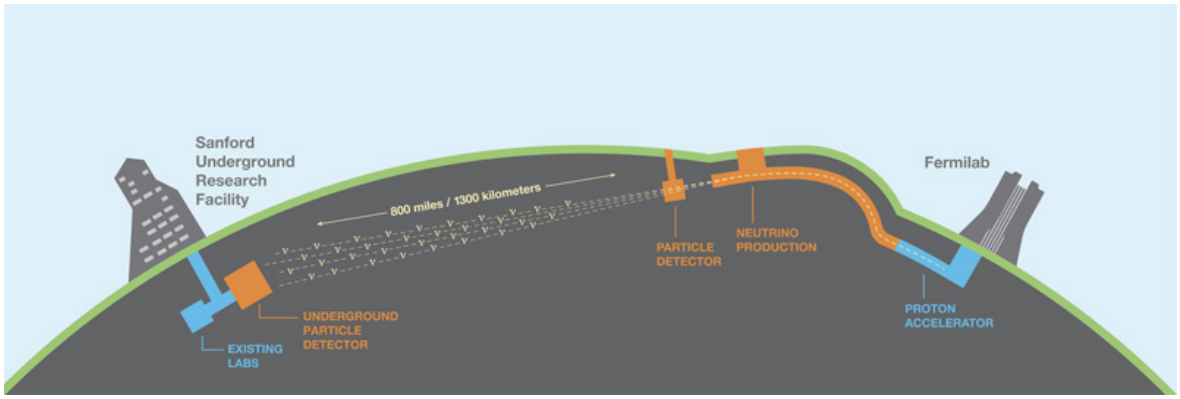

FIGURE 4.3 Schematics of the experimental configuration used in the next generation long baseline neutrino experiment DUNE. The experiment sends an intense neutrino beam over a 1300 km baseline, along which it goes more than 30 km deep underground. The experiment consists of the proton accelerator, pion decay tunnel, near detector, and far detector. This image is taken from Ref. [116].

detector modules will be based on the dual phase design, while the rest will employ the conventional single phase configuration. In the single phase version, the anode is located on the side of the detector, where it is perpendicular to the neutrino beam and completely immersed in the liquid argon. Whereas the dual phase version is yet to be proved in a full-scale experiment, the effectiveness of the single phase method has already been established in the ICARUS experiment [113].

The performance of both the single and dual phase detector designs will be demonstrated in the so called ProtoDUNE project, which consists of two $6\times6\times6$ m^3 detectors and are currently under construction at CERN. The design of the single phase demonstrator is described in the respective technical design report [114]. The dual phase detector was preluded by the smaller $3\times1\times1$ m^3 facility, which holds 4 tonnes of liquid argon. The demonstrator was constructed at CERN in 2016 and operated in 2017 [115].

According to the CDR documents, DUNE is expected to be able to resolve the mass hierarchy problem at a $5\,\sigma$ CL or better for all possible δ_{CP} values, after running 3.5 years in the neutrino mode and 3.5 years in the antineutrino mode. For similar exposures, DUNE will also be able to establish the CP violation at approximately $3\,\sigma$ CL for 60% of δ_{CP} values. With its near detector, DUNE will also be able to study neutrino oscillations at $L/E \sim 1$, which provides a limited sensitivity to the active–sterile neutrino oscillations in the $\Delta m^2_{41} \sim \mathcal{O}(1\ \mathrm{eV}^2)$ regime.

4.2 Principles of the statistical analysis

GLoBES is a computer software that simulates the process of neutrino production, propagation, detection and reconstruction, and data analysis in neutrino oscillation

experiments [100,101]. The software is primarily used for the simulation of the long baseline neutrino experiments, but it is also fit for the simulation of the experiments that are based on nuclear reactors, beta beams and neutrino factories. GLoBES calculates the event rates for the given experimental configuration and determines the χ^2 distributions for the chosen oscillation parameter values. The software can be used to estimate the sensitivities of planned neutrino oscillation experiments, compare the performance of competing technical solutions, and for many other tasks.

In GLoBES, the χ^2 distributions are evaluated by using the following routine. Using the input data regarding the beam production, flux composition, cross sections, detector response, and other relevant matters, GLoBES computes the event rates for each neutrino oscillation channel $\nu_l \rightarrow \nu_{l'}$ (l, $l' = e$, μ, τ) and energy bin E_i. The software computes the oscillation probabilities from two sets of oscillation parameter values, one of which is the so called true values (ω_0) and the other test values (ω). The event rates that are computed from these values, $O_i(\omega_0)$ and $T_i(\omega)$, respectively, define the statistical part of the χ^2 function:

$$\chi^2(\omega, \omega_0) = \sum_i 2 \left[T_i - O_i \left(1 - \ln \frac{T_i}{O_i} \right) \right], \tag{4.1}$$

where i runs through the available energy bins.

The χ^2 presented in equation (4.1) compares the binned event rates originating from the test values (T_1, T_2, ...) to the rates that correspond to the true values (O_1, O_2, ...). The true values are typically chosen from the best-fit values that represent the present experimental data (see Table 2.1 in Chapter 2 for a recent global fit).

The event rate calculated from the true values ω_0 is given by:

$$O_i = N_i^{\mathrm{sg}}(\omega_0) + N_i^{\mathrm{bg}}(\omega_0), \tag{4.2}$$

where N_i^{sg} stands for the rate of the signal events and N_i^{bg} the rate of the background events, both of which are determined from neutrino events collected from the energy bin E_i.

The event rate that corresponds to the test values ω is also dependent on the systematical errors, which are intrinsic for the simulated experiment. For example, the normalization errors are typically accounted as systematics that implements a tilt on the reconstructed neutrino spectrum. In such case, the event rate in the case of the test values is given by:

$$T_i = N_i^{\mathrm{sg}}(\omega)[1 + \pi_1 \zeta_1] + N_i^{\mathrm{bg}}(\omega)[1 + \pi_2 \zeta_2], \tag{4.3}$$

where ζ_1 and ζ_2 are the so called nuisance parameters, which simulate the systematic errors arising from the normalization of the signal and background, respectively.

GLoBES addresses the systematics with the so called pull method, where the

χ^2 function is minimized over the nuisance parameters ζ_1 and ζ_2:

$$\chi^2_{\text{pull}}(\omega, \omega_0) = \min_{\zeta_1,\zeta_2} \left[\chi^2(\omega, \omega_0) + \zeta_1^2 + \zeta_2^2\right], \tag{4.4}$$

where χ^2 is the statistical part given by equation (4.1), and the event rates corresponding to the true and test values, O_i and T_i, are calculated from equations (4.2) and (4.3), respectively. The systematics defined in this manner must be mutually independent, and there can be no correlation between ζ_1 and ζ_2.

The uncertainties pertaining to the true values ω_0 are taken into account as a priori errors, or priors. In this work, the uncertainties related to the standard oscillation parameters are treated with the prior function

$$\begin{aligned}\chi^2_{\text{prior}}(\omega, \omega_0) \;=\; & \left(\frac{\sin^2\theta_{12}(\omega) - \sin^2\theta_{12}(\omega_0)}{\sigma(\sin^2\theta_{12})}\right)^2 + \left(\frac{\sin^2\theta_{13}(\omega) - \sin^2\theta_{13}(\omega_0)}{\sigma(\sin^2\theta_{13})}\right)^2 \\ & + \left(\frac{\sin^2\theta_{23}(\omega) - \sin^2\theta_{23}(\omega_0)}{\sigma(\sin^2\theta_{23})}\right)^2 + \left(\frac{\Delta m^2_{21}(\omega) - \Delta m^2_{21}(\omega_0)}{\sigma(\Delta m^2_{21})}\right)^2 \\ & + \left(\frac{\Delta m^2_{31}(\omega) - \Delta m^2_{31}(\omega_0)}{\sigma(\Delta m^2_{31})}\right)^2 + \left(\frac{\rho(\omega) - \rho(\omega_0)}{\sigma(\rho)}\right)^2, \end{aligned} \tag{4.5}$$

where $\sigma(\sin^2\theta_{12})$, $\sigma(\sin^2\theta_{13})$ and $\sigma(\sin^2\theta_{23})$ are the standard deviations of the parameters $\sin^2\theta_{12}$, $\sin^2\theta_{13}$ and $\sin^2\theta_{23}$, $\sigma(\Delta m^2_{21})$ and $\sigma(\Delta m^2_{31})$ are the standard deviations of the square-mass differences Δm^2_{21} and Δm^2_{31}, and $\sigma(\rho)$ is the standard deviation of the matter density parameter ρ. When new physics effects such as the non-unitarity of the mixing matrix or NSI are present, their respective parameters $\alpha_{ll'}$ and $\varepsilon^m_{\alpha\beta}$ (l, l', α, $\beta = e$, μ, τ) can be included in the prior function in a similar manner.

The overall χ^2 function is obtained from the sum of the pull and prior functions, which is then minimized over the test values, that is, over ω:

$$\chi^2_{\text{total}}(\omega_0) = \min_{\omega} \left[\chi^2_{\text{pull}}(\omega, \omega_0) + \chi^2_{\text{prior}}(\omega, \omega_0)\right]. \tag{4.6}$$

The χ^2_{total} function is therefore minimized over all oscillation parameters in ω, with the pull function χ^2_{pull} controlling the systematics, and the prior function χ^2_{prior} constraining the value ranges over which χ^2_{total} may converge.

In the work presented in this thesis, the experimental sensitivities are calculated as follows. In the case of the determination of the θ_{23} octant, the value that corresponds to the false octant, $90^\circ - \theta_{23}$, can be ruled out at a statistical significance that is obtained from the relative difference:

$$\Delta\chi^2 = \chi^2_{\text{total}}(90^\circ - \theta_{23}) - \chi^2_{\text{total}}(\theta_{23}), \tag{4.7}$$

where $\chi^2_{\text{total}}(90^\circ - \theta_{23})$ projects the value of the overall χ^2 value at the false octant, and $\chi^2_{\text{total}}(\theta_{23})$ at the true octant. Similarly, the standard three-neutrino oscillations

can be ruled out with the significance that is defined by the following function:

$$\Delta\chi^2 = \chi^2_{\rm SI} - \chi^2_{\rm NSI} \tag{4.8}$$

where $\chi^2_{\rm SI}$ corresponds to the value of $\chi^2_{\rm total}$ at which all of the NSI parameters are set to zero, that is, $\varepsilon^s_{\alpha\beta} = \varepsilon^d_{\alpha\beta} = \varepsilon^m_{\alpha\beta} = 0$ for $\alpha, \beta = e, \mu, \tau$. Conversely, $\chi^2_{\rm NSI}$ corresponds to the value of $\chi^2_{\rm total}$ at which at least one of the NSI parameters is non-zero.

If the subtracted χ^2 function values differ only by one degree of freedom (d.o.f.), e.g. by the value of θ_{23} or $\varepsilon^m_{\alpha\beta}$, the $\Delta\chi^2$ distributions in equations (4.7) and (4.8) can be approximated as χ^2 distributions of 1 d.o.f. As such, the 90% CL corresponds to the $\Delta\chi^2 = 2.71$ contour. In terms of the standard deviations, the statistical significance is obtained from the square-root of $\Delta\chi^2$ with 1 d.o.f.

4.3 Simulation details

In the work that is presented in this thesis, the experimental configurations are defined for GLoBES using the so called Abstract Experiment Definition Language (AEDL). The AEDL description for the LBNO configuration that is used in this thesis is described in Ref. [36], and it is based mainly on Refs. [104, 117, 118]. The relevant experimental parameters that define the LBNO configuration for GLoBES are presented in Table 4.1. The DUNE configuration, on the other hand, is simulated with a more sophisticated description, originally used in the DUNE CDR documents [51, 107–109], and its simulation setup is detailed in Ref. [119].

In the LAGUNA–LBNO design study, the experiment was planned to produce a continuous muon neutrino beam for 5 years and a muon antineutrino beam for another 5 years. In the first stage the neutrino beam would have been produced with 1.125×10^{20} POT/year, whereas the second stage would have increased the number to 3.0×10^{21} POT/year. The produced neutrinos were planned to be observed in the detector facility, which in the first phase would have consisted of a single detector of 20 kton fiducial mass, and it would have been upgraded into a two detector system of 50 kton total fiducial mass for the second phase.

In our simulation of LBNO, the neutrinos would traverse through 2288.0 km of matter, along which the matter density ρ is modeled with a 20-step PREM distribution, which is treated with a Gaussian error. The standard deviation of the error is given by $\sigma(\rho) = 0.02 \times \rho$.

The detector facility we have used in our simulations is sensitive to the four neutrino species, that is, ν_μ, ν_e, $\bar{\nu}_\mu$ and $\bar{\nu}_e$. The signal consists of the muon and electron neutrinos that undergo the CC neutrino-nucleon interaction in the detector, which reconstructs the corresponding events at approximately 90% efficiency. The detector is assumed to reconstruct the flavour and energy of the neutrinos in the [0.1 GeV, 10.0 GeV] energy range, which is divided into 80 bins of 0.125 GeV width.

TABLE 4.1 The experiment parameters that are used to describe the LBNO configuration. The LBNO has been proposed to be realized in two phases, where the first one runs on the SPS accelerator and 20 kton of fiducial mass, and the second one on HPPS and 70 kton. This table is taken from Ref. [36].

Parameter	Value
Beam power [SPS] (10^{20} POT/yr)	1.125
Beam power [HPPS] (10^{21} POT/yr)	3.0
Baseline length (km)	2288
Running times (yr)	5+5
Detection efficiency (%)	90
ν_μ NC rejection (%)	99.5
ν_μ CC rejection (%)	99.5
Energy resolution (GeV)	$0.15 \times \sqrt{E_\nu}$
Energy window (GeV)	$[0.1,\ 10.0]$
Number of bins	80
Bin width (GeV)	0.125

The neutrino energy is assumed to be reconstructed at a resolution that is approximated with a Gaussian function, where the standard deviation follows the function $\sigma(E_\nu) = 0.15 \times \sqrt{E_\nu}$. Regarding the systematics, the reconstruction is treated in our simulation with the normalization error that is described in Section 4.2. The weight parameter of the signal events is set to $\pi_1 = 0.05$.

In our simulation, the background is assumed to be composed mainly of the impurities in the neutrino beam, which would account approximately 1% of the neutrinos. The ν_e, $\bar{\nu}_e$ and $\bar{\nu_\mu}$ components in the neutrino beam (similarly ν_e, $\bar{\nu}_e$ and ν_μ in the antineutrino beam) may oscillate into the final states and result in events that resemble that of the expected signal. In the simulation, the LArTPC detector is assumed to accept 0.5% of the observed ν_μ and $\bar{\nu}_\mu$ as ν_e and $\bar{\nu}_e$ events, respectively, to account for the fact that some of the background events are mistaken as the signal.

The other source of the background originates from the ν_τ and $\bar{\nu}_\tau$ that are produced in the $\nu_\mu \to \nu_\tau$ and $\bar{\nu}_\mu \to \bar{\nu}_\tau$ oscillations. The ν_τ and $\bar{\nu}_\tau$ created this way would be energetic enough to create tau leptons in the process, which have a 3.5 GeV production threshold. The tau particles created this way would account for about 6% of all of the produced charged leptons. These particles would decay via the $\tau \to e\,\nu_e\,\nu_\tau$ process at 17.6% branching ratio, contaminating the ν_e signal with an irreducible background of approximately 1% of all leptons.

The simulation for the DUNE configuration is in many ways analogous to that of LBNO. Whereas the LBNO configuration is implemented in the v3.1.11 build of GLoBES and using the details described above, the DUNE simulation is based on the more recent version v3.2.16, which provides a more accurate treatment of certain areas, including the systematics correlation. The AEDL description of DUNE and

the related input files were provided to us by the DUNE collaboration.

Chapter 5

Determination of the θ_{23} octant in long baseline experiments

In this Chapter, the results from the simulation of the long baseline neutrino experiments in the determination of the θ_{23} octant are presented. This Chapter presents the experimental sensitivities that have been calculated for the LBNO and DUNE configurations, and summarizes the main findings of the work that has been presented in Publications I, II and III. Section 5.1 presents the sensitivities for the determination of the θ_{23} octant in LBNO, and Section 5.2 elaborates how the sensitivity can be optimized by utilizing the matter effects. Finally, in Section 5.3 it is discussed how the presence of the new physics effects, such as the non-unitarity of the neutrino mixing matrix and the active–sterile neutrino mixing, may change the sensitivity to the θ_{23} octant in DUNE to the worse.

5.1 Determination of the θ_{23} octant in LBNO

In this Section, we discuss the main results of Publication I, which presents a new, improved simulation model for LBNO, and describes its sensitivity to the octant of the atmospheric mixing angle θ_{23}. Whereas the theoretical background of the θ_{23} octant question is described in Chapter 2, the experimental configuration of LBNO and the main principles of the simulation method is summarized in Chapter 4.

In Publication I, we calculated the experimental sensitivities to the θ_{23} octant for four different configurations. On the one hand, the sensitivities were calculated for the proposed LBNO configuration in its first and second phases, where the proposed experiment features the SPS accelerator and a 20 kton LArTPC detector, and the HPPS accelerator and a detector system with a total of 70 kton fiducial mass. On the other hand, the sensitivities were also provided for the possible intermediate setups, where SPS is paired with the 70 kton fiducial mass detector, and HPPS with the 20 kton mass.

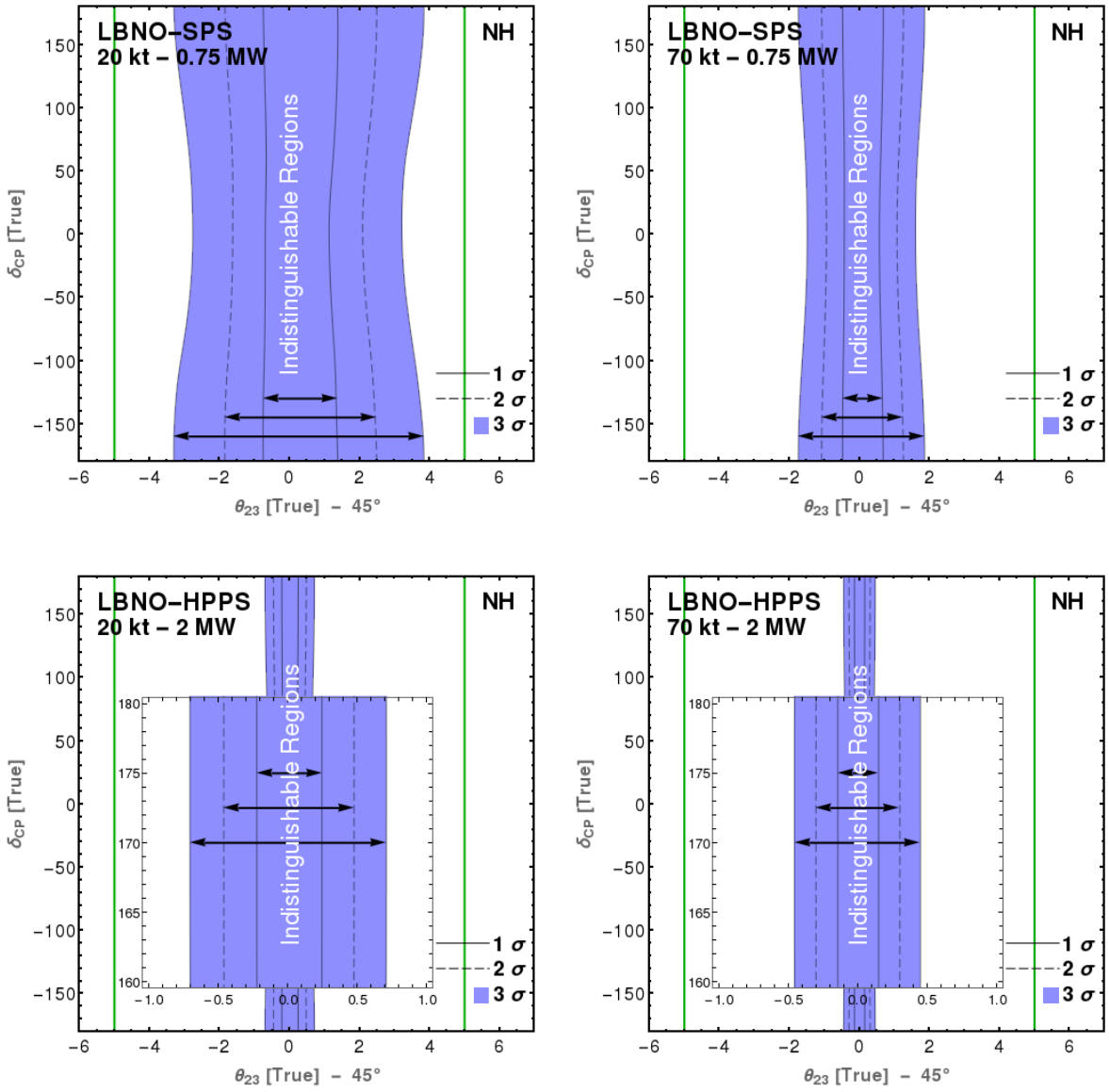

FIGURE 5.1 The octant discovery potential in the LBNO configuration when the normal mass hierarchy (NH) is assumed. The coloured regions show the values of θ_{23} and δ_{CP} where the false octant can be ruled out at a $3\,\sigma$ confidence level or less, whereas the white areas show the values where the θ_{23} octant can be determined at a $3\,\sigma$ confidence level or better. The $1\,\sigma$ and $2\,\sigma$ confidence level contours are shown with the solid and dashed lines, respectively. The MINOS–favoured values $\theta_{23} = 40°$ and $50°$ are illustrated with the green lines. The sensitivities are shown for the four combinations of the SPS and HPPS accelerators, and the 20 and 70 kton detectors. In the center of the two HPPS panels an enlarged view of a part of the plot is displayed.

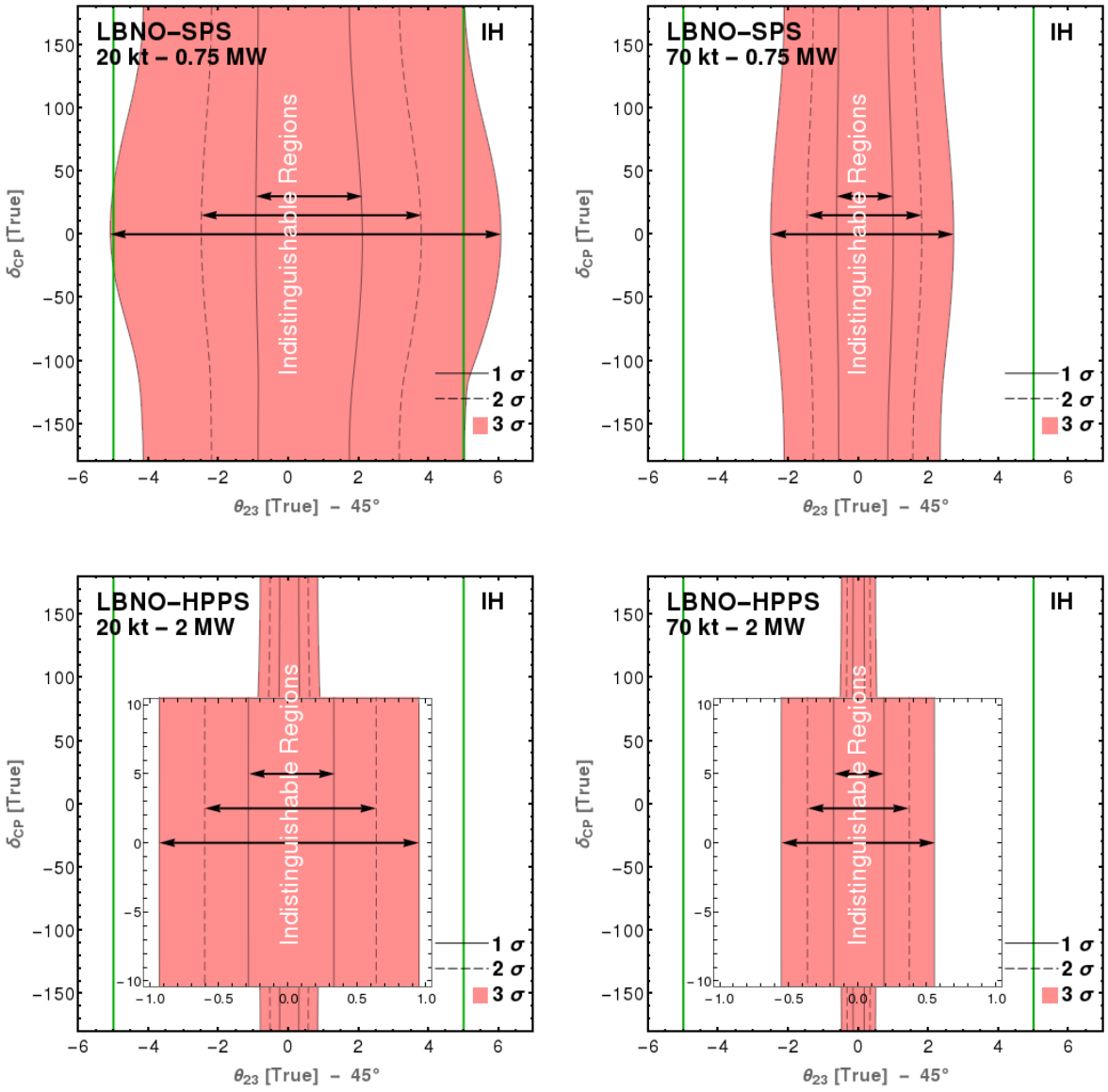

FIGURE 5.2 The octant discovery potential in the LBNO configuration when the normal mass hierarchy (IH) is assumed. The coloured regions show the values of θ_{23} and δ_{CP} where the false octant can be ruled out at a $3\,\sigma$ confidence level or less, whereas the white areas show the values where the θ_{23} octant can be determined at a $3\,\sigma$ confidence level or better. The $1\,\sigma$ and $2\,\sigma$ confidence level contours are shown with the solid and dashed lines, respectively. The MINOS–favoured values $\theta_{23} = 40^\circ$ and 50° are illustrated with the green lines. The sensitivities are shown for the four combinations of the SPS and HPPS accelerators, and the 20 and 70 kton detectors. In the center of the two HPPS panels an enlarged view of a part of the plot is displayed.

Using GLoBES, we calculated the $\Delta\chi^2$ distribution for the determination of the θ_{23} octant over a grid of 120×360 points in the ($\theta_{23} - 45°$, $\delta_{\rm CP}$)—projection plane, where true values of θ_{23} and $\delta_{\rm CP}$ go through the values $\theta_{23} =$ 39°..... 52° and $\delta_{\rm CP} =$ –180°.....+180°. At each grid point, the χ^2 were computed twice: first at the given θ_{23} and $\delta_{\rm CP}$ values, defined by the axes, and one more time after the conversion $\theta_{23} \to 90° - \theta_{23}$, which corresponds to the false octant. Both times, the χ^2 function was minimized over all oscillation parameters except for θ_{23} and $\delta_{\rm CP}$, which were fixed throughout the calculation. The resulting $\Delta\chi^2$ distribution can be approximated as a χ^2 distribution of 1 d.o.f., meaning that the null hypothesis $90° - \theta_{23}$ can be ruled out at $1\,\sigma$, $2\,\sigma$ and $3\,\sigma$ CL at $\Delta\chi^2 = 1$, 4 and 9, respectively.

The results of this work are presented for NH in Figure 5.1, and for IH in Figure 5.2. Both of the figures present the LBNO sensitivities under the four different configurations, which are labeled as SPS–20 kt, SPS–70 kt, HPPS–20 kt and HPPS–70 kt.

The figures are to be interpreted as follows: The coloured regions show the true values of $\theta_{23} - 45°$ and $\delta_{\rm CP}$, for which the wrong octant solution $90° - \theta_{23}$ can be ruled out by less than $3\,\sigma$ CL significance. Conversely, in the white region the correct octant is known at a $3\,\sigma$ CL or better. For illustration, the corresponding $1\,\sigma$ and $2\,\sigma$ CL contours are also shown. The sensitivities corresponding to the SPS accelerator and 20 kton detector is shown in the top-left panel, the SPS–70 kton combination is represented in the top-right panel, HPPS–20 kton in the bottom-left panel, and HPPS–70 kton in the bottom-right panel. For comparison, the $\theta_{23} - 45° = \pm 5°$ contours are shown with the green lines, which approximately correspond to the best-fit values of θ_{23} of the MINOS experiment (see e.g. Ref. [64]).

In summary, the octant sensitivities presented in Figures 5.1 and 5.2 show the LBNO configuration to have an excellent sensitivity for the determination of the θ_{23} at the $3\,\sigma$ CL significance. Whereas the proposed first phase of the LBNO configuration (20kt–0.75MW) appears to achieve this benchmark for NH when $\theta_{23} \lesssim 41.2°$ and $\theta_{23} \gtrsim 48.9°$, the $3\,\sigma$ CL is reached for IH when $\theta_{23} \lesssim 39.9°$ and $\theta_{23} \gtrsim 51.1°$. Correspondingly, in the second phase (70kt – 2MW) the sensitivity can be obtained for $\theta_{23} \lesssim 44.5°$ and $\theta_{23} \gtrsim 45.5°$ in NH, and $\theta_{23} \lesssim 44.4°$ and $\theta_{23} \gtrsim 45.6°$ in IH. The sensitivity is found to increase when either the accelerator is upgraded from SPS to HPPS, and when the detector mass is increased from 20 kton to 70 kton, the accelerator upgrade bringing the higher impact.

5.2 Optimizing the θ_{23} octant search with matter effects

In this Section, we discuss how the MSW matter effect may be used to enhance the sensitivity to the determination of the θ_{23} octant in a long baseline neutrino experiment. The results presented in this Section are the main findings of Publication II.

The connection of the matter effects and the determination of the θ_{23} octant

can be understood with the analytical probability formula that has been derived for the atmospheric neutrino oscillations, and also works in the case of a very-long baseline neutrino experiment [120–122]. In the leading order, neglecting the terms proportional to the ratio $\Delta m^2_{21}/\Delta m^2_{31}$, the $\nu_\mu \to \nu_\mu$ survival probability is given by

$$\begin{aligned} P^m_{\nu_\mu \to \nu_\mu} \simeq 1 &- \cos^2\theta^m_{13} \sin^2 2\theta_{23} \sin^2\left(1.27\,\frac{L}{E}\left(\frac{\Delta m^2_{31} + A + (\Delta m^2_{31})_m}{2}\right)\right) \\ &- \sin^2\theta^m_{13} \sin^2 2\theta_{23} \sin^2\left(1.27\,\frac{L}{E}\left(\frac{\Delta m^2_{31} + A - (\Delta m^2_{31})_m}{2}\right)\right) \\ &- \sin^4\theta_{23} \sin^2 2\theta^m_{13} \sin^2\left(1.27\,\frac{L}{E}(\Delta m^2_{31})_m\right), \end{aligned} \tag{5.1}$$

where $A = 2\sqrt{2}G_F N_e E/\Delta m^2_{31}$ and the $\delta_{\rm CP}$ parameter is averaged out. The effective mixing angle θ^m_{13} and square-mass difference $(\Delta m^2_{31})_m$ are given by

$$\begin{aligned} (\Delta m^2_{31})_m &= \sqrt{(\Delta m^2_{31}\cos 2\theta_{13} - A)^2 + (\Delta m^2_{31}\sin 2\theta_{13})^2} \\ \sin 2\theta^m_{13} &= \frac{\Delta m^2_{31}}{(\Delta m^2_{31})_m}\sin 2\theta_{13}. \end{aligned} \tag{5.2}$$

The octant-sensitive and degenerate terms can now be identified by looking for the θ_{23}–dependent terms in the probability formula 5.1. Whilst the first three terms in equation (5.1) are degenerate with respect to the θ_{23} octant, the fourth term is in fact sensitive to the θ_{23} octant. Hence, the survival probability $P^m_{\nu_\mu \to \nu_\mu}$ can be expected to contribute to the sensitivity to the θ_{23} octant to some extent in the long baseline neutrino experiments.

In the same approximation, the conversion probability for $\nu_\mu \to \nu_e$ is given by

$$P^m_{\nu_\mu \to \nu_e} \simeq \sin^2\theta_{23} \sin^2 2\theta^m_{13} \sin^2\left(1.27\,\frac{L}{E}(\Delta m^2_{31})_m\right), \tag{5.3}$$

where the sensitivity to the θ_{23} octant arises in the leading term.

The survival and conversion probabilities for the antineutrino oscillations are obtained by replacing $A \to -A$ in equation (5.1).

Both the survival and conversion probabilities have terms that are sensitive to the θ_{23} octant, and they are both subjects to the MSW resonance, which was introduced in Chapter 2. The fourth term of the survival probability in equation (5.1) and the only term of the conversion probability in equation (5.3) can be expected to attain their largest values when the resonance condition, $A = \Delta m^2_{31}\cos 2\theta_{13}$, is fulfilled. The MSW condition requires A and Δm^2_{31} to have the same sign, which indicates that the MSW resonance may boost the sensitivity to the θ_{23} octant in the survival probability $P^m_{\nu_\mu \to \nu_\mu}$ only when the mass hierarchy is normal. Respectively, the MSW resonance boosts the antineutrino probability $P^m_{\bar\nu_\mu \to \bar\nu_\mu}$ only when the mass

hierarchy is inverted. The conversion probabilities $P^m_{\nu_\mu \to \nu_e}$ and $P^m_{\bar{\nu}_\mu \to \bar{\nu}_e}$ are affected by the same condition.

In the LBNO configuration, the MSW resonance can be expected to occur around the neutrino energies $E_\nu \simeq 11$ GeV. Though this condition is inaccessible for the majority of the neutrinos produced in LBNO, the very high energy tail of the flux spectrum (shown in Figure 4.2 in Chapter 4) will be affected by the MSW resonance. Moreover, the large statistics of the muon neutrinos and antineutrinos not oscillating to the other flavour states also gives an advantage over the electron appearance spectra, which are limited by the relatively small values of the conversion probabilities $P^m_{\nu_\mu \to \nu_e}$ and $P^m_{\bar{\nu}_\mu \to \bar{\nu}_e}$.

In the work that is presented in Publication II, we studied the influence of the matter effects on the determination of the θ_{23} octant by probing the sensitivity as a function of the baseline length, the ratio that defines the sharing of the beam between the neutrino and antineutrino run modes, and finally, the weight parameters that describe the systematics representing the signal normalization errors in the ν_μ, ν_e, $\bar{\nu}_\mu$ and $\bar{\nu}_e$ events, respectively (for a detailed description of the systematics, see Chapter 4).

In Figure 5.3, the $5\,\sigma$ CL sensitivity of LBNO to the θ_{23} octant is presented as a function of the baseline length L, using the LBNO configuration and its four different realizations as a reference. We plotted the $5\,\sigma$ CL contours for the parameter values $\delta_{\mathrm{CP}} = -180°.....+180°$, creating a continuous band for each configuration. The width of each band therefore also reflects the correlation between δ_{CP} and the θ_{23} octancy. The sensitivities are shown for the true values $\theta_{23} = 45°..... 57°$, and they correspond to four different integrated luminosities. Above each contour, the θ_{23} octant can be determined at a $5\,\sigma$ CL significance or better for an individual δ_{CP} value. Above each band, the θ_{23} octant can be determined out regardless of the value of δ_{CP}. Conversely, the sensitivity falls below the $5\,\sigma$ CL significance below each contour or band.

Figure 5.3 reveals how the sensitivity to the θ_{23} octant behaves as the function of the baseline length L. In the NH case, the sensitivity generally improves when the baseline length L is increased for the configurations that represent the integrated luminosities of the order of 10^{22} POT $\cdot$ kton. This improvement may result from the increasing production of the ν_μ and $\bar{\nu}_\mu$ particles near the resonance condition, but also from the cross sections, which generally grows proportionately with respect to the neutrino energy. When the luminosity is increased to the orders of 10^{23} and 10^{24}, however, there is a shallow minimum around 1800 km baseline length. The IH case of the figure exhibits similar behaviour, though there is a brief worsening in the sensitivity when the baseline length L is increases from 1500 km to 2200 km.

Because the neutrino fluxes used in the LBNO configuration (see Figure 4.2) are optimized for the 2288-km-long baseline length in such a way that the ν_μ and $\bar{\nu}_\mu$ production is high near the first and second oscillation maxima, changing the value

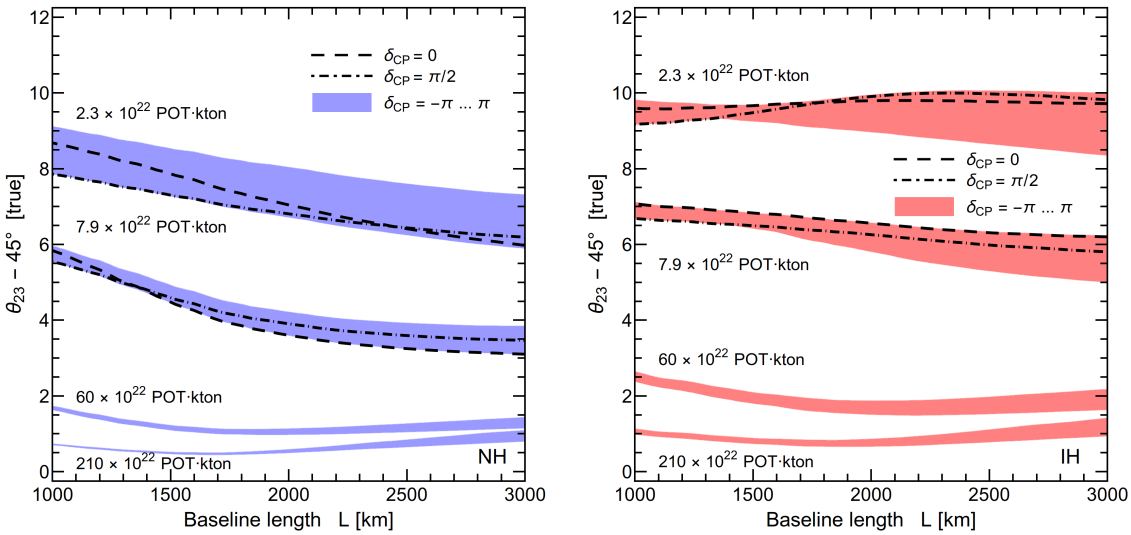

FIGURE 5.3 Sensitivity to the θ_{23} octant as function of the baseline length L. The coloured regions show the $5\,\sigma$ CL sensitivity to the octant for $\delta_{CP} = -180°.....+180°$, representing the four different exposures of the experiment. The contours corresponding to $\delta_{CP} = 0$ and $\delta_{CP} = \pi/2$ are shown as the dashed and dot-dashed lines, respectively. Whereas the left panel shows the sensitivities for the normal hierarchy (NH), the right panel shows those for the inverted hierarchy (IH).

of the baseline length L also requires that the beam fluxes are adjusted to the new baseline length. In the sensitivities presented in Figure 5.3, we adjusted the neutrino and antineutrino fluxes for each baseline length by shifting the the flux histograms along the E axis, so that the L/E ratio remains unchanged. This ensured that the oscillation probabilities for the $\nu_\mu \to \nu_e$ and $\bar{\nu}_\mu \to \bar{\nu}_e$ are the same regardless of the baseline length L. This essentially means that the average beam energy E increases at the same rate with the baseline length L, whilst the shape of the produced flux spectra stays the same.

The dependence between the sensitivity to the θ_{23} octant and the matter effects are also tested in the context of the beam sharing. In Figure 5.4, the octant sensitivity is presented as a function of the ratio that defines the fraction at which the experiment runs in the neutrino mode. In this example, we calculated the sensitivity to the θ_{23} octant as a function of the ratio $\nu_\mu/(\nu_\mu + \bar{\nu}_\mu)$, which defines the fraction of the 10-year total running time dedicated to running in the neutrino mode. For example, at $\nu_\mu/(\nu_\mu + \bar{\nu}_\mu) = 0$ the simulated experiment would run zero years in the neutrino mode and 10 in the antineutrino mode, whereas at 0.5 the share would be 5 years in the neutrino mode and 5 years in the antineutrino mode etc. The other parameters are the same as in the reference configuration.

Varying the beam sharing ratio $\nu_\mu/(\nu_\mu+\bar{\nu}_\mu)$ illustrates how the sensitivity to the θ_{23} octant depends on the mass hierarchy. Figure 5.4 shows that the sensitivity to de-

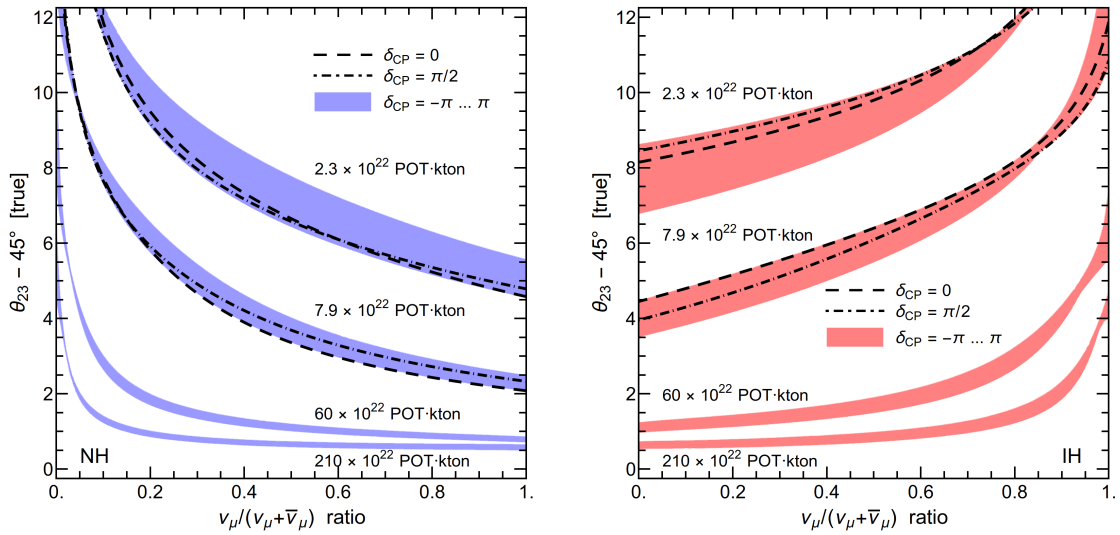

FIGURE 5.4 The $5\,\sigma$ confidence level discovery reach of the determination of the θ_{23} octant as a function of the beam sharing ratio. Above the curves the θ_{23} octant is known at more than $5\,\sigma$ certainty. The band shows the variation of the bound when δ_{CP} varies within the range $\delta_{CP} = -180^\circ$ ..... $+180^\circ$ and corresponds to the correlation between δ_{CP} and the θ_{23} octant. The left panel presents the sensitivities for the normal mass hierarchy (NH) and the right panel for the inverted mass hierarchy (IH).

termine the θ_{23} octant increases in the NH case when the beam operates longer times in the neutrino mode, and conversely decreases when the share of the antineutrino mode is increased. In the IH case, however, this behaviour is flipped, as the sensitivity bands begin to decrease as the time in the neutrino mode is increased. This is the clearest sign of the contribution of the MSW effect, which is known to affect only the neutrino mode in the NH case and the antineutrino mode in the IH case.

In the third example, we examined the impact of the systematic errors that arise from the normalization of the signal events in the detection and reconstruction of the ν_μ, ν_e, $\bar{\nu}_\mu$ and $\bar{\nu}_e$ events. In Figures 5.5 and 5.6, the $5\,\sigma$ CL sensitivity for the determination of the θ_{23} octant is presented as a function of the weight parameter π_1 that defines the strength of the systematic error that is associated with the signal normalization. The default value of the weight parameter is $\pi_1 = 0.05$ for all of the four neutrino types (ν_μ, ν_e, $\bar{\nu}_\mu$ and $\bar{\nu}_e$), and in each panel one of the four weight parameters is varied through the values $\pi_1 = 0\%$ ..... 10%. The sensitivities in the NH case are plotted in Figure 5.5 and those in the IH case in Figure 5.6.

The signal normalization error appears to have very little effect on the octant sensitivity, as it can be seen from Figures 5.5 and 5.6. When the mass hierarchy is assumed to be NH, Figure 5.5 indicates that the sensitivity to the octancy is not affected by the signal normalization error in the case of the $\bar{\nu}_e$ and $\bar{\nu}_\mu$ detection, whereas several changes are observable when the systematics are altered in the ν_e

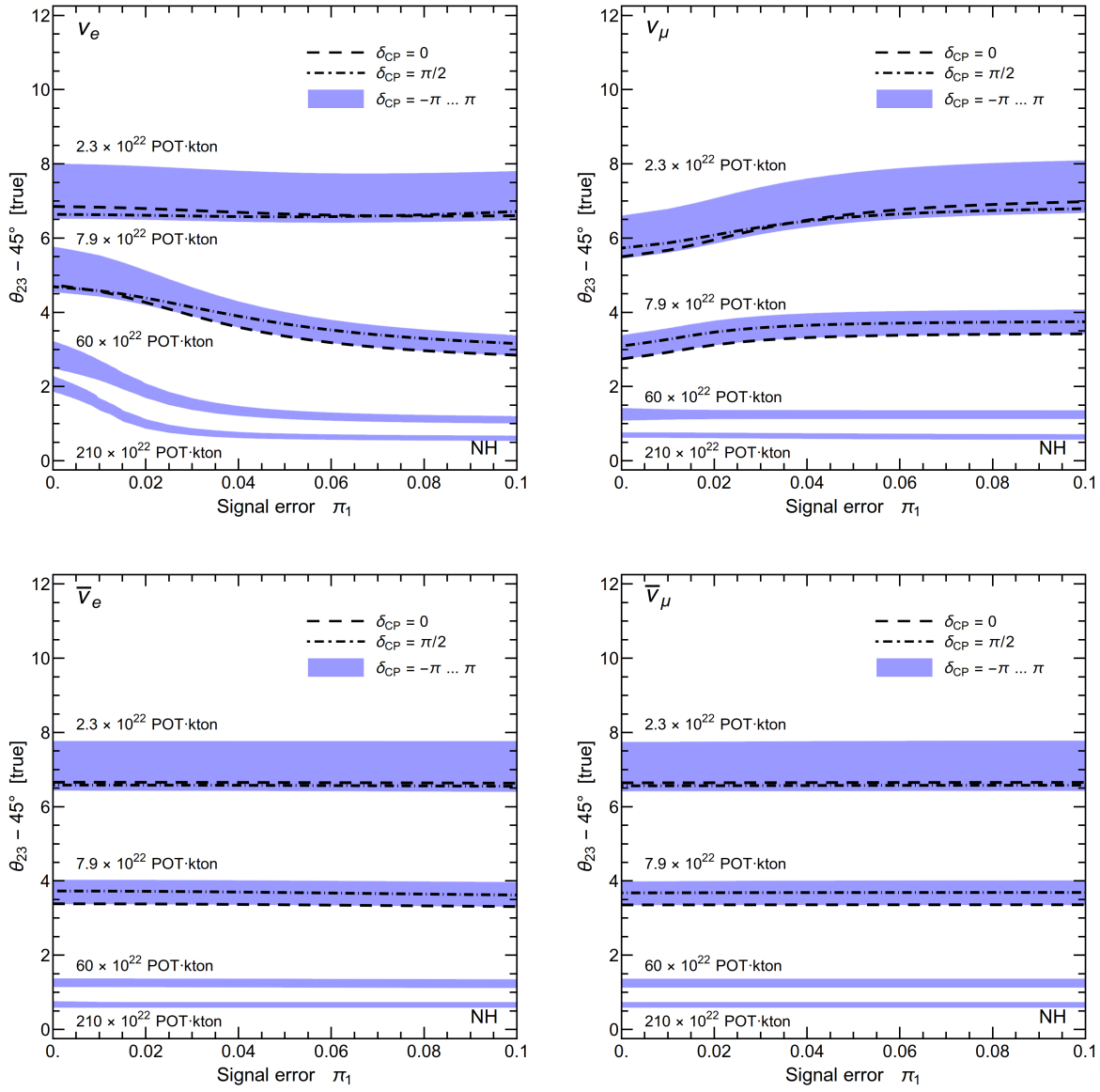

FIGURE 5.5 The $5\,\sigma$ confidence level (CL) discovery reach of θ_{23} octant as a function of the signal weight parameter π_1 for four different luminosities and detection modes (ν_e, ν_μ, $\bar{\nu}_e$, $\bar{\nu}_\mu$) in the case of normal hierarchy (NH). Above the curves the octant of θ_{23} will be determined with more than $5\,\sigma$ CL certainty. The band shows the variation of the bound when δ_{CP} varies in the range –180°.....+180° and corresponds to the correlation between δ_{CP} and the θ_{23} octant.

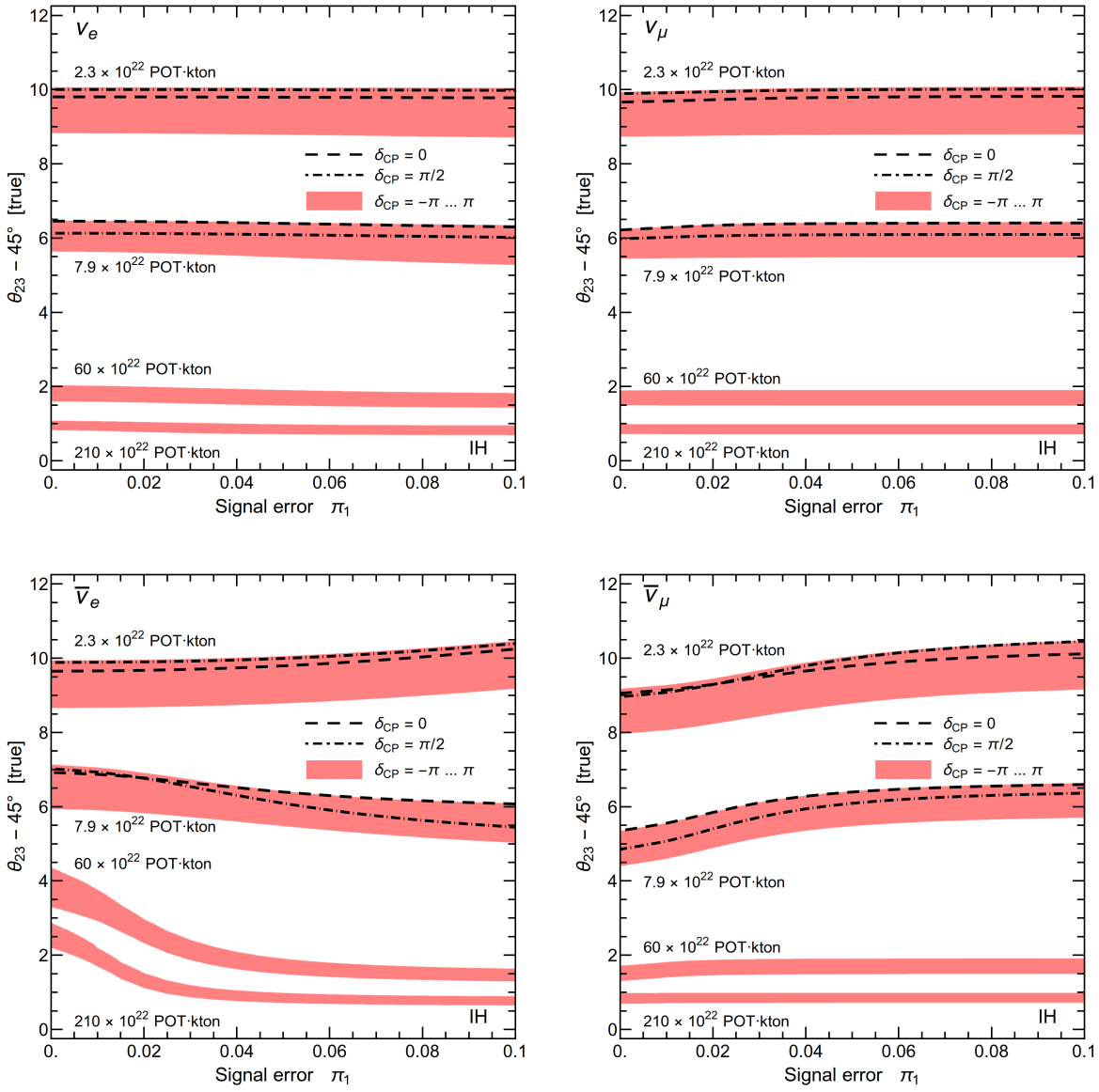

FIGURE 5.6 The 5 σ confidence level (CL) discovery reach of θ_{23} octant as a function of the signal weight parameter π_1 for four different luminosities and detection modes (ν_e, ν_μ, $\bar{\nu}_e$, $\bar{\nu}_\mu$) in the case of inverted hierarchy (IH). Above the curves the octant of θ_{23} will be determined with more than 5 σ CL certainty. The band shows the variation of the bound when δ_{CP} varies in the range –180°.....+180° and corresponds to the correlation between δ_{CP} and the θ_{23} octant.

and ν_μ detection. When the hierarchy is assumed to be IH, however, this behaviour is flipped, which again hints of a connection to the MSW effect.

Figures 5.3–5.6 show the values of θ_{23} for which the low octant solution $90^\circ - \theta_{23}$ can be ruled out by at least $5\,\sigma$ CL significance. We also investigated the sensitivities to rule out the high octant for the true values $\theta_{23} = 33^\circ ..... 45^\circ$, and the results suggest either similar or slightly better sensitivities than the ones that are presented in this Section. In all cases, the sensitivity to the θ_{23} octant improves as the integrated luminosity is increased. Increasing the luminosity also improves the θ_{23} octant – δ_{CP} correlation.

Altogether, we found that the long baseline neutrino oscillation experiments offer a good sensitivity for the determination of the θ_{23} octant, and their sensitivity to the octant question can be further optimized by adjusting the beam sharing carefully, whereas the systematics from the signal normalization bear only a subtle effect. The baseline length affects the sensitivity to some extent, and we found the distances between 1500 km and 2000 km being favourable for the determination.

5.3 The effect of beyond the Standard Model physics on octant determination

In this Section, we discuss the main results of Publication III. As it was discussed in Chapter 3, the existence of the neutrino oscillations confirms that neutrinos do indeed have mass, which is a sign that there is physics that goes beyond the Standard Model. Depending on the mechanism that gives rise to the small neutrino masses, this new physics may manifest itself as the existence of the sterile neutrinos, the non-unitarity of the neutrino mixing matrix, the non-standard neutrino interactions, or something else that can affect the neutrino oscillations. In this Section, we investigate how the presence of such new physics can alter the determination to the θ_{23} octant in long baseline neutrino experiments, using the DUNE configuration as an adequate example.

In Publication III, we calculated the experimental sensitivities for the determination of the θ_{23} octant in the DUNE configuration, using the simulation setup that was described in Chapter 4. In the first part, the sensitivities to the octant determination were calculated for the standard three-neutrino oscillations, using the same numerical methods as we had used to calculate the LBNO sensitivities in Publication I. The results are presented in Figure 5.7, which shows that DUNE will be able to determine the θ_{23} octant by a $3\,\sigma$ CL or better when $\theta_{23} \lesssim 43.5^\circ$ or $\theta_{23} \gtrsim 46.5^\circ$, irrespective of the mass hierarchy.

In the second part of Publication III, we investigated how the sensitivity to the θ_{23} octant changes when some degree of non-unitarity is introduced to the neutrino mixing matrix that governs the oscillation between the three active neutrino states

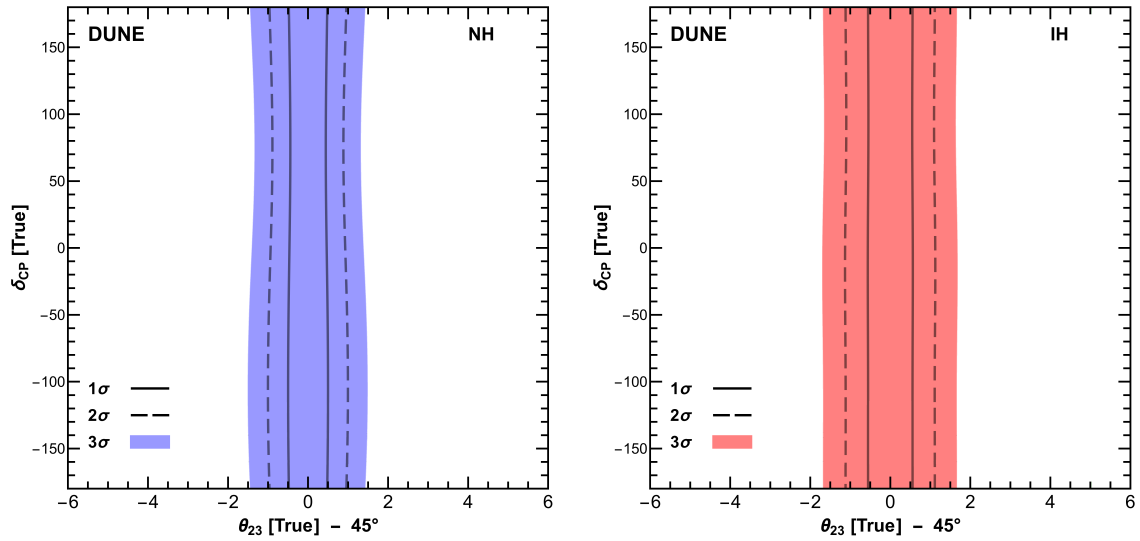

FIGURE 5.7 Sensitivity to the θ_{23} octant in DUNE in the standard three-neutrino paradigm. The coloured regions show the values of θ_{23} and δ_{CP} for which the octant of θ_{23} can be determined up to $3\,\sigma$ CL, whereas the $2\,\sigma$ and $1\,\sigma$ CL contours are shown with the dashed and solid lines, respectively. Conversely, the octant of θ_{23} can be determined by the minimum of $3\,\sigma$ CL anywhere in the white regions. Whereas the left panel shows the sensitivity for the normal hierarchy (NH), the right panel shows the sensitivity for the inverted hierarchy (IH).

ν_e, ν_μ and ν_τ. This kind of non-unitarity may emerge upon the introduction of a sterile neutrino resulting in the fourth neutrino mass state ν_4, such that $\Delta m^2_{41} = m^2_4 - m^2_1 \gg 1\ \mathrm{eV}^2$.

Some of the new physics models that predict the existence of sterile neutrinos are subjects of constraints from various high precision tests of the SM parameters, which should be taken into account when the non-unitarity effects are studied in the long baseline neutrino experiments. Depending on the specific model that introduces the new physics, the effects of the non-unitarity may be studied in the future long baseline neutrino experiments with the high precision constraints that have been derived from the recent precision tests of the SM electroweak parameters (cf. Chapter 3).

In Publication III, we investigated the effect of the non-unitary mixing by simulating DUNE with a modified version of GLoBES. The probability calculation of GLoBES was augmented to include the parameters α_{ij} and $\alpha_{ll'}$ (i, $j = 1, 2, 3$ and l, $l' = e, \mu, \tau$) of the non-unitarity defined in Chapter 3, and the prior function χ^2_{prior} was modified to enable the inclusion of the Gaussian priors also for the parameters α_{ij} and $\alpha_{ll'}$. The normalization factor $(N^\dagger N)^2_{ll'}$ was not taken into account, as its effect was deemed negligible.

The non-unitarity of the neutrino mixing matrix $N = N^{\mathrm{NP}} U_{\mathrm{PMNS}}$ can be con-

TABLE 5.1 Bounds on non-unitary parameters in both α_{ij} and $\alpha_{ll'}$ representations, originally taken from Refs. [82] and [94], respectively. The bounds are given in 90% and 2 σ confidence levels. See Ref. [38] for more details.

Parameter	Upper bound (90% CL)	Parameter	Upper bound (2σ CL)
α_{11}	0.98	α_{ee}	1.3×10^{-3}
α_{22}	0.99	$\alpha_{\mu\mu}$	2.2×10^{-4}
α_{33}	0.93	$\alpha_{\tau\tau}$	2.8×10^{-3}
$\lvert\alpha_{21}\rvert$	1.0×10^{-2}	$\lvert\alpha_{\mu e}\rvert$	6.8×10^{-4}
$\lvert\alpha_{31}\rvert$	4.2×10^{-2}	$\lvert\alpha_{\tau e}\rvert$	2.7×10^{-3}
$\lvert\alpha_{32}\rvert$	9.8×10^{-3}	$\lvert\alpha_{\tau\mu}\rvert$	1.2×10^{-3}

strained not only in the neutrino oscillation experiments, but one may also be able to use the information on the various electroweak parameters, and the $W^{\pm}$ and Z^0 boson masses, whose theoretical expressions can also be affected by the SM extension which introduces the non-unitarity. In Chapter 3, we discussed the main properties of the Type I and Type II Seesaw mechanism and presented some examples of their low energy effects by using the effective field theory approach. In this approach, the operators of dimension $d = 6$ and higher can be used to derive model-dependent bounds on the non-unitarity parameters by utilizing the experimental values of the electroweak parameters, many of which have been measured in a high precision. An example of a work, where such approach is used, can be found in Ref. [94], where the non-unitarity parameters α_{ee}, $\alpha_{\mu\mu}$, $\alpha_{\tau\tau}$, $|\alpha_{\mu e}|$, $|\alpha_{\tau e}|$ and $|\alpha_{\tau\mu}|$ have been constrained using a combination of the neutrino oscillation and electroweak data. These constraints will not hold as such, however, if there is any other kind of new physics present in the low energies other than the non-unitarity of the Type I Seesaw mechanism.

If the electroweak precision parameters are not applicable, as is the case when the exact form of the new physics is not known, it is also possible to derive constraints for the parameters α_{ij} and $\alpha_{ll'}$ by using the existing short baseline oscillation data. This kind of approach was used in Ref. [82], where the short baseline oscillation data from the CHORUS and NOMAD experiments was used to derive constraints on the non-unitarity parameters α_{11}, α_{22}, α_{33}, $|\alpha_{21}|$, $|\alpha_{31}|$ and $|\alpha_{32}|$. These constraints, as well as the ones based on both the neutrino oscillation and electroweak data are summarized in Table 5.1.

Implementing the constrains that are available for the parameters α_{ij} and $\alpha_{ll'}$, we determined the experimental sensitivities for the determination of the θ_{23} octant in DUNE with GLoBES, using the two parametrizations of the non-unitarity given

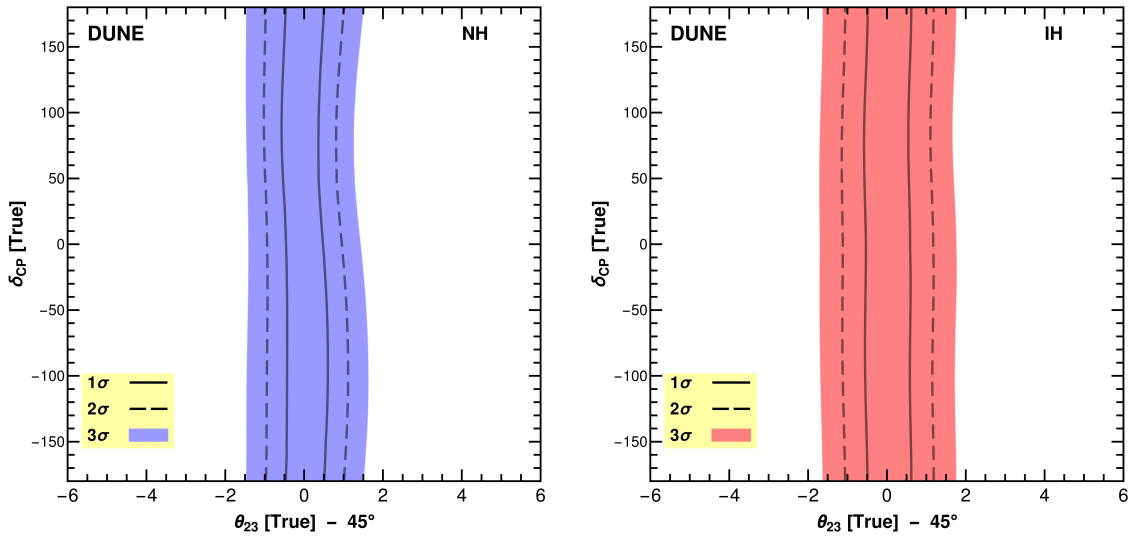

FIGURE 5.8 Sensitivity to the θ_{23} octant in the presence of non-unitary mixing, when only the neutrino oscillation data is used (see Ref. [38] for the list of constraints). The white region shows the values of θ_{23} and δ_{CP} at which the θ_{23} octant can be determined at $3\,\sigma$ CL or better, the coloured regions showing the values at which the sensitivity falls below $3\,\sigma$ CL. The $2\,\sigma$ and $1\,\sigma$ CL are shown with the dashed and solid lines, respectively. The sensitivities are plotted for both normal hierarchy (NH) and inverted hierarchy (IH).

in equations (3.18) and (3.19) in Chapter 3. We implemented the constraints on the α_{ij} and $\alpha_{ll'}$ parameters in GLoBES as a priori errors, which are approximated as Gaussian errors. The results from the oscillation-only data are shown in Figure 5.8.

We discovered that both of the parameter sets α_{ij} (i, $j = 1, 2, 3$) and $\alpha_{ll'}$ (l, $l' = e$, μ, τ), and their associated constraints lead to nearly identical results. Figure 5.8 shows that the change from the sensitivities that have been derived for the three-neutrino oscillations is tiny, the $3\,\sigma$ CL boundaries moving less than 0.2° to each side. Moreover, we found that using the combined electroweak and oscillation constraints from Ref. [94] did little change.

In the third part of Publication III, we examined the effect of the new Majorana neutrino on the determination of the θ_{23} octant in DUNE. Although the light sterile neutrino, corresponding to the square-mass difference $\Delta m^2_{41} \simeq 1$ eV^2, is motivated by the LSND and MiniBooNE anomalies, we were also interested in studying the effects of heavier sterile neutrinos in the sensitivity to the θ_{23} octancy. These heavier sterile neutrinos could be much heavier than the ones that are inspired by the short baseline and solar neutrino anomalies, but in the same time they ought to be light enough to be kinematically accessible to develop the active–sterile oscillations.

When completed, DUNE will be able to study the active–sterile neutrino oscillations to a limited extent with its near and far detectors, which are located at around

TABLE 5.2 Bounds on non-unitary parameters in $\alpha_{ll'}$ representation, taken from [94]. In this scenario the constraints would correspond to mixing with a light sterile neutrino in two mass scales: $\Delta m^2_{41} \sim 0.1 - 1\,\text{eV}^2$ (left column) and $\Delta m^2_{41} \gtrsim 100\,\text{eV}^2$ (right column). The constraints are presented at a 95% confidence level.

Parameter	$\Delta m^2_{41} \sim 0.1 - 1\,\text{eV}^2$	$\Delta m^2_{41} \gtrsim 100\,\text{eV}^2$
α_{ee}	1.0×10^{-2}	2.4×10^{-2}
$\alpha_{\mu\mu}$	1.4×10^{-2}	2.2×10^{-2}
$\alpha_{\tau\tau}$	1.0×10^{-1}	1.0×10^{-1}
$\lvert\alpha_{\mu e}\rvert$	1.7×10^{-2}	2.5×10^{-2}
$\lvert\alpha_{\tau e}\rvert$	4.5×10^{-2}	6.9×10^{-2}
$\lvert\alpha_{\tau\mu}\rvert$	5.3×10^{-2}	1.2×10^{-2}

0.5 km and 1300 km distance from the neutrino source, respectively. This permits the study of active–sterile neutrino oscillations in the square-mass difference regimes of $\Delta m^2_{41} \sim 0.1 - 1\,\text{eV}^2$ and $\Delta m^2_{41} \gtrsim 100\,\text{eV}^2$, when the data is analysed in the 3+1–neutrino scheme [94]. The lower square-mass difference regime corresponds to the active–sterile oscillations that develop before the near detector at $L \sim 0.5$ km. On the other hand, the sensitivity to the higher regime arises from the muon neutrinos and antineutrinos which oscillate into the sterile neutrino states between the near and far detectors, that is, their oscillation length should fall between $L \sim 0.5$ km and 1300 km. The heavier sterile neutrino masses prompt the active–sterile oscillations to yield only an averaged-out effect, whilst the lower masses can be probed to a greater sensitivity due to the interplay of the near and far detectors. A priori constraints of the $\alpha_{ll'}$ for the two square-mass difference regimes are compiled in Table 5.2.

We first examined the effect of the light sterile neutrino from the heavier square-mass difference range $\Delta m^2_{41} \gtrsim 100\,\text{eV}^2$. Using the non-unitarity parametrization we implemented in GLoBES and the constraints from the left-column of Table 5.2, we calculated the sensitivity to the θ_{23} octancy while simulating the DUNE configuration. The results are presented in Figure 5.9. In a similar manner, we also calculated the sensitivities for the low square-mass difference regime $\Delta m^2_{41} \sim 0.1 - 1\,\text{eV}^2$, in which case the results are shown in Figure 5.10.

The results from the case where the fourth neutrino has mass in a range such that $\Delta m^2_{41} \simeq 0.1 - 1\,\text{eV}^2$ show that the sterile neutrino has relatively small influence on the determination of the θ_{23} octant in DUNE. Whereas the heavier light sterile neutrino with $\Delta m^2_{41} \gtrsim 100\,\text{eV}^2$ has a negative effect on the sensitivity by moving the $3\,\sigma$ CL boundary by about 0.5° on each side from that of the standard three-neutrino oscillations, the light sterile neutrino (that is, the one corresponding to $\Delta m^2_{41} \simeq 0.1 -$

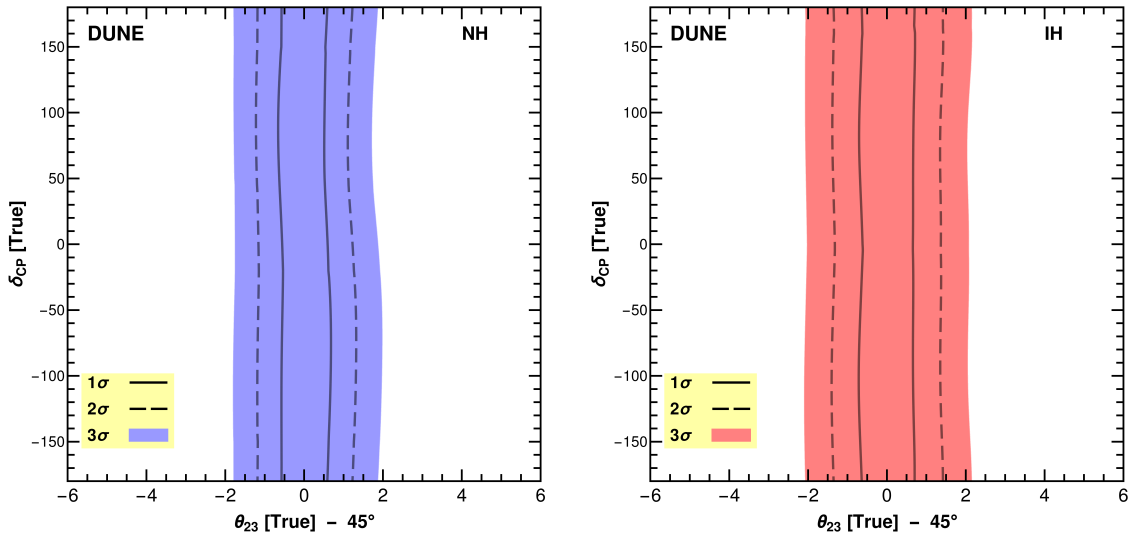

FIGURE 5.9 Sensitivity to the θ_{23} octant in DUNE, but in the presence of a heavy sterile neutrino which corresponds to the $\Delta m^2_{41} \gtrsim 100\,\text{eV}^2$ regime. The white region shows the values of θ_{23} and δ_{CP} at which the θ_{23} octant can be determined at $3\,\sigma$ CL or better, the coloured regions showing the values at which the sensitivity falls below $3\,\sigma$ CL. The $2\,\sigma$ and $1\,\sigma$ CL are shown with the dashed and solid lines, respectively. The sensitivities are plotted for both normal hierarchy (NH, left panel) and inverted hierarchy (IH, right panel).

$1\,\text{eV}^2$) decreases the sensitivity even less. Though the effect of the light sterile neutrinos is stronger than that of the non-unitarity, the change is relatively small. The limited effect on the determination of the θ_{23} octant is also in line with the findings of Ref. [94], where it was concluded that the constraints on the non-unitarity parameters $\alpha_{ll'}$ are strict enough not to allow significant departures from the standard three-neutrino oscillations.

In the last part of Publication III, we studied the extent of the effect which the new physics could have on the sensitivity to the determination of the θ_{23} octant. Simulating the DUNE configuration, we investigated the effect of the non-unitarity parameters in the case where no a priori constraints were applied for the parameters α_{ij}, and then as a function of the $1\,\sigma$ upper bound of the off-diagonal parameter $|\alpha_{21}|$. The resulting sensitivities are presented in Figures 5.11 and 5.12, respectively.

The results show that when the non-unitarity parameters are not constrained, the sensitivity to the θ_{23} octancy is heavily affected, as it can be seen in Figure 5.11. In the NH case, the $3\,\sigma$ CL boundary shifts by more than 2° from its value in the three-neutrino case on both sides of the maximal mixing value $\theta_{23} = 45^\circ$, and in the IH case the shift is at least 1.5° to the worse. Moreover, our other Figure 5.12 shows that as the $1\,\sigma$ CL upper bound on the value of the $|\alpha_{21}|$ parameter gets larger, the sensitivity to the θ_{23} octancy decreases, the steepest drop taking place when the $1\,\sigma$

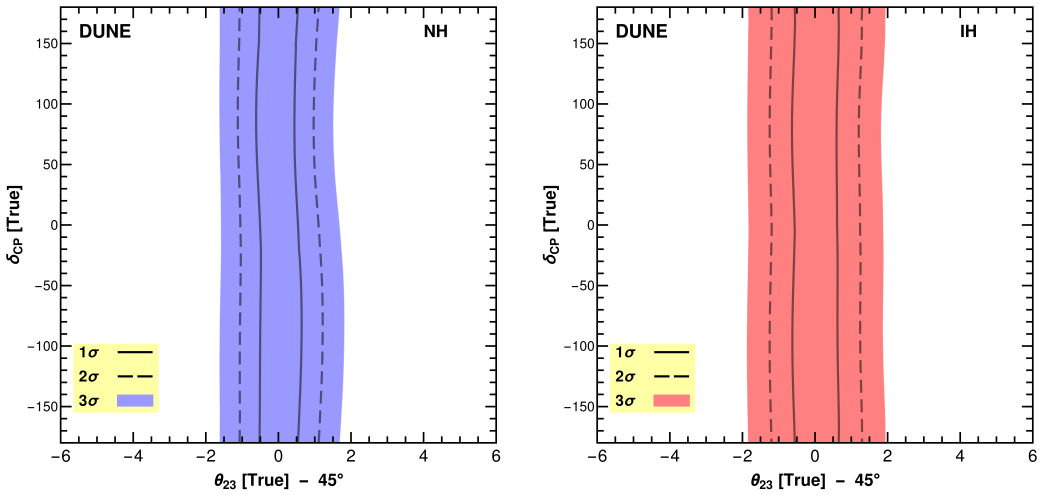

FIGURE 5.10 Sensitivity to the θ_{23} octant in DUNE, but in the presence of a light sterile neutrino which corresponds to the $0 \lesssim \Delta m^2_{41} \lesssim 1\,\text{eV}^2$ regime. The white region shows the values of θ_{23} and δ_{CP} at which the θ_{23} octant can be determined at $3\,\sigma$ CL or better, the coloured regions showing the values at which the sensitivity falls below $3\,\sigma$ CL. The $2\,\sigma$ and $1\,\sigma$ CL are shown with the dashed and solid lines, respectively. The sensitivities are plotted for both normal hierarchy (NH, left panel) and inverted hierarchy (IH, right panel).

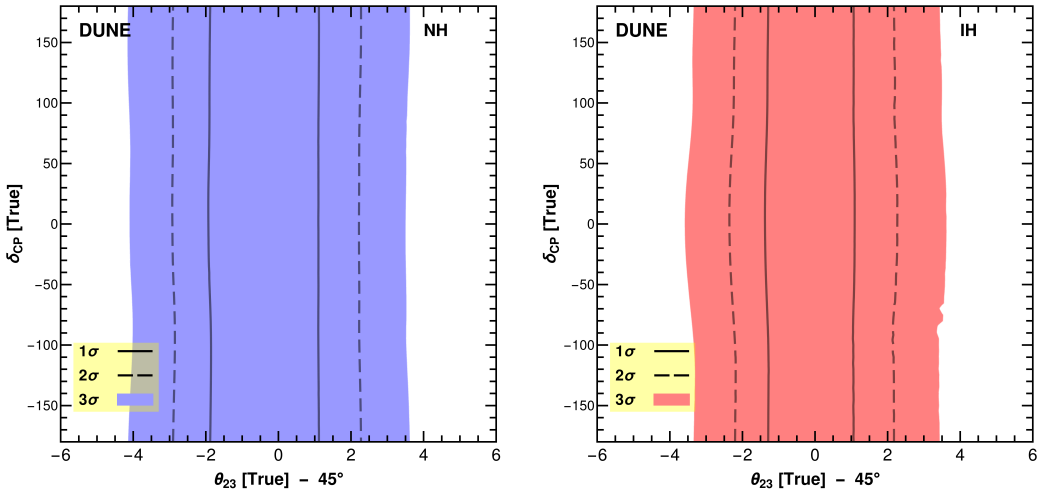

FIGURE 5.11 Sensitivity to the θ_{23} octant in DUNE in the presence of new physics, when no a priori constraints are applied for the parameters α_{ij}, $i,\ j = 1, 2, 3$. The white region shows the values of θ_{23} and δ_{CP} at which the θ_{23} octant can be determined at $3\,\sigma$ CL or better, the coloured regions showing the values at which the sensitivity falls below $3\,\sigma$ CL. The $2\,\sigma$ and $1\,\sigma$ CL are shown with the dashed and solid lines, respectively. The sensitivities are plotted for both normal hierarchy (NH, left panel) and inverted hierarchy (IH, right panel).

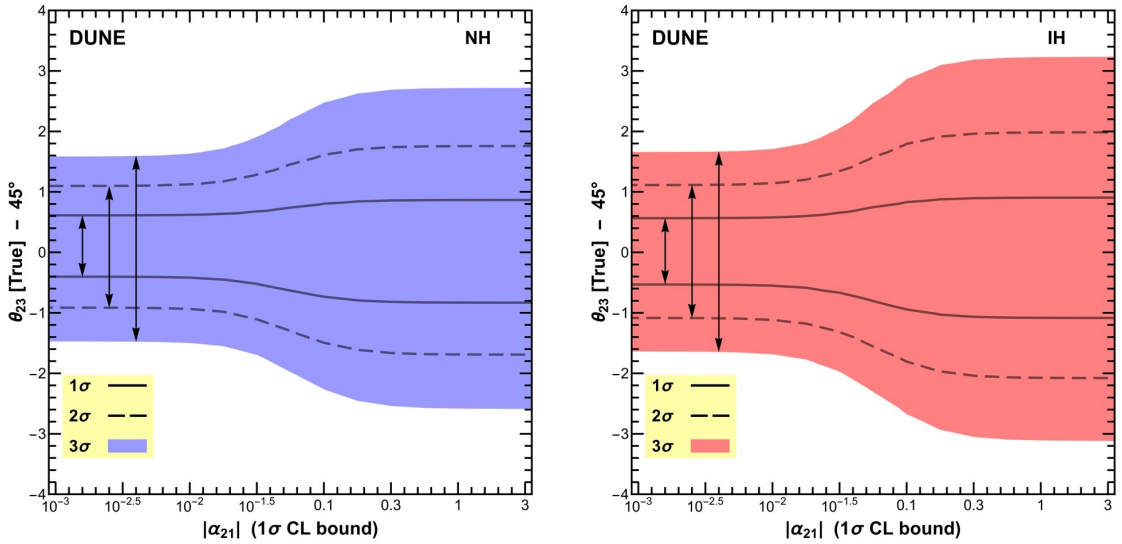

FIGURE 5.12 The sensitivity to the θ_{23} octant in DUNE as a function of the upper bound on the $|\alpha_{21}|$ parameter. While the constraints on the other non-unitarity parameters are assumed to be the same as in the non-unitary mixing matrix case [94], the sensitivities to the octant determination are presented in $3\,\sigma$, $2\,\sigma$ and $1\,\sigma$ CL limits with the coloured regions, the dashed and the solid lines, respectively. The sensitivities are plotted for both normal hierarchy (NH, left panel) and inverted hierarchy (IH, right panel).

CL upper bound is $|\alpha_{21}| \gtrsim 10^{-2}$.

There is one caveat, which must be kept in mind when considering the results presented in Figures 5.11 and 5.12. In our implementation of the non-unitarity parameters in GLoBES, the normalization factor $((N^\dagger N)_{ll})^2$ is approximated as unity. Though this approximation is justified for the cases where the non-unitary mixing matrix or the active–sterile neutrino mixing are considered, that is, when $|\alpha_{\mu e}| \ll 1$, it may undermine the accuracy of the results where no constraints are applied for the non-unitarity parameters.

All the results considered, we found that impact of the new physics on the determination of the θ_{23} octant remains very limited when the constraints from the existing neutrino oscillation data are applied in the calculation of the experimental sensitivities. Hence, DUNE can be expected to have a great sensitivity to the determination of the θ_{23} octant, better than it is known at present.

Chapter 6

Probing non-standard interactions in long baseline experiments

In this Chapter, we discuss the results of our simulation study concerning the non-standard neutrino interactions in long baseline experiments. The Chapter is composed of two parts, which summarize the main findings of Publications IV and V. In Section 6.1, the experimental sensitivities are provided to the discovery of the non-standard neutrino interactions (NSI) in matter. The matter–NSI $\varepsilon^m_{\alpha\beta}$ ($\alpha, \beta = e, \mu, \tau$) parameters are constrained by simulating the LBNO configuration at different baseline lengths. In Section 6.2, the upper bounds on the matter–NSI parameters derived from DUNE are analyzed in the framework of the Type II Seesaw mechanism, where the properties of the triplet Higgs bosons $\Delta = (\Delta^{++}, \Delta^{+}, \Delta^{0})$ can be probed by using the neutrino oscillation data.

6.1 Constraining the non-standard neutrino interaction parameters

In this Section, we discuss the main results of Publication IV. As described in Chapter 3, the non-standard neutrino interactions in matter may affect the oscillation probabilities in long baseline neutrino experiments. The neutrino oscillation data can therefore be used to probe the strength of the non-standard interactions. This Section describes how the future long baseline neutrino experiments can be used to constrain the matter–NSI parameters $\varepsilon^m_{\alpha\beta}$ ($\alpha, \beta = e, \mu, \tau$), and how the individual matter–NSI parameters correlate with the CP violation parameter $\delta_{\rm CP}$.

In Publication IV, we performed simulations for determining the 90% Cl sensitivity limit for the matter–NSI parameters $\varepsilon^m_{\alpha\beta}$ using the LBNO configuration as benchmark. The sensitivities to the individual parameters were obtained as a function of the baseline length L. In contrast to the procedure we performed in the similar study for the determination of the θ_{23} octant in Chapter 5, the fluxes of the LBNO

configuration were not adjusted to match each baseline length, which means that the L/E ratio did not stay fixed in the simulation. The results are presented in Figure 6.1.

The 90% CL upper bounds in Figure 6.1 show that the standard interactions hypothesis, where $\varepsilon^m_{\alpha\beta} = 0$ for α, $\beta = e$, μ, τ, can be ruled out by more than 90% CL significance whenever the absolute value of the studied matter-NSI parameter $\varepsilon^m_{\alpha\beta}$ is sufficiently large, that is, whenever the true value of $\log_{10}\left|\varepsilon^m_{\alpha\beta}\right|$ is above the plotted contours. Respectively, the significance falls below the 90% CL benchmark under the contours. We plotted the 90% CL contours while the true value of the δ_{CP} parameter was varied over the values $\delta_{\text{CP}} \in (0, 2\pi)$, which caused the contours to merge into the bands. The thickness of the bands show the correlation between the matter–NSI parameter $\varepsilon^m_{\alpha\beta}$ and the CP phase δ_{CP}.

It can be seen in Figure 6.1 that the sensitivity of long baseline oscillation experiments to the matter–NSI parameters $\varepsilon^m_{\alpha\beta}$ depends greatly on the baseline length L. The sensitivity appears to generally improve as the function of the baseline length, although two of the bands, that is, the sensitivities for the parameters $\varepsilon^m_{e\mu}$ and $\varepsilon^m_{\mu\tau}$ seem to take an upturn after approximately 2000 km and 3000 km, respectively. This behaviour could be a consequence of the L/E ratio varying as the function of L, which suppresses the conversion probabilities $P^m_{\nu_\mu\to\nu_e}$ and $P^m_{\bar{\nu}_\mu\to\bar{\nu}_e}$ when the value of L/E differs significantly from that of the default LBNO configuration. However, this possibility was ruled out for the parameters $\varepsilon^m_{e\mu}$ and $\varepsilon^m_{e\tau}$ in another study [123], where the baseline-dependence of the matter–NSI parameters was examined using the method we introduced in the octant determination study in Chapter 5. Therefore, we can conclude that the sensitivity to the individual matter–NSI parameters generally improves as a function of the baseline length, until it reaches its peak at about 2000 km and remains approximately constant from there on.

The upper bounds shown in Figure 6.1 were obtained by setting GLoBES to compute the $\Delta\chi^2$ distribution over a grid of baseline lengths $L = 100$ km ..... 5000 km and parameter values $\log_{10}\left|\varepsilon^m_{\alpha\beta}\right| = -2.5$ ..... -0.5, while assuming the NSI parameters associated with the source and detection to be negligible. The χ^2 function was estimated two times for each grid point; once for the standard interactions case where $\varepsilon^m_{\alpha\beta} = 0$ for all α, $\beta = e$, μ, τ, and then again for the non-standard interactions case where $\varepsilon^m_{\alpha\beta}$ was set according to the horizontal axis. The χ^2 functions were then minimized over the standard oscillation parameters except for δ_{CP}, while keeping the NSI parameters fixed. The resulting $\Delta\chi^2$ distribution is then treated as a 1 d.o.f. χ^2 distribution, whence the 90% CL sensitivity can be obtained as the $\Delta\chi^2 = 2.71$ contour.

The main results of Figure 6.1 are the baseline-dependence and the $\varepsilon^m_{\alpha\beta} - \delta_{\text{CP}}$ correlation, which can be inferred from the curvature and the thickness of the 90% CL contours, respectively. The accuracy of the numerical methodology used in this part is sufficient to make these observations. For more quantitative interpretations,

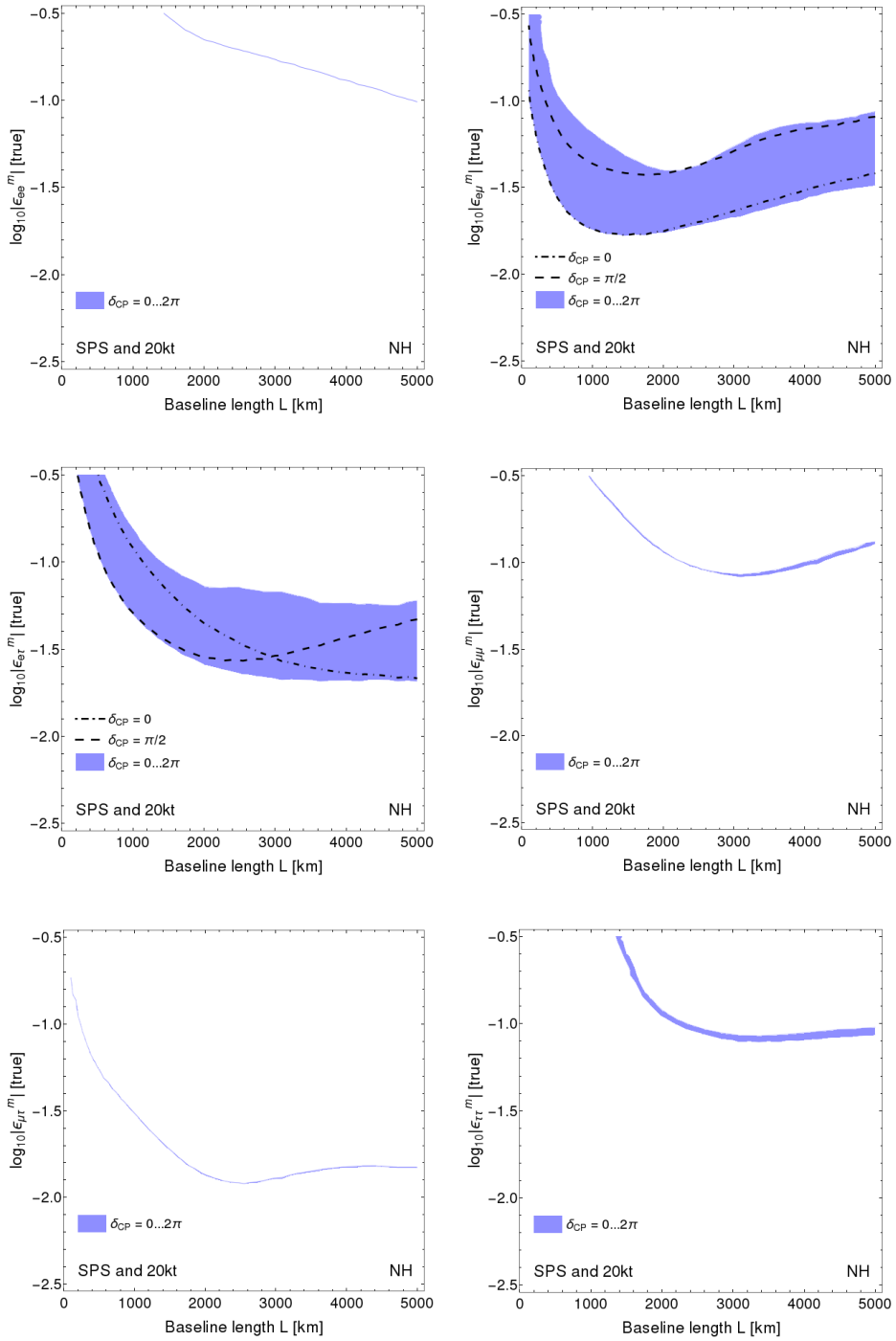

FIGURE 6.1 The 90% CL upper limits on the matter–NSI parameters $|\varepsilon^m_{\alpha\beta}|$ (α, $\beta = e$, μ, τ) as the function of the baseline length L in LBNO–like configurations. The CP violation parameter is varied over the values $\delta_{\rm CP} \in (0, 2\pi)$, whereas the $\delta_{\rm CP} = 0$ and $\delta_{\rm CP} = \pi/2$ contours are indicated with the dot-dashed and dashed lines, respectively. The results are presented for the normal hierarchy and the high θ_{23} octant.

the numerical results shown in Figure 6.1 could be improved by taking into account the source and detection–NSI parameters $\varepsilon^{s}_{\alpha\beta}$ and $\varepsilon^{d}_{\alpha\beta}$ (α, $\beta = e$, μ, τ) and the complex phases $\arg\left[\varepsilon^{m}_{\alpha\beta}\right]$ in the minimization of the χ^2 function.

Another matter of interest is the correlation between the individual matter-NSI parameters $\varepsilon^{m}_{\alpha\beta}$ and the CP phase δ_{CP}, reflected by the thickness of each sensitivity band. Figure 6.1 shows that the correlation is very small in all but the bands that correspond to the parameters $\varepsilon^{m}_{e\mu}$ and $\varepsilon^{m}_{e\tau}$, which exhibit significant correlation.

In Publication IV, we also studied the correlation between $\varepsilon^{m}_{\alpha\beta}$ and δ_{CP} with an alternative method, where the correlation is estimated by using the vacuum probabilities. When all of the NSI parameters except $\varepsilon^{m}_{ll'}$ are set to zero, the vacuum probabilities can be expressed in terms on δ_{CP} using only simple analytical functions.

In the leading order, the vacuum probabilities $P_{\nu_l \to \nu_{l'}}$ can be approximated as

$$P_{\nu_l \to \nu_{l'}} \simeq \left| \sum_{j,k=1}^{3} \frac{L}{2\,E_\nu} U_{lj} H_{jk} \left(U^\dagger\right)_{kl'} \right|^2 , \tag{6.1}$$

where l, $l' = e$, μ, τ, E_ν is the neutrino energy, H is the effective Hamiltonian in the mass basis, and U is the PMNS matrix. When the mixing angles θ_{12}, θ_{13} and θ_{23}, and the square-mass differences Δm^2_{21} and Δm^2_{21} are fixed to their best-fit values (see Ref. [39] for the exact details), the dependence between $P_{\nu_l \to \nu_{l'}}$ and δ_{CP} can be identified for each value of $\varepsilon^{m}_{ll'}$. For instance, the vacuum probability for the $\nu_e \leftrightarrow \nu_\mu$ oscillations lead to the following proportionality:

$$P_{\nu_e \to \nu_\mu} \propto (1.56 - 1.22 \cos\delta_{\text{CP}}) \cdot 10^{-7}. \tag{6.2}$$

The correlation between $\varepsilon^{m}_{ll'}$ and δ_{CP} can be obtained from the relative variation of the oscillation probability, which is defined as follows:

$$R = \frac{P^{\text{max}}_{\nu_l \to \nu_{l'}} - P^{\text{min}}_{\nu_l \to \nu_{l'}}}{P^{\text{min}}_{\nu_l \to \nu_{l'}}}, \tag{6.3}$$

where $P^{\text{min}}_{\nu_l \to \nu_{l'}}$ and $P^{\text{max}}_{\nu_l \to \nu_{l'}}$ are the minimum and maximum values of the oscillation probability, when the CP phase is varied in the range $(0, 2\pi)$.

Identifying the δ_{CP}–dependent terms such as the one in equation (6.2) from the vacuum probabilities (6.1), one may calculate the relative variations for each parameter $\varepsilon^{m}_{ll'}$ with equation (6.3). In this work, we calculated the relative variation R for all of the six matter–NSI parameters as the function of $\varepsilon^{2}_{ll'}$. The results are presented in Figure 6.2.

Figure 6.2 shows that the relative variation for the parameters $\varepsilon^{m}_{ll'}$, where l, $l' = e$, μ, τ, produces its largest values for the parameters $\varepsilon^{m}_{e\mu}$ and $\varepsilon^{m}_{e\tau}$, whereas the other matter–NSI parameters lead to only small variations. This variation remains constant for all of the six matter–NSI parameters when $\varepsilon^{m}_{ll'} \lesssim 10^{-2}$. These observa-

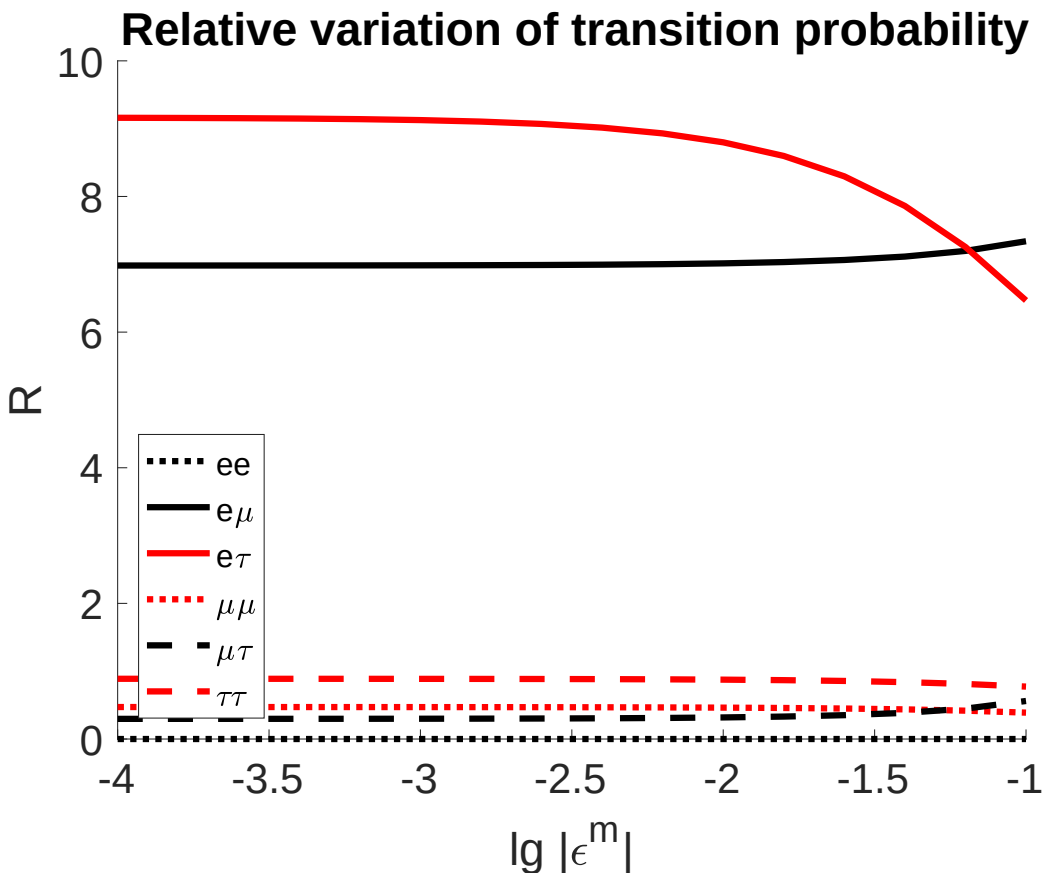

FIGURE 6.2 The relative variation $R = (P^{\text{max}}_{\nu_l \to \nu_{l'}} - P^{\text{min}}_{\nu_l \to \nu_{l'}})/P^{\text{min}}_{\nu_l \to \nu_{l'}}$ of the vacuum oscillation probability $P_{\nu_l \to \nu_{l'}}$ as a function of the absolute value of the matter–NSI parameter $\varepsilon^m_{ll'}$ ($l, l' = e, \mu, \tau$), when the Dirac CP phase δ_{CP} is varied over 0 ..... 2π. The vacuum probabilities are estimated for the LBNO configuration.

tions are in line with the 90% CL contour bands in Figure 6.1.

6.2 The effects of the triplet Higgs bosons in neutrino oscillations

In this Section, we discuss how the constraints for the NSI parameters $\varepsilon^{\rho\sigma}_{\alpha\beta}$ ($\alpha, \beta, \rho, \sigma = e, \mu, \tau$) can be used to determine the properties the triplet scalar bosons $\Delta = (\Delta^{++}, \Delta^{+}, \Delta^{0})$. Focusing on the findings of Publication V, this Section describes how the 90% CL bounds on the matter–NSI parameters $\varepsilon^m_{\alpha\beta} \equiv \varepsilon^{ee}_{\alpha\beta}$ can be used to constrain the ratio $|\lambda_\phi / M_\Delta|$, where λ_ϕ is the dimensionful strength of the $\Delta\phi\phi$ couplings and M_Δ is the degenerate mass of the scalars Δ^{++}, Δ^{+} and Δ^{0}.

In the low energy limit, where the triplet masses are degenerate with respect to the neutrino interaction energies in matter, the square of the ratio of the triplet

mass M_Δ and the trilinear coupling constant λ_ϕ, which is a dimensionful quantity, can be written as (see equation (3.34) in Chapter 3)

$$\frac{M_\Delta^2}{\lambda_\phi^2} = -\frac{8\sqrt{2}\, G_F\, \hat{v}^4\, \varepsilon^m_{\alpha\beta}}{(m_\nu)_{e\beta}(m_\nu^\dagger)_{\alpha e}}, \tag{6.4}$$

where m_ν is the neutrino mass matrix, given in the flavour basis, $\hat{v} \simeq 174$ GeV is the vacuum expectation value of the SM Higgs doublet ϕ, G_F is the Fermi coupling constant, and $\varepsilon^m_{\alpha\beta}$ is a non-diagonal parameter of the matter–NSI matrix ε^m, where $\alpha, \beta = e, \mu, \tau$.

Knowing that the neutrino oscillation experiments are not sensitive to the absolute scale of the diagonal parameters ε^m_{ee}, $\varepsilon^m_{\mu\mu}$ and $\varepsilon^m_{\tau\tau}$, these parameters can only be analyzed by their relative differences. For example, an analogue to the equation (6.4) but for $\varepsilon^m_{ee} - \varepsilon^m_{\mu\mu}$ is given by

$$\frac{M_\Delta^2}{\lambda_\phi^2} = -\frac{8\sqrt{2}\, G_F\, \hat{v}^4\, (\varepsilon^m_{ee} - \varepsilon^m_{\mu\mu})}{(m_\nu)_{ee}(m_\nu^\dagger)_{ee} - (m_\nu)_{e\mu}(m_\nu^\dagger)_{\mu e}}. \tag{6.5}$$

It is clear from equations (6.4) and (6.5) that the upper limits for $|\varepsilon^m_{\alpha\beta}|$ and $|\varepsilon^m_{\rho\rho} - \varepsilon^m_{\sigma\sigma}|$ translate to the upper limits of $M_\Delta^2/\lambda_\phi^2$. This means that the stronger the constraints are for the matter–NSI parameters $\varepsilon^m_{\alpha\beta}$, the stronger the constraints are also for the ratio $M_\Delta^2/\lambda_\phi^2$. Conversely, a large $M_\Delta^2/\lambda_\phi^2$ indicates significant matter–NSI effects.

In the work presented in Publication V, we analyzed the upper bounds measured for the matter–NSI parameters $\left|\varepsilon^m_{\alpha\beta}\right|$ and $\left|\varepsilon^m_{\rho\rho} - \varepsilon^m_{\sigma\sigma}\right|$ in neutrino oscillation experiments [124] and the 90% CL experimental sensitivities achievable in DUNE [125]. These upper bounds are compiled in Table 6.1.

We calculated the elements of the neutrino mass matrix m_ν in matter from the equation

$$(m_\nu)^2 = U \begin{pmatrix} m_1^2 & 0 & 0 \\ 0 & m_2^2 & 0 \\ 0 & 0 & m_3^2 \end{pmatrix} U^\dagger + A \begin{pmatrix} 1 + \varepsilon^m_{ee} - \varepsilon^m_{\mu\mu} & \varepsilon^m_{e\mu} & \varepsilon^m_{e\tau} \\ \varepsilon^{m*}_{e\mu} & 0 & \varepsilon^m_{\mu\tau} \\ \varepsilon^{m*}_{e\tau} & \varepsilon^{m*}_{\mu\tau} & \varepsilon^m_{\tau\tau} - \varepsilon^m_{\mu\mu} \end{pmatrix}, \tag{6.6}$$

where the neutrino masses m_1, m_2 and m_3 are determined from the oscillation parameters [40] $\Delta m^2_{21} \simeq 7.50{\times}10^{-5}$ eV^2 and $\Delta m^2_{31} \simeq 2.524{\times}10^{-3}$ eV^2 in the case of the normal hierarchy. In the case of the inverted hierarchy, the latter is replaced by $\Delta m^2_{32} \simeq$ –2.514$\times10^{-3}$ eV^2. For example, in the case of NH, the masses m_2 and m_3 are given by $m_2 = \sqrt{m_1^2 + \Delta m^2_{21}}$ and $m_3 = \sqrt{m_1^2 + \Delta m^2_{31}}$.

Assuming the normal hierarchy, we calculated the values of the matrix m_ν from equation (6.5) as a function of the lowest mass m_1, which was run through the values $m_1 = 0$ ... 0.2 eV, while the standard oscillation parameters were varied within their 90% CL error limits. Using equations (6.4) and (6.5), we obtained the

TABLE 6.1 Current experimental upper limits of the matter NSI parameters [124] and expected upper bounds after the first run with DUNE [125]. All of the limits are given at the 90 $\%$ confidence level significance.

Constraint on	Global bound	DUNE bound
$\lvert\varepsilon^m_{ee} - \varepsilon^m_{\mu\mu}\rvert$	4.2	0.9
$\lvert\varepsilon^m_{e\mu}\rvert$	0.3	0.074
$\lvert\varepsilon^m_{e\tau}\rvert$	3.0	0.19
$\lvert\varepsilon^m_{\mu\tau}\rvert$	0.04	0.038
$\lvert\varepsilon^m_{\tau\tau} - \varepsilon^m_{\mu\mu}\rvert$	0.15	0.08

90% CL upper bounds for the ratio $M_\Delta/\left|\lambda_\phi\right|$ by inserting the 90% CL constraints on the matter–NSI parameters. The results are presented in Figure 6.3, where the allowed values for $M_\Delta/\left|\lambda_\phi\right|$ from the current global constraints and the DUNE sensitivities are depicted with the yellow and green regions, respectively. We also determined the corresponding 90% CL contours for the inverted hierarchy, which are shown with the dot-dashed and dashed lines.

It is also possible that the scalar triplet Δ is accompanied by some other new physics elements in addition to the non-standard neutrino interactions. For example, the scalar triplet can be understood as a low energy effective theory of the left-right symmetric electroweak theory, which is based on the gauge group $\mathrm{SU(3)_C}$ $\times\mathrm{SU(2)_L}\times\mathrm{SU(2)_R}\times\mathrm{U(1)_{B-L}}$, where R stands for the right-handed chirality, and B and L for the baryon and lepton numbers, respectively. In a typical left-right symmetric model, the particle content of the SM is extended with the right-handed neutrinos, resulting in three additional Majorana neutrinos with a heavy mass, and the triplet Higgs bosons. These elements give rise to both the non-unitarity of the neutrino mixing matrix and the non-standard neutrino interactions, causing departures from the standard three neutrino oscillation patterns. Furthermore, these new physics effects are of the kind where one form can mimic the other.

We calculated the portion of the 90% CL allowed values for $M_\Delta/\left|\lambda_\phi\right|$, where the non-unitarity of the light neutrino mixing matrix may mimic the matter–NSI signal arising from the triplet Higgs interactions. These 90% CL contours were obtained by converting the experimental bounds on the non-unitarity parameters $\alpha_{ll'}$ (l, $l' = e$, μ, τ), presented in Table 5.1, by using the conversion relations shown in equation (3.29) in Chapter 3. In Figure 6.3, the region where the non-unitarity can be misinterpreted as the matter–NSI signal is shown with the blue colour, when NH is assumed. The corresponding 90% CL contour for the IH case is shown with the dotted line.

Our results indicate that the presently available neutrino oscillation data can

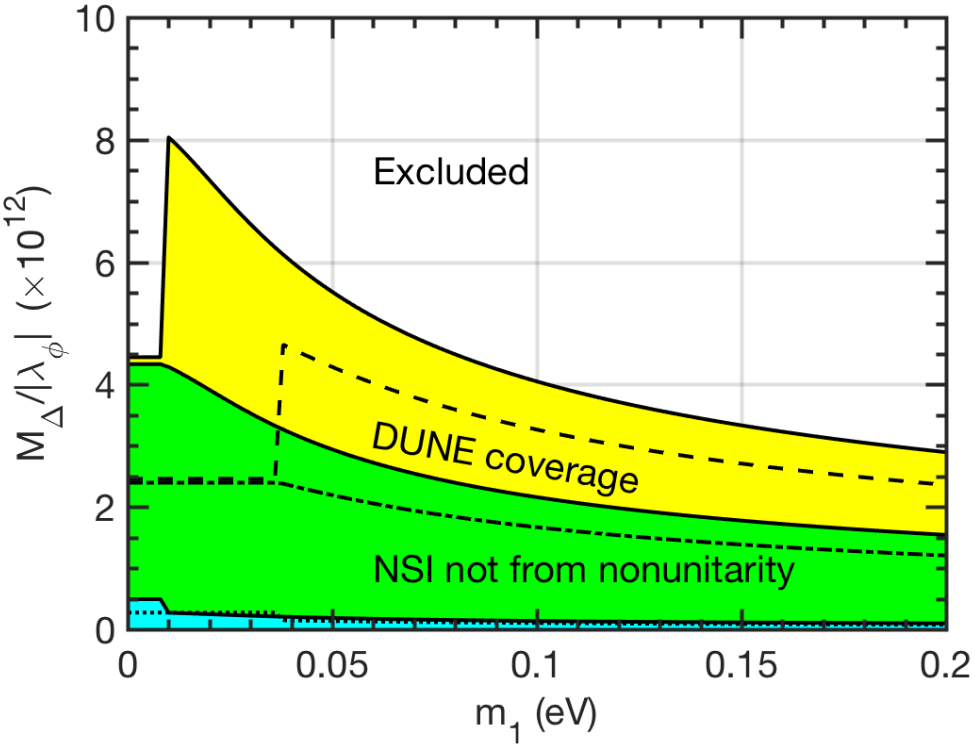

FIGURE 6.3 The allowed values of $M_\Delta/|\lambda_\phi|$ as a function of the smallest neutrino mass m_1, when the non-standard neutrino interactions in matter are considered. The white region shows the values of $M_\Delta/|\lambda_\phi|$ which can be excluded by a 90% confidence level (CL) or better by the experimental data that is currently available from the neutrino oscillations. Conversely, the yellow and green regions show the allowed values for the experimental data and the DUNE sensitivities, respectively. The blue region shows the potential contribution from the non-unitarity of the neutrino mixing matrix. Whereas the coloured regions are obtained assuming the normal mass hierarchy, the dashed, dot-dashed and dotted lines show the 90% CL contours for the experimental data, DUNE sensitivities, and non-unitarity in the inverted hierarchy, respectively.

TABLE 6.2 The experimental constraints and the expected DUNE sensitivities converted into the lower bounds of the 90 % confidence level for the trilinear coupling constant λ_ϕ, when the mass of the scalar triplet is taken to be $M_\Delta \gtrsim 750$ GeV. Here NH and IH correspond to normal and inverse neutrino mass hierarchy, respectively.

	Global λ_ϕ (eV)		**DUNE** λ_ϕ (eV)	
m_1 (eV)	**NH**	**IH**	**NH**	**IH**
0.0	0.031	0.045	0.120	0.178
0.1	0.129	0.133	0.509	0.526
0.2	0.251	0.253	0.997	1.006

exclude the values $M_\Delta/|\lambda_\phi| \gtrsim 8{\times}10^{12}$ at 90% CL, regardless of the value of the lightest neutrino mass m_1. It can be seen in Figure 6.3 that the 90% CL exclusion limit varies within $M_\Delta/|\lambda_\phi| \simeq 3....8{\times}10^{12}$ when the mass hierarchy is NH, whereas the higher values of $M_\Delta/|\lambda_\phi|$ can be excluded at 90% CL or better. When the projected experimental sensitivities for the DUNE configuration are considered, the 90% CL contour is brought down to $1.5.....4.5{\times}10^{12}$. When the mass hierarchy is IH, though, the experimental data and the DUNE sensitivities predict the 90% CL contours to be within $2.5.....4.5{\times}10^{12}$ and $1.2.....2.5{\times}10^{12}$, respectively. The impact of the non-unitarity, on the other hand, falls below $0.5{\times}10^{12}$ in both NH and IH, and it therefore has only a small effect compared to the total sensitivity.

We also investigated what the allowed values of the trilinear coupling constant λ_ϕ would be if the degenerate mass of the triplet members was assumed to be $M_\Delta \gtrsim 750$ GeV, which is the 90% CL lower bound for the mass of Δ^{++} that has been obtained for a specific scalar triplet model by analysing the proton-proton collision data from the LHC experiment (see Ref. [126] for more details). Using this 90% CL lower bound of the triplet mass M_Δ, we were able to obtain the 90% CL upper bounds for the coupling strength λ_ϕ. The numerical values of these upper bounds are listed for the neutrino masses $m_1 = 0.0$, 0.1 and 0.2 and both the mass hierarchies in Table 6.2.

As it was discussed in Chapter 3, the presence of the scalar triplet Δ may also have observable signatures in some leptonic decay channels. More specifically, the triplet interactions may give a significant contribution to the decay processes where the charged lepton flavour is no longer conserved, such as the muon decay into an electron and a positronium, that is, $\mu^- \to e^- e^+ e^-$. In the SM, the branching ratio of this process is heavily suppressed, whereas the decay width of the corresponding NSI process is directly proportional to the square of the NSI parameter $\varepsilon_{ee}^{e\mu}$. Analyzing the experimental upper limits for the decay widths of the various LFV processes, the 90% CL upper bounds can be obtained for the NSI parameters $\varepsilon_{\alpha\beta}^{\rho\sigma}$

TABLE 6.3 The experimental constraints on the parameters $\varepsilon^{\rho\sigma}_{\alpha\beta}$ (updated from [83] using [127]) from the $\ell \to \ell\ell\ell$, one-loop $\ell \to \ell\gamma$ and $\mu^+e^- \to \mu^-e^+$ processes. All bounds are given at 90% confidence level.

Decay	Constraint on	Bound
$\mu^- \to e^-e^+e^-$	$\lvert\varepsilon^{e\mu}_{ee}\rvert$	3.5×10^{-7}
$\tau^- \to e^-e^+e^-$	$\lvert\varepsilon^{e\tau}_{ee}\rvert$	1.4×10^{-4}
$\tau^- \to \mu^-\mu^+\mu^-$	$\lvert\varepsilon^{\mu\tau}_{\mu\mu}\rvert$	1.2×10^{-4}
$\tau^- \to e^-\mu^+e^-$	$\lvert\varepsilon^{e\tau}_{e\mu}\rvert$	1.0×10^{-4}
$\tau^- \to \mu^-e^+\mu^-$	$\lvert\varepsilon^{\mu\tau}_{\mu e}\rvert$	1.0×10^{-4}
$\tau^- \to e^-\mu^+\mu^-$	$\lvert\varepsilon^{e\tau}_{\mu\mu}\rvert$	1.0×10^{-4}
$\tau^- \to e^-e^+\mu^-$	$\lvert\varepsilon^{e\tau}_{\mu e}\rvert$	9.9×10^{-5}
$\mu^- \to e^-\gamma$	$\lvert\sum_\alpha \varepsilon^{e\mu}_{\alpha\alpha}\rvert$	2.6×10^{-5}
$\tau^- \to e^-\gamma$	$\lvert\sum_\alpha \varepsilon^{e\tau}_{\alpha\alpha}\rvert$	1.8×10^{-2}
$\tau^- \to \mu^-\gamma$	$\lvert\sum_\alpha \varepsilon^{\mu\tau}_{\alpha\alpha}\rvert$	2.0×10^{-4}
$\mu^+e^- \to \mu^-e^+$	$\lvert\varepsilon^{\mu e}_{\mu e}\rvert$	3.0×10^{-3}

($\alpha, \beta, \rho, \sigma = e, \mu, \tau$) by using relations like the one that is shown in equation (3.36). In the work that is presented in Publication V, we provided the updated values for the 90% CL from the various LFV processes. The results are presented in Table 6.3.

The NSI effects arising from the LFV interactions such as that of $\mu^- \to e^-e^+e^-$ can be used to constrain the ratio $M_\Delta/\lvert\lambda_\phi\rvert$. The relation between the ratio $M_\Delta/\lvert\lambda_\phi\rvert$ and the NSI parameter $\varepsilon^{e\mu}_{ee}$, for example, is given by

$$\frac{M^2_\Delta}{\lambda^2_\phi} = -\frac{8\sqrt{2}\, G_F\, \hat{v}^4\, \varepsilon^{e\mu}_{\alpha\beta}}{(m_\nu)_{e\beta}(m^\dagger_\nu)_{\alpha\mu}}. \tag{6.7}$$

We analyzed the upper bounds for the NSI parameters from the LFV interactions in Table 6.3, and derived the 90% CL upper bound for the ratio $M_\Delta/\lvert\lambda_\phi\rvert$. The strictest bound is provided on the parameter $\lvert\varepsilon^{e\mu}_{ee}\rvert$ by the process $\mu^- \to e^-e^+e^-$, which constrains the NSI parameter to the order of 10^{-7}. The resulting 90% CL upper bound for the ratio $M_\Delta/\lvert\lambda_\phi\rvert$ is presented in Figure 6.4 as a function of m_1, where the allowed values for $M_\Delta/\lvert\lambda_\phi\rvert$ and m_1 are shown at 90% CL by the red colour. The white region, on the other hand, shows the values that are excluded by a 90% CL or greater significance.

The allowed values of the ratio $M_\Delta/\lvert\lambda_\phi\rvert$ at 90% CL are shown to fall between

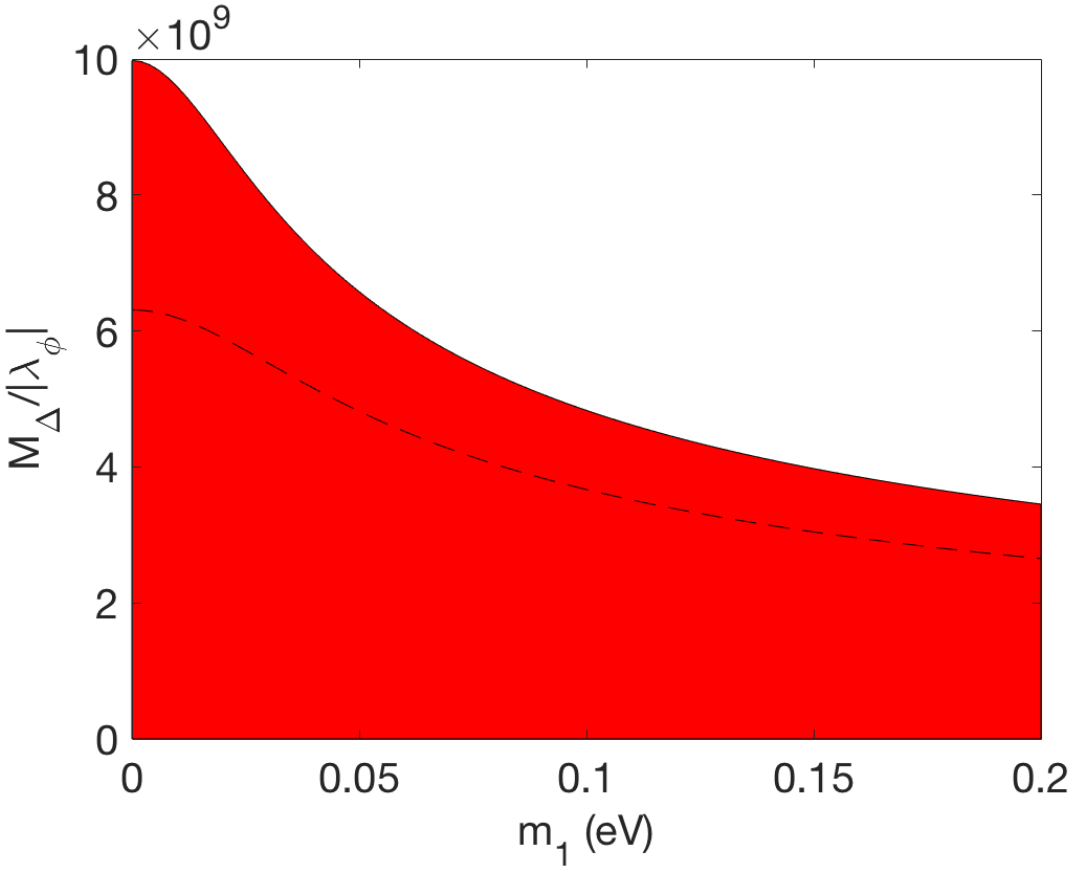

FIGURE 6.4 The allowed values of $M_\Delta/|\lambda_\phi|$ as a function of m_1, when the four-lepton non-standard interactions in the lepton flavour violating process $\mu^- \to e^-e^+e^-$ is considered. Whereas the white region shows the values that are excluded at a 90% confidence level (CL) or better, the red region shows the values which are still allowed by the experiments. The red colour represents the normal mass hierarchy and the dashed line contour the inverted hierarchy.

4.....10×10^9, when the four-lepton NSI from the lepton flavour violating decay $\mu^- \to e^-e^+e^-$ is considered under the normal mass hierarchy. When the inverted hierarchy is assumed, the sensitivity improves slightly. The non-observation of the LFV decays therefore provides much stricter bounds on $M_\Delta/|\lambda_\phi|$ than the neutrino oscillation experiments, where the 90% CL constraints are roughly three orders of magnitude less stringent.

We have established that the non-standard interactions arising from the scalar triplet $\Delta = (\Delta^{++}, \Delta^{+}, \Delta^{0})$ can be studied in the neutrino oscillation experiments. Although the neutrino oscillation data does not constrain the ratio $M_\Delta/|\lambda_\phi|$ as much as the process $\mu^- \to e^-e^+e^-$ does, the two methods could provide independent measurements on the triplet parameters should the non-standard interaction effects be sufficiently large.

Chapter 7

Summary and outlook

In the work that is presented in this thesis, we explored the prospects of the next generation long baseline neutrino experiments, focusing on two particular experimental configurations. On the one hand, we simulated the configuration of the Long Baseline Neutrino Observatory (LBNO), which was designed as a pan-European infrastructure for studying neutrino oscillations on a long baseline. If realized, LBNO would have provided an intense beam of muon neutrinos and antineutrinos to traverse 2300 km underground from CERN to the Pyhäsalmi mine in central Finland. We also simulated the configuration for the Deep Underground Neutrino Experiment (DUNE), which is the next generation long baseline neutrino experiment that is currently being constructed in the United States. DUNE will feature a similar configuration to that of LBNO, but with a 1300-km-long baseline between Fermilab and Sanford Underground Research Laboratory. In this thesis, I have described the similarities and differences of the LBNO and DUNE configurations, and the main principles of how the two experimental configurations are simulated with General Long-Baseline Experiment Simulator (GLoBES).

The research that is presented in this thesis can be divided into two distinct parts. First, we investigated the octancy of the atmospheric mixing angle θ_{23}, where it is sought whether the true value of the mixing angle θ_{23} lies in the low octant, $\theta_{23} < 45°$, or in the high octant, $\theta_{23} > 45°$. Simulating the LBNO and DUNE configurations with GLoBES, we determined experimental sensitivities for the determination of the θ_{23} octant, investigated how the sensitivities depend on the baseline length or in the event when the beam sharing between neutrinos and antineutrinos is changed in such an experiment, and showed how the systematic uncertainty arising from the normalization of the signal events affects the sensitivity to the θ_{23} octancy. We also examined how the presence of the new physics, such as the mixing between active neutrinos and hypothetical sterile neutrinos, the non-unitarity of the neutrino mixing matrix, or the non-standard neutrino interactions could change the sensitivity to the θ_{23} octant from that of the standard three-neutrino oscillation paradigm.

We also studied the experimental sensitivity to constrain the non-standard

neutrino interaction (NSI) parameters $\varepsilon^m_{ll'}$ ($l, l' = e, \mu, \tau$), which describe the coupling strengths of the non-standard neutrino interactions that would affect the propagation of the neutrinos. Using the LBNO configuration, we examined how this constraining power would change as a function of the baseline length, assuming that no evidence of the NSI is found. In a subsequent publication, we analysed the experimental sensitivities of the DUNE configuration and calculated the experimental sensitivities for the properties of the triplet Higgs bosons in the case where the NSI effects arise from the Type II Seesaw mechanism. Using the experimental sensitivities that had been calculated in Ref. [125], we derived the 90% confidence level (CL) upper bounds for the ratio $M_\Delta / |\lambda_\phi|$, where M_Δ is the degenerate mass of the scalar triplet $\Delta = (\Delta^{++}, \Delta^{+}, \Delta^{0})$, λ_ϕ is the dimensionful strength of the trilinear coupling $\phi\phi\Delta$, and $\phi = (\phi^{+}, \phi^{0})$ is the SM Higgs doublet.

The main results presented in Publications I–V are summarized as follows:

In Publication I, we described a new, improved simulation for the LBNO configuration and provided the detailed sensitivities to distinguish between the low and high octants of the mixing angle θ_{23}. We found that the LBNO configuration could determine the octancy at a $3\,\sigma$ CL or higher significance when $\theta_{23} \lesssim 41.2^\circ$ or $\theta_{23} \gtrsim 48.9^\circ$ in the first phase, and $\theta_{23} \lesssim 41.2^\circ$ or $\theta_{23} \gtrsim 48.9^\circ$ in the second phase of the experiment, and the mass hierarchy is assumed to be normal. When the mass hierarchy is inverted, the $3\,\sigma$ CL significance is reached when $\theta_{23} \lesssim 39.9^\circ$ or $\theta_{23} \gtrsim 51.1^\circ$ in the first phase, and $\theta_{23} \lesssim 44.4^\circ$ or $\theta_{23} \gtrsim 45.6^\circ$ in the second phase, respectively.

In Publication II, we analyzed the impact of the so called Mikheyev-Smirnov-Wolfenstein (MSW) matter effect on the probability level, and discussed how the experimental sensitivity to the determination of the θ_{23} octant can be optimized in the LBNO–like long baseline neutrino experiments. Utilizing the simulation, which we had developed for the LBNO configuration in Publication I, we calculated the experimental sensitivities for the determination of the θ_{23} octant under different baseline lengths, beam sharing options and systematics. Our results show that the sensitivity to the θ_{23} octancy depends significantly on the baseline length and the beam sharing. When the mass hierarchy is not known, we found that sharing the beam evenly with the neutrino and antineutrino modes yields the best result, whereas the knowledge of the hierarchy would allow to improve the sensitivity by fine-tuning the sharing between the neutrino and antineutrino modes.

In Publication III, we evaluated the impact of the new physics effects arising from the active–sterile neutrino mixing and the possible non-unitarity of the neutrino mixing matrix in the determination of the θ_{23} octant in DUNE. Simulating the configuration developed by the DUNE collaboration, we found that DUNE could determine the octancy at a $3\,\sigma$ CL or higher significance when $\theta_{23} \lesssim 43.5^\circ$ or $\theta_{23} \gtrsim 46.5^\circ$ regardless of the mass hierarchy. This sensitivity shifts on each side by approximately 0.2° in the case of the non-unitarity, and 0.5° in the case of a light sterile neutrino. Therefore, the presence of the new physics appears to have only limited

effects on the sensitivity to the θ_{23} octancy, when the constraints from the existing electroweak and short baseline oscillation data properly taken into account.

In Publication IV, we simulated the LBNO configuration with baseline lengths $L = 100$ km.....5000 km and calculated the 90% CL exclusion contours for the matter–NSI parameters $\varepsilon^m_{ll'}$. We also estimated the $\varepsilon^m_{ll'} - \delta_{\rm CP}$ correlation both analytically and by simulating the LBNO configuration. We discovered that the correlation is the strongest with the parameters $\varepsilon^m_{e\mu}$ and $\varepsilon^m_{e\tau}$, both methods confirming the result. We also found that the baseline lengths near 2000 km and beyond provided the best sensitivity to constrain the matter–NSI parameters.

In PublicationV, we calculated the 90% CL exclusion limits for the ratio $M_\Delta / |\lambda_\phi|$ from the present experimental constraints on the matter–NSI parameters $\varepsilon^m_{ll'}$, as well as from the experimental sensitivities that have been estimated for DUNE. We obtained the present 90% CL upper bound to be within 3.....8$\times 10^{12}$ and the DUNE sensitivities to imply 1.5.....4.5$\times 10^{12}$, when the mass hierarchy is taken to be normal. When the hierarchy is inverted, we found the present and DUNE bounds to be 1.2.....2.5$\times 10^{12}$ and 2.5.....4.5$\times 10^{12}$, respectively. For the lower bound $M_\Delta \gtrsim 750$ GeV, the DUNE sensitivities correspond to $|\lambda_\phi| \gtrsim 0.031$ eV and 0.045 eV in normal and inverted hierarchy, respectively.

The credibility of the simulation method that was used in Publications I–IV is concerned by several challenges, which motivates the development of more advanced techniques. The main difficulty in the simulation of the experimental configuration at various baseline lengths concerns the eligibility of the neutrino fluxes, which were initially provided for the LBNO configuration and are therefore optimized for the 2300 km baseline length. In Publication II, we resolved this issue by shifting the beam fluxes along the energy axis, in order to preserve the L/E value. In Publication IV, we did not adjust the beam fluxes to match each baseline length, which affected the calculated sensitivities especially at the very long baseline lengths. There are also other issues, ranging from the minimization of the χ^2 functions to the treatment of the a priori errors. Although the accuracy of our simulation results has clearly improved from Publication I through IV, it is evident that there is still room for development in the simulation technique.

Altogether, it is found that the next generation of the long baseline neutrino oscillation experiments will have great potential for the determination of the θ_{23} octant, as well as in the probing of the new physics effects, such as the non-standard neutrino interactions from the triplet Higgs bosons. In this thesis, it has been demonstrated that the new physics effects originating beyond the SM may be studied in the long baseline neutrino experiments, and the interplay of the experimental data from the short baseline and other experiments will have an important role in maintaining the future experiments' physics potential in the presence of the new physics.

Bibliography

[1] GIUNTI, C. AND KIM, C. W., *Fundamentals of Neutrino Physics and Astrophysics* (Oxford, UK: Univ. Pr. (2007) 710 p, 2007).

[2] BILENKY, S. M., *Bruno Pontecorvo and Neutrino Oscillations*. Adv. High Energy Phys. **2013** (2013) 873236.

[3] PONTECORVO, B., *Mesonium and anti-mesonium*. Sov. Phys. JETP **6** (1957) 429.

[4] KAJITA, T. (Kamiokande, Super-Kamiokande), *Atmospheric neutrino results from Super-Kamiokande and Kamiokande: Evidence for neutrino(mu) oscillations*. Nucl. Phys. Proc. Suppl. **77** (1999) 123–132. hep-ex/9810001.

[5] MCGREGOR, G. A. (SNO), *First results from the Sudbury Neutrino Observatory*, in *Proceedings, 37th Rencontres de Moriond on Electroweak Interactions and Unified Theories: Les Arcs, France, March 9-16, 2002* (2002), pp. 249–256. nucl-ex/0205006, URL http://inspirehep.net/record/586804/files/Pages_from_C02-03-09_249.pdf.

[6] BRANCO, G. C., FELIPE, R. G., AND JOAQUIM, F. R., *Leptonic CP Violation*. Rev. Mod. Phys. **84** (2012) 515–565. arXiv:1111.5332.

[7] MOFFAT, K., PASCOLI, S., PETCOV, S. T., AND TURNER, J., *Leptogenesis from Low Energy CP Violation* (2018). arXiv:1809.08251.

[8] FOGLI, G. L. AND LISI, E., *Tests of three flavor mixing in long baseline neutrino oscillation experiments*. Phys. Rev. **D54** (1996) 3667–3670. hep-ph/9604415.

[9] CAPOZZI, F., LISI, E., MARRONE, A., AND PALAZZO, A., *Current unknowns in the three neutrino framework*. Prog. Part. Nucl. Phys. **102** (2018) 48–72. arXiv:1804.09678.

[10] ŁAGODA, J., *Current and Future Neutrino Experiments*. Acta Phys. Polon. **B49** (2018) 1213–1228.

[11] ABE, K. *et al.* (T2K), *The T2K Experiment*. Nucl. Instrum. Meth. **A659** (2011) 106–135. arXiv:1106.1238.

[12] AYRES, D. S. *et al.* (NOvA), *The NOvA Technical Design Report* (2007).

[13] ARDELLIER, F. *et al.* (Double Chooz), *Double Chooz: A Search for the neutrino mixing angle theta(13)* (2006). hep-ex/0606025.

[14] AHN, J. K. *et al.* (RENO), *RENO: An Experiment for Neutrino Oscillation Parameter θ_{13} Using Reactor Neutrinos at Yonggwang* (2010). arXiv:1003.1391.

[15] GUO, X. *et al.* (Daya Bay), *A Precision measurement of the neutrino mixing angle θ_{13} using reactor antineutrinos at Daya-Bay* (2007). hep-ex/0701029.

[16] AHRENS, J. *et al.* (IceCube), *Icecube - the next generation neutrino telescope at the south pole*. Nucl. Phys. Proc. Suppl. **118** (2003) 388–395. astro-ph/0209556.

[17] ASLANIDES, E. *et al.* (ANTARES), *A deep sea telescope for high-energy neutrinos* (1999). astro-ph/9907432.

[18] FUKUDA, Y. *et al.* (Super-Kamiokande), *Evidence for oscillation of atmospheric neutrinos*. Phys. Rev. Lett. **81** (1998) 1562–1567. hep-ex/9807003.

[19] ALIMONTI, G. *et al.* (Borexino), *Science and technology of BOREXINO: A Real time detector for low-energy solar neutrinos*. Astropart. Phys. **16** (2002) 205–234. hep-ex/0012030.

[20] KEMP, E., *The Deep Underground Neutrino Experiment: The Precision Era of Neutrino Physics*. Astron. Nachr. **338** (2017) 993–999. arXiv:1709.09385.

[21] ADRIAN-MARTINEZ, S. *et al.* (KM3Net), *Letter of intent for KM3NeT 2.0*. J. Phys. **G43** (2016) 084001. arXiv:1601.07459.

[22] AHMED, S. *et al.* (ICAL), *Physics Potential of the ICAL detector at the India-based Neutrino Observatory (INO)*. Pramana **88** (2017) 79. arXiv:1505.07380.

[23] AN, F. *et al.* (JUNO), *Neutrino Physics with JUNO*. J. Phys. **G43** (2016) 030401. arXiv:1507.05613.

[24] ABE, K. *et al.*, *Letter of Intent: The Hyper-Kamiokande Experiment — Detector Design and Physics Potential —* (2011). arXiv:1109.3262.

[25] ATHANASSOPOULOS, C. *et al.* (LSND), *Candidate events in a search for anti-muon-neutrino —> anti-electron-neutrino oscillations*. Phys. Rev. Lett. **75** (1995) 2650–2653. nucl-ex/9504002.

[26] AGUILAR-AREVALO, A. *et al.* (LSND), *Evidence for neutrino oscillations from the observation of anti-neutrino(electron) appearance in a anti-neutrino(muon) beam*. Phys. Rev. **D64** (2001) 112007. hep-ex/0104049.

[27] AGUILAR-AREVALO, A. A. *et al.* (MiniBooNE), *Observation of a Significant Excess of Electron-Like Events in the MiniBooNE Short-Baseline Neutrino Experiment* (2018). arXiv:1805.12028.

[28] MINKOWSKI, P., $\mu \to e\gamma$ *at a Rate of One Out of* 10^9 *Muon Decays?* Phys. Lett. **67B** (1977) 421–428.

[29] YANAGIDA, T., *Horizontal Symmetry and Masses of Neutrinos*. Prog. Theor. Phys. **64** (1980) 1103.

[30] GELL-MANN, M., RAMOND, P., AND SLANSKY, R., *Complex Spinors and Unified Theories*. Conf. Proc. **C790927** (1979) 315–321. arXiv:1306.4669.

[31] HETTMANSPERGER, H., LINDNER, M., AND RODEJOHANN, W., *Phenomenological Consequences of sub-leading Terms in See-Saw Formulas*. JHEP **04** (2011) 123. arXiv:1102.3432.

[32] FARZAN, Y. AND TORTOLA, M., *Neutrino oscillations and Non-Standard Interactions*. Front.in Phys. **6** (2018) 10. arXiv:1710.09360.

[33] GARIAZZO, S., GIUNTI, C., LAVEDER, M., LI, Y. F., AND ZAVANIN, E. M., *Light sterile neutrinos*. J. Phys. **G43** (2016) 033001. arXiv:1507.08204.

[34] WOLFENSTEIN, L., *Neutrino Oscillations in Matter*. Phys. Rev. **D17** (1978) 2369–2374.

[35] MIKHEYEV, S. P. AND SMIRNOV, A. YU., *Resonance Amplification of Oscillations in Matter and Spectroscopy of Solar Neutrinos*. Sov. J. Nucl. Phys. **42** (1985) 913–917.

[36] DAS, C. R., MAALAMPI, J., PULIDO, J., AND VIHONEN, S., *Determination of the* θ_{23} *octant in LBNO*. JHEP **02** (2015) 048. arXiv:1411.2829.

[37] DAS, C. R., MAALAMPI, J., PULIDO, J., AND VIHONEN, S., *On the determination of the* θ_{23} *octant in long baseline neutrino experiments* (2016). arXiv:1606.02504.

[38] DAS, C. R., PULIDO, J., MAALAMPI, J., AND VIHONEN, S., *Determination of the* θ_{23} *octant in long baseline neutrino experiments within and beyond the standard model*. Phys. Rev. **D97** (2018) 035023. arXiv:1708.05182.

[39] HUITU, K., KÄRKKÄINEN, T. J., MAALAMPI, J., AND VIHONEN, S., *Constraining the nonstandard interaction parameters in long baseline neutrino experiments*. Phys. Rev. **D93** (2016) 053016. arXiv:1601.07730.

[40] HUITU, K., KÄRKKÄINEN, T. J., MAALAMPI, J., AND VIHONEN, S., *Effects of triplet Higgs bosons in long baseline neutrino experiments*. Phys. Rev. **D97** (2018) 095037. arXiv:1711.02971.

[41] MAKI, Z., NAKAGAWA, M., AND SAKATA, S., *Remarks on the unified model of elementary particles*. Prog. Theor. Phys. **28** (1962) 870–880.

[42] BILENKY, S. M., HOSEK, J., AND PETCOV, S. T., *On Oscillations of Neutrinos with Dirac and Majorana Masses*. Phys. Lett. **94B** (1980) 495–498.

[43] SCHECHTER, J. AND VALLE, J. W. F., *Neutrino Masses in SU(2) x U(1) Theories*. Phys. Rev. **D22** (1980) 2227.

[44] DOI, M., KOTANI, T., NISHIURA, H., OKUDA, K., AND TAKASUGI, E., *CP Violation in Majorana Neutrinos*. Phys. Lett. **102B** (1981) 323–326.

[45] LIU, J., *Neutrino coherent forward scattering and its index of refraction*. Phys. Rev. **D45** (1992) 1428–1431.

[46] ROSEN, S. P. AND GELB, J. M., *Mikheev-Smirnov-Wolfenstein Enhancement of Oscillations as a Possible Solution to the Solar Neutrino Problem*. Phys. Rev. **D34** (1986) 969.

[47] HALPRIN, A., *Neutrino Oscillations in Nonuniform Matter*. Phys. Rev. **D34** (1986) 3462–3466.

[48] PONTECORVO, B., *Neutrino Experiments and the Problem of Conservation of Leptonic Charge*. Sov. Phys. JETP **26** (1968) 984–988.

[49] ROULET, E., *MSW effect with flavor changing neutrino interactions*. Phys. Rev. **D44** (1991) 935–938.

[50] GUZZO, M. M., MASIERO, A., AND PETCOV, S. T., *On the MSW effect with massless neutrinos and no mixing in the vacuum*. Phys. Lett. **B260** (1991) 154–160.

[51] ACCIARRI, R. *et al.* (DUNE), *Long-Baseline Neutrino Facility (LBNF) and Deep Underground Neutrino Experiment (DUNE)* (2015). arXiv:1512.06148.

[52] COWAN, C. L., REINES, F., HARRISON, F. B., KRUSE, H. W., AND MCGUIRE, A. D., *Detection of the free neutrino: A Confirmation*. Science **124** (1956) 103–104.

[53] TANABASHI, M. *et al.* (Particle Data Group), *Review of Particle Physics*. Phys. Rev. **D98** (2018) 030001.

[54] CLEVELAND, B. T., DAILY, T., DAVIS, R., JR., DISTEL, J. R., LANDE, K., LEE, C. K., WILDENHAIN, P. S., AND ULLMAN, J., *Measurement of the solar electron neutrino flux with the Homestake chlorine detector*. Astrophys. J. **496** (1998) 505–526.

[55] FUKUDA, Y. *et al.* (Kamiokande), *Solar neutrino data covering solar cycle 22*. Phys. Rev. Lett. **77** (1996) 1683–1686.

[56] ALTMANN, M. *et al.* (GNO), *GNO solar neutrino observations: Results for GNO I*. Phys. Lett. **B490** (2000) 16–26. hep-ex/0006034.

[57] ABDURASHITOV, J. N. *et al.* (SAGE), *Solar neutrino flux measurements by the Soviet-American Gallium Experiment (SAGE) for half the 22 year solar cycle*. J. Exp. Theor. Phys. **95** (2002) 181–193. astro-ph/0204245.

[58] ABE, K. *et al.* (Super-Kamiokande), *Atmospheric neutrino oscillation analysis with external constraints in Super-Kamiokande I-IV*. Phys. Rev. **D97** (2018) 072001. arXiv:1710.09126.

[59] ADRIAN-MARTINEZ, S. *et al.* (ANTARES), *Measurement of Atmospheric Neutrino Oscillations with the ANTARES Neutrino Telescope*. Phys. Lett. **B714** (2012) 224–230. arXiv:1206.0645.

[60] AARTSEN, M. G. *et al.* (IceCube), *Measurement of Atmospheric Neutrino Oscillations at 6–56 GeV with IceCube DeepCore*. Phys. Rev. Lett. **120** (2018) 071801. arXiv:1707.07081.

[61] ADEY, D. *et al.* (Daya Bay), *Measurement of electron antineutrino oscillation with 1958 days of operation at Daya Bay* (2018). arXiv:1809.02261.

[62] SEO, S. H. *et al.* (RENO), *Spectral Measurement of the Electron Antineutrino Oscillation Amplitude and Frequency using 500 Live Days of RENO Data*. Phys. Rev. **D98** (2018) 012002. arXiv:1610.04326.

[63] GIL BOTELLA, I. (Double Chooz), *Latest results from Double Chooz*. PoS **EPS-HEP2017** (2017) 109.

[64] DE SALAS, P. F., FORERO, D. V., TERNES, C. A., TORTOLA, M., AND VALLE, J. W. F., *Status of neutrino oscillations 2018: 3σ hint for normal mass ordering and improved CP sensitivity*. Phys. Lett. **B782** (2018) 633–640. arXiv:1708.01186.

[65] ESTEBAN, I., GONZALEZ-GARCIA, M. C., MALTONI, M., MARTINEZ-SOLER, I., AND SCHWETZ, T., *Updated fit to three neutrino mixing: exploring the accelerator-reactor complementarity*. JHEP **01** (2017) 087. arXiv:1611.01514.

[66] ARAFUNE, J., KOIKE, M., AND SATO, J., *CP violation and matter effect in long baseline neutrino oscillation experiments*. Phys. Rev. **D56** (1997) 3093–3099. [Erratum: Phys. Rev. D60 (1999) 119905], hep-ph/9703351.

[67] OLIVE, K. A. *et al.* (Particle Data Group), *Review of Particle Physics*. Chin. Phys. **C38** (2014) 090001.

[68] ABE, K. *et al.* (T2K), *Measurement of neutrino and antineutrino oscillations by the T2K experiment including a new additional sample of ν_e interactions at the far detector*. Phys. Rev. **D96** (2017) 092006. [Erratum: Phys. Rev. D98, no.1 (2018) 019902], arXiv:1707.01048.

[69] KING, S. F., *Models of Neutrino Mass, Mixing and CP Violation*. J. Phys. **G42** (2015) 123001. arXiv:1510.02091.

[70] AGHANIM, N. *et al.* (Planck), *Planck 2018 results. VI. Cosmological parameters* (2018). arXiv:1807.06209.

[71] KRAUS, C. *et al.*, *Final results from phase II of the Mainz neutrino mass search in tritium beta decay*. Eur. Phys. J. **C40** (2005) 447–468. hep-ex/0412056.

[72] BRONCANO, A., GAVELA, M. B., AND JENKINS, E. E., *Neutrino physics in the seesaw model*. Nucl. Phys. **B672** (2003) 163–198. hep-ph/0307058.

[73] ABADA, A., BIGGIO, C., BONNET, F., GAVELA, M. B., AND HAMBYE, T., *Low energy effects of neutrino masses*. JHEP **12** (2007) 061. arXiv:0707.4058.

[74] CAI, Y., HERRERO-GARCÍA, J., SCHMIDT, M. A., VICENTE, A., AND VOLKAS, R. R., *From the trees to the forest: a review of radiative neutrino mass models*. Front.in Phys. **5** (2017) 63. arXiv:1706.08524.

[75] PATI, J. C. AND SALAM, A., *Lepton Number as the Fourth Color*. Phys. Rev. **D10** (1974) 275–289. [Erratum: Phys. Rev. D11 (1975) 703].

[76] MOHAPATRA, R. N. AND SIDHU, D. P., *Gauge Theories of Weak Interactions with Left-Right Symmetry and the Structure of Neutral Currents*. Phys. Rev. **D16** (1977) 2843.

[77] SENJANOVIC, G. AND MOHAPATRA, R. N., *Exact Left-Right Symmetry and Spontaneous Violation of Parity*. Phys. Rev. **D12** (1975) 1502.

[78] MOHAPATRA, R. N. AND PATI, J. C., *A Natural Left-Right Symmetry*. Phys. Rev. **D11** (1975) 2558.

[79] MOHAPATRA, R. N. AND PATI, J. C., *Left-Right Gauge Symmetry and an Isoconjugate Model of CP Violation*. Phys. Rev. **D11** (1975) 566–571.

[80] BRDAR, V. AND SMIRNOV, A. YU., *Low Scale Left-Right Symmetry and Naturally Small Neutrino Mass* (2018). arXiv:1809.09115.

[81] FERNANDEZ-MARTINEZ, E., HERNANDEZ-GARCIA, J., AND LOPEZ-PAVON, J., *Global constraints on heavy neutrino mixing*. JHEP **08** (2016) 033. arXiv:1605.08774.

[82] ESCRIHUELA, F. J., FORERO, D. V., MIRANDA, O. G., TÓRTOLA, M., AND VALLE, J. W. F., *Probing CP violation with non-unitary mixing in long-baseline neutrino oscillation experiments: DUNE as a case study*. New J. Phys. **19** (2017) 093005. arXiv:1612.07377.

[83] MALINSKY, M., OHLSSON, T., AND ZHANG, H., *Non-Standard Neutrino Interactions from a Triplet Seesaw Model*. Phys. Rev. **D79** (2009) 011301. arXiv:0811.3346.

[84] MENTION, G., FECHNER, M., LASSERRE, T., MUELLER, T. A., LHUILLIER, D., CRIBIER, M., AND LETOURNEAU, A., *The Reactor Antineutrino Anomaly*. Phys. Rev. **D83** (2011) 073006. arXiv:1101.2755.

[85] DENTLER, M., HERNÁNDEZ-CABEZUDO, L., KOPP, J., MALTONI, M., AND SCHWETZ, T., *Sterile neutrinos or flux uncertainties? — Status of the reactor antineutrino anomaly*. JHEP **11** (2017) 099. arXiv:1709.04294.

[86] ACCIARRI, R. *et al.* (MicroBooNE), *Design and Construction of the MicroBooNE Detector*. JINST **12** (2017) P02017. arXiv:1612.05824.

[87] ANTONELLO, M. *et al.* (LAr1-ND, ICARUS-WA104, MicroBooNE), *A Proposal for a Three Detector Short-Baseline Neutrino Oscillation Program in the Fermilab Booster Neutrino Beam* (2015). arXiv:1503.01520.

[88] ASHENFELTER, J. *et al.* (PROSPECT), *The PROSPECT Reactor Antineutrino Experiment* (2018). arXiv:1808.00097.

[89] CONRAD, J. M. AND SHAEVITZ, M. H., *Sterile Neutrinos: An Introduction to Experiments*. Adv. Ser. Direct. High Energy Phys. **28** (2018) 391–442. arXiv:1609.07803.

[90] OKUBO, S., *Note on Unitary Symmetry in Strong Interaction. II Excited States of Baryons*. Prog. Theor. Phys. **28** (1962) 24–32.

[91] ANTUSCH, S., BIGGIO, C., FERNANDEZ-MARTINEZ, E., GAVELA, M. B., AND LOPEZ-PAVON, J., *Unitarity of the Leptonic Mixing Matrix*. JHEP **10** (2006) 084. hep-ph/0607020.

[92] ESCRIHUELA, F. J., FORERO, D. V., MIRANDA, O. G., TORTOLA, M., AND VALLE, J. W. F., *On the description of nonunitary neutrino mixing*. Phys. Rev. **D92** (2015) 053009. [Erratum: Phys. Rev. D93, no.11 (2016) 119905], arXiv:1503.08879.

[93] MIRANDA, O. G., TORTOLA, M., AND VALLE, J. W. F., *New ambiguity in probing CP violation in neutrino oscillations*. Phys. Rev. Lett. **117** (2016) 061804. arXiv:1604.05690.

[94] BLENNOW, M., COLOMA, P., FERNANDEZ-MARTINEZ, E., HERNANDEZ-GARCIA, J., AND LOPEZ-PAVON, J., *Non-Unitarity, sterile neutrinos, and Non-Standard neutrino Interactions*. JHEP **04** (2017) 153. arXiv:1609.08637.

[95] MARTINEZ-SOLER, I. AND MINAKATA, H., *Standard versus Non-Standard CP Phases in Neutrino Oscillation in Matter with Non-Unitarity* (2018). arXiv:1806.10152.

[96] HERNANDEZ-GARCIA, J. AND LOPEZ-PAVON, J., *Non-Unitarity vs sterile neutrinos at DUNE*, in *Proceedings, Prospects in Neutrino Physics (NuPhys2016): London, UK, December 12-14, 2016* (2017). arXiv:1705.01840.

[97] MIRANDA, O. G. AND NUNOKAWA, H., *Non standard neutrino interactions: current status and future prospects*. New J. Phys. **17** (2015) 095002. arXiv:1505.06254.

[98] OHLSSON, T., *Status of non-standard neutrino interactions*. Rept. Prog. Phys. **76** (2013) 044201. arXiv:1209.2710.

[99] GROSSMAN, Y., *Nonstandard neutrino interactions and neutrino oscillation experiments*. Phys. Lett. **B359** (1995) 141–147. hep-ph/9507344.

[100] HUBER, P., LINDNER, M., AND WINTER, W., *Simulation of long-baseline neutrino oscillation experiments with GLoBES (General Long Baseline Experiment Simulator)*. Comput. Phys. Commun. **167** (2005) 195. hep-ph/0407333.

[101] HUBER, P., KOPP, J., LINDNER, M., ROLINEC, M., AND WINTER, W., *New features in the simulation of neutrino oscillation experiments with GLoBES 3.0: General Long Baseline Experiment Simulator*. Comput. Phys. Commun. **177** (2007) 432–438. hep-ph/0701187.

[102] RUBBIA, A. (LAGUNA), *The LAGUNA design study: Towards giant liquid based underground detectors for neutrino physics and astrophysics and proton decay searches*. Acta Phys. Polon. **B41** (2010) 1727–1732.

[103] ANGUS, D. *et al.* (LAGUNA), *The LAGUNA design study-towards giant liquid based underground detectors for neutrino physics and astrophysics and proton decay searches*, in *European strategy for future neutrino physics. Proceedings, Workshop, Geneva, Switzerland, October 1-3, 2009* (2010), pp. 226–229. arXiv:1001.0077.

[104] STAHL, A. *et al.*, *Expression of Interest for a very long baseline neutrino oscillation experiment (LBNO)*. CERN-SPSC-2012-021, SPSC-EOI-007 (2012).

[105] TRZASKA, W. H., BEZRUKOV, L., ENQVIST, T., JOUTSENVAARA, J., KUSINIEMI, P., LOO, K., LUBSANDORZHIEV, B., SINEV, V., AND SLUPECKI, M., *Possibilities for Underground Physics in the Pyhäsalmi mine*, in *13th Conference on*

the Intersections of Particle and Nuclear Physics (CIPANP 2018) Palm Springs, California, USA, May 29-June 3, 2018 (2018). arXiv:1810.00909.

[106] AGARWALLA, S. K. *et al.* (LAGUNA-LBNO), *The LBNO long-baseline oscillation sensitivities with two conventional neutrino beams at different baselines* (2014). arXiv:1412.0804.

[107] ACCIARRI, R. *et al.* (DUNE), *Long-Baseline Neutrino Facility (LBNF) and Deep Underground Neutrino Experiment (DUNE)* (2016). arXiv:1601.05471.

[108] STRAIT, J. *et al.* (DUNE), *Long-Baseline Neutrino Facility (LBNF) and Deep Underground Neutrino Experiment (DUNE)* (2016). arXiv:1601.05823.

[109] ACCIARRI, R. *et al.* (DUNE), *Long-Baseline Neutrino Facility (LBNF) and Deep Underground Neutrino Experiment (DUNE)* (2016). arXiv:1601.02984.

[110] ABI, B. *et al.* (DUNE), *The DUNE Far Detector Interim Design Report Volume 1: Physics, Technology and Strategies* (2018). arXiv:1807.10334.

[111] ABI, B. *et al.* (DUNE), *The DUNE Far Detector Interim Design Report, Volume 2: Single-Phase Module* (2018). arXiv:1807.10327.

[112] ABI, B. *et al.* (DUNE), *The DUNE Far Detector Interim Design Report, Volume 3: Dual-Phase Module* (2018). arXiv:1807.10340.

[113] AMERIO, S. *et al.* (ICARUS), *Design, construction and tests of the ICARUS T600 detector*. Nucl. Instrum. Meth. **A527** (2004) 329–410.

[114] ABI, B. *et al.* (DUNE), *The Single-Phase ProtoDUNE Technical Design Report* (2017). arXiv:1706.07081.

[115] AIMARD, B. *et al.*, *A 4 tonne demonstrator for large-scale dual-phase liquid argon time projection chambers*. JINST **13** (2018) P11003. 1806.03317.

[116] SANDBOX, *Long Baseline Neutrino Facility - Cutaway of Earth Illustration LBNF with 800 miles / 1300 kilometers*, https://vms.fnal.gov/asset/detail?recid=1933693 (2015). [Online; accessed 20-August-2018].

[117] AGARWALLA, S. K., LI, T., AND RUBBIA, A., *An Incremental approach to unravel the neutrino mass hierarchy and CP violation with a long-baseline Superbeam for large θ_{13}*. JHEP **05** (2012) 154. arXiv:1109.6526.

[118] COLOMA, P., LI, T., AND PASCOLI, S., *A Comparative Study of Long-Baseline Superbeams within LAGUNA for large θ_{13}* (2012). arXiv:1206.4038.

[119] ALION, T. *et al.* (DUNE), *Experiment Simulation Configurations Used in DUNE CDR* (2016). arXiv:1606.09550.

[120] CHATTERJEE, A., GHOSHAL, P., GOSWAMI, S., AND RAUT, S. K., *Octant sensitivity for large theta(13) in atmospheric and long baseline neutrino experiments*. JHEP **06** (2013) 010. arXiv:1302.1370.

[121] AKHMEDOV, E. K., JOHANSSON, R., LINDNER, M., OHLSSON, T., AND SCHWETZ, T., *Series expansions for three flavor neutrino oscillation probabilities in matter*. JHEP **04** (2004) 078. hep-ph/0402175.

[122] GANDHI, R., GHOSHAL, P., GOSWAMI, S., MEHTA, P., SANKAR, S. U., AND SHALGAR, S., *Mass Hierarchy Determination via future Atmospheric Neutrino Detectors*. Phys. Rev. **D76** (2007) 073012. arXiv:0707.1723.

[123] KÄRKKÄINEN, T. J., *Pursuit for optimal baseline for matter nonstandard interactions in long baseline neutrino oscillation experiments*, in *18th Lomonosov Conference on Elementary Particle Physics Moscow, Russia, August 24-30, 2017* (2017). arXiv:1710.01080.

[124] BIGGIO, C., BLENNOW, M., AND FERNANDEZ-MARTINEZ, E., *General bounds on non-standard neutrino interactions*. JHEP **08** (2009) 090. arXiv:0907.0097.

[125] BLENNOW, M., CHOUBEY, S., OHLSSON, T., PRAMANIK, D., AND RAUT, S. K., *A combined study of source, detector and matter non-standard neutrino interactions at DUNE*. JHEP **08** (2016) 090. arXiv:1606.08851.

[126] COLLABORATION, C. (CMS), *A search for doubly-charged Higgs boson production in three and four lepton final states at* $\sqrt{s} = 13$ TeV (2017).

[127] PATRIGNANI, C. *et al.* (Particle Data Group), *Review of Particle Physics*. Chin. Phys. **C40** (2016) 100001.

Publications I-V

Publication I

I

C.R. Das, J. Maalampi, J. Pulido and S. Vihonen,
Determination of the θ_{23} octant in LBNO,
JHEP **02** (2015) 048,
arXiv:1411.2829 [hep-ph]

Published for SISSA by Springer

Received: December 3, 2014
Accepted: January 18, 2015
Published: February 9, 2015

Determination of the θ_{23} octant in LBNO

C.R. Das,[a,b,c] **Jukka Maalampi,**[a] **João Pulido**[b] **and Sampsa Vihonen**[a]

[a] *University of Jyvaskyla, Department of Physics, P.O. Box 35, FIN-40014 Jyvaskyla, Finland*

[b] *Centro de Física Teórica das Partículas (CFTP) Departamento de Física, Instituto Superior Técnico Av. Rovisco Pais, P-1049-001 Lisboa, Portugal*

[c] *Theoretical Physics Division, Physical Research Laboratory, Navrangpura, Ahmedabad 380 009, India*

E-mail: crdas@prl.res.in, jukka.maalampi@jyu.fi, pulido@cftp.ist.utl.pt, sampsa.p.vihonen@student.jyu.fi

Abstract: According to the recent results of the neutrino oscillation experiment MINOS, the neutrino mixing angle θ_{23} may not be maximal (45°). Two nearly degenerate solutions are possible, one in the lower octant (LO) where $\theta_{23} < 45°$, and one in the higher octant (HO) where $\theta_{23} > 45°$. Long baseline experiments measuring the $\nu_\mu \to \nu_e$ are capable of resolving this degeneracy. In this work we study the potential of the planned European LBNO experiment to distinguish between the LO and HO solutions.

Keywords: Oscillation, Neutrino Detectors and Telescopes

ArXiv ePrint: 1411.2829v2

doi:10.1007/JHEP02(2015)048

Contents

JHEP02(2015)048

1 Introduction

Neutrino oscillations are described in terms of six physical variables: the three mixing angles θ_{12}, θ_{23} and θ_{13}, the Dirac CP phase $\delta_{\rm CP}$, and the two squared-mass differences $\Delta m^2_{21} = m^2_2 - m^2_1$ and $\Delta m^2_{31} = m^2_3 - m^2_1$. Most of these quantities are experimentally measured with good accuracy [1–3]. However, one still does not know the sign of Δm^2_{31}, that is, whether the masses obey the normal hierarchy (NH) $m_1, m_2 < m_3$ or the inverted hierarchy (IH) $m_1, m_2 > m_3$, and the value of the CP phase $\delta_{\rm CP}$ also is undetermined, all values in the range $-180°$ to $+180°$ being still allowed. In addition of these two unknowns, which are expected to be resolved in the future long baseline oscillation experiments, there is a third intriguing question known as the octant or θ_{23}-degeneracy problem [4–7]. In the leading order the muon neutrino disappearance in the transition $\nu_\mu \to \nu_\mu$ is not sensitive to the octancy of θ_{23}, that is, whether this angle lies in the lower octant (LO) $\theta_{23} < 45°$ or in the higher octant (HO) $\theta_{23} > 45°$, both alternatives giving the same disappearance probability. In contrast, the leading term of the probability of the electron neutrino appearance $\nu_\mu \to \nu_e$ is octant sensitive [8]. Hence an accurate measurement of the transition probability $P(\nu_\mu \to \nu_e)$ in the future long baseline neutrino oscillation experiments might be capable of resolving the octant degeneracy.

Of course, the octant degeneracy problem would not exist if the angle θ_{23} mixing were maximal, i.e. $\theta_{23} = 45°$. The recent results of the MINOS oscillation experiment [9] seem to indicate, however, that this is not the case. Two degenerate solutions were found, one in the lower octant (LO) with $\sin^2\theta_{23} \simeq 0.4$ and one in the higher octant (HO) with $\sin^2\theta_{23} \simeq 0.6$. This corresponds to a deviation of about $5°$ downwards or upwards, correspondingly, from the maximal-mixing value $\theta_{23} = 45°$. On the other hand the T2K collaboration [10] has recently reported a θ_{23} central value lying close to the borderline between both octants, being unable to exclude any of the two possibilities.

The octant affects the event rates both for the neutrino transition $\nu_\mu \to \nu_e$ and the antineutrino transition $\bar\nu_\mu \to \bar\nu_e$, the HO corresponding to more events than the LO. This is true for both the NH and IH mass hierarchies. In addition to the dependence on the θ_{23} octant, the event rates are quite strongly affected by the value of the CP phase $\delta_{\rm CP}$. A balanced neutrino and anti-neutrino data is requisite for the separation of LO and HO (for a recent analysis, see [11]).

In this paper, we analyze the potential of the planned long baseline neutrino oscillation experiment LBNO [12] for resolving the θ_{23} octant degeneracy. In LBNO the aim is to send neutrino and antineutrino beams, produced at the CERN SPS accelerator, towards the Pyhäsalmi mine, located in central Finland at the distance 2288 km from CERN, where they will be measured using a two-phase Liquid Argon Time Projection Chamber (LArTPC) [13, 14] combined with a magnetized muon detector (MIND) [15, 16]. In the first phase, the size of the LArTPC detector is planned to have 20 kton fiducial mass. In this phase a 0.75 MW conventional neutrino beam from the CERN SPS will be used. In the second phase the total detector mass will be extended to 70 kton, and a powerful 2 MW HPPS proton driver [17] is foreseen to be in use. We will determine for both phases the $1\,\sigma$, $2\,\sigma$ and $3\,\sigma$ sensitivity limit of the angle θ_{23} that LBNO can achieve with 5+5 -years neutrino and antineutrino run, allowing the CP phase to vary in the range $-180°$ to $+180°$.

2 Numerical analysis

The sensitivity for determining the θ_{23} octant has been previously analysed for NOνA [18] and T2K [10], as well as for the proposed very long baseline experiment of the future, LBNO [19] and LBNE [8]. According to recent reviews (see e.g. [11]), the LBNO offers the best potential for determining the octancy of θ_{23}. In this work we present a detailed numerical analysis for the LBNO. The numerical simulation method we use is in most parts adopted from [19], however, using for our calculations the GLoBES simulation program [20, 21] instead of Monte Carlo simulations.

GLoBES is a simulator that predicts the propagation of neutrinos from the moment they are created in the source to the point they reach the detector and interact with its content. The software evaluates the effect of matter potentials induced by the traversed medium and calculates the resulting event rates that follow from the detection and reconstruction of neutrino events that take place in the detector. The estimated event rates are then used to evaluate the likelihood of different oscillation parameter values with χ^2-distributions.

The muon neutrino beam is assumed to be produced in the CERN SPS accelerator with a power of 750 kW, shared between neutrino and antineutrino modes at a 50%/50% ratio. (This is the same set-up proposed in [19] for the determination of the mass hierarchy.) This corresponds to 1.125×10^{20} POT per year for each beam, and it builds up a total yield of 1.125×10^{21} over the course of the 5+5 -year running time. We also consider the HPPS setup by increasing the annual POT number to 3.0×10^{21}. The key parameters concerning the LBNO are presented in table 1.

The muon neutrino beam is assumed to be nearly pure, though it is contaminated by small numbers of electron neutrinos and antineutrinos. The contamination is an irreducible side product of the muon neutrino creation through meson decays in a hadronic beam and it cannot be removed. We have obtained the respective neutrino fluxes from dedicated flux files based on a GEANT4 simulation [22].

In this work we assume the following detecting properties [23, 24]. The LArTPC detector is capable of detecting electron and muon neutrinos by observing secondary electron

JHEP02(2015)048

Parameter	Value
Beam power [SPS] (10^{20} POT/yr)	1.125
Beam power [HPPS] (10^{21} POT/yr)	3.0
Baseline length (km)	2288
Running times (yr)	5+5
Detection efficiency (%)	90
ν_μ NC rejection (%)	99.5
ν_μ CC rejection (%)	99.5
Energy resolution (GeV)	$0.15 \times \sqrt{E}$
Energy window (GeV)	[0.1, 10.0]
Number of bins	80
Bin width (GeV)	0.125

Table 1. Experiment parameters.

and muon leptons at approximately constant 90% rate. The LBNO neutrinos are detected within [0.1 GeV, 10.0 GeV] energy range, which is divided into 80 energy bins, each bin 0.125 GeV wide. The detection and reconstruction process has the following parameters: whenever a neutrino interacts with the detector substance, the counting system reconstructs the energy and flavor of the incident neutrino and identifies the event with the corresponding energy bin. The reconstructed energy is assumed to be normally distributed with a resolution of $0.15 \times \sqrt{E}$, where E is the neutrino energy in GeV. The cross sections of the charged current (CC) and neutral current (NC) neutrino-nucleon interactions are given in cross section files simulated for LArTPC with a dedicated GENIE simulation [25]. The simulation is specifically dedicated to LArTPC systems, and it takes the oscillations to tau neutrinos into account better than any previous simulation.

The LBNO experiment is designed to study the electron appearance probabilities $P(\nu_\mu \to \nu_e)$ and $P(\bar{\nu}_\mu \to \bar{\nu}_e)$ by counting the corresponding CC events in the detector. These CC events constitute the signal, whereas background consists of any type of events that have similar final state properties. On one hand, the electron appearance channels gain background from CC and NC events with ν_e and $\bar{\nu}_e$ arising from the oscillations of the impurities in the muon neutrino beam. On the other hand, the detector is also assumed to have a 0.5% chance to accept ν_μ and $\bar{\nu}_\mu$ from $\nu_\mu \to \nu_\mu$ and $\bar{\nu}_\mu \to \bar{\nu}_\mu$ as ν_e and $\bar{\nu}_e$ from both CC and NC event categories. Lastly, ν_τ and $\bar{\nu}_\tau$ neutrinos originated from $\nu_\mu \to \nu_\tau$ and $\bar{\nu}_\mu \to \bar{\nu}_\tau$ oscillations also contribute to the background. The number of τ leptons produced in the detector from these neutrinos accounts for approximately 6% of the total number of leptons produced [12]. Inserting the branching ratio of the τ subsequent decay into electrons through $\tau \to e\,\nu_e\,\nu_\tau$ (∼17.8%) [26] together with the detector efficiency (90%), one sees that the corresponding ν_e contamination is 1%, hence of the same order of magnitude as the intrinsic beam contamination.

JHEP02(2015)048

Besides electron appearance, also the muon disappearance probabilities $P(\nu_\mu \to \nu_\mu)$ and $P(\bar{\nu}_\mu \to \bar{\nu}_\mu)$ are studied. In this case the signal composes of the respective CC events whereas the background consists of $\nu_\mu \to \nu_\mu$ and $\bar{\nu}_\mu \to \bar{\nu}_\mu$ NC neutrinos and $\nu_e \to \nu_\mu$ and $\bar{\nu}_e \to \bar{\nu}_\mu$ CC neutrinos that are mistakenly accepted as signal neutrinos. We assume in our analysis the experiment to be able to distinguish between neutrinos and antineutrinos, reducing the background of $\nu_\mu \to \nu_\mu$ and $\nu_\mu \to \nu_e$ to only neutrino channels and $\bar{\nu}_\mu \to \bar{\nu}_\mu$ and $\bar{\nu}_\mu \to \bar{\nu}_e$ only to antineutrino channels, respectively. Also, $\nu_\mu \to \nu_\tau$ and $\bar{\nu}_\mu \to \bar{\nu}_\tau$ oscillations contribute to ν_μ and $\bar{\nu}_\mu$ background through $\tau \to \mu\,\nu_\mu\,\nu_\tau$ decay.

The χ^2 values are calculated as follows (see e.g. [20, 21]). The statistical part is computed with the Poissonian function

$$\chi^2(\omega, \omega_0) = \sum_{i=1}^{80} 2\left[T_i - O_i\left(1 - \ln\frac{T_i}{O_i}\right)\right], \tag{2.1}$$

where the number of observed events (O_i) in the ith bin is computed from the so called true values (ω_0) and the number of test events (T_i) from the test values (ω), respectively.

The observed events is the category of events that would result from oscillation parameter values that one considers to be closest to the truth. They are based on the best-fit values obtained from the most recent experiments. We denote these values with ω_0. Since all parameter values are not precisely known, such as the sign of Δm^2_{31}, the χ^2 values need to be computed for all possible scenarios. The number of observed events is taken to be the sum of events from signal and background components:

$$O_i = N_i^{\mathrm{sg}}(\omega_0) + N_i^{\mathrm{bg}}(\omega_0), \tag{2.2}$$

where N_i^{sg} and N_i^{bg} stand for the numbers of signal and background events.

The test values on the other hand stand for event numbers that are computed with whatever oscillation parameter values one wants to test. We denote these values with ω. We also apply systematic errors to both signal and background events by incorporating two nuisance parameters [20, 21], ζ_1 and ζ_2, with error weights π_1 and π_2:

$$T_i = N_i^{\mathrm{sg}}(\omega)[1 + \pi_1\zeta_1] + N_i^{\mathrm{bg}}(\omega)[1 + \pi_2\zeta_2]. \tag{2.3}$$

The systematic errors are included by minimizing the χ^2 function over nuisance parameters ζ_1 and ζ_2:

$$\chi^2_{\mathrm{pull}}(\omega, \omega_0) = \min_{\zeta_1,\zeta_2}\left[\chi^2(\omega, \omega_0) + \zeta_1^2 + \zeta_2^2\right], \tag{2.4}$$

where $\chi^2(\omega, \omega_0)$ is the Poissonian function given by equation (2.1). We assume 5 % systematical error weights in both signal and background by setting $\pi_1, \pi_2 = 0.05$. This corresponds to the normalization error in the LArTPC detectors [11].

We also assume that the values of θ_{12}, θ_{13}, Δm^2_{21}, Δm^2_{31}, δ_{CP} and ρ are associated with standard deviations $\sigma(\theta_{12})$, $\sigma(\theta_{13})$, $\sigma(\Delta m^2_{21})$, $\sigma(\Delta m^2_{31})$ and $\sigma(\rho)$. We include these

JHEP02(2015)048

Parameter	Value	Error ($1\,\sigma$)
$\sin^2\theta_{12}$	0.304	0.013
$\sin^2\theta_{13}$ (NH)	0.0218	0.0010
$\sin^2\theta_{13}$ (IH)	0.0219	0.0011
$\sin^2\theta_{23}$	varied	0
δ_{CP} [°]	varied	0
Δm^2_{21} [$10^{-5}\,\mathrm{eV}^2$]	7.50	0.19
Δm^2_{31} (NH) [$10^{-3}\,\mathrm{eV}^2$]	2.457	0.047
Δm^2_{31} (IH) [$10^{-3}\,\mathrm{eV}^2$]	-2.449	0.048

Table 2. Oscillation parameters.

parameter uncertainties via the so called priors [20, 21]. The prior function is given by:

$$\begin{aligned}\chi^2_{\mathrm{prior}}(\omega,\omega_0) = &\left(\frac{\sin^2\theta_{12}(\omega)-\sin^2\theta_{12}(\omega_0)}{\sigma(\sin^2\theta_{12})}\right)^2+\left(\frac{\sin^2 2\theta_{13}(\omega)-\sin^2 2\theta_{13}(\omega_0)}{\sigma(\sin^2 2\theta_{13})}\right)^2\\&+\left(\frac{\Delta m^2_{21}(\omega)-\Delta m^2_{21}(\omega_0)}{\sigma(\Delta m^2_{21})}\right)^2+\left(\frac{\Delta m^2_{31}(\omega)-\Delta m^2_{31}(\omega_0)}{\sigma(\Delta m^2_{31})}\right)^2\\&+\left(\frac{\rho(\omega)-\rho(\omega_0)}{\sigma(\rho)}\right)^2.\end{aligned} \tag{2.5}$$

The overall χ^2 value is calculated as the sum of the pull and prior parts from equations (2.4) and (2.5), which is then minimized over the test values:

$$\chi^2_{\mathrm{total}}(\omega_0) = \min_{\omega}\left[\chi^2_{\mathrm{pull}}(\omega,\omega_0)+\chi^2_{\mathrm{prior}}(\omega,\omega_0)\right]. \tag{2.6}$$

The matter density parameter ρ is taken into account as a variable in equation (2.6). The density distribution of the Earth's crust between CERN and Pyhäsalmi is known to a good accuracy [27], but for this study we consider it sufficient to evaluate the matter density function with a 20-step PREM distribution [28], and assume 2% error value ($1\,\sigma$).

The final χ^2 value is calculated by minimizing χ^2_{total} over all oscillation parameters in the test values, that is, over ω. The prior function constrains the value ranges over which χ^2_{total} may converge, and the absence of δ_{CP} in equation (2.5) indicates that no such constraints are assumed for δ_{CP}. We also choose to keep θ_{23} fixed in the minimization process.

We calculate the $1\,\sigma$, $2\,\sigma$ and $3\,\sigma$ confidence levels for the event that the LBNO experiment will be able to rule out one octant when the other octant is assumed to be correct. This is done by computing χ^2 first for θ_{23} and then $90^\circ-\theta_{23}$, and calculating the difference between the two χ^2 values, both calculated as given in equation (2.6):

$$\Delta\chi^2 = \chi^2_{\mathrm{total}}(90^\circ-\theta_{23})-\chi^2_{\mathrm{total}}(\theta_{23}). \tag{2.7}$$

We take the true values from [29], which contains a recent compilation on experimentally determined parameter values. These values are also presented in table 2.

JHEP02(2015)048

The Gaussian errors shown in table 2 are distributed for parameters $\sin^2\theta_{12}$, $\sin^2 2\theta_{13}$, Δm^2_{21} and Δm^2_{31}, respectively. The errors of $\delta_{\rm CP}$ and $\sin^2\theta_{23}$ are not present in the prior function $\chi^2_{\rm prior}$ and therefore they are both marked with zero. This follows from our choice that $\delta_{\rm CP}$ is not assigned with constraints and θ_{23} is kept fixed in the minimization of χ^2.

The minimization of the χ^2 function in equation (2.6) is carried out keeping θ_{23} fixed and other parameters free. Since θ_{23} and $\delta_{\rm CP}$ are not precisely known, we calculate the χ^2 values for different possible values of θ_{23} and $\delta_{\rm CP}$, and for both mass hierarchies as well.

3 Results and discussion

We have investigated the ability of the LBNO experiment to determine the octancy of the neutrino mixing angle θ_{23} up to a $3\,\sigma$ confidence limit (CL) for all values of the phase $\delta_{\rm CP}$. This was done by computing the $\Delta\chi^2$ distribution for a range of θ_{23} and $\delta_{\rm CP}$ values. The $\Delta\chi^2$ distribution was computed with a grid of 120×360 points, interpolating the intermediate values.

The contour plots were produced for four different setups: SPS beam with 20 kt LArTPC, SPS beam with 70 kt LArTPC, HPPS beam with 20 kt LArTPC and HPPS beam with 70 kt LArTPC. Figures 1 and 2 present the resulting $1\,\sigma$, $2\,\sigma$ and $3\,\sigma$ CL contours for the normal and inverted hierarchy, respectively. In each figure the white regions in the plots are the areas for which the values of θ_{23}, $\delta_{\rm CP}$ can be established with CL greater than $3\,\sigma$. So for all θ_{23}, $\delta_{\rm CP}$ data points in these areas, one can eliminate with a CL larger than $3\,\sigma$ the possibility for these parameters to lie in the other octant. Conversely the coloured regions illustrate the cases where no such distinction is possible with the indicated CL. Some details of these contours are presented numerically in table 3.

We have marked in figures 1 and 2 by green lines the MINOS favoured θ_{23} values 40° and 50°. It is seen that for all the different setups considered the right θ_{23} octant can be asserted in NH with at least $3\,\sigma$ CL. As for IH this limit is reached for the lower octant in all cases, whereas for the higher octant it fails to be reached in the sole case of the 20 kt setup with 0.75 MW. All other setup versions yield improved sensitivities so that the $3\,\sigma$ limit can be reached for all of them regardless of the mass hierarchy and $\delta_{\rm CP}$ value. The graphs also show by themselves that increasing beam power (by a factor of 2.7 i.e. from 0.75 MW to 2 MW) with the same detector is a lot more effective than increasing detector size from 20kt to 70 kt with the same beam power.

We also studied the scenario in which the neutrino and antineutrino beam modes are divided by a 75%/25% ratio, which has been suggested to optimize the LBNO for the CP violation search [19]. Our results show decreased sensitivity for determining the θ_{23} octant. Furthermore we also found that a 25%/75% share between neutrinos and antineutrinos improves the sensitivity to θ_{23} octant determination relative to the 50%/50% share. Hence the shorter running times with neutrinos combined with the longer running times with antineutrinos is found to improve the octant sensitivity, whereas the opposite combination worsens it.

In principle, any increase in the exposure moves the $3\,\sigma$ CL contour closer to the $\theta_{23} = 45^\circ$ value. If one is to expect that the real value of θ_{23} is to be 5° off from 45°, then

JHEP02(2015)048

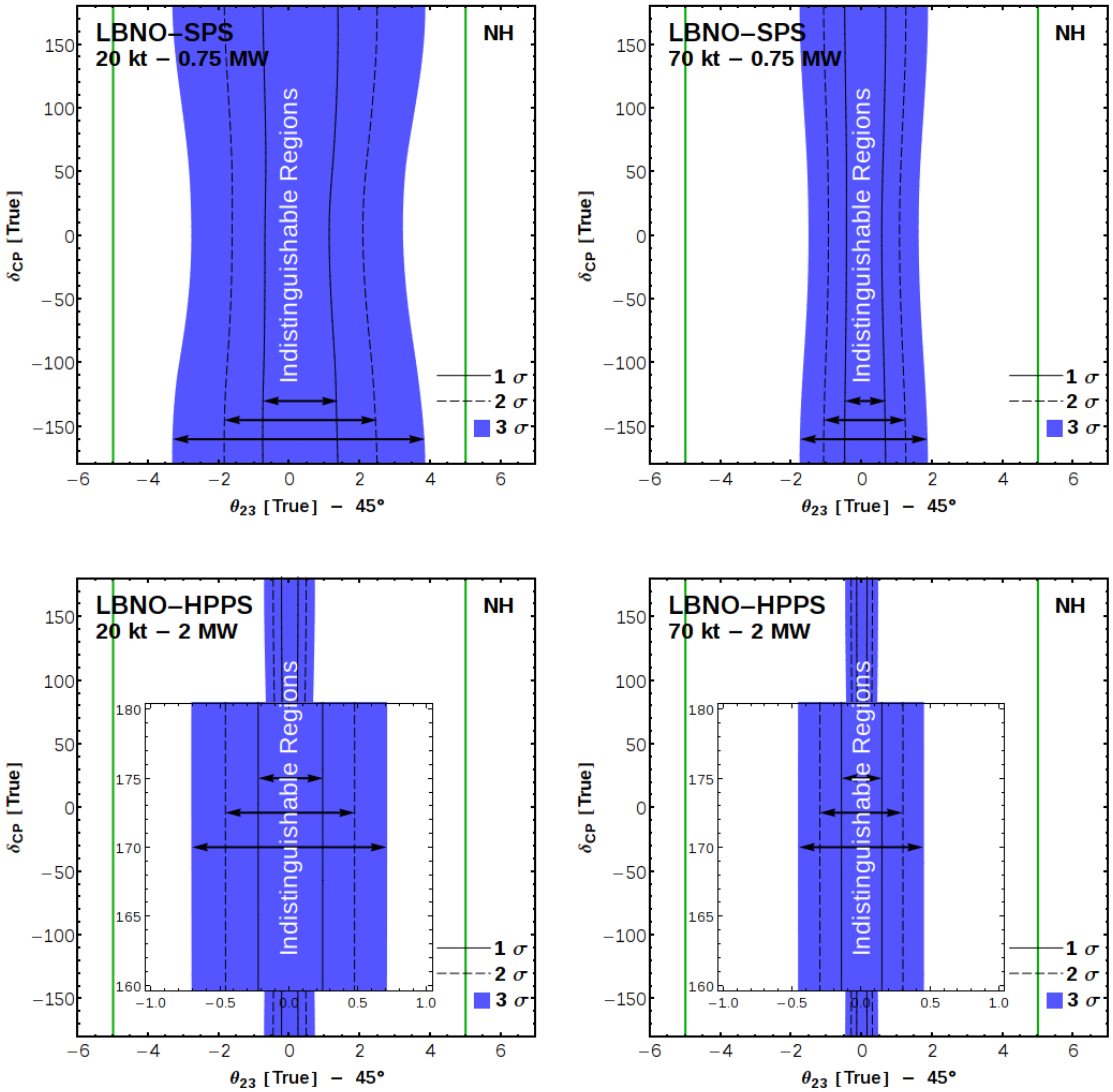

Figure 1. Octant discovery potential in the LBNO when normal mass hierarchy (NH) is assumed. The coloured regions show values of θ_{23} and $\delta_{\rm CP}$ where the two octant solutions can be distinguished from each other in the LBNO at less than $3\,\sigma$ confidence level (i.e. the two octants are indistinguishable up to this limit). The white areas show the values where the other octant can be rejected at $3\,\sigma$ or better. The $1\,\sigma$ and $2\,\sigma$ contours are shown with solid and dashed lines, respectively. The MINOS favoured $\theta_{23} - 45^\circ = \pm 5^\circ$ values are marked with green lines.

even the SPS setup with 20 kt detector may be sufficient to reach the $3\,\sigma$ CL for both mass hierarchies. The sensitivity is worse near 45°, however, and it would require an upgrade to reach the $3\,\sigma$ CL benchmark. A future HPPS facility with a 70 kt LArTPC detector, for instance, could solve this problem as it would set the limit to less than $\pm 0.6^\circ$. Furthermore, LBNO will most likely be able to measure the mass hierarchy with a 0.75 MW SPS beam and a 20 kt LArTPC detector, in which case the acquired data could be used to narrow down the estimate on the θ_{23} octant. The determination of the θ_{23} octancy would hence be a logical follow-up of the mass hierarchy measurement.

JHEP02(2015)048

Indistinguishable Regions	20 kt Detector								70 kt Detector							
	SPS (0.75 MW)				HPPS (2 MW)				SPS (0.75 MW)				HPPS (2 MW)			
	NH		IH		NH		IH		NH		IH		NH		IH	
	θ_{23} [True] $- 45°$		θ_{23} [True] $- 45°$		θ_{23} [True] $- 45°$		θ_{23} [True] $- 45°$		θ_{23} [True] $- 45°$		θ_{23} [True] $- 45°$		θ_{23} [True] $- 45°$		θ_{23} [True] $- 45°$	
	$(-)$	$(+)$	$(-)$	$(+)$	$(-)$	$(+)$	$(-)$	$(+)$	$(-)$	$(+)$	$(-)$	$(+)$	$(-)$	$(+)$	$(-)$	$(+)$
$1\,\sigma$	0.75°	1.38°	0.94°	2.11°	0.22°	0.25°	0.28°	0.34°	0.48°	0.68°	0.63°	0.99°	0.14°	0.15°	0.17°	0.19°
$2\,\sigma$	1.85°	2.49°	2.50°	3.80°	0.46°	0.48°	0.60°	0.64°	1.08°	1.25°	1.47°	1.81°	0.30°	0.30°	0.36°	0.37°
$3\,\sigma$	3.31°	3.85°	5.10°	6.07°	0.70°	0.71°	0.93°	0.95°	1.75°	1.87°	2.51°	2.72°	0.45°	0.45°	0.55°	0.56°
Maximum at $\delta_{\rm CP}$ [True]	180°		0°		180°		0°		180°		0°		180°		0°	

Table 3. Octant discovery potential in LBNO. The highest and lowest $45° - \theta_{23}$ values at which the $1\,\sigma$, $2\,\sigma$ and $3\,\sigma$ confidence levels can be reached are shown in the case of normal hierarchy (NH) and inverted hierarchy (IH).

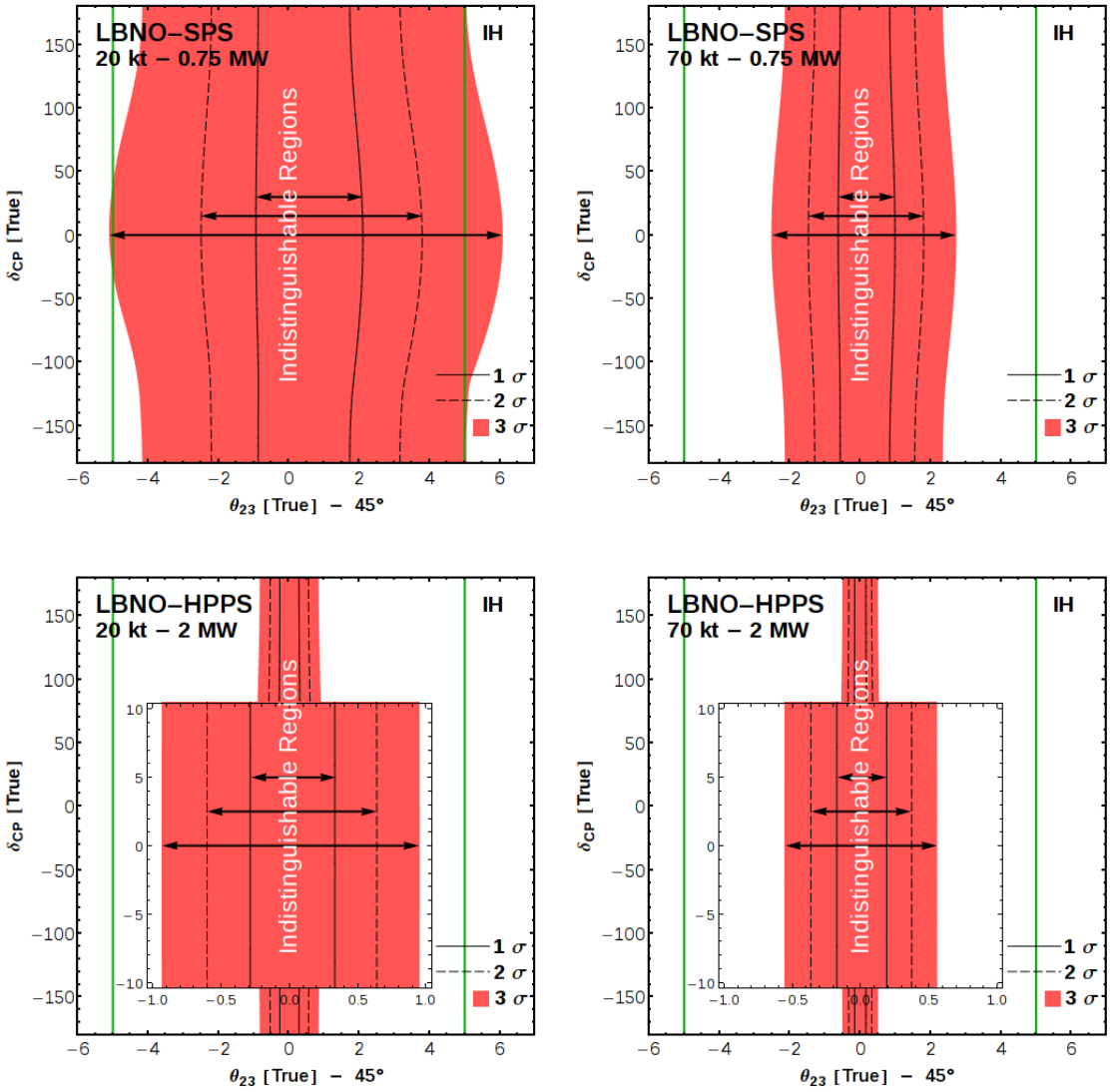

Figure 2. Octant discovery potential in the LBNO when inverted mass hierarchy (IH) is assumed. The coloured regions show values of θ_{23} and $\delta_{\rm CP}$ where the two octant solutions can be distinguished from each other in the LBNO at less than $3\,\sigma$ confidence level (i.e. the two octants are indistinguishable up to this limit). The white areas show the values where the other octant can be rejected at $3\,\sigma$ or better. The $1\,\sigma$ and $2\,\sigma$ contours are shown with solid and dashed lines, respectively. The MINOS favoured $\theta_{23} - 45^\circ = \pm 5^\circ$ values are marked with green lines.

Acknowledgments

SV would like to thank Kai Loo and Peter Ballet for useful conversations that led to improvements in the GLoBES simulations. CRD sincerely thanks Physical Research Laboratory and Prof. Utpal Sarkar (Dean) for Visiting Scientist position, also greatly thanks the Department of Physics, University of Jyväskylä, where the work was initiated, for hospitality and financial support. JP acknowledges financial support from FCT neutrino project PTDC/FIS-NUC/0548/2012 and expresses his thanks to the Department of Physics, University of Jyväskylä, for hospitality and partial financial support.

JHEP02(2015)048

References

[1] D.V. Forero, M. Tortola and J.W.F. Valle, *Global status of neutrino oscillation parameters after Neutrino-2012*, *Phys. Rev.* **D 86** (2012) 073012 [arXiv:1205.4018] [INSPIRE].

[2] G.L. Fogli et al., *Global analysis of neutrino masses, mixings and phases: entering the era of leptonic CP-violation searches*, *Phys. Rev.* **D 86** (2012) 013012 [arXiv:1205.5254] [INSPIRE].

[3] M.C. Gonzalez-Garcia, M. Maltoni, J. Salvado and T. Schwetz, *Global fit to three neutrino mixing: critical look at present precision*, *JHEP* **12** (2012) 123 [arXiv:1209.3023] [INSPIRE].

[4] G.L. Fogli and E. Lisi, *Tests of three flavor mixing in long baseline neutrino oscillation experiments*, *Phys. Rev.* **D 54** (1996) 3667 [hep-ph/9604415] [INSPIRE].

[5] A. Chatterjee, P. Ghoshal, S. Goswami and S.K. Raut, *Octant sensitivity for large θ_{13} in atmospheric and long baseline neutrino experiments*, *JHEP* **06** (2013) 010 [arXiv:1302.1370] [INSPIRE].

[6] S.K. Raut, *Effect of non-zero θ_{13} on the measurement of θ_{23}*, *Mod. Phys. Lett.* **A 28** (2013) 1350093 [arXiv:1209.5658] [INSPIRE].

[7] M. Ghosh, P. Ghoshal, S. Goswami and S.K. Raut, *Synergies between neutrino oscillation experiments: an 'adequate' configuration for LBNO*, *JHEP* **03** (2014) 094 [arXiv:1308.5979] [INSPIRE].

[8] K. Bora, D. Dutta and P. Ghoshal, *Determining the octant of θ_{23} at LBNE in conjunction with reactor experiments*, arXiv:1405.7482 [INSPIRE].

[9] MINOS collaboration, P. Adamson et al., *Combined analysis of ν_μ disappearance and $\nu_\mu \to \nu_e$ appearance in MINOS using accelerator and atmospheric neutrinos*, *Phys. Rev. Lett.* **112** (2014) 191801 [arXiv:1403.0867] [INSPIRE].

[10] T2K collaboration, K. Abe et al., *Precise measurement of the neutrino mixing parameter θ_{23} from muon neutrino disappearance in an off-axis beam*, *Phys. Rev. Lett.* **112** (2014) 181801 [arXiv:1403.1532] [INSPIRE].

[11] S.K. Agarwalla, *Physics potential of long-baseline experiments*, *Adv. High Energy Phys.* **2014** (2014) 457803 [arXiv:1401.4705] [INSPIRE].

[12] A. Stahl et al., *Expression of interest for a very Long Baseline Neutrino Oscillation experiment (LBNO)*, CERN-SPSC-2012-021 (2012).

[13] A. Rubbia, *Experiments for CP-violation: a giant liquid argon scintillation, Cerenkov and charge imaging experiment?*, hep-ph/0402110 [INSPIRE].

[14] A. Rubbia, *Underground Neutrino Detectors for Particle and Astroparticle Science: The Giant Liquid Argon Charge Imaging ExpeRiment (GLACIER)*, *J. Phys. Conf. Ser.* **171** (2009) 012020 [arXiv:0908.1286] [INSPIRE].

[15] ISS Detector Working Group collaboration, T. Abe et al., *Detectors and flux instrumentation for future neutrino facilities*, 2009 *JINST* **4** T05001 [arXiv:0712.4129] [INSPIRE].

JHEP02(2015)048

[16] A. Cervera, A. Laing, J. Martin-Albo and F.J.P. Soler, *Performance of the MIND detector at a neutrino factory using realistic muon reconstruction*, *Nucl. Instrum. Meth.* **A 624** (2010) 601 [arXiv:1004.0358] [INSPIRE].

[17] Y. Papaphilippou et al., *Design options of a high-power proton synchrotron for LAGUNA-LBNO*, in the proceedings of the 4th *International Particle Accelerator Conference (IPAC2013)*, May 12–17, Shanghai, China (2013).

[18] S. Choubey and A. Ghosh, *Determining the octant of θ_{23} with PINGU, T2K, NOνA and reactor data*, *JHEP* **11** (2013) 166 [arXiv:1309.5760] [INSPIRE].

[19] LAGUNA-LBNO collaboration, S.K. Agarwalla et al., *The mass-hierarchy and CP-violation discovery reach of the LBNO long-baseline neutrino experiment*, *JHEP* **05** (2014) 094 [arXiv:1312.6520] [INSPIRE].

[20] P. Huber, M. Lindner and W. Winter, *Simulation of long-baseline neutrino oscillation experiments with GLoBES (General Long Baseline Experiment Simulator)*, *Comput. Phys. Commun.* **167** (2005) 195 [hep-ph/0407333] [INSPIRE].

[21] P. Huber, J. Kopp, M. Lindner, M. Rolinec and W. Winter, *New features in the simulation of neutrino oscillation experiments with GLoBES 3.0: General Long Baseline Experiment Simulator*, *Comput. Phys. Commun.* **177** (2007) 432 [hep-ph/0701187] [INSPIRE].

[22] K. Loo, private communications, University of Jyväskylä, Finland.

[23] S.K. Agarwalla, T. Li and A. Rubbia, *An incremental approach to unravel the neutrino mass hierarchy and CP-violation with a long-baseline Superbeam for large θ_{13}*, *JHEP* **05** (2012) 154 [arXiv:1109.6526] [INSPIRE].

[24] P. Coloma, T. Li and S. Pascoli, *A comparative study of long-baseline superbeams within LAGUNA for large θ_{13}*, arXiv:1206.4038 [INSPIRE].

[25] P. Ballet, private communications, Durham University, U.K.

[26] Particle Data Group collaboration, K.A. Olive et al., *Review of particle physics*, *Chin. Phys.* **C 38** (2014) 090001, http://pdg.lbl.gov [INSPIRE].

[27] E. Kozlovskaya, J. Peltoniemi and J. Sarkamo, *The density distribution in the Earth along the CERN-Pyhasalmi baseline and its effect on neutrino oscillations*, hep-ph/0305042 [INSPIRE].

[28] A. Dziewonski and D. Anderson, *Preliminary reference earth model*, *Phys. Earth Planet. Interiors* **25** (1981) 297.

[29] M.C. Gonzalez-Garcia, M. Maltoni and T. Schwetz, *Updated fit to three neutrino mixing: status of leptonic CP-violation*, *JHEP* **11** (2014) 052 [arXiv:1409.5439] [INSPIRE].

JHEP02(2015)048

Publication II

II

C.R. Das, J. Maalampi, J. Pulido and S. Vihonen,
On the determination of the θ_{23} octant in long baseline neutrino experiments,
Submitted to International Journal of Modern Physics A,
arXiv:1606.02504 [hep-ph]

On the determination of the θ_{23} octant in long baseline neutrino experiments

C.R. Das [†a], Jukka Maalampi [‡b], João Pulido [*c], and Sampsa Vihonen [‡d]

[†] *Bogoliubov Laboratory of Theoretical Physics,*

Joint Institute of Nuclear Research, Joliot-Curie 6,

141980 Dubna, Moscow region, Russia

[‡] *University of Jyvaskyla, Department of Physics,*

P.O. Box 35, FI-40014 University of Jyvaskyla, Finland, and

[*] *Centro de Física Teórica das Partículas (CFTP),*

Instituto Superior Técnico, Av. Rovisco Pais, P-1049-001 Lisboa, Portugal

(Dated: October 31, 2018)

Abstract

We study the possibility of determining the octant of the neutrino mixing angle θ_{23}, that is, whether $\theta_{23} > 45°$ or $\theta_{23} < 45°$, in long baseline neutrino experiments. Here we numerically derived the sensitivity limits within which these experiments can determine, by measuring the probability of the $\nu_\mu \to \nu_e$ transitions, the octant of θ_{23} with a 5σ certainty. The interference of the CP violation angle δ with these limits, as well as the effects of the baseline length and the run-time ratio of neutrino and antineutrino modes of the beam have been analyzed.

PACS numbers: 14.60.Pq

Keywords: Neutrino oscillations, neutrino mixing, long baseline

[a] e-mail: das@theor.jinr.ru

[b] e-mail: jukka.maalampi@jyu.fi

[c] e-mail: pulido@cftp.ist.utl.pt

[d] e-mail: sampsa.p.vihonen@student.jyu.fi

I. INTRODUCTION

The past few decades have witnessed amazing progress in neutrino physics. The existence of neutrino masses was firmly established by the observation of the oscillation of atmospheric neutrinos by the Super-Kamiokande experiment [1, 2], the flux measurements of the solar neutrinos by the SNO experiment [3] and the earlier solar neutrino experiments [4]. A great variety of the atmospheric, solar, accelerator and reactor neutrino experiments have determined the parameters related to neutrino masses and the mixing of neutrino flavours to a high precision (see e.g. Refs. [5–9]). A global fit to the data gives the parameter values presented in Table I. Nevertheless, some crucial information is still lacking. In fact, not only the question of the absolute value of the neutrino masses is an open one, but also their hierarchy is still unknown. To this end two possibilities are open: the normal hierarchy (NH), whereby there exist two light neutrinos and a heavier one and the inverse hierarchy (IH) with two comparatively heavy and a lighter one. Furthermore, the issue of the possible CP violation in the leptonic sector has not been resolved yet.

In this paper we will address another still open question, the so-called octant problem of the neutrino mixing angle θ_{23} [10]. It is known from experiments that the value of θ_{23} is close to 45° but it is not known whether it lies in the higher octant (HO, $\theta_{23} > 45^\circ$) or in the lower one (LO, $\theta_{23} < 45^\circ$), as the present experiments are not sensitive enough to trace the difference on a reliable level. In our previous work [11] we studied the prospects of the long baseline neutrino oscillation experiments (see e.g. [12–16]) to resolve this ambiguity. The question has been investigated in several other publications recently, e.g. in [17–30]. Running θ_{23} around 45^o, we investigated in our study [11] the parameter range outside which the first and second octant solutions can be distinguished as a function of a given confidence limit. Of course, the sensitivity and hence the corresponding maximal vicinity of 45° depends on the neutrino mass hierarchy and on the specifications of the experiment at hand. These include the intensity of the neutrino beam, the systematic error estimate and the share of the total run time between the neutrino and antineutrino modes.

The most precise determination of the mixing angle θ_{23} is the one by the T2K experiment [9]. When combining their results with the existing reactor neutrino data they obtain $\sin^2\theta_{23} = 0.528^{+0.055}_{-0.038}$ [31]. The recent results of the MINOS oscillation experiment [32] show two degenerate solutions, one in the lower octant (LO) with $\sin^2\theta_{23} \simeq 0.43$ and one

in the higher octant (HO) with $\sin^2\theta_{23} \simeq 0.60$. This corresponds to a deviation of about 5° downwards or upwards, correspondingly, from the maximal value $\theta_{23} = 45^\circ$. The Super Kamiokande has found in its atmospheric neutrino study the best-fit at $\sin^2\theta_{23} \simeq 0.575$ for both mass hierarchies with a preference for the higher octant [33]. The preliminary results of the NOνA experiment, based on still quite limited exposure, show a best-fit close to the maximal mixing ($\sin^2\theta_{23} = 0.51 \pm 0.10$ [34]).

Using the numerical simulations based on the GLoBES software [35, 36], we analyze in this paper the dependence of the θ_{23} octant sensitivity on the baseline length, the neutrino-antineutrino beam share and the systematic errors. We find for normal mass hierarchy a sensitivity that improves with the neutrino component in the beam, maximal sensitivity being reached when this component reaches 100%. For the inverse mass hierarchy, we find the opposite result, namely a maximal sensitivity for 100% of the antineutrino component. Furthermore, the sensitivity to the systematic errors is flat for all neutrino and antineutrino channels, with the exception of the muon neutrino one in NH and the muon antineutrino in IH which both become poorer as the error increases. The analysis is done for $\delta_{\rm CP} \in [-\pi, \pi]$.

The plan of the paper is as follows. In Section II we will describe the octant problem and review the present situation of the determination of the value of θ_{23}. In Section III we describe the numerical method we use in our analysis, and in Section IV we present our results. A summary and conclusions are presented in Section V.

II. THE OCTANT DEGENERACY

The oscillations of three neutrinos can be described in terms of six parameters, the three mixing angles θ_{12}, θ_{23} and θ_{13}, the CP phase δ and two mass-squared differences Δm^2_{21} and Δm^2_{31}. Also, the probabilities of the $\nu_\ell \leftrightarrow \nu_{\ell'}$ transitions, $P^m_{\ell\ell'}$ $(\ell, \ell' = e, \mu, \tau)$ depend on these parameters, the neutrino energy E and the baseline L, as well as on the density profile of the medium neutrinos traverse on their way from a source to a detector. The values of the oscillation parameters can be determined by comparing the measured event rates with their theoretical expectations which follow from the probability expressions and the specifications of the experiment at hand. However, the determination is hampered by parameter degeneracies, i.e. by situations where two or more choices of the parameter value sets are consistent with the same probability and thus the same data. As was discussed

in [17, 37, 38] there can be eightfold degeneracies in the oscillation probabilities caused by the θ_{13} – δ degeneracy, the mass hierarchy – δ degeneracy, and the octant degeneracy. The precise determinations of the mixing angle θ_{13} [39, 40] have made the θ_{13} – δ degeneracy less serious than it was before. Indeed the mass hierarchy – δ degeneracy will be resolved once the value of one or both of these quantities is accurately determined in the future long baseline oscillation or in other neutrino experiments. On the other hand, the octant degeneracy refers to situations where the parameter interchange $\theta_{23} \leftrightarrow \pi/2 - \theta_{23}$ leads to the same calculated value of an experimentally measured quantity. The possibility of removing such an ambiguity in very long baseline neutrino experiments has been first discussed some time ago, see e.g. [17, 41, 42]. For more recent discussions, see e.g. [18, 19].

In long baseline experiments one is interested mainly in the oscillation channels $\nu_\mu \to \nu_\mu$ (disappearance channel) and $\nu_\mu \to \nu_e$ (appearance channel). In leading order, whereby omitting terms proportional to the small quantity $\Delta m^2_{21}/\Delta m^2_{31}$, the survival probability takes the following form [43–45]:

$$\begin{aligned} P^m_{\mu\mu} =& 1 - \cos^2\theta^m_{13}\sin^2 2\theta_{23}\sin^2\left(1.27\,\frac{L}{E}\left(\frac{\Delta m^2_{31} + A + (\Delta m^2_{31})_m}{2}\right)\right) \\ & - \sin^2\theta^m_{13}\sin^2 2\theta_{23}\sin^2\left(1.27\,\frac{L}{E}\left(\frac{\Delta m^2_{31} + A - (\Delta m^2_{31})_m}{2}\right)\right) \\ & - \sin^4\theta_{23}\sin^2 2\theta^m_{13}\sin^2\left(1.27\,\frac{L}{E}(\Delta m^2_{31})_m\right) \end{aligned} \tag{1}$$

where terms have been shown up to the first θ_{23} octant non-degenerate term. The matter enhanced parameters $(\Delta m^2_{31})_m$, $\cos^2\theta^m_{13}$ and $\sin^2\theta^m_{13}$ are defined by

$$\begin{aligned} (\Delta m^2_{31})_m &= \sqrt{(\Delta m^2_{31}\cos 2\theta_{13} - A)^2 + (\Delta m^2_{31}\sin 2\theta_{13})^2} \\ \sin 2\theta^m_{13} &= \frac{\Delta m^2_{31}}{(\Delta m^2_{31})_m}\sin 2\theta_{13} \\ \cos 2\theta^m_{13} &= \frac{\Delta m^2_{31}}{(\Delta m^2_{31})_m}(\cos 2\theta_{13} - A). \end{aligned} \tag{2}$$

Here A is due to the effects of matter on the neutrinos propagating through Earth's crust, $A \equiv 2EV$, with $V = \sqrt{2}G_F n_e$ and n_e is the electron number density. The corresponding formula for antineutrinos is obtained by replacing $V \to -V$.

The first three terms of the oscillation probability $P_{\mu\mu}$ are insensitive to the θ_{23} octancy, as their dependence comes through $\sin^2 2\theta_{23}$. Therefore, neglecting the last term, one would have

$$P_{\mu\mu}(\theta_{23}) = P_{\mu\mu}(\pi/2 - \theta_{23}). \tag{3}$$

However, owing to the octant sensitivity exhibited by the fourth term in Eq. (1), $P_{\mu\mu}$ may still contribute to the determination of the θ_{23} octant provided a suitable choice of parameters A, L and E is made.

The oscillation probability $P^m_{\mu e}$ of the appearance channel $\nu_\mu \to \nu_e$ is given in the leading order by

$$P^m_{\mu e} = \sin^2\theta_{23}\sin^2 2\theta^m_{13}\sin^2\left(1.27\,\frac{L}{E}(\Delta m^2_{31})_m\right). \tag{4}$$

This probability does not have an intrinsic degeneracy like (3) but it suffers from a combined ambiguity involving the parameters θ_{13}, Δm_{31}, and θ_{23}. Nevertheless, the sensitivity for the θ_{23} octant comes mainly from this oscillation channel.

As can be seen from Eqs. (1) and (4), a comparatively large $\sin^2 2\theta^m_{13}$ term magnifies the θ_{23} octant sensitivity in both $\nu_\mu \to \nu_e$ and $\nu_\mu \to \nu_\mu$ modes. This is provided by a comparatively small $(\Delta m^2_{31})_m$ parameter which requires the quantities Δm^2_{31} and A to have the same sign (see Eq. (2)). Hence, as will be seen in section IV, octant sensitivity becomes maximal for a normal hierarchy with neutrinos and inverse hierarchy with antineutrinos. Since $\nu_\mu \to \nu_e$ and $\nu_\mu \to \nu_\mu$ modes contribute, an analysis using combined data from the two gives a better capability to ascertain the octancy of θ_{23} than one using just a single mode.

III. SIMULATION METHOD

In this work we use the GLoBES software [35, 36] to calculate the sensitivities for the θ_{23} octant determination. As per our previous work [11], the analysis is done by calculating χ^2 values with the same approach. The octant discovery potential is obtained from the $\Delta\chi^2$ distribution defined as:

$$\Delta\chi^2 = \chi^2(\pi/2 - \theta_{23}) - \chi^2(\theta_{23}), \tag{5}$$

where $\chi^2(\theta_{23})$ represents the χ^2 value for any given θ_{23} value and $\chi^2(\pi/2 - \theta_{23})$ its value in the opposite octant. The 5σ confidence level is then obtained as the $\Delta\chi^2 = 25$ contour along this distribution. In each calculation of $\Delta\chi^2$ we keep θ_{23} and δ fixed to their assigned values.

We analyse the octant sensitivity by calculating the $\Delta\chi^2$ distribution for various θ_{23} angles with Eq. (5). We take the other intrinsic oscillation parameter values from the current best-fits as given by recent experimental data. These best-fit values are presented in Table I.

Parameter	Value ± Error (NH)	Value ± Error (IH)
$\sin^2\theta_{12}$	0.321 ± 0.018	
$\sin^2\theta_{13}$	0.02155 ± 0.00090	0.02140 ± 0.00085
$\sin^2\theta_{23}$	varied	
$\delta_{\rm CP}$	varied	
Δm^2_{21}	$(7.56 \pm 0.19) \times 10^{-5}$ eV^2	
Δm^2_{31}	$(2.55 \pm 0.04) \times 10^{-3}$ eV^2	$(-2.49 \pm 0.04) \times 10^{-3}$ eV^2

TABLE I. The best fit values and standard deviations of the neutrino oscillation parameters used in our numerical calculations [47]. For the CP phase $\delta_{\rm CP}$ we allow any value from 0 to 2π.

We conduct the simulations using the experimental setup considered in the LBNO Design Study [12] as our model of reference. This design assumes a 2288 km baseline and a double phase liquid argon time projection chamber (LArTPC) detector concept. Because of its similarity with other proposed long baseline experiments, e.g., the DUNE [46], we consider LBNO as our benchmark with its four beam intensity and detector size setups. In the following work, we parametrize the LBNO as defined in Table II. We consider the SPS and HPPS setups (1.125×10^{20} POT/year and 3.0×10^{21} POT/year, respectively) both with the 20kt and 70kt double phase LArTPC detectors and present the results from these four different exposures. We stress that while the specifications are for the LBNO setup, the results obtained to give a correct generic picture.

IV. RESULTS

A. Octant and baseline

In this subsection, we investigate the impact of matter effects on the octant sensitivity of θ_{23} at 5σ confidence level in long baseline experiments. We use the GLoBES software with LBNO as our benchmark setup and analyse the effect of changing the baseline length. All other experiment parameters are fixed to their default values.

We compute the octant sensitivity for four different exposures. The results are presented for higher octant in both NH and IH in Fig. 1. As a measure of exposure, we use the

Runtime ($\nu + \overline{\nu}$ years)	5+5
LAr detector mass (kt)	20 & 70
Neutrino beam power (MW)	0.75 & 2.4
POT per year	1.125×10^{20} & 3.0×10^{21}
Baseline length (km)	2288
Energy resolution function	$0.15\sqrt{E}$
Energy window (GeV)	0 — 10
Bin width (GeV)	0.125
Bins	80

TABLE II. The benchmark values of various experimental parameters used in the numerical calculations. In the energy resolution function, E is in units of GeV.

integrated luminosity, which is defined as the product of the beam's annual protons-on-target (POT) number, the fiducial mass of the detector and the total running time of the experiment.

We also investigate the θ_{23} octant – δ correlation by plotting the 5σ contours for δ values in the interval $[-\pi, \pi]$. This generates the appearance of bands, which are plotted in Fig. 1 for the NH and IH cases. In our calculation, for each baseline L the factor $\sin^2[1.27\, L/E\, (\Delta m^2_{31})_m]$ is maximized in order to maximize the sensitivity of both probabilities (1) and (4) to the θ_{23} octancy. Therefore, neutrino beam energy is shifted along bin by bin in direct proportionality with L, so that L/E is kept constant throughout the simulation. Longer baselines thus correspond to greater matter effects. For illustration, we also show the $\delta_{\rm CP} = 0$ and $\delta_{\rm CP} = \pi/2$ contours in the plots.

Two important features are clearly seen from Fig. 1: the θ_{23} octant – $\delta_{\rm CP}$ correlation becomes less significant and the octant sensitivity becomes less dependent on the baseline length as the statistics is increased from 2.3×10^{22} POT×kton to 210×10^{22} POT×kton. Moreover, the CP-conserving contour $\delta_{\rm CP} = 0$ appears to yield in general a better sensitivity than the maximally CP violating contour $\delta_{\rm CP} = \pi/2$ in NH, but this behaviour is flipped in the case of IH.

Finally, from Fig. 1, the sensitivity contours seem to have a shallow minimum, corresponding to maximum sensitivity, which ranges from 1700km to more than 3000km.

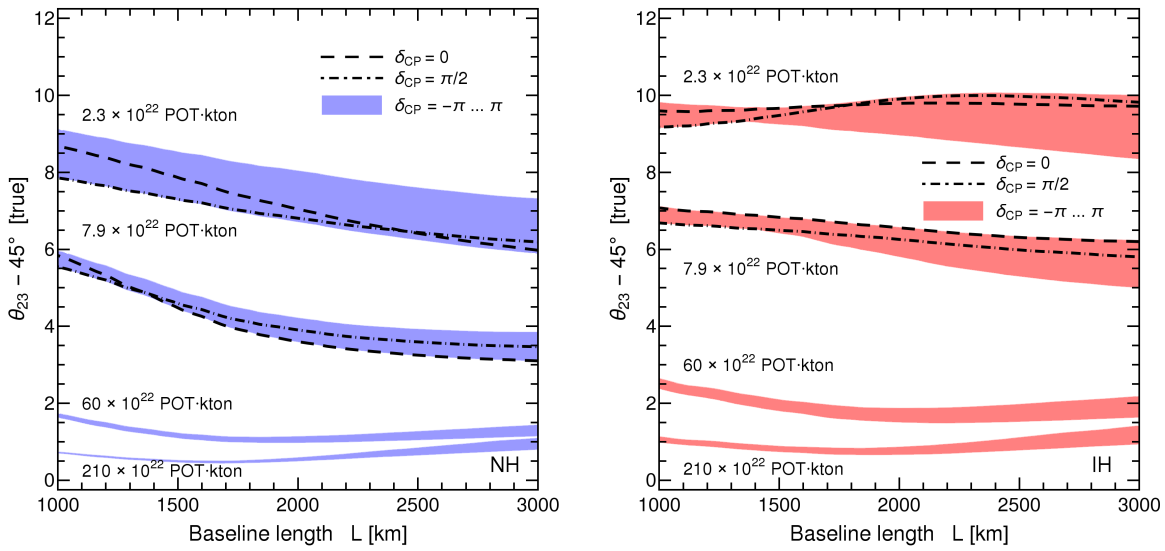

FIG. 1. The 5σ discovery reach of θ_{23} octant as a function of baseline length for different luminosities. Above the curves, the octant of θ_{23} will be determined with more than 5σ certainty. The band shows the variation of the bound when $\delta_{\rm CP}$ varies in the range $(-\pi, \pi)$ and corresponds to the correlation between $\delta_{\rm CP}$ and the θ_{23} octant. The left panel is for the normal mass hierarchy (NH) and the right panel for the inverted hierarchy (IH).

We also studied the sensitivities in the case where θ_{23} lies in the lower octant. However, we found the sensitivities to be approximately symmetric in the lower octant, hence they are not shown.

B. Octant and beam sharing

In this subsection, we study the effect of sharing between neutrino and antineutrino run modes in the experiment's ability to determine the θ_{23} octant.

We plot the octant sensitivity as a function of the running time in the neutrino mode in both NH and IH. The sensitivities are shown for higher octant at 5σ CL in Fig. 2 and the sensitivities concerning the lower octant have not shown because they are approximately symmetric in shape.

The $\nu_\mu/(\nu_\mu + \bar{\nu}_\mu)$ ratio in Fig. 2 is defined as the fraction at which the experiment runs in neutrino mode. The sum of the two running times is fixed at 10 years. For example,

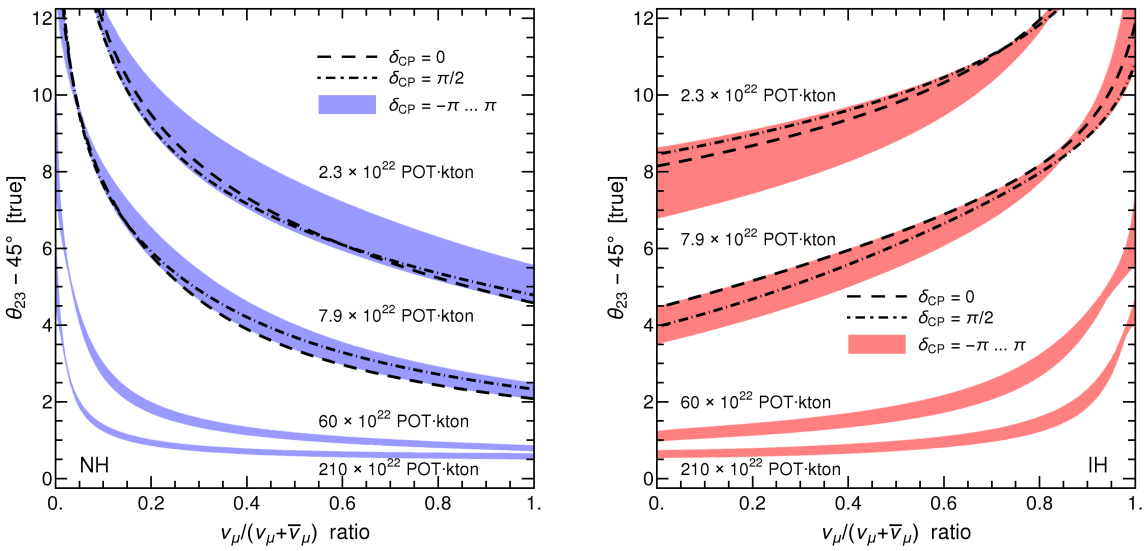

FIG. 2. The 5σ discovery reach of θ_{23} octant as a function of the beam sharing ratio. Above the curves, the octant of θ_{23} will be determined with more than 5σ certainty. The band shows the variation of the bound when $\delta_{\rm CP}$ varies in the range $(-\pi, \pi)$ and corresponds to the correlation between $\delta_{\rm CP}$ and the θ_{23} octant. The left panel is for the normal mass hierarchy (NH) and the right panel for the inverted hierarchy (IH).

the experiment operates all 10 years in antineutrino mode when $\nu_\mu/(\nu_\mu + \bar{\nu}_\mu) = 0$ and in neutrino mode when $\nu_\mu/(\nu_\mu + \bar{\nu}_\mu) = 1$. Conversely, the fraction of the antineutrino mode is given by $1 - \nu_\mu/(\nu_\mu + \bar{\nu}_\mu)$.

The immediate result of Fig. 2 is that the sensitivity to the θ_{23} octant improves monotonously in the case of NH and declines in the case of IH as the running time in neutrino mode is increased. Thus the best octant sensitivity is achieved in the NH case by maximizing the ν_μ runtime and in the IH case by maximizing the $\bar{\nu_\mu}$ runtime.

The impact of the $\delta_{\rm CP}$ parameter also seems to be inverted when one moves from NH to IH. This can be seen from the $\delta_{\rm CP} = 0, \pi/2$ contours in Fig. 2.

C. Octant and systematic errors

In this subsection, we investigate the impact of systematic errors on the experiment's ability to determine the θ_{23} octant. We parametrize the systematic errors related to the

neutrino detection and event reconstruction phase with a single normalization error in each channel (cf. [11] for a more detailed description). The strength of the systematic errors is parametrized for each channel by two weight factors, π_1 and π_2, the first referring to the signal and the second to the background component.

In this work, we concentrate on the signal error parameter π_1. We test the impact of each neutrino detection channel by varying the corresponding signal error π_1 in the interval $[0, 10\%]$ in one neutrino channel and keep the others fixed at their default values. We repeat the calculation for all four neutrino types (ν_e, ν_μ, $\bar{\nu}_e$, $\bar{\nu}_\mu$) and present the resulting octant sensitivities in Fig. 3 and 4. In these figures, the sensitivities are shown for higher octant for all four exposures, as well as for both mass hierarchies. The sensitivities concerning the lower octant are again found to be approximately symmetric in shape and are not shown.

Fig. 3 shows that the sensitivities obtained with GLoBES are flat for almost all exposures and neutrino types in NH, the only non-flat curves being ν_μ, which shows a clear slope for the lowest exposure, and ν_e, which has slopes in the higher exposures, exhibiting an unexpected negative slope. However for an inverse hierarchy (see Fig. 4) the pattern of sensitivities is the same as for a normal hierarchy with the interchange of neutrinos and antineutrinos: significant slopes in the sensitivities appear for $\bar{\nu}_e$ and (the highest exposures) and $\bar{\nu}_\mu$ (the lowest exposures), the remaining curves being flat. The ν_μ and $\bar{\nu}_\mu$ panels show a similar pattern here as in the beam sharing case expound in Subsection IV B: for improving systematics, the detector sensitivity to the θ_{23} octant appears to be enhanced for neutrino events in NH (Fig. 3, upper right panel) and for antineutrino events in IH (Fig. 4, lower right panel). In other words, we find that if the mass hierarchy turns out to be normal, the improvement of the systematics can only lead to an improvement in the sensitivity to θ_{23} determination in the case of the ν_μ events in the detector. Conversely, for IH, it is an improved systematics in $\bar{\nu}_\mu$ event reconstruction that appears to lead to a better sensitivity to θ_{23} octancy. For ν_e events in NH (Fig. 3, upper left panel) and $\bar{\nu}_e$ events in IH (Fig. 4, lower left panel), not only no such an enhanced sensitivity effect appears, but improving the systematics may be counterproductive.

The possible explanation of the downturn observed in ν_e and $\bar{\nu}_e$ is the relatively high precision of the currently known value of $\sin^2\theta_{13}$ (see Table I) which may be unfavourable for the determination of the octant of θ_{23}, in comparison with less accurate values of $\sin^2\theta_{13}$, in the simulation code we utilize. This effect is smeared not only for larger systematic errors,

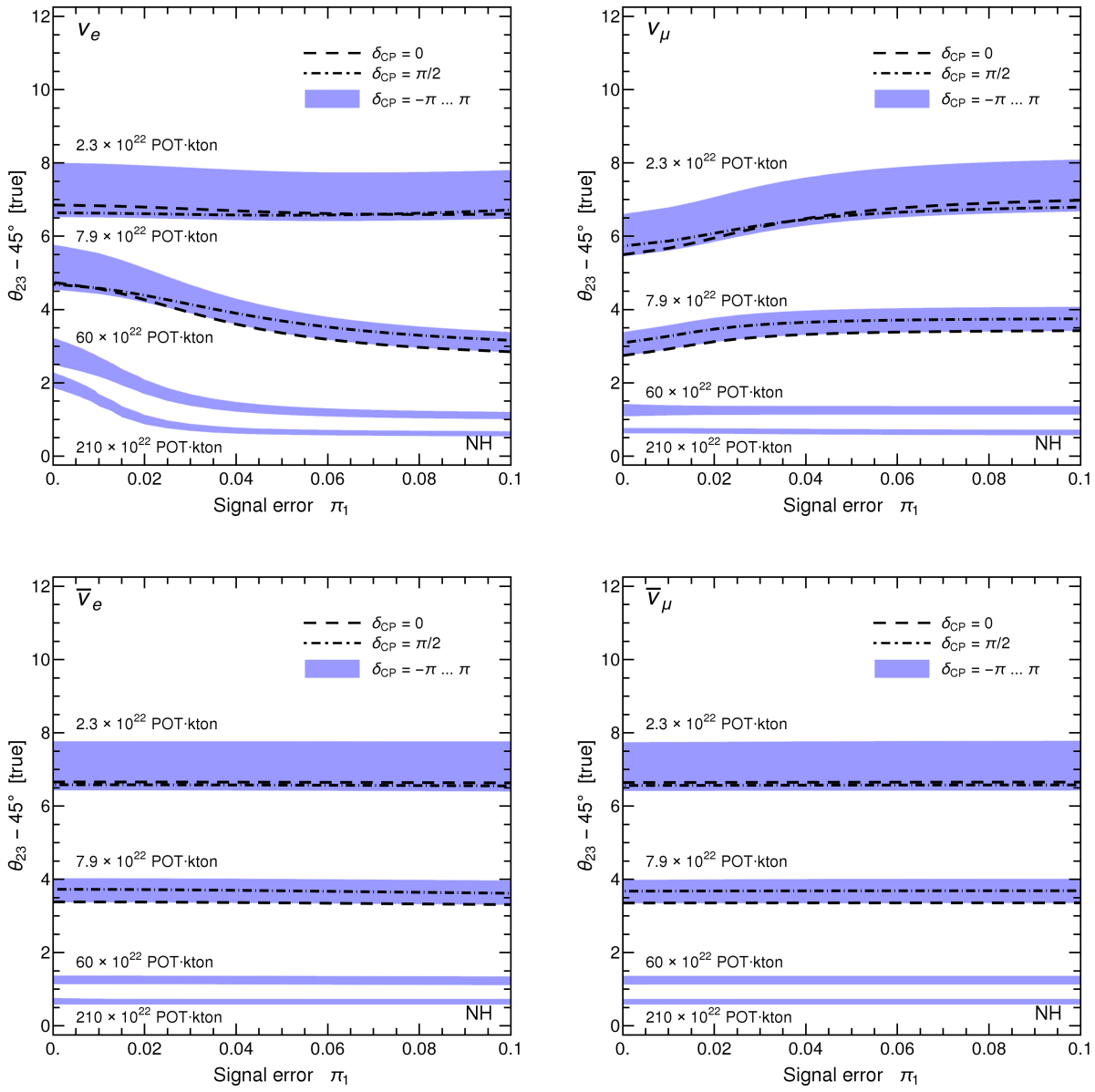

FIG. 3. The 5σ discovery reach of θ_{23} octant as a function of the signal weight parameter π_1 for different luminosities and detection modes $(\nu_e, \nu_\mu, \bar{\nu}_e, \bar{\nu}_\mu)$ in the case of normal hierarchy (NH). Above the curves the octant of θ_{23} will be determined with more than 5σ certainty. The band shows the variation of the bound when $\delta_{\rm CP}$ varies in the range $(-\pi, \pi)$ and corresponds to the correlation between $\delta_{\rm CP}$ and the θ_{23} octant.

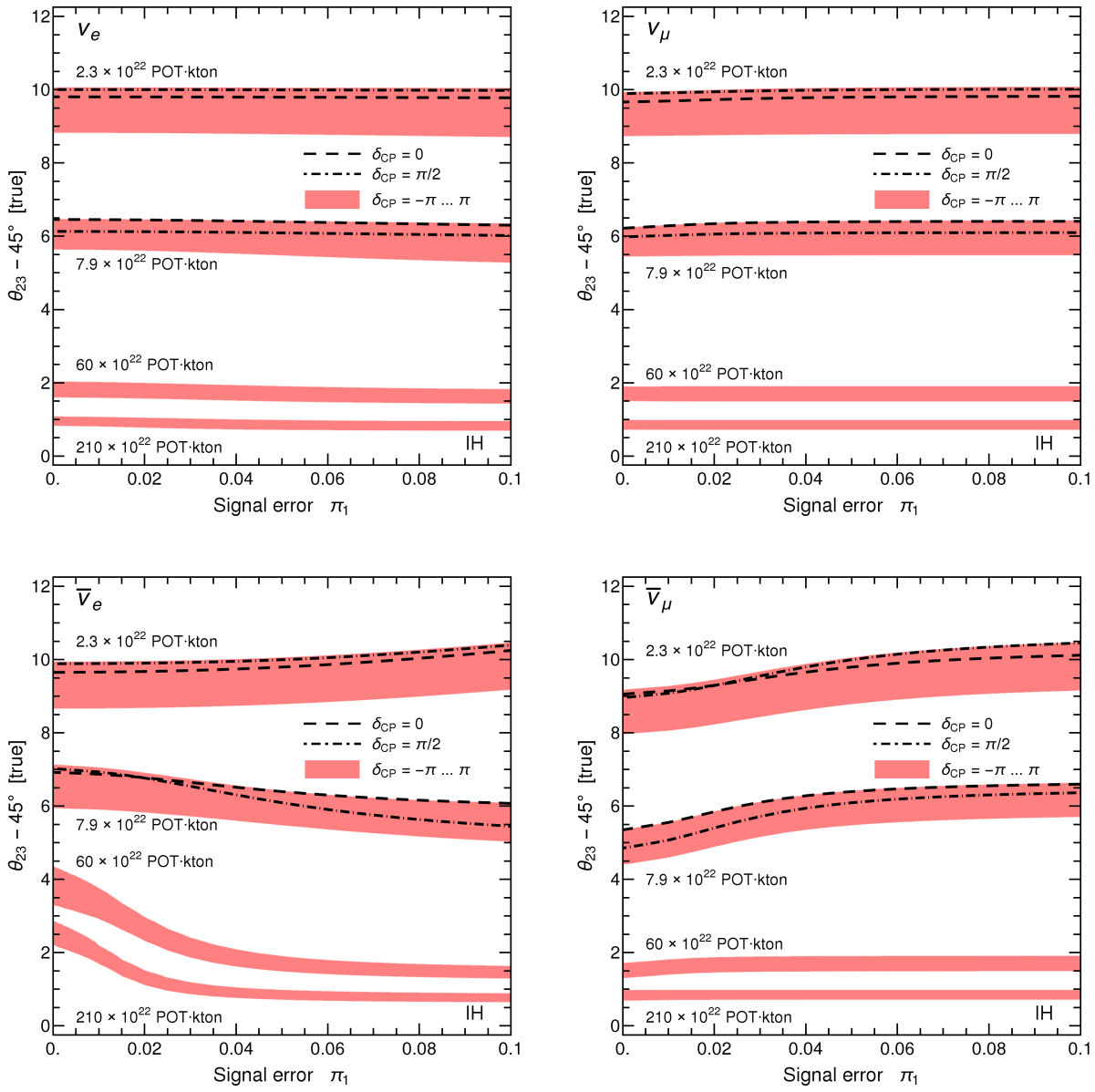

FIG. 4. The 5σ discovery reach of θ_{23} octant as a function of the signal weight parameter π_1 for different luminosities and detection modes $(\nu_e, \nu_\mu, \bar{\nu}_e, \bar{\nu}_\mu)$ in the case of inverted hierarchy (IH). Above the curves the octant of θ_{23} will be determined with more than 5σ certainty. The band shows the variation of the bound when $\delta_{\rm CP}$ varies in the range $(0, 2\pi)$ and corresponds to the correlation between $\delta_{\rm CP}$ and the θ_{23} octant.

as can be seen in Figs. 3 and 4, but also for larger $\sin^2\theta_{13}$ error.

V. SUMMARY

We have analysed the prospects for the θ_{23} octant determination in long baseline neutrino oscillation experiments at the 5σ confidence level. Using the GLoBES [35, 36] software and the methods of our previous work [11], we simulated the performance of these experiments with the LBNO design one as our benchmark setup.

We investigated the octant sensitivity from three different points of view: the baseline length, the beam sharing between neutrino and antineutrino run modes, and the systematic errors concerning the event reconstruction. We found that the sensitivity to the θ_{23} octant improves in the normal hierarchy as the ν_μ time share of the beam is increased. On the contrary, in the case of an inverted hierarchy, the increase in the $\bar{\nu}_\mu$ share leads to an improvement in the sensitivity. We also found that an enhancement in the sensitivity is obtained in the normal hierarchy for ν_μ events or in the inverted hierarchy for $\bar{\nu}_\mu$ events upon improvement in the systematic errors. On the other hand, for ν_e events in the normal hierarchy or $\bar{\nu}_e$ events in the inverted hierarchy, not only such behaviour is absent, but the sensitivity to the θ_{23} octant appears to be deteriorated if systematic errors are improved, especially for higher exposures. We discovered that this unexpected negative effect is connected to the precision of $\sin^2\theta_{13}$. Our main conclusion is therefore that a ν_μ beam in the normal hierarchy or a $\bar{\nu}_\mu$ in an inverted hierarchy provide the best prospects for θ_{23} octant determination.

We also found that the correlation between the $\delta_{\rm CP}$ and octant sensitivity decreases as the number of events is increased: this is readily seen in all figures 1–4, as the bands become thinner for higher exposures. Therefore, not only we get better sensitivity but also its uncertainty connected to the $\delta_{\rm CP}$ uncertainty decreases. This means less ambiguity in sensitivity determination.

The preference for the asymmetric run-time, which depends on the mass hierarchy, has been observed indirectly in [19] for the case of θ_{23} octant determination. The origin of this behaviour can be traced to the leading terms of $P^m_{\mu e}$ and, to a lesser extent, to the subleading term of $P^m_{\mu\mu}$. These are octant sensitive and subject to matter resonant effects. In our simulation, we fixed the L/E ratio that affects these terms so as maximizing octant

sensitivity. The resulting proportionality between neutrino beam energy and baseline length implies the matter effects to become stronger as the baseline length is increased. The weakness of short baselines was previously pointed out in Ref. [48].

Altogether our results show that long baseline neutrino oscillation experiments offer a strong improvement in the still large current ambiguity as to which octant does the θ_{23} mixing angle belong.

ACKNOWLEDGMENTS

SV expresses his gratitude to CFTP of the University of Lisbon, where part of this work was done, for financial support and hospitality. JP is grateful to the Department of Physics of the University of Jyväskylä, for hospitality and acknowledges financial support from project UID/FIS/00777/2013. CRD is thankful to Prof. D.I. Kazakov, Director BLTP, JINR for support.

---

[1] C. K. Jung, C. McGrew, T. Kajita, and T. Mann, Ann. Rev. Nucl. Part. Sci. **51**, 451 (2001).

[2] T. Kajita and Y. Totsuka, Rev. Mod. Phys. **73**, 85 (2001).

[3] Q. R. Ahmad *et al.* (SNO), Phys. Rev. Lett. **87**, 071301 (2001), arXiv:nucl-ex/0106015 [nucl-ex].

[4] R. Davis, Jr., D. S. Harmer, and K. C. Hoffman, Phys. Rev. Lett. **20**, 1205 (1968).

[5] R. Wendell *et al.* (Super-Kamiokande), Phys. Rev. **D81**, 092004 (2010), arXiv:1002.3471 [hep-ex].

[6] P. Adamson *et al.* (MINOS), Phys. Rev. Lett. **110**, 251801 (2013), arXiv:1304.6335 [hep-ex].

[7] K. Abe *et al.* (T2K), Phys. Rev. Lett. **112**, 061802 (2014), arXiv:1311.4750 [hep-ex].

[8] P. Adamson *et al.* (MINOS), Phys. Rev. Lett. **110**, 171801 (2013), arXiv:1301.4581 [hep-ex].

[9] K. Abe *et al.* (T2K), Phys. Rev. Lett. **112**, 181801 (2014), arXiv:1403.1532 [hep-ex].

[10] G. L. Fogli and E. Lisi, Phys. Rev. **D54**, 3667 (1996), arXiv:hep-ph/9604415 [hep-ph].

[11] C. R. Das, J. Maalampi, J. Pulido, and S. Vihonen, JHEP **02**, 048 (2015), arXiv:1411.2829 [hep-ph].

[12] A. Stahl *et al.*, *Expression of Interest for a very long baseline neutrino oscillation experiment (LBNO)*, Tech. Rep. CERN-SPSC-2012-021. SPSC-EOI-007 (CERN, Geneva, 2012).

[13] L. Agostino *et al.*, (2014), arXiv:1409.4405 [physics.ins-det].

[14] K. Bora, G. Ghosh, and D. Dutta (2015) arXiv:1511.02452 [hep-ph].

[15] S. Ahmed *et al.* (ICAL), Pramana **88**, 79 (2017), arXiv:1505.07380 [physics.ins-det].

[16] F. An *et al.* (JUNO), J. Phys. **G43**, 030401 (2016), arXiv:1507.05613 [physics.ins-det].

[17] V. Barger, D. Marfatia, and K. Whisnant, Phys. Rev. **D65**, 073023 (2002), arXiv:hep-ph/0112119 [hep-ph].

[18] S. Kumar Agarwalla, S. Prakash, and S. Uma Sankar, *Proceedings, 2013 European Physical Society Conference on High Energy Physics (EPS-HEP 2013): Stockholm, Sweden, July 18-24, 2013*, PoS **EPS-HEP2013**, 534 (2013).

[19] N. Nath, M. Ghosh, and S. Goswami, Nucl. Phys. **B913**, 381 (2016), arXiv:1511.07496 [hep-ph].

[20] S. K. Agarwalla, S. Prakash, and S. Uma Sankar, JHEP **07**, 131 (2013), arXiv:1301.2574 [hep-ph].

[21] S. K. Agarwalla, S. Prakash, and S. Uma Sankar, JHEP **03**, 087 (2014), arXiv:1304.3251 [hep-ph].

[22] M. Ghosh, P. Ghoshal, S. Goswami, and S. K. Raut, JHEP **03**, 094 (2014), arXiv:1308.5979 [hep-ph].

[23] S. C, K. N. Deepthi, and R. Mohanta, Adv. High Energy Phys. **2016**, 9139402 (2016), arXiv:1408.6071 [hep-ph].

[24] S. K. Agarwalla, Adv. High Energy Phys. **2014**, 457803 (2014), arXiv:1401.4705 [hep-ph].

[25] S. K. Raut, Mod. Phys. Lett. **A28**, 1350093 (2013), arXiv:1209.5658 [hep-ph].

[26] V. Barger, A. Bhattacharya, A. Chatterjee, R. Gandhi, D. Marfatia, and M. Masud, Phys. Rev. **D89**, 011302 (2014), arXiv:1307.2519 [hep-ph].

[27] V. Barger, A. Bhattacharya, A. Chatterjee, R. Gandhi, D. Marfatia, and M. Masud, Int. J. Mod. Phys. **A31**, 1650020 (2016), arXiv:1405.1054 [hep-ph].

[28] S. K. Agarwalla, S. S. Chatterjee, and A. Palazzo, Phys. Rev. Lett. **118**, 031804 (2017), arXiv:1605.04299 [hep-ph].

[29] C. Soumya and R. Mohanta, Eur. Phys. J. **C76**, 302 (2016), arXiv:1605.00523 [hep-ph].

[30] A. D. Hanlon, S.-F. Ge, and W. W. Repko, Phys. Lett. **B729**, 185 (2014), arXiv:1308.6522

[hep-ph].

[31] K. Abe *et al.* (T2K), Phys. Rev. **D91**, 072010 (2015), arXiv:1502.01550 [hep-ex].

[32] P. Adamson *et al.* (MINOS), Phys. Rev. Lett. **112**, 191801 (2014), arXiv:1403.0867 [hep-ex].

[33] F. De Maria Blaszczyk (Super-Kamiokande), *Proceedings, 2017 International Workshop on Neutrinos from Accelerators (NuFact17): Uppsala University Main Building, Uppsala, Sweden, September 25-30, 2017*, PoS **NuFact2017**, 059 (2018).

[34] P. Adamson *et al.* (NOvA), Phys. Rev. **D93**, 051104 (2016), arXiv:1601.05037 [hep-ex].

[35] P. Huber, M. Lindner, and W. Winter, Comput. Phys. Commun. **167**, 195 (2005), arXiv:hep-ph/0407333 [hep-ph].

[36] P. Huber, J. Kopp, M. Lindner, M. Rolinec, and W. Winter, Comput. Phys. Commun. **177**, 432 (2007), arXiv:hep-ph/0701187 [hep-ph].

[37] J. Liao, D. Marfatia, and K. Whisnant, Phys. Rev. **D93**, 093016 (2016), arXiv:1601.00927 [hep-ph].

[38] K. Bora, G. Ghosh, and D. Dutta, Adv. High Energy Phys. **2016**, 9496758 (2016), arXiv:1606.00554 [hep-ph].

[39] F. P. An *et al.* (Daya Bay), Phys. Rev. Lett. **108**, 171803 (2012), arXiv:1203.1669 [hep-ex].

[40] J. K. Ahn *et al.* (RENO), Phys. Rev. Lett. **108**, 191802 (2012), arXiv:1204.0626 [hep-ex].

[41] S. Antusch, P. Huber, J. Kersten, T. Schwetz, and W. Winter, Phys. Rev. **D70**, 097302 (2004), arXiv:hep-ph/0404268 [hep-ph].

[42] H. Minakata, M. Sonoyama, and H. Sugiyama, Phys. Rev. **D70**, 113012 (2004), arXiv:hep-ph/0406073 [hep-ph].

[43] R. Gandhi, P. Ghoshal, S. Goswami, P. Mehta, S. Uma Sankar, and S. Shalgar, Phys. Rev. **D76**, 073012 (2007), arXiv:0707.1723 [hep-ph].

[44] A. Chatterjee, P. Ghoshal, S. Goswami, and S. K. Raut, JHEP **06**, 010 (2013), arXiv:1302.1370 [hep-ph].

[45] E. K. Akhmedov, R. Johansson, M. Lindner, T. Ohlsson, and T. Schwetz, JHEP **04**, 078 (2004), arXiv:hep-ph/0402175 [hep-ph].

[46] R. Acciarri *et al.* (DUNE), (2015), arXiv:1512.06148 [physics.ins-det].

[47] P. F. de Salas, D. V. Forero, C. A. Ternes, M. Tortola, and J. W. F. Valle, Phys. Lett. **B782**, 633 (2018), arXiv:1708.01186 [hep-ph].

[48] M. Bass *et al.*, Phys. Rev. **D91**, 052015 (2015), arXiv:1311.0212 [hep-ex].

Publication III

III

C.R. Das, J. Maalampi, J. Pulido and S. Vihonen,
Determination of the θ_{23} octant in long baseline neutrino experiments within and beyond the standard model,
Phys. Rev. D **97** (2018) no.3, 035023,
arXiv:1708.05182 [hep-ph]

Determination of the θ_{23} octant in long baseline neutrino experiments within and beyond the standard model

C. R. Das[*]
Bogoliubov Laboratory of Theoretical Physics, Joint Institute of Nuclear Research, Joliot-Curie 6, 141980 Dubna, Moscow region, Russia

João Pulido[†]
Centro de Física Teórica das Partículas, Instituto Superior Técnico (CFTP-IST), Avenida Rovisco Pais, P-1049-001 Lisboa, Portugal

Jukka Maalampi[‡] and Sampsa Vihonen[§]
University of Jyvaskyla, Department of Physics, P.O. Box 35, FI-40014 University of Jyvaskyla, Finland

(Received 23 October 2017; published 28 February 2018)

The recent data indicate that the neutrino mixing angle θ_{23} deviates from the maximal-mixing value of 45°, showing two nearly degenerate solutions, one in the lower octant (LO) ($\theta_{23} < 45°$) and one in the higher octant (HO) ($\theta_{23} > 45°$). We investigate, using numerical simulations, the prospects for determining the octant of θ_{23} in the future long baseline oscillation experiments. We present our results as contour plots on the $(\theta_{23} - 45°, \delta)$–plane, where δ is the CP phase, showing the true values of θ_{23} for which the octant can be experimentally determined at 3σ, 2σ and 1σ confidence level. In particular, we study the impact of the possible nonunitarity of neutrino mixing on the experimental determination of θ_{23} in those experiments.

DOI: 10.1103/PhysRevD.97.035023

I. INTRODUCTION

Many solar, atmospheric, reactor, and accelerator neutrino experiments have firmly established the existence of neutrino oscillations. Neutrino oscillations can be parametrized in terms of six physical variables, namely by three mixing angles θ_{12}, θ_{23}, and θ_{13}, a phase δ_{CP}, and two squared-mass differences $\Delta m^2_{21} = m^2_2 - m^2_1$ and $\Delta m^2_{31} = m^2_3 - m^2_1$. These parameters are by now experimentally quite precisely determined, with the exception of the CP phase δ_{CP}. As to the mixing angle θ_{23}, one still do not know in which octant it lies ($\theta_{23} < 45°$ or $\theta_{23} > 45°$). Also the order of the masses of three light neutrinos (ν_1, ν_2, ν_3) remains unknown, namely whether it is $m_3 \geq m_1, m_2$ (normal hierarchy, NH) or $m_3 \leq m_1, m_2$ (inverted hierarchy, IH).

As to the mixing angle θ_{23}, also known as the atmospheric angle, the fits on global data indicate that θ_{23} deviates from the maximal-mixing value 45° showing two degenerate solutions, a low-octant (LO) solution with $\theta^2_{23} < 45°$ and a high-octant (HO) solution with $\theta_{23} > 45°$ [1–4]. This octant degeneracy is one of many parameter degeneracies that hamper the interpretation of neutrino oscillation data [5]. The NOνA experiment has recently excluded the maximal-mixing value $\theta_{23} = 45°$ at the 2.6σ confidence level [6]. Two statistically degenerate values for $\sin^2\theta_{23}$ were found, $0.404^{+0.030}_{-0.022}$ and $0.624^{+0.022}_{-0.030}$, which both explain the data on muon neutrino disappearance at the 68% confidence level. Earlier experimental results are compatible with $\theta_{23} = 45°$ [7–10]. The prospects of resolving the θ_{23} octant in next generation experiments have been studied in, e.g., [11–17].

Identifying the true value of θ_{23} is an important goal for future experiments, given its importance for understanding the mechanism behind neutrino masses and mixing. For example, one symmetry of the neutrino sector under the interchange of ν_μ and ν_τ would predict θ_{23} to have the maximal mixing value of 45° (see, e.g., [18]). In that case, the ν_μ and ν_τ flavors would have an equal weight in the ν_3 mass state. In some models the octant of θ_{23} is directly related to the neutrino mass hierarchy, e.g., in the model considered in [19], the mass hierarchy for the higher octant is normal and for the lower octant the mass hierarchy is inverted.

[*]das@theor.jinr.ru
[†]pulido@cftp.ist.utl.pt
[‡]jukka.maalampi@jyu.fi
[§]sampsa.p.vihonen@student.jyu.fi

In interpreting the data, one should take into account the possibility of beyond the standard model effects, which may appear as nonunitarity of the mixing of light neutrinos. In particular, the possible existence of sterile neutrinos and nonstandard neutrino interactions would influence the experimental determination of θ_{23} and the octant where the angle lies. The effects of some new physics in octant determination have been studied in future long baseline neutrino experiments in, e.g., [20–24].

In this paper, we will consider the determination of the mixing angle θ_{23} in long baseline neutrino experiments taking possible nonunitarity effects into account. First, we will update our previous studies [25,26], done for the standard model case with three conventional neutrinos. We apply the results of the most recent fits for the values of mixing parameters and use as our benchmark the setup of the proposed Deep Underground Neutrino Experiment (DUNE). Our main goal is to find out how the possible nonunitarity of the mixing matrix of the light neutrinos affect the sensitivity of the experiments in identifying the octant of θ_{23}. Such nonunitarity may arise, e.g., if one adds to the particle content of the standard model sterile neutrinos that mix with the conventional neutrinos. We also study to which extent the still unknown value of the CP phase interferes with the determination of the octant of θ_{23}, and we present our results for both the normal and inverted mass hierarchy.

This work is organized as follows. In Sec. II we will present a brief review of the formalism we will use. In Sec. III the simulation method is described. The results of simulations are presented and discussed in Sec. IV. Section V contains a summary and conclusions.

II. BRIEF REVIEW OF THE FORMALISM

We start our analysis by investigating the prospects for θ_{23} octant determination in long baseline experiments in the case of standard neutrinos. For these, the matter evolution is determined by the Hamiltonian which in the mass basis reads

$$H = \frac{1}{2E}\begin{pmatrix} 0 & 0 & 0 \\ 0 & \Delta m^2_{21} & 0 \\ 0 & 0 & \Delta m^2_{31} \end{pmatrix} + U^\dagger \begin{pmatrix} V_{CC}+V_{NC} & 0 & 0 \\ 0 & V_{NC} & 0 \\ 0 & 0 & V_{NC} \end{pmatrix} U. \quad (1)$$

Here U is the conventional neutrino mixing matrix (PMNS matrix), $V_{CC} = \sqrt{2} G_F N_e$ and $V_{NC} = -G_F N_n/\sqrt{2}$ are respectively the charged current and the neutral current matter potentials.

Owing to their smallness, the most common understanding of the origin of neutrino masses lies in the assumption of a new physics scale associated with the general seesaw mechanism, whereby heavy right-handed neutrinos are added to the particle content of the Standard Model. These $SU(3)_C \otimes SU(2)_L \otimes U(1)_Y$ singlet neutrinos mix with the standard neutrino flavors ν_e, ν_μ, ν_τ and, although in the likely case they are too heavy to be kinematically produced, they should leave traces at the energies within experimental reach. These traces appear in the oscillation probabilities through the $n \times n$ unitary matrix $\mathcal{U}$ connecting the neutrino mass and flavor eigenstates which generalizes the conventional 3×3 U matrix of the standard case. The $\mathcal{U}$ matrix can be written in the form [27]

$$\mathcal{U} = \begin{pmatrix} N & S \\ T & V \end{pmatrix} \quad (2)$$

where N and S are (3×3) submatrices that contain respectively the mixing in the light (active) neutrino sector and the active-sterile mixing. Submatrices T and V define the mixing of the sterile states with the active and sterile states respectively. In this way, Eq. (1) is modified to

$$H = \frac{1}{2E}\begin{pmatrix} 0 & 0 & 0 \\ 0 & \Delta m^2_{21} & 0 \\ 0 & 0 & \Delta m^2_{31} \end{pmatrix} + N^\dagger \begin{pmatrix} V_{CC}+V_{NC} & 0 & 0 \\ 0 & V_{NC} & 0 \\ 0 & 0 & V_{NC} \end{pmatrix} N. \quad (3)$$

The unitarity of $\mathcal{U}$ implies that the matrix describing the mixing in the light sector, namely N, is no longer unitary. In [28], the matrix N was presented in the form $N = N^{\rm NP} U$, where U is the conventional unitary 3×3 matrix and $N^{\rm NP}$ the triangular matrix

$$N^{\rm NP} = \begin{pmatrix} \alpha_{11} & 0 & 0 \\ \alpha_{21} & \alpha_{22} & 0 \\ \alpha_{31} & \alpha_{32} & \alpha_{33} \end{pmatrix}, \quad (4)$$

parametrizing the deviations from unitarity. The description of the unitarity violation therefore requires three real parameters α_{ii} which are close to unity and three complex ones α_{ij} $(i \neq j)$, which are close to zero.

A slightly different notation for the prefactor matrix $N^{\rm NP}$ was given in [29],

$$N^{\rm NP} = \begin{pmatrix} 1-\alpha_{ee} & 0 & 0 \\ \alpha_{\mu e} & 1-\alpha_{\mu\mu} & 0 \\ \alpha_{\tau e} & \alpha_{\tau\mu} & 1-\alpha_{\tau\tau} \end{pmatrix}. \quad (5)$$

Here $\alpha_{\ell\ell'}$ directly parametrize deviations from the unitarity and since these deviations are known to be small one

has $\alpha_{\ell\ell} \ll 1$ and $|\alpha_{\ell\ell'}| \ll 1$. The difference between the parametrizations (4) and (5) is purely aesthetic, but as both of them are used parallel in the literature, we give them both here for convenience.

Since current experiments involve mainly electron and muon neutrinos, only α_{11}, α_{22} and α_{21} (or equivalently α_{ee}, $\alpha_{\mu\mu}$ and $\alpha_{\mu e}$) need to be considered, hence four new parameters are effectively required in the analysis. Constraints for α_{ij} and $\alpha_{\ell\ell'}$ are given in Refs. [29,28]. No constraint exists, however, for the off-diagonal phases.

One should note that the nonunitary of the mixing of the neutrino flavors ν_e, ν_μ, and ν_τ would, in general, affect the determination of the mixing angles θ_{12}, θ_{23}, and θ_{31} from the existing neutrino oscillation data. However, in the triangular parametrizations of Eqs. (4) and (5) the nonunitarity effects disappear in the leading order and are hence negligible in comparison with the uncertainties of the experimental results used in the fits done [29]. Hence, the matrix U has in good approximation the same numerical form as is obtained in the standard analysis of the data where the unitarity assumed to hold.

Our analysis, which follows the lines presented in [25], is based on numerical simulations where we utilize the GLoBES software [30,31]. Let us note that whereas analytical expressions for survival and conversion probabilities both in vacuum and matter have been given in the literature [32,33], for the nonunitarity effect in neutrino oscillations only the vacuum expressions exist [28]. Brief discussions of the matter potential in the nonunitary case are given in Refs. [34,35].

III. NUMERICAL METHODS

We evaluate the effect of nonunitary mixing on the determination of θ_{23} octant by simulating a long baseline oscillation experiment with the DUNE specifications with the GLoBES program. Since the nonunitary mixing matrix is not available in the standard GLoBES package, we modify the program by introducing our own add-on, which replaces the standard PMNS mixing matrix with its nonunitary version given by Eq. (4), or alternatively Eq. (5), and replaces the standard Hamiltonian shown in Eq. (1) with its nonunitary version (3).

The octant discovery potential is evaluated for a given θ_{23} value as

$$\Delta\chi^2(\theta_{23}) = \chi^2(90° - \theta_{23}) - \chi^2(\theta_{23}), \tag{6}$$

where $\chi^2(\theta_{23})$ evaluates the chi-square distribution at the given true value θ_{23}, whilst in $\chi^2(90° - \theta_{23})$ it is evaluated at the wrong octant solution $90° - \theta_{23}$. This leaves the subtraction of the two, $\Delta\chi^2$, an approximate chi-square distribution with one degree of freedom, and hence the sensitivity for ruling out the wrong octant at 1σ, 2σ, and 3σ confidence levels is reached at $\Delta\chi^2 = 1$, 4, and 9, respectively.

The simulation of the DUNE setup is performed using the same experimental configuration that was used in the DUNE conceptual design report [36] and was published in Ref. [37]. The octant discovery potential is evaluated using Eq. (6) as described above.

In this work, we assess the sensitivity to the θ_{23} octant in DUNE in four different scenarios. On the one hand, we update the octant sensitivity plots for the standard model case, where no sterile neutrinos exist and the oscillations would follow the standard three-neutrino paradigm. On the other hand, we also evaluate the octant sensitivity in scenarios, where sterile neutrinos do exist, manifesting themselves as nonunitarity of the mixing matrix of the three active neutrinos. The effects of sterile neutrinos to the oscillations would depend on the scale of the lightest sterile mass.

For the standard oscillation parameters, we employ the best-fit values and their associated errors, which have been obtained from the experimental data collected from the past and ongoing neutrino experiments (see Ref. [38]). We take the central values and standard deviations of these parameter best-fits and take them into account as Gaussian distributions. For the mixing angles the Gaussian distributions are set for $\sin^2\theta_{12}$, $\sin^2\theta_{13}$, and $\sin^2\theta_{23}$. These values are presented in Table I [39].

In addition to the standard oscillation parameters, we also need to consider the new physics parameters α_{ij}, i, $j = 1, 2, 3$, and $\alpha_{\ell\ell'}$, $\ell, \ell' = e, \mu, \tau$, as indicated in Eqs. (4) and (5), respectively. Since no significant signs of physics

TABLE I. The experimental best-fit values and standard deviations for the standard neutrino oscillation parameters. These values are shown for both mass hierarchies and are taken from a recent global analysis [38]. Note that Δm^2_{3l} stands for Δm^2_{31} in normal hierarchy (NH) and Δm^2_{32} in inverted hierarchy (IH).

Parameter	Central value (NH)	Error (NH)	Central value (IH)	Error (IH)
$\sin^2\theta_{12}$	0.306	0.012	0.306	0.012
$\sin^2\theta_{13}$	0.02166	0.00075	0.02179	0.00076
$\sin^2\theta_{23}$	0.441	0.027	0.587	0.024
δ_{CP} (°)	261	59	277	46
Δm^2_{21} (10^{-5} eV^2)	7.50	0.19	7.50	0.19
Δm^2_{3l} (10^{-3} eV^2)	2.524	0.040	−2.514	0.041

beyond the standard model has been observed in oscillation experiments, there exist only upper bounds on the different α parameters. In this work we consider the possibility of sterile neutrino induced new physics by allowing the α_{ij} and $\alpha_{\ell\ell'}$ parameters to have Gaussian distributions, where central values are set at zero and standard deviations to match the appropriate upper bounds. The standard three-neutrino paradigm is restored by setting α_{11}, α_{22}, $\alpha_{33} = 1$ and α_{21}, α_{31}, $\alpha_{32} = 0$, or alternatively $\alpha_{\ell\ell'} = 0$ for all $\ell, \ell' = e, \mu, \tau$ combinations.

We start the investigation on the new physics scenarios by assuming that all three sterile neutrinos are too massive to be produced in the experiment. In this scenario, the sterile neutrinos do not contribute to the oscillations kinematically, but they affect the neutrino oscillation probabilities through the nonunitarity of the 3×3 mixing matrix that controls the mixing of active neutrinos. These bounds have been evaluated for nonunitary mixing in two independent references; for the α_{ij} basis they are provided in Ref. [35] and for $\alpha_{\ell\ell'}$ in Ref. [29], and they are both shown in Table II.

We also consider the scenario where at least one of the sterile neutrinos is sufficiently light to be produced kinematically in the experiment. In such case, sterile neutrinos could contribute to the oscillations in two different ways depending on their mass range. If the lightest sterile neutrino has its mass m_4 in the range such that $\Delta m^2_{41} \equiv m^2_4 - m^2_1 \sim 0.1$–$1\ \text{eV}^2$, the active neutrinos could oscillate to the sterile neutrino state between the near and far detectors. It is also possible, however, that the oscillations to the sterile neutrino are too rapid to be observed in the far detector, i.e., they average out, but sufficiently light to occur before the near detector. In either case, not all constraints used in deriving the upper bounds in Table II are applicable, and therefore new bounds must be derived. This topic has been thoroughly reviewed in Ref. [29], where appropriate bounds were provided for $\alpha_{\ell\ell'}$, $\ell, \ell' = e, \mu, \tau$ in mass ranges $\Delta m^2_{41} \sim 0.1$–$1\ \text{eV}^2$ and $\Delta m^2_{41} \geq 100\ \text{eV}^2$. These bounds are shown in Table III.

TABLE II. Bounds on nonunitary parameters in both α_{ij} and $\alpha_{\ell\ell'}$ representations, taken from [35,29], respectively. The bounds are given in 90% and 2σ confidence levels.

Parameter	Upper bound (90% CL)	Parameter	Upper bound (2σ CL)
α_{11}	0.9974	α_{ee}	1.3×10^{-3}
α_{22}	0.9994	$\alpha_{\mu\mu}$	2.2×10^{-4}
α_{33}	0.9988	$\alpha_{\tau\tau}$	2.8×10^{-3}
$\lvert\alpha_{21}\rvert$	2.6×10^{-2}	$\lvert\alpha_{\mu e}\rvert$	6.8×10^{-4}
$\lvert\alpha_{31}\rvert$	2.0×10^{-3}	$\lvert\alpha_{\tau e}\rvert$	2.7×10^{-3}
$\lvert\alpha_{32}\rvert$	1.5×10^{-2}	$\lvert\alpha_{\tau\mu}\rvert$	1.2×10^{-3}

TABLE III. Bounds on nonunitary parameters in $\alpha_{\ell\ell'}$ representation, taken from [29]. In this scenario the constraints would correspond to mixing with a light sterile neutrino in two mass scales: $\Delta m^2_{41} \sim 0.1$–$1\ \text{eV}^2$ (left column) and $\Delta m^2_{41} \geq 100\ \text{eV}^2$ (right column). The constraints are presented at a 95% confidence level.

Parameter	$\Delta m^2_{41} \sim 0.1$–$1\ \text{eV}^2$	$\Delta m^2_{41} \geq 100\ \text{eV}^2$
α_{ee}	1.0×10^{-2}	2.4×10^{-2}
$\alpha_{\mu\mu}$	1.4×10^{-2}	2.2×10^{-2}
$\alpha_{\tau\tau}$	1.0×10^{-1}	1.0×10^{-1}
$\lvert\alpha_{\mu e}\rvert$	1.7×10^{-2}	2.5×10^{-2}
$\lvert\alpha_{\tau e}\rvert$	4.5×10^{-2}	6.9×10^{-2}
$\lvert\alpha_{\tau\mu}\rvert$	5.3×10^{-2}	1.2×10^{-2}

IV. RESULTS

We restrict our study to four different scenarios that could take place in the presence (or absence) of physics beyond the standard model. These scenarios include the standard three-neutrino paradigm, nonunitary neutrino mixing, mixing with a light sterile neutrino, and finally, a scenario where no constraints are set for the new physics parameters.

A. The standard model case

In the standard model there exist three active neutrinos (ν_e, ν_μ, and ν_τ) and no sterile neutrinos. Using the best-fit values and errors presented in Table I we plotted the 1σ, 2σ, and 3σ confidence level contours for various possible true values of θ_{23} and δ_{CP} in both NH and IH. The results are presented in Fig. 1. We obtained this figure by keeping θ_{23} and δ_{CP} fixed to their assigned values, whilst the other four oscillation parameters (θ_{12}, θ_{13}, Δm^2_{21}, Δm^2_{31}) and the matter density were included in the χ^2 minimization.

Fig. 1 is to be read as follows. The white regions correspond to the θ_{23} and δ_{CP} values where the octant of θ_{23} can be determined by DUNE at a 3σ confidence level or better. In the colored region the sensitivity falls below 3σ, 2σ, or 1σ, where the latter two are indicated by the dashed and solid lines, respectively. In other words, if the values of θ_{23} and δ_{CP} fall in the region outside the band bordered by the dashed (solid) lines the octant of θ_{23} can be determined at a 2σ (3σ) confidence level or better.

B. The nonunitary mixing case

In the case of nonunitary mixing, the sensitivity to the θ_{23} octant is evaluated by using Eq. (4) or Eq. (5) to calculate the mixing matrix and Eq. (3) to construct the corresponding Hamiltonian.

We take parameters α_{ij}, $i, j = 1, 2, 3$, and $\alpha_{\ell\ell'}$, $\ell, \ell' = e, \mu, \tau$, into account as Gaussian priors, where central values are set to match the standard three-neutrino case and the standard deviations are taken from the 1σ bounds corresponding to the 90% CL ones presented in Table II.

In Fig. 2, we present the 1σ, 2σ, and 3σ contours for the octant determination under nonunitary mixing in the $\alpha_{\ell\ell'}$

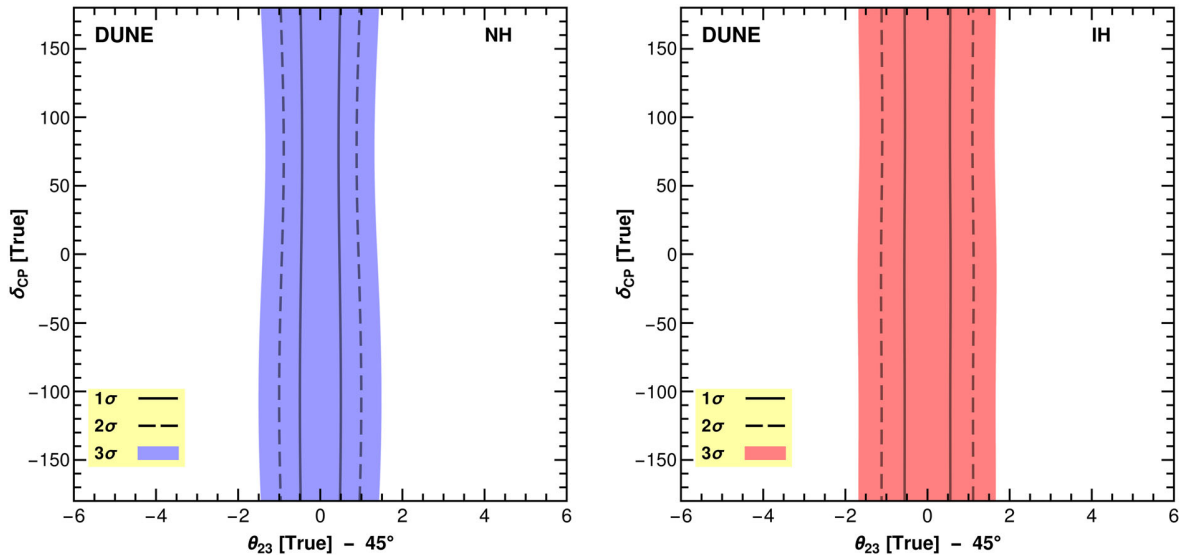

FIG. 1. Octant determination in DUNE under the standard three-neutrino paradigm. The white regions show the values of θ_{23} and δ_{CP} at which the octant of θ_{23} could be determined at a 3σ CL or better. In the colored regions, conversely, the significance falls under 3σ. The 1σ and 2σ CL contours are shown with dashed and solid lines, and the sensitivities are presented for both NH (blue, left panel) and IH (red, right panel) mass orderings.

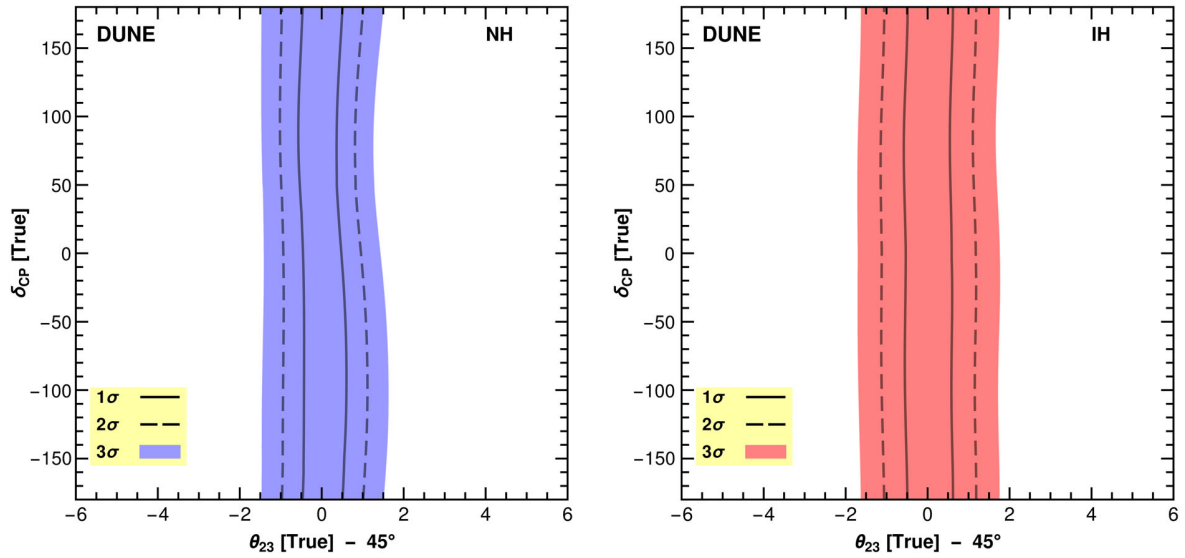

FIG. 2. Octant determination in DUNE under nonunitary mixing. The white regions show the values of θ_{23} and δ_{CP} at which the octant of θ_{23} could be determined at a 3σ CL or better. In the colored regions, conversely, the significance falls under 3σ. The 1σ and 2σ CL contours are shown with dashed and solid lines, and the sensitivities are presented for both NH (blue, left panel) and IH (red, right panel) mass orderings.

basis. The sensitivity plots are shown both in the NH and IH cases. We also studied the sensitivities in the $\alpha_{\ell\ell'}$ basis, and found the results to be nearly identical to the ones obtained in the α_{ij} basis.

C. The light sterile neutrino case

Using the bounds derived for the mixing with a light sterile neutrino of $\Delta m^2_{41} \geq 100$ eV^2 mass range, shown in the centre column of Table III, we obtained the sensitivity contours shown in Fig. 3. We also studied the case of $0 < \Delta m^2_{41} < 1$ eV^2 by using the bounds presented in the right column of Table III, but we did not find any significant difference to the $\Delta m^2_{41} \geq 100$ eV^2 case.

D. The unconstrained new physics case

Since it is unknown what may lie beyond the standard model, it is also necessary to discuss the scenario where

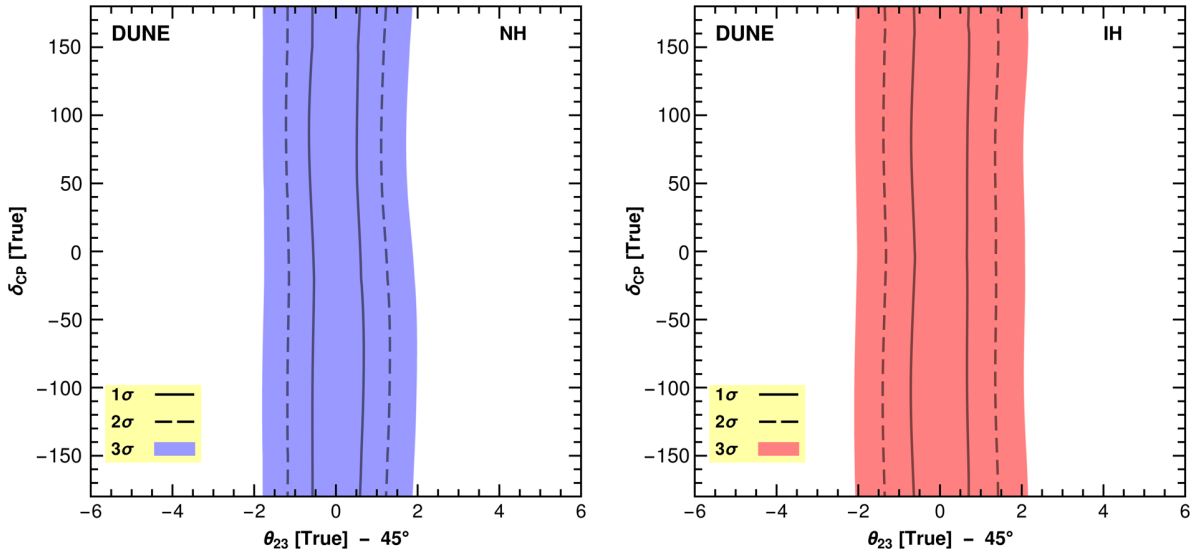

FIG. 3. Octant determination in DUNE in the presence of light sterile mixing with $\Delta m_{41} \geq 100$ eV^2. The white regions show the values of θ_{23} and δ_{CP} at which the octant of θ_{23} could be determined at a 3σ CL or better. In the colored regions, conversely, the significance falls under 3σ. The 1σ and 2σ CL contours are shown with dashed and solid lines, and the sensitivities are presented for both NH (blue, left panel) and IH (red, right panel) mass orderings.

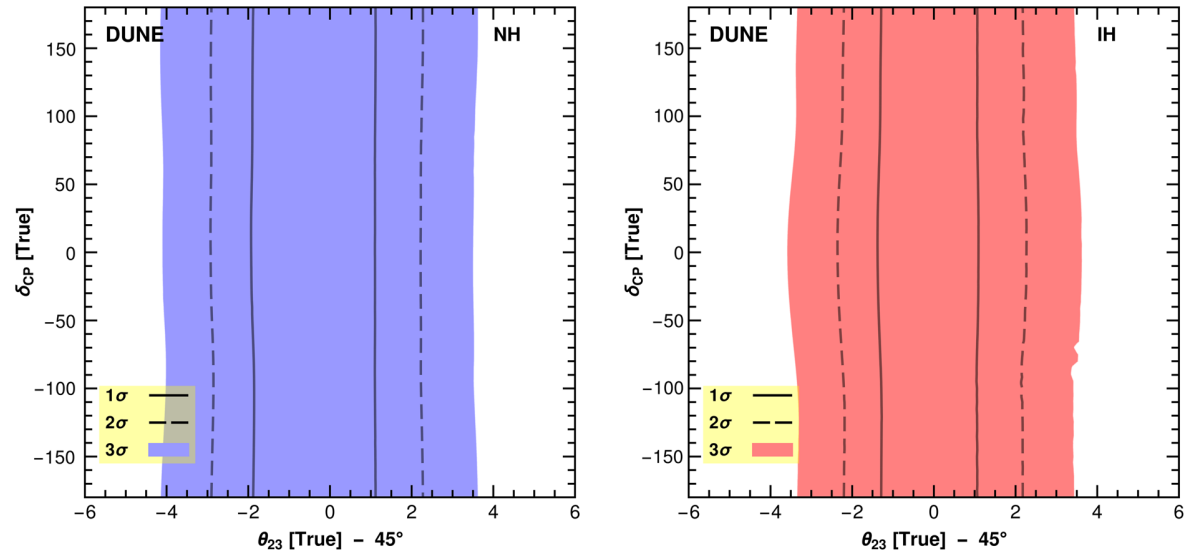

FIG. 4. Octant determination in DUNE with unconstrained $\alpha_{\ell\ell'}$ parameters. The white regions show the values of θ_{23} and δ_{CP} at which the octant of θ_{23} could be determined at a 3σ CL or better. In the colored regions, conversely, the significance falls under 3σ. The 1σ and 2σ CL contours are shown with dashed and solid lines, and the sensitivities are presented for both NH (blue, left panel) and IH (red, right panel) mass orderings.

none of the bounds that have been derived for nonunitary mixing or light sterile neutrinos may apply. An example of this situation could be a scenario where the sterile neutrinos are accompanied by nonstandard interactions (see e.g. [35]) mediated by new Higgs particles, as is the case in left-right symmetric models. Due to its unknown nature, we consider an arbitrary form of new physics by calculating the χ^2 values with no constraints on the α parameters.

We calculated the sensitivity of DUNE to the θ_{23} octant in DUNE after removing all priors that concern α_{ij} where, i, $j = 1, 2, 3$. The results are presented in Fig. 4. One notices that maximizing the effects of nonunitary and light sterile neutrinos roughly worsens the sensitivity of DUNE to the octant in terms of the angle.

In order to get an understanding on how the magnitude of the α parameters affects the worsening of the sensitivity to the θ_{23} octant in the event where only α_{21} is taken

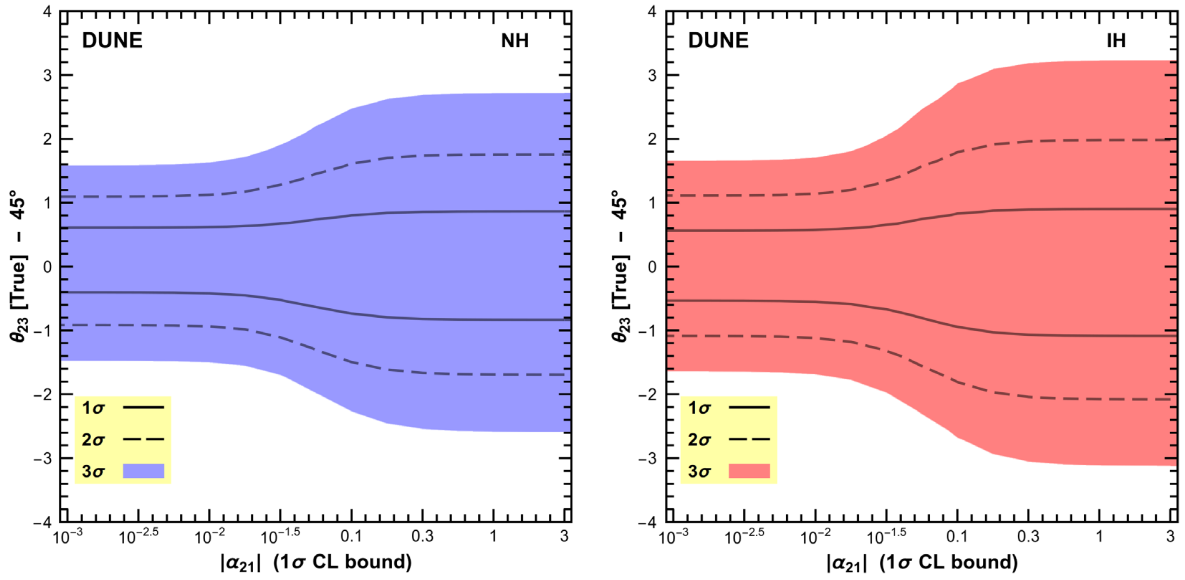

FIG. 5. Octant determination in DUNE as function of the 1σ upper bound on $|\alpha_{21}|$. The phase of α_{21} is allowed to vary freely in the range $[0, 2\pi]$ and the other alpha parameters are set to correspond to the standard three-neutrino paradigm.

into account, whereas the other alpha parameters are excluded from the χ^2 calculation. In Fig. 5 we show the octant sensitivity as a function of the 1σ upper bound of $|\alpha_{21}|$, and allow the phase of α_{21} vary freely in the range $[0, 2\pi]$. Clearly, the contours in Fig. 5 show that the constraint on α_{21} affects the octant determination when $\alpha_{21} \gtrsim 10^{-2}$.

V. CONCLUSIONS

We have presented the sensitivity to the determination of the θ_{23} octant ($\theta_{23} \leq \pi/4$ or $\theta_{23} \geq \pi/4$) in DUNE in four different scenarios. On the one hand, we have updated the 1σ, 2σ, and 3σ confidence level contours for the standard model, where oscillations are constituted between three active neutrinos. On the other hand, we have also given these contours for three different scenarios where the octant sensitivity is interfered by sterile neutrinos and other potential sources for physics beyond the standard model. We analyzed these scenarios by parametrizing the new physics with the methods that were originally introduced in Refs. [28,29] to describe nonunitarity of the light neutrino mixing matrix.

We found that the nonunitarity of the mixing matrix caused the sensitivity θ_{23} octant to decrease from the standard model case. Nevertheless, due to the strictness of the existing bounds for the nonunitarity parameters α_{ij}, $i, j = 1, 2, 3$ derived in Ref. [35] and for $\alpha_{\ell\ell'}$, $\ell, \ell' = e, \mu, \tau$ derived in Ref. [29] the observed drop in the octant sensitivity was found to be very small. The worsening of the octant sensitivity due to sterile neutrino was found larger than this. The sensitivity was calculated in this case using the bounds on $\alpha_{\ell\ell'}$ given in Ref. [29]. The worsening of the sensitivity was found to be less than 1° in each octant.

We found the decrease in sensitivity due to the light sterile neutrino to be substantially less significant than that reported in Ref. [21] where the impact of a sterile neutrino with mixing angles $\theta_{14} = \theta_{24} = 9°$ and $\theta_{34} = 0°$ was considered in the determination of the θ_{23} octant in DUNE. Evidence of this sensitivity decrease can be seen from the comparison between our Fig. 1 with Fig. 3 of Ref. [21]. When converted to the nonunitarity formalism (see the Appendix of Ref. [28]), this kind of sterile neutrino would imply nonunitarity whose parameter values lie close to the existing bounds we presented for $0 < \Delta m^2_{41} < 1$ eV^2 in Table III. On the other hand, our investigation takes into account all possibilities for light sterile neutrinos, whereas the authors of Ref. [21] consider a specific model. Thus our results are in this respect more general, therefore statistically favored by comparison and hence the difference between the two sets. If the model of Ref. [21] is realized in nature, then the ability of DUNE to tell the θ_{23} octancy is deteriorated.

We also tested how the octant sensitivity changed when the new physics parameters α_{ij} were left unconstrained. This type of simulation corresponds to a new physics scenario, where sterile neutrinos are associated with other new physics effects, not taken into account in Refs. [29,35] when deriving the bounds for the nonunitary and light sterile mixing effects. An example of this could be nonstandard interactions involved in the neutrino propagation. Our simulations showed that in the worst case the octant could be determined at 3σ CL or better for $\theta_{23} \lesssim 41.0°$ and $\theta_{23} \gtrsim 48.5°$ for the normal hierarchy to be compared with the bounds $\theta_{23} \lesssim 43.5°$ and $\theta_{23} \gtrsim 46.5°$ of the standard case.

In conclusion, we found that nonunitarity of the neutrino mixing matrix or the possible existence of light sterile neutrinos affect only mildly the sensitivity of DUNE to determine the octant of θ_{23}. This is in contrast with the determination of the CP violation, where the presence of sterile neutrinos could jeopardize the sensitivity [29,34,35].

After submitting our paper, we became aware of Ref. [40], which covers partly the same topics we consider in this paper.

ACKNOWLEDGMENTS

S. V. would like to express his gratitude for the Centro de Física Teórica de Partículas for the hospitality during his visit at the University of Lisbon, and the University of Jyväskylä for a mobility grant that made this visit possible. C. R. D. thanks, Professor Dmitri I. Kazakov, Director, BLTP, JINR for his kind support.

[1] G. L. Fogli and E. Lisi, Phys. Rev. D **54**, 3667 (1996).
[2] D. V. Forero, M. Tortola, and J. W. F. Valle, Phys. Rev. D **90**, 093006 (2014).
[3] F. Capozzi, E. Lisi, A. Marrone, D. Montanino, and A. Palazzo, Nucl. Phys. **B908**, 218 (2016).
[4] M. C. Gonzalez-Garcia, M. Maltoni, and T. Schwetz, Nucl. Phys. **B908**, 199 (2016).
[5] G. L. Fogli, E. Lisi, A. Marrone, D. Montanino, A. Palazzo, and A. M. Rotunno, Phys. Rev. D **86**, 013012 (2012).
[6] P. Adamson *et al.* (NOvA Collaboration), Phys. Rev. Lett. **118**, 231801 (2017).
[7] R. Wendell *et al.* (Super-Kamiokande Collaboration), Phys. Rev. D **81**, 092004 (2010).
[8] P. Adamson *et al.* (MINOS Collaboration), Phys. Rev. Lett. **112**, 191801 (2014).
[9] K. Abe *et al.* (T2K Collaboration), Phys. Rev. D **91**, 072010 (2015).
[10] P. Adamson *et al.* (NOvA Collaboration), Phys. Rev. D **93**, 051104 (2016).
[11] S. K. Agarwalla, S. Prakash, and S. U. Sankar, J. High Energy Phys. 07 (2013) 131.
[12] M. Ghosh, S. Goswami, and S. K. Raut, Eur. Phys. J. C **76**, 114 (2016).
[13] N. Nath, M. Ghosh, and S. Goswami, Nucl. Phys. **B913**, 381 (2016).
[14] S. Fukasawa, M. Ghosh, and O. Yasuda, Nucl. Phys. **B918**, 337 (2017).
[15] P. Ballett, S. F. King, S. Pascoli, N. W. Prouse, and T. C. Wang, Phys. Rev. D **96**, 033003 (2017).
[16] S. Sachi Chatterjee, P. Pasquini, and J. W. F. Valle, Phys. Rev. D **96**, 011303 (2017).
[17] S. K. Agarwalla, M. Ghosh, and S. K. Raut, J. High Energy Phys. 05 (2017) 115.
[18] G. Altarelli and F. Feruglio, Rev. Mod. Phys. **82**, 2701 (2010).
[19] A. E. Carcamo Hernandez, S. Kovalenko, J. W. F. Valle, and C. A. Vaquera-Araujo, J. High Energy Phys. 07 (2017) 118.
[20] A. D. Hanlon, S.-F. Ge, and W. W. Repko, Phys. Lett. B **729**, 185 (2014).
[21] S. K. Agarwalla, S. S. Chatterjee, and A. Palazzo, Phys. Rev. Lett. **118**, 031804 (2017).
[22] S. K. Agarwalla, S. S. Chatterjee, and A. Palazzo, Phys. Lett. B **762**, 64 (2016).
[23] D. Dutta, P. Ghoshal, and S. K. Sehrawat, Phys. Rev. D **95**, 095007 (2017).
[24] S. Choubey, D. Dutta, and D. Pramanik, Phys. Rev. D **96**, 056026 (2017).
[25] C. R. Das, J. Maalampi, J. Pulido, and S. Vihonen, J. Phys. Conf. Ser. **888**, 012219 (2017).
[26] C. R. Das, J. Maalampi, J. Pulido, and S. Vihonen, J. High Energy Phys. 02 (2015) 048.
[27] H. Hettmansperger, M. Lindner, and W. Rodejohann, J. High Energy Phys. 04 (2011) 123.
[28] F. J. Escrihuela, D. V. Forero, O. G. Miranda, M. Tortola, and J. W. F. Valle, Phys. Rev. D **92**, 053009 (2015); **93**, 119905(E) (2016).
[29] M. Blennow, P. Coloma, E. Fernandez-Martinez, J. Hernandez-Garcia, and J. Lopez-Pavon, J. High Energy Phys. 04 (2017) 153.
[30] P. Huber, M. Lindner, and W. Winter, Comput. Phys. Commun. **167**, 195 (2005).
[31] P. Huber, J. Kopp, M. Lindner, M. Rolinec, and W. Winter, Comput. Phys. Commun. **177**, 432 (2007).
[32] E. K. Akhmedov, R. Johansson, M. Lindner, T. Ohlsson, and T. Schwetz, J. High Energy Phys. 04 (2004) 078.
[33] H. Nunokawa, S. J. Parke, and J. W. F. Valle, Prog. Part. Nucl. Phys. **60**, 338 (2008).
[34] S.-F. Ge, P. Pasquini, M. Tortola, and J. W. F. Valle, Phys. Rev. D **95**, 033005 (2017).
[35] F. J. Escrihuela, D. V. Forero, O. G. Miranda, M. Tortola, and J. W. F. Valle, New J. Phys. **19**, 093005 (2017).
[36] R. Acciarri *et al.* (DUNE Collaboration), arXiv:1512.06148.
[37] T. Alion *et al.* (DUNE Collaboration), arXiv:1606.09550.
[38] I. Esteban, M. C. Gonzalez-Garcia, M. Maltoni, I. Martinez-Soler, and T. Schwetz, J. High Energy Phys. 01 (2017) 087.
[39] Let us note that these values are not on any statistical level sensitive to the nonunitarity effects we consider [29].
[40] J. Tang, Y. Zhang, and Y.-F. Li, Phys. Lett. B **774**, 217 (2017).

Publication IV

IV

K. Huitu, T. J. Kärkkäinen, J. Maalampi and S. Vihonen,
Constraining the nonstandard interaction parameters in long baseline neutrino experiments,
Phys. Rev. D **93** (2016) no.5, 053016,
arXiv:1601.07730 [hep-ph]

PHYSICAL REVIEW D **93,** 053016 (2016)

Constraining the nonstandard interaction parameters in long baseline neutrino experiments

Katri Huitu[*]
Department of Physics, and Helsinki Institute of Physics, P.O. Box 64, FIN-00014 University of Helsinki, Finland

Timo J. Kärkkäinen[†]
Department of Physics, University of Helsinki, P.O. Box 64, FI-00014 University of Helsinki, Finland

Jukka Maalampi[‡] and Sampsa Vihonen[§]
University of Jyvaskyla, Department of Physics, P.O. Box 35, FI-40014 University of Jyvaskyla, Finland
(Received 8 February 2016; published 28 March 2016)

In this article we investigate the prospects for probing the strength of the possible nonstandard neutrino interactions (NSI) in long baseline neutrino oscillation experiments. We find that these experiments are sensitive to NSI couplings down to the level of 0.01–0.1 depending on the oscillation channel and the baseline length, as well as on the detector's fiducial mass. We also investigate the interference of the leptonic CP angle δ_{CP} with the constraining of the NSI couplings. It is found that the interference is strong in the case of the $\nu_e \leftrightarrow \nu_\mu$ and $\nu_e \leftrightarrow \nu_\tau$ transitions but not significant in other transitions. In our numerical analysis we apply the GLoBES software and use the LBNO setup as our benchmark.

DOI: 10.1103/PhysRevD.93.053016

I. INTRODUCTION

The discovery of neutrino oscillation and neutrino flavor conversion belongs to the major achievements of particle physics in past few decades. The observation of the oscillation of atmospheric neutrinos by the Super-Kamiokande experiment [1,2] and the flux measurements of the solar neutrinos by the SNO experiment [3] and the earlier solar neutrino experiments [4], firmly establish that neutrinos are massive particles and lepton flavors mix. The parameters describing neutrino masses and flavor mixing have been extensively studied in many atmospheric, solar, accelerator and reactor neutrino experiments, resulting in high-precision constraints on their values, see e.g. Refs. [5–9]. The present experimental values of the oscillation parameters are presented in Table I. There still are, however, some unknowns in the neutrino mixing scheme of the standard three neutrinos. One of them is the question of mass hierarchy, namely does there exist two light neutrinos and one heavier neutrino [the normal hierarchy (NH)] or one light neutrino and two heavier ones [the inverted hierarchy (IH)]. Also, the question of possible CP violation in the lepton sector is still open, as is the octant of the leptonic mixing angle θ_{23}, too. All these open questions will be addressed in future experimental studies, such as the long baseline neutrino oscillation experiments which have been under discussions recently, see e.g. [10–15].

The masses of neutrinos and neutrino flavor mixing cannot be explained in the framework of the minimal Standard Model (SM), since in the SM neutrinos are considered to be massless particles. The observation of neutrino oscillations and flavor conversion thus indicate that there is some physics beyond the SM. Besides being responsible for neutrino masses and mixing, this new physics may manifest itself also as new interactions affecting the processes through which neutrinos are created and detected, and they can also give rise to new effects on neutrinos propagating in matter. Such new interactions are called nonstandard neutrino interactions (NSI).

The possible impacts of NSI have been widely studied, and constraints on the parameters modeling their effects at low energies have been derived from a great variety of experimental results. For recent reviews on NSI, see Refs. [18,19]. No definite evidence of NSI has appeared but all observations made so far can be explained in terms of the standard interactions of the known three neutrinos, some of them with the help of sterile neutrino(s). In some cases NSI can give an alternative explanation to experimental results (see e.g. [20]) but so far such explanations have never been the only possibility.

In this paper we shall investigate the potential of the future long baseline neutrino oscillation experiments for detecting NSI. In these experiments, NSI can affect both neutrino production in the source and the detection process at detectors, as well as the neutrino propagation in the Earth's crust. We will concentrate on the matter effect in

[*]katri.huitu@helsinki.fi
[†]timo.j.karkkainen@helsinki.fi
[‡]jukka.maalampi@jyu.fi
[§]sampsa.p.vihonen@student.jyu.fi

TABLE I. Standard neutrino oscillation parameters. (See Refs. [16,17].) For the unknown δ_{CP} we have denoted the values considered in numerical calculations.

Parameter	Value ± Error
$\sin^2\theta_{12}$	0.304 ± 0.013
$\sin^2\theta_{13}$	0.0218 ± 0.001
$\sin^2\theta_{23}$	0.562 ± 0.032
Δm^2_{21}	$(7.500 \pm 0.019) \times 10^{-5}$ eV^2
Δm^2_{31}	$\begin{pmatrix} 2.457 \pm 0.045 \\ -2.449 \pm 0.048 \end{pmatrix} \times 10^{-3}$ eV^2
δ_{CP}	$\{2\pi n/25 \vert n = 1, \ldots, 25\} \pm 0$

this study. We will also study the interference of the CP angle δ_{CP}, whose value is still unknown, with the determination of the NSI parameters from the oscillation data.

II. THE BASIC NSI FORMALISM

In the low-energy regime, NSI can be parametrized in terms of effective charged current like (CC) and neutral current like (NC) Lagrangians, given respectively by [21]

$$\mathcal{L}^{\rm CC}_{\rm NSI} = -2\sqrt{2}G_F\varepsilon^{ff',C}_{\alpha\beta}(\bar{\nu}_\alpha\gamma^\mu P_L\ell_\beta)(\bar{f}\gamma^\mu P_C f'),$$
$$\mathcal{L}^{\rm NC}_{\rm NSI} = -2\sqrt{2}G_F\varepsilon^{f,C}_{\alpha\beta}(\bar{\nu}_\alpha\gamma^\mu P_L\nu_\beta)(\bar{f}\gamma^\mu P_C f). \quad (1)$$

Here f and f' label charged leptons or quarks ($\ell_i, u_i, d_i, i = 1, 2, 3$), $G_F = 1.166 \times 10^{-5}$ GeV^{-2} is the Fermi coupling constant, α, β refer to neutrino flavor (e, μ, τ), and $C = L$, R refers to the chirality structure of the charged lepton interaction, P_L and P_R being the chiral projection operators. The NSI parameters $\varepsilon^{ff',C}_{\alpha\beta}$ and $\varepsilon^{f,C}_{\alpha\beta}$ are dimensionless numbers. It is assumed here that the effective nonstandard interactions have V–A Lorentz structure, and for the charged fermions we allow both left-handed ($P_C = P_L$) and right-handed ($P_C = P_R$) couplings. The charged current Lagrangian $\mathcal{L}^{\rm CC}_{\rm NSI}$ is relevant for the NSI effects in the source and detector, since both in the creation and detection processes involve charged fermions. The neutral current Lagrangian $\mathcal{L}^{\rm NC}_{\rm NSI}$ in turn is relevant for the NSI matter effects. The effective low-energy Lagrangians (1) are assumed to follow from some unspecified beyond-the-standard-model theory after integrating out heavy degrees of freedom.

In the presence of NSI the neutrino states produced in a source and detected at a detector are not necessarily pure flavor states but they may consist of several flavors as NSI may be flavor nondiagonal. Furthermore, these states are not necessarily the same in the source and at the detector as the physical processes involved may be different in these two places. We express these states in the following way [19]:

$$|\nu^s_\alpha\rangle = |\nu_\alpha\rangle + \varepsilon^s_{\alpha\beta}|\nu_\beta\rangle,$$
$$\langle\nu^d_\beta| = \langle\nu_\beta| + \varepsilon^d_{\alpha\beta}\langle\nu_\alpha|, \quad (2)$$

where the superscripts s and d refer to the source and the detector, respectively. The matrices ε^s and ε^d, which parametrize the effect of NSI, are in general different. Their elements are defined through the parameters $\varepsilon^{ff',C}_{\alpha\beta}$ appearing in the CC Lagrangian given in Eq. (1), depending on the processes the neutrino production and detection are based on.

The current experimental upper bounds for the source and detection NSI parameters $\varepsilon^{s,d}_{\alpha\beta}$ are given e.g. in [22], and they range from 0.013 to 0.078. In the following we will assume that $\varepsilon^{s,d}_{\alpha\beta}$ vanish, in other words, we assume that the effects of NSI on the production and detection of neutrinos is negligible and concentrate on the possible NSI effects on neutrinos propagating in matter.

Concerning the propagation in matter, NSI could contribute to the coherent forward scattering of neutrinos in the Earth's crust. The effective Hamiltonian describing the time evolution of a neutrino state would take the form

$$H = \frac{1}{2E_\nu}[U\,\mathrm{diag}(m_1^2, m_2^2, m_3^2)U^\dagger + \mathrm{diag}(A, 0, 0) + A\varepsilon^m], \quad (3)$$

where E_ν is the energy of the neutrino. The matrix ε^m parametrizes the NSI effects (the superscript m stands for matter), U is the ordinary neutrino mixing matrix, m_i are masses of the three active neutrinos. The elements of the matrix ε^m, denoted by $\varepsilon^m_{\alpha\beta}$, $\alpha, \beta = e, \mu, \tau$, are determined by the neutral current NSI parameters $\varepsilon^{f,C}_{\alpha\beta}$ through the equation [19]

$$\varepsilon^m_{\alpha\beta} = \sum_{f,C}\varepsilon^{f,C}_{\alpha\beta}\frac{N_f}{N_e}. \quad (4)$$

The effective matter potential, including both the SM and NSI matter effects, is given by the matrix

$$V = A\begin{pmatrix} 1+\varepsilon^m_{ee} & \varepsilon^m_{e\mu} & \varepsilon^m_{e\tau} \\ \varepsilon^{m*}_{e\mu} & \varepsilon^m_{\mu\mu} & \varepsilon^m_{\mu\tau} \\ \varepsilon^{m*}_{e\tau} & \varepsilon^{m*}_{\mu\tau} & \varepsilon^m_{\tau\tau} \end{pmatrix}. \quad (5)$$

The effective Hamiltonian can be then written as

$$H = \frac{1}{2E_\nu}\left[U\begin{pmatrix} 0 & 0 & 0 \\ 0 & \Delta m^2_{21} & 0 \\ 0 & 0 & \Delta m^2_{31} \end{pmatrix}U^\dagger + V\right]. \quad (6)$$

The probability of the transition $\nu^s_\alpha \to \nu^d_\beta$ is given by

TABLE II. Current experimental limits of the matter NSI parameters [22], and the expected limits from benchmark setup with different detector masses at $\delta_{CP} = \pi/2$. All limits are at 90% confidence limit.

Parameter	Experimental limit	20 kt	50 kt	70 kt	150 kt
$\lvert\varepsilon^m_{ee}\rvert$	<4.2	<0.28	<0.18	<0.16	<0.084
$\lvert\varepsilon^m_{e\mu}\rvert$	<0.33	<0.040	<0.025	<0.022	<0.018
$\lvert\varepsilon^m_{e\tau}\rvert$	<3.0	<0.028	<0.021	<0.019	<0.015
$\lvert\varepsilon^m_{\mu\mu}\rvert$	<0.068	<0.10	<0.063	<0.056	<0.040
$\lvert\varepsilon^m_{\mu\tau}\rvert$	<0.33	<0.013	<0.008	<0.007	<0.005
$\lvert\varepsilon^m_{\tau\tau}\rvert$	<21	<0.10	<0.063	<0.056	<0.040

$$P_{\nu^s_\alpha \to \nu^d_\beta} = |\langle \nu^d_\beta | e^{-iHL} | \nu^s_\alpha \rangle|^2, \tag{7}$$

where L is the baseline length. One can extract bounds on the NSI parameters by confronting this theoretical expression with the results of oscillation experiments. The current bounds on the parameters describing the matter-induced NSI effects, as quoted in [22], are given in Table II, in the column experimental bounds.

III. NUMERICAL SIMULATIONS

We study numerically how the future neutrino oscillation experiments would constrain various NSI parameters. We will concentrate here on the future long baseline neutrino experiments, using the LBNO setup with a high-intensity beam, a baseline of 2300 km and 20 kt double-phase liquid argon detector as our benchmark, see Table III. The analysis is done by using the GLoBES simulation software [23–26].

GLoBES calculates the oscillation probabilities and the corresponding neutrino rates for any given set of oscillation parameter values. The standard set of the software simulates the neutrino propagation from source to detector and computes the standard matter interactions (SI) for the distance that neutrinos travel. A software extension then allows us to perform the same calculation but also includes all matter-induced NSI effects in the propagation. The software computes χ^2 distributions to compare different sets of oscillation parameter values. We determine the 90% CL upper bounds for $\varepsilon^m_{\alpha\beta}$ by evaluating the NSI discovery potential, that is, the sensitivity to rule out SI in favor of NSI. The nonobservation of NSI then allows us to set new 90% CL limits for $\varepsilon^m_{\alpha\beta}$.

TABLE III. The benchmark values of various experimental parameters used in the numerical calculations.

Runtime ($\nu + \bar{\nu}$ years)	$5 + 5$
LAr detector mass (kt)	20
Neutrino beam power (MW)	0.75
POT (1/year)	1.125×10^{20}
Baseline length (km)	2288
Energy resolution function	$0.15\sqrt{E}$
Energy window (GeV)	0.1–10
Bin width (GeV)	0.2
Bins	50

The NSI discovery potential is calculated as follows. The χ^2 distributions are calculated from both SI and NSI theories. The SI value $\chi^2_{\rm SI}$ is computed by assuming the standard three-neutrino mixing parameters, and setting all NSI parameters in Eq. (5) to zero. The NSI values $\chi^2_{\rm NSI}$, on the other hand, are defined by assigning one $\varepsilon^m_{\alpha\beta}$ parameter with a nonzero value. The $\Delta\chi^2$ value is then obtained from the difference between the two χ^2 values:

$$\Delta\chi^2 = \chi^2_{\rm SI} - \chi^2_{\rm NSI}. \tag{8}$$

The 90% confidence level is hence obtained at $\Delta\chi^2 = 2.71$. We take the standard oscillation parameter values from the current best fits as determined from global analysis of experimental data [27]. The best-fit values and their 1σ errors are presented in Table I.

For each δ_{CP} value, we have calculated the $\Delta\chi^2$ value in a baseline range 100–5000 km and $\log_{10}|\varepsilon^m_{\alpha\beta}|$ range from -3.0 to -0.5. In every case, a 90% confidence level contour is found and the results merged in a contour band. The bands in $(L, \varepsilon^m_{\alpha\beta})$-plane are plotted in Fig 1.

The vertical width of the band corresponds to the strength of correlation between $\varepsilon^m_{\alpha\beta}$ and δ_{CP}. Immediately we observe that the discovery potentials reach their maximums at ~2000 km baseline. This tells us that the LBNO setup used in our numerical studies, with the baseline of 2300 km, which is close to optimal for the detection of the neutrino mass hierarchy and the leptonic CP violation, is also suitable for the NSI studies. Note that this maximum is specific for our benchmark setup: other sources will imply the maximum to be at a different baseline. However, there are common features for all setups: for example, the discovery potential is greatly reduced at shorter baselines. Correlation between δ_{CP} and NSI parameters is notable for $|\varepsilon^m_{e\mu}|$ and $|\varepsilon^m_{e\tau}|$.

Other parameters have only weak or nonexistent correlation, which results in the narrow bands in Fig. 1. We find that for the cases of normal and inverted mass hierarchy, there is only little difference in the confidence limits, and thus the corresponding plots for inverted hierarchy would be almost identical. We have taken all $\varepsilon_{\alpha\beta}$ to be real, and kept only δ_{CP} as a CP-violating phase. Letting the off-diagonal NSI parameters to be complex would widen the bands for $|\varepsilon^m_{e\mu}|$, $|\varepsilon^m_{e\tau}|$, and $|\varepsilon^m_{\mu\tau}|$. Some effects of nonzero $\epsilon^m_{\alpha\beta}$ phases were studied in [28].

We have given the expected model independent bounds for NSI parameters for our benchmark setup in Table II. Increasing the neutrino energy for this baseline does not increase significantly the sensitivity for matter NSI, as was observed in [29]. We have studied the effect of increasing

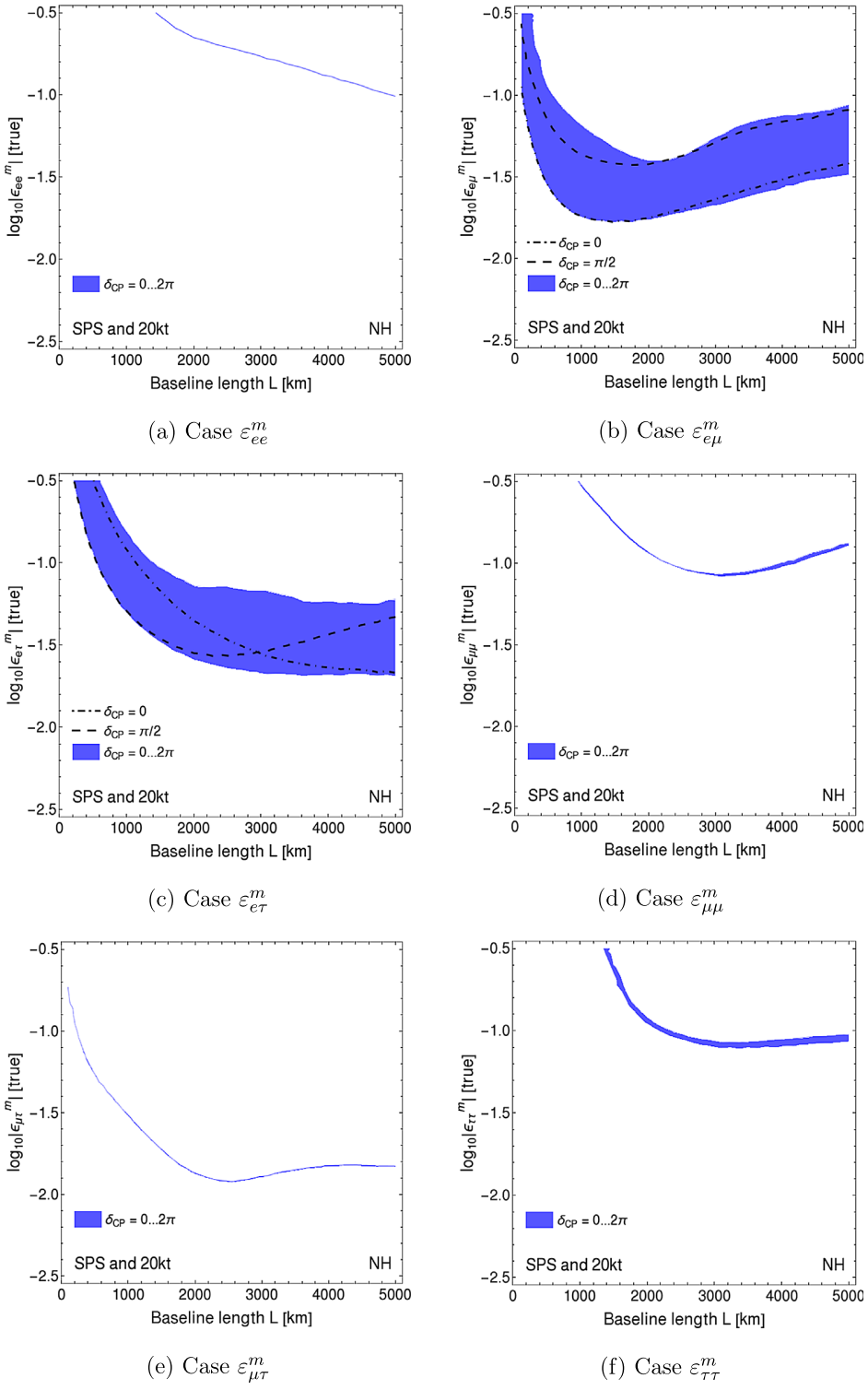

(a) Case ε^m_{ee} (b) Case $\varepsilon^m_{e\mu}$

(c) Case $\varepsilon^m_{e\tau}$ (d) Case $\varepsilon^m_{\mu\mu}$

(e) Case $\varepsilon^m_{\mu\tau}$ (f) Case $\varepsilon^m_{\tau\tau}$

FIG. 1. 90% confidence limit discovery reach of NSI parameters as a function of baseline length. Band thickness corresponds to the strength of correlation between δ_{CP} and $\varepsilon^m_{\alpha\beta}$.

the LAr detector mass, while keeping all the other parameters of the benchmark setup as previously. In addition to 20 kt, the expected bounds have been given also for several other detector masses. Comparing with the present experimental bounds for the NSI parameters [22], see Table II, it is seen that with the benchmark setup, it is possible to significantly improve constraints for several NSI parameters.

However, one should notice that for large detector masses, the limits on various NSI parameters become so stringent that the detector and source NSI parameter bounds are of the same order, and for a precise limit those should be considered as well. Thus the bounds given for larger detector masses are only indicative.

IV. CORRELATION BETWEEN THE *CP* ANGLE AND NSI PARAMETERS

Let us now investigate analytically the correlation between the CP angle δ and the various NSI parameters $\varepsilon^m_{\ell\ell'}$ in the transition probabilities $P(\nu_\ell \to \nu_{\ell'}) \equiv P_{\ell\ell'}$, where $\ell, \ell' = e, \mu, \tau$.

The transition amplitude for $\nu_\ell \to \nu_{\ell'}$ is given by

$$A(\nu_\ell \to \nu_{\ell'}) \equiv A_{\ell\ell'} = \sum_{j,k=1}^{3} \frac{L}{2E_\nu} U_{\ell j} H_{jk} (U^\dagger)_{k\ell'} \quad (9)$$

and the transition probability correspondingly by

$$P_{\ell\ell'} = |A_{\ell\ell'}|^2 = \left| \sum_{j,k=1}^{3} \frac{L}{2E_\nu} U_{\ell j} H_{jk} (U^\dagger)_{k\ell'} \right|^2. \quad (10)$$

We keep all the oscillation angles θ_{ij} and mass squared differences Δm^2_{ij} fixed to their best-fit values, given in Table I, and treat the CP-violating phase $\delta = \delta_{CP}$ and the NSI parameters $\varepsilon^m_{\ell\ell'}$, the latter one at the time, as the only variables.

The approximative expressions for the amplitudes $A_{\ell\ell'}$ are in general of the form

$$\frac{2E_\nu}{L} A_{\ell\ell'} = N_{\ell\ell'} + K_{\ell\ell'} e^{-i\delta} \quad (11)$$

for appearance processes ($\ell \neq \ell'$) and

$$\frac{2E_\nu}{L} A_{\ell\ell} = N_{\ell\ell} + K_{\ell\ell} \cos\delta \quad (12)$$

for disappearance processes. The expressions are accurate to first power in s_{13} and $\varepsilon^m_{\ell\ell'}$. An exception to these rules is the transition $\nu_\mu \to \nu_\tau$, for which we obtain

$$\frac{2E_\nu}{L} A_{\mu\tau} = N_{\mu\tau} + K^{(-)}_{\mu\tau} e^{-i\delta} + K^{(c)}_{\mu\tau} \cos\delta. \quad (13)$$

In Eqs. (11), (12) and (13) the dependence on the NSI parameters and neutrino mixing angles and squared mass differences are given in terms of the functions $N_{\ell\ell}$, $N_{\ell\ell'}$, $K_{\ell\ell}$ and $K_{\ell\ell'}$, which are defined in Table IV. In these functions, the relevant NSI parameter $\varepsilon^m_{\ell\ell}$ or $\varepsilon^m_{\ell\ell'}$, as well as $\sin\theta_{31}$, are taken into account to the first order. Similar expressions are calculated in [26].

Let us consider the $\nu_e \to \nu_\mu$ transition. For the amplitude of this process we obtain the expression

$$\begin{aligned}\frac{2E_\nu}{L} A_{e\mu} &= A c_{12} c_{13} (-s_{12} c_{23} - s_{23} s_{13} e^{-i\delta}) \\ &\quad + s_{12} c_{13} \Delta m^2_{21} (c_{12} c_{23} - s_{12} s_{13} s_{23} e^{-i\delta}) \\ &\quad + s_{13} e^{-i\delta} (\Delta m^2_{31} s_{23} c_{13}) \\ &\quad + A c_{12} c_{13} \varepsilon^m_{e\mu} (c_{12} c_{23} - s_{12} s_{23} s_{13} e^{-i\delta}) \\ &\quad + A s_{12} c_{13} \varepsilon^m_{e\mu} (-s_{12} c_{23} - s_{23} s_{13} e^{-i\delta}) + O(s^2_{13}) \\ &\equiv N_{e\mu} + K_{e\mu} e^{-i\delta} + O(s^2_{13}), \end{aligned} \quad (14)$$

where we have denoted $s_{ij} \equiv \sin\theta_{ij}$ and $c_{ij} \equiv \cos\theta_{ij}$ ($i, j = 1, 2, 3$). We find the transition probability to have the structure

$$P_{e\mu} \propto N^2_{e\mu} + K^2_{e\mu} + 2 N_{e\mu} K_{e\mu} \cos\delta. \quad (15)$$

The effect of the CP-violating angle δ becomes evident when we evaluate the values of the functions $N_{e\mu}$ and $K_{e\mu}$ for some value of the NSI parameter $\varepsilon^m_{e\mu}$. E.g. for $\varepsilon^m_{e\mu} = 10^{-3}$, we get

$$P_{e\mu} \propto (1.56 - 1.22 \cos\delta) \times 10^{-7}. \quad (16)$$

It is seen that varying δ causes large variation in the transition probability $P_{e\mu}$. Thereby it strongly interferes with the determination of the NSI parameter $\varepsilon^m_{e\mu}$. The wide band in the numerical plot of Fig. 1(b) is explained, since the plot is obtained by allowing δ to vary in the range 0 to 2π. Similarly we find in the case of $P_{e\tau}$ that $P_{e\tau} \propto (1.32 + 1.08 \cos\delta) \times 10^{-7}$, and again a wide band is caused by variation of δ.

Let us next consider the probability of the transition $\nu_\tau \to \nu_\tau$ for comparison. One can show that the dependence on the CP angle is in this case of the form

$$P_{\tau\tau} \propto N^2_{\tau\tau} + K^2_{\tau\tau} \cos^2\delta - 2 N_{\tau\tau} K_{\tau\tau} \cos\delta. \quad (17)$$

Taking here $\varepsilon^m_{\tau\tau} = 10^{-3}$, we find

$$P_{\tau\tau} \propto (3.200 + 0.120 \cos\delta + 0.001 \cos^2\delta) \times 10^{-6}. \quad (18)$$

Hence, the transition probability $P_{\tau\tau}$ has significantly smaller dependence on the CP angle than the transition probability $P_{e\mu}$. This is seen in the discovery reach plot of the NSI parameter $\varepsilon^m_{\tau\tau}$ in Fig. 1(f), where the CP variation band is much narrower than the corresponding band in the case of the $\nu_e \to \nu_\mu$ transition in Fig. 1(b).

Similarly as in the cases considered above, one can qualitatively understand the CP angle dependence of the discovery reach plots of all the other NSI parameters $\varepsilon^m_{\ell\ell'}$

TABLE IV. The expressions of the functions $K_{\ell\ell'}$ and $N_{\ell\ell'}$, where $\varepsilon^m_{\ell\ell'} \ll 1$ is assumed.

Function	Expression
$K_{e\mu}$	$(-Ac_{12}c_{13}s_{23} - s^2_{12}c_{13}\Delta m^2_{21}s_{23} + \Delta m^2_{31}s_{23}c_{13} - Ac_{13}\varepsilon^m_{e\mu}(c_{12}+1)s_{12}s_{23})s_{13}$
$N_{e\mu}$	$-Ac_{12}c_{13}s_{12}c_{23} + s_{12}c_{13}\Delta m^2_{21}c_{12}c_{23} + Ac_{13}c_{23}\varepsilon^m_{e\mu}(c^2_{12} - s^2_{12})$
K_{ee}	0
N_{ee}	$A(1+\varepsilon^m_{ee})c^2_{12}c^2_{13} + \Delta m^2_{21}s^2_{12}c^2_{13} + \Delta m^2_{31}s^2_{13}$
$K_{e\tau}$	$(-Ac^2_{12}c_{13}c_{23} - \Delta m^2_{21}s^2_{12}c_{13}s_{23} + A\varepsilon^m_{e\tau}s_{13}s_{23} + c_{23}c_{13}\Delta m^2_{31})s_{13}$
$N_{e\tau}$	$Ac_{12}c_{13}(s_{12}s_{23} + \varepsilon^m_{e\tau}c_{23}c_{13}) - \Delta m^2_{21}s_{12}c_{13}c_{12}c_{23}$
$K_{\mu\mu}$	$2s_{12}s_{13}s_{23}c_{12}c_{23}((1-\varepsilon^m_{\mu\mu})A - \Delta m^2_{21})$
$N_{\mu\mu}$	$A(s^2_{12}c^2_{23} + c^2_{12}s^2_{23}s^2_{13}) + (\Delta m^2_{21} + A\varepsilon^m_{\mu\mu})(c^2_{12}c^2_{23} + s^2_{12}s^2_{23}s^2_{13}) + \Delta m^2_{31}s^2_{23}c^2_{13}$
$K_{\tau\tau}$	$\Delta m^2_{21}(c^2_{12}s^2_{23} + s^2_{12}c^2_{23}s^2_{13} + 2c_{12}s_{23}s_{12}c_{23}s_{13}) - 2As_{12}s_{23}c_{12}c_{23}s_{13}$
$N_{\tau\tau}$	$A(s^2_{12}s^2_{23} + c^2_{12}c^2_{23}s^2_{13}) + (\Delta m^2_{31} + A\varepsilon^m_{\tau\tau})c_{23}c_{13}$
$N_{\mu\tau}$	$-s^2_{12}s_{23}c_{23}A + \Delta m^2_{21}s_{23}c_{23}(-c^2_{12} + s^2_{12}s^2_{13}) + s_{23}c^2_{13}\Delta m^2_{31}c_{23} + A\varepsilon^m_{\mu\tau}c_{12}c_{13}(c^2_{23} - s^2_{23})$
$K^{(c)}_{\mu\tau}$	$-4A\varepsilon^m_{\mu\tau}s_{12}s_{13}s_{23}c_{13}c_{23} + 2s^2_{23}\Delta m^2_{21}s_{12}s_{13}c_{12} - 2s^2_{23}As_{12}s_{13}c_{12}$
$K^{(-)}_{\mu\tau}$	$-\Delta m^2_{21}s_{12}s_{13}c_{12} + As_{12}s_{13}c_{12}$

shown in Fig. 1. As seen in the plots, there are two transitions, where the effect of the CP angle δ on the determination of the NSI parameters is much larger than in the rest of the transitions, namely the $\nu_e \to \nu_\mu$ and $\nu_e \to \nu_\tau$. Note in particular that $K_{ee}(\varepsilon) = 0$, meaning that survival probability P_{ee} is independent of δ_{CP}.

We have elaborated the effect of the CP angle on the experimental reach of the NSI parameters further in Fig. 2. There we have plotted the relative variation of the discovery reach as a function of the NSI parameter for different transitions for the CP angle δ varying in the range 0 to 2π.

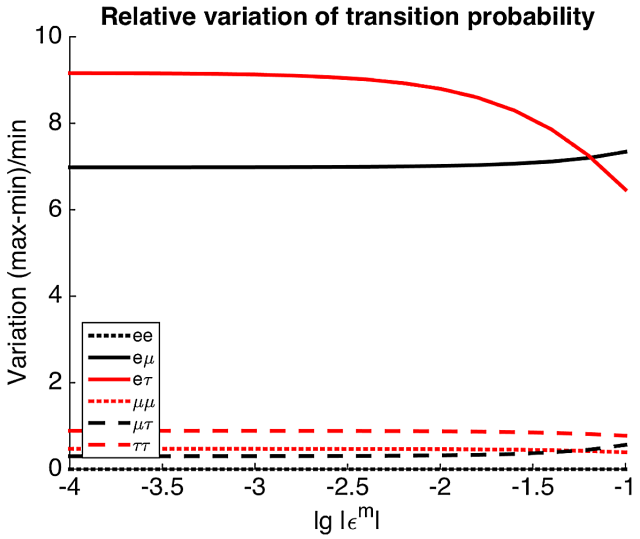

FIG. 2. Relative variation R of six different matter NSI parameter as a function of $\log_{10}|\varepsilon^m_{\ell\ell'}|$. The CP angle δ is varied in the range $(0,2\pi)$.

More precisely, the curves plotted present, as a function of the relevant NSI parameter $\varepsilon^m_{\ell\ell'}$, the quantities

$$R \equiv \frac{P^{\max}_{\ell\ell'} - P^{\min}_{\ell\ell'}}{P^{\min}_{\ell\ell'}}, \tag{19}$$

where $P^{\max}_{\ell\ell'}$ and $P^{\min}_{\ell\ell'}$ are, respectively, the largest and the smallest value the transition probability achieves when δ_{CP} varies in the range 0 to 2π for a given value of $\varepsilon^m_{\ell\ell'}$. The magnitude of the variation is approximately constant when $\log_{10}|\varepsilon^m| < -2.5$ for all parameters. For an example value of $\varepsilon^m_{\ell\ell'}$, the variation with respect to CP angle as a function of energy was considered in [30,31].

V. SUMMARY

We have investigated the prospects of long baseline neutrino experiments to probe the possible existence of the nonstandard neutrino interactions, or NSI, using the LBNO setup as our benchmark. We have neglected the effects of NSI at the source or detector and taken into account only the effects during neutrinos traveling in the Earth's crust. This is justified, because the bounds on the source and detector NSI are about an order of magnitude stricter than on matter NSI [22,32]. It is found that the discovery sensitivity depends on the baseline length, the best sensitivity for this experimental setup being achievable at about 2000 km. We also found that the CP angle δ quite severely interferes with the NSI search in the $\nu_\mu \leftrightarrow \nu_e$ and $\nu_\tau \leftrightarrow \nu_e$ transitions, while in all the other transitions the effect is negligible. The most sensitive probe would be the $\nu_\mu \leftrightarrow \nu_e$ and $\nu_\mu \leftrightarrow \nu_\tau$ transitions. In the former channel one would

be able to limit the value of the NSI parameter ε^m below 0.02, if the CP angle is close to $\delta_{CP} = \pi/2$, for other values of δ the achievable bound is less stringent. In the case of the $\nu_\mu \leftrightarrow \nu_\tau$ channel the sensitivity is 0.01 independently of the value of δ. In both cases the most stringent limit requires the baseline to exceed 2000 km.

The role of baseline length in studying matter NSI effects can be demonstrated by comparing the potential of T2HK [33] and DUNE [34] whose abilities to constrain ε^m have been studied in [32,35–37]. It is shown in these studies that the 295-km-long T2HK experiment provides significantly lower sensitivity to constrain $\varepsilon^m_{\alpha\beta}$ than the 1300-km-long DUNE project. Similarly, the benchmark setup used in this work with 2300-km-long baseline improves the sensitivity compared to DUNE even with the 20 kt detector mass. Comparing the baseline length using otherwise our benchmark setup shows that for each NSI parameter, there is an optimal baseline length which also depends on the CP-violating phase.

ACKNOWLEDGMENTS

K. H. acknowledges the H2020-MSCA-RICE-2014 Grant No. 645722 (NonMinimalHiggs). T. K. expresses his gratitude to the Magnus Ehrnrooth foundation for financial support.

[1] C. K. Jung, C. McGrew, T. Kajita, and T. Mann, Annu. Rev. Nucl. Part. Sci. **51**, 451 (2001).
[2] T. Kajita and Y. Totsuka, Rev. Mod. Phys. **73**, 85 (2001).
[3] Q. R. Ahmad *et al.* (SNO Collaboration), Phys. Rev. Lett. **87**, 071301 (2001).
[4] R. Davis, Jr., D. S. Harmer, and K. C. Hoffman, Phys. Rev. Lett. **20**, 1205 (1968).
[5] R. Wendell *et al.* (Super-Kamiokande Collaboration), Phys. Rev. D **81**, 092004 (2010).
[6] P. Adamson *et al.* (MINOS Collaboration), Phys. Rev. Lett. **110**, 251801 (2013).
[7] K. Abe *et al.* (T2K Collaboration), Phys. Rev. Lett. **112**, 181801 (2014).
[8] P. Adamson *et al.* (MINOS Collaboration), Phys. Rev. Lett. **110**, 171801 (2013).
[9] K. Abe *et al.* (T2K Collaboration), Phys. Rev. Lett. **112**, 061802 (2014).
[10] A. Stahl *et al.*, Report No. CERN-SPSC-2012-021, 2012.
[11] L. Agostino *et al.*, arXiv:1409.4405.
[12] K. Bora, G. Ghosh, and D. Dutta, arXiv:1511.02452.
[13] S. Ahmed *et al.* (ICAL Collaboration), arXiv:1505.07380.
[14] F. An *et al.* (JUNO Collaboration), J. Phys. G **43**, 030401 (2016).
[15] C. R. Das, J. Maalampi, J. Pulido, and S. Vihonen, J. High Energy Phys. 02 (2015) 048.
[16] J. Bergstrom, M. C. Gonzalez-Garcia, M. Maltoni, and T. Schwetz, J. High Energy Phys. 09 (2015) 200.
[17] M. C. Gonzalez-Garcia, M. Maltoni, and T. Schwetz, J. High Energy Phys. 11 (2014) 052.
[18] O. G. Miranda and H. Nunokawa, New J. Phys. **17**, 095002 (2015).
[19] T. Ohlsson, Rep. Prog. Phys. **76**, 044201 (2013).
[20] I. Girardi, D. Meloni, and S. T. Petcov, Nucl. Phys. **B886**, 31 (2014).
[21] Y. Grossman, Phys. Lett. B **359**, 141 (1995).
[22] C. Biggio, M. Blennow, and E. Fernandez-Martinez, J. High Energy Phys. 08 (2009) 090.
[23] P. Huber, M. Lindner, and W. Winter, Comput. Phys. Commun. **167**, 195 (2005).
[24] P. Huber, J. Kopp, M. Lindner, M. Rolinec, and W. Winter, Comput. Phys. Commun. **177**, 432 (2007).
[25] J. Kopp, Int. J. Mod. Phys. C **19**, 523 (2008).
[26] J. Kopp, M. Lindner, T. Ota, and J. Sato, Phys. Rev. D **77**, 013007 (2008).
[27] D. V. Forero, M. Tortola, and J. W. F. Valle, Phys. Rev. D **90**, 093006 (2014).
[28] D. V. Forero and P. Huber, arXiv:1601.03736.
[29] R. Adhikari, A. Dasgupta, and Z. Rahman, arXiv:1204.1750.
[30] A. Friedland and I. M. Shoemaker, arXiv:1207.6642.
[31] M. Masud, A. Chatterjee, and P. Mehta, arXiv:1510.08261.
[32] J. Liao, D. Marfatia, and K. Whisnant, arXiv:1601.00927.
[33] K. Abe *et al.* (Hyper-Kamiokande Proto-Collaboration), Prog. Theor. Exp. Phys. (**2015**), 053C02.
[34] R. Acciarri *et al.* (DUNE Collaboration), arXiv:1512.06148.
[35] M. Bass *et al.* (LBNE Collaboration), Phys. Rev. D **91**, 052015 (2015).
[36] P. Coloma, J. High Energy Phys. 03 (2016) 016..
[37] A. de Gouvêa and K. J. Kelly, arXiv:1511.05562.

Publication V

V

K. Huitu, T. J. Kärkkäinen, J. Maalampi and S. Vihonen,
The effects of triplet Higgs bosons in long baseline neutrino experiments,
Phys. Rev. D **97** (2018) no.9, 095037,
arXiv:1711.02971 [hep-ph]

Effects of triplet Higgs bosons in long baseline neutrino experiments

K. Huitu[*] and T. J. Kärkkäinen[†]

Department of Physics, and Helsinki Institute of Physics, P. O. Box 64, FI-00014 University of Helsinki, Finland

J. Maalampi[‡] and S. Vihonen[§]

University of Jyvaskyla, Department of Physics, P.O. Box 35, FI-40014 University of Jyvaskyla, Finland

(Received 22 November 2017; published 29 May 2018)

The triplet scalars $(\Delta = \Delta^{++}, \Delta^{+}, \Delta^{0})$ utilized in the so-called type-II seesaw model to explain the lightness of neutrinos, would generate nonstandard interactions (NSI) for a neutrino propagating in matter. We investigate the prospects to probe these interactions in long baseline neutrino oscillation experiments. We analyze the upper bounds that the proposed DUNE experiment might set on the nonstandard parameters and numerically derive upper bounds, as a function of the lightest neutrino mass, on the ratio the mass M_Δ of the triplet scalars, and the strength $|\lambda_\phi|$ of the coupling $\phi\phi\Delta$ of the triplet Δ and conventional Higgs doublet ϕ. We also discuss the possible misinterpretation of these effects as effects arising from a nonunitarity of the neutrino mixing matrix and compare the results with the bounds that arise from the charged lepton flavor violating processes.

DOI: 10.1103/PhysRevD.97.095037

I. INTRODUCTION

The discovery of neutrino oscillations in atmospheric and solar neutrino measurements [1,2] proved that the $\mathrm{SU(2)_L \times U(1)_Y}$ Standard Model (SM) is not capable to fully explain the particle physics world. The existence of oscillations indicates that neutrinos are massive particles, in contrast with the prediction of the SM. One has to go beyond the SM in order to discover the origin of neutrino masses. At the same time, one has to find a convincing explanation for the lightness of neutrinos as compared with the other basic particles, i.e., quarks and charged leptons. The most popular answer to the latter question is the so-called seesaw mechanism [3–7], where the suppression of neutrino masses follows from the existence of a new mass scale much higher than the electroweak scale $\mathcal{O}(10^2)$ GeV. In the type-I seesaw mechanism, the new mass scale is set by sterile right-handed neutrinos by which the particle content of the SM is extended. The type-II seesaw mechanism is based on the existence of a set of new scalars $\Delta = (\Delta^{++}, \Delta^{+}, \Delta^{0})$ transforming as a triplet under the $\mathrm{SU(2)_L}$ gauge symmetry. The masses of neutrinos are proportional to the ratio $\lambda_\phi v^2/M_\Delta^2$, where $v \simeq 174$ GeV is the vacuum expectation value of the SM Higgs field ϕ, M_Δ is the mass of triplet scalar, and λ_ϕ is the dimensionful strength of the $\phi\phi\Delta$ coupling.

While the seesaw mechanism itself cannot be experimentally verified, the extension of the SM it is based on generally leads to experimentally testable phenomena. For example, the doubly charged scalar Δ^{++} would have clear experimental signatures, e.g., in high-energy proton-proton collision experiments [8–13]. One theoretical framework where a scalar triplet, as well as right-handed neutrinos, naturally appear is the left-right symmetric electroweak model based on the gauge symmetry $\mathrm{SU(3)_C \times SU(2)_L \times SU(2)_R \times U(1)_{B-L}}$ [14–18].

In this paper, we will concentrate on the type-II seesaw mechanism and investigate how the triplet scalar bosons Δ would affect neutrino propagation in matter (for earlier studies, see, e.g., [19]) and how these effects could be probed in long baseline neutrino experiments, particularly in the planned DUNE. Applying the bounds derived for DUNE in Ref. [20], together with the constraints one has for the elements of the neutrino mass matrix from earlier oscillation experiments, we compute an upper limit of the ratio $M_\Delta/|\lambda_\phi|$ as a function of the absolute neutrino mass scale (the mass m_1 of the lightest neutrino). For comparison, we also compute the upper bound for this ratio using the existing constraints on the charged lepton flavor violation (CLFV) processes.

[*]katri.huitu@helsinki.fi
[†]timo.j.karkkainen@helsinki.fi
[‡]jukka.maalampi@jyu.fi
[§]sampsa.p.vihonen@student.jyu.fi

II. NONSTANDARD INTERACTIONS AND NEUTRINO MASSES IN A TRIPLET MODEL

Our theoretical framework is the $\mathrm{SU}(2)_\mathrm{L} \times U(1)_\mathrm{Y}$ electroweak model added with a scalar triplet field $\Delta = (\Delta_1, \Delta_2, \Delta_3) \sim (\mathbf{3}, 2)$, which can also be understood as a low-energy effective theory of the left-right symmetric $\mathrm{SU}(3)_\mathrm{C} \times \mathrm{SU}(2)_\mathrm{L} \times \mathrm{SU}(2)_\mathrm{R} \times \mathrm{U}(1)_{B-L}$ theory, where all the other nonstandard degrees of freedom except the triplet scalar are so heavy that they do not have observable effects in the oscillation experiments. The interactions of the triplet Δ relevant for the neutrino oscillation are described with the following Lagrangian:

$$\mathcal{L}_\Delta = Y_{\alpha\beta} L^T_{\alpha L} C i\sigma_2 \Delta L_{\beta L} + \lambda_\phi \phi^T i\sigma_2 \Delta^\dagger \phi + \mathrm{H.c.}, \quad (1)$$

where $Y_{\alpha\beta}$ ($\alpha, \beta = e, \mu, \tau$) are Yukawa coupling constants, C is the charge conjugation operator, ϕ is the SM Higgs doublet, and the triplet Δ is presented in the 2×2 matrix form

$$\Delta = \frac{1}{\sqrt{2}} \sigma_i \Delta_i = \begin{pmatrix} \frac{\Delta^+}{\sqrt{2}} & \Delta^{++} \\ \Delta^0 & -\frac{\Delta^+}{\sqrt{2}} \end{pmatrix}, \quad (2)$$

where σ_i are the Pauli matrices. When written in terms of component fields, Eq. (1) takes the form

$$\mathcal{L}_Y = Y_{\alpha\beta} \left[\Delta^0 \overline{\nu^C_{\alpha R}} \nu_{\beta L} - \frac{1}{\sqrt{2}} \Delta^+ (\overline{\ell^C_{\alpha R}} \nu_{\beta L} + \overline{\nu^C_{\alpha R}} \ell_{\beta L}) - \Delta^{++} \overline{\ell^C_{\alpha R}} \ell_{\beta L} \right] + \mathrm{H.c.} \quad (3)$$

These interactions lead in the second order of perturbation theory to the four-fermion interactions presented in the Fig. 1. The amplitude presented in Fig. 1(a) gives rise to Majorana mass terms for the neutrinos when the $\mathrm{SU}(2)_\mathrm{L} \times \mathrm{U}(1)_\mathrm{Y}$ symmetry is spontaneously broken, while the amplitudes in Figs. 1(b) and 1(c) correspond to new, nonstandard interactions among leptons. In the limit, where the mass of the triplet scalars M_Δ, assumed to be the same for all members of the triplet, is large compared with the momenta of the processes, the amplitudes are described by the following effective Lagrangians [19]:

$$\mathcal{L}^m_\nu = \frac{Y_{\alpha\beta} \lambda_\phi v^2}{M^2_\Delta} \left(\overline{\nu^C_{\alpha R}} \nu_{\beta L} \right) = -\frac{1}{2} (m_\nu)_{\alpha\beta} \overline{\nu^C_{\alpha R}} \nu_{\beta L}, \quad (4)$$

$$\mathcal{L}_\mathrm{NSI} = \frac{Y_{\sigma\beta} Y^\dagger_{\alpha\rho}}{M^2_\Delta} (\overline{\nu_{\alpha L}} \gamma_\mu \nu_{\beta L}) (\overline{\ell_{\rho L}} \gamma^\mu \ell_{\sigma L}), \quad (5)$$

where m_ν is the neutrino mass matrix, M_Δ is the degenerate mass of the Δ particles, and v is the vacuum expectation value of the SM scalar Higgs field. The connection to the effective field theory can be derived by solving the Yukawa coupling $Y_{\alpha\beta}$ from the Majorana mass term in Eq. (4) and inserting it to the neutrino matter NSI term in Eq. (5). Comparing the result with the effective NSI Lagrangian

$$\mathcal{L}_\mathrm{NSI} = -2\sqrt{2} G_F \varepsilon^{f f' C}_{\alpha\beta} (\bar{\nu}_{\alpha L} \gamma^\mu \nu_{\beta L}) (\bar{f} \gamma_\mu P_C f'), \quad (6)$$

where P_C is chiral projection operator ($C = L, R$), G_F is Fermi coupling constant, f, f' are any fermions, $\alpha, \beta = e, \mu, \tau$, and allowing only left-handed lepton terms (since Δ is leptophilic), one obtains the following expression for the nonstandard interaction parameters:

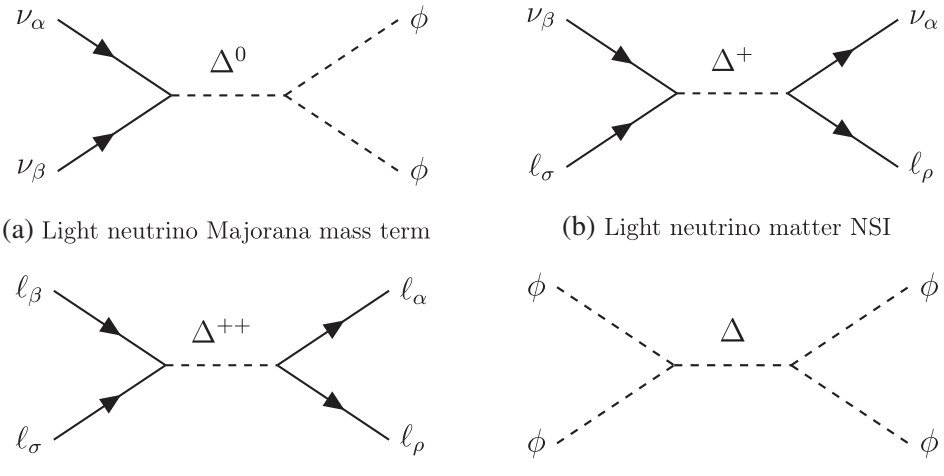

(a) Light neutrino Majorana mass term

(b) Light neutrino matter NSI

(c) Four-lepton NSI

(d) SM Higgs self-coupling

FIG. 1. Tree level Feynman diagrams for interactions between neutrinos ν, leptons ℓ, and the Standard Model Higgs scalar ϕ, are mediated by the triplet Higgs fields Δ.

$$\varepsilon_{\alpha\beta}^{\rho\sigma} = -\frac{M_\Delta^2}{8\sqrt{2}G_F v^4 \lambda_\phi^2}(m_\nu)_{\sigma\beta}(m_\nu^\dagger)_{\alpha\rho}, \tag{7}$$

where α, β, ρ, and σ are flavor indices. The expression (7) indicates the larger the ratio $M_\Delta^2/\lambda_\phi^2$, the stronger are the nonstandard interactions of light neutrinos. Conversely, stricter bounds on $\varepsilon_{\alpha\beta}^{\rho\sigma}$ also mean better constraints on $M_\Delta^2/\lambda_\phi^2$.

III. NONSTANDARD INTERACTIONS AND NONUNITARY MIXING

In the context of long baseline experiments, neutrino oscillations are strongly influenced by matter effects, arising from the charged current (CC) and neutral current (NC) weak interactions of neutrinos with the medium they traverse. In the case of the SM, these interactions take place via an exchange of W and Z bosons. In the framework of our model, the matter effects are also contributed by the charged current interactions mediated by the scalar Δ^+.

In the low energy limit, nonstandard interactions stem from the effective CC- and NC-like Lagrangians, which are given by [21],

$$\begin{aligned}\mathcal{L}_{\rm NSI}^{\rm CC} &= -2\sqrt{2}G_F\varepsilon_{\alpha\beta}^{ff',C}(\bar{\nu}_{L\alpha}\gamma^\mu\nu_{L\beta})(\bar{f}\gamma^\mu P_C f'),\\ \mathcal{L}_{\rm NSI}^{\rm NC} &= -2\sqrt{2}G_F\varepsilon_{\alpha\beta}^{f,C}(\bar{\nu}_{L\alpha}\gamma^\mu\nu_{L\beta})(\bar{f}\gamma^\mu P_C f).\end{aligned} \tag{8}$$

The CC Lagrangian $\mathcal{L}_{\rm NSI}^{\rm CC}$ in Eq. (8) is responsible for the NSI effects involved in the neutrino source and detector. The NC Lagrangian $\mathcal{L}_{\rm NSI}^{\rm NC}$, on the other hand, is relevant for neutrino propagation in matter. In the context of a triplet model, CC interactions arise from Fig. 1(b) at the low energy limit, when $f \neq f'$. The CC Lagrangian, where $f = f'$ is generated also, but such a case corresponds to a NC Lagrangian, and by definition $\varepsilon_{\alpha\beta}^{f,C} \equiv \varepsilon_{\alpha\beta}^{ff,C}$.

Most of the charged current NSI parameters have been studied comprehensively in lepton decay experiments resulting in strict constraints. The current bounds on the CC NSI parameters $\varepsilon_{\alpha\beta}^{ff',C}$, as quoted in Ref. [19], are presented in Table I.

In the future long baseline experiments, the NSI effects become particularly relevant in the neutrino propagation in matter, where they are covered by the effective NC Lagrangian $\mathcal{L}_{\rm NSI}^{\rm NC}$. For previous studies, see [20,23–36]. The effective Hamiltonian takes the form

$$H = \frac{1}{2E_\nu}[U\,\mathrm{diag}(m_1^2, m_2^2, m_3^2)U^\dagger + \mathrm{diag}(A,0,0) + A\varepsilon^m], \tag{9}$$

where E_ν is the energy of the propagating neutrino, U is the light neutrino mixing matrix, and m_1, m_2, and m_3 are the three masses of the active neutrinos.

TABLE I. Constraints on the parameters $\varepsilon_{\alpha\beta}^{\rho\sigma}$ (updated from [19] using [22]) from the $\ell \to \ell\ell\ell$, one-loop $\ell \to \ell\gamma$, and $\mu^+e^- \to \mu^-e^+$ processes. All bounds are given at 90% confidence level.

Decay	Constraint on	Bound
$\mu^- \to e^-e^+e^-$	$\lvert\varepsilon_{ee}^{e\mu}\rvert$	3.5×10^{-7}
$\tau^- \to e^-e^+e^-$	$\lvert\varepsilon_{ee}^{e\tau}\rvert$	1.4×10^{-4}
$\tau^- \to \mu^-\mu^+\mu^-$	$\lvert\varepsilon_{\mu\mu}^{\mu\tau}\rvert$	1.2×10^{-4}
$\tau^- \to e^-\mu^+e^-$	$\lvert\varepsilon_{e\mu}^{e\tau}\rvert$	1.0×10^{-4}
$\tau^- \to \mu^-e^+\mu^-$	$\lvert\varepsilon_{\mu e}^{\mu\tau}\rvert$	1.0×10^{-4}
$\tau^- \to e^-\mu^+\mu^-$	$\lvert\varepsilon_{\mu\mu}^{e\tau}\rvert$	1.0×10^{-4}
$\tau^- \to e^-e^+\mu^-$	$\lvert\varepsilon_{\mu e}^{e\tau}\rvert$	9.9×10^{-5}
$\mu^- \to e^-\gamma$	$\lvert\sum_\alpha \varepsilon_{\alpha\alpha}^{e\mu}\rvert$	2.6×10^{-5}
$\tau^- \to e^-\gamma$	$\lvert\sum_\alpha \varepsilon_{\alpha\alpha}^{e\tau}\rvert$	1.8×10^{-2}
$\tau^- \to \mu^-\gamma$	$\lvert\sum_\alpha \varepsilon_{\alpha\alpha}^{\mu\tau}\rvert$	2.0×10^{-4}
$\mu^+e^- \to \mu^-e^+$	$\lvert\varepsilon_{\mu e}^{\mu e}\rvert$	3.0×10^{-3}

In this formalism, the so-called matter NSI effects are parametrized as

$$\varepsilon_{\alpha\beta}^m = \sum_{f,C}\varepsilon_{\alpha\beta}^{f,C}\frac{N_f}{N_e}, \tag{10}$$

where $\varepsilon_{\alpha\beta}^{f,C}$ are the NSI parameters from the low energy NC Lagrangian of Eq. (8) and N_f/N_e is the fraction of fermions of flavor f over electrons in the medium the neutrino traverses.

The effective matter potential is given by the matrix

$$V = A\begin{pmatrix} \pm 1 + \varepsilon_{ee}^m & \varepsilon_{e\mu}^m & \varepsilon_{e\tau}^m \\ \varepsilon_{e\mu}^{m*} & \varepsilon_{\mu\mu}^m & \varepsilon_{\mu\tau}^m \\ \varepsilon_{e\tau}^{m*} & \varepsilon_{\mu\tau}^{m*} & \varepsilon_{\tau\tau}^m \end{pmatrix}, \tag{11}$$

where $A = \sqrt{2}G_F N_e$, G_F is the Fermi coupling constant and N_e is the electron number density of the medium. Positive (negative) sign in (1,1) element of the matrix corresponds to matter potential for (anti)neutrinos. In this work, we consider only the former case. The matter NSI effects are incorporated in the SM matter effects via parameters $\varepsilon_{\alpha\beta}^m$, $\alpha, \beta = e, \mu, \tau$. The effective Hamiltonian can therefore be written as

$$H = \frac{1}{2E_\nu}\left[U\begin{pmatrix} 0 & 0 & 0 \\ 0 & \Delta m_{21}^2 & 0 \\ 0 & 0 & \Delta m_{31}^2 \end{pmatrix}U^\dagger + V\right], \tag{12}$$

and the probability for the transition $\nu_\alpha \to \nu_\beta$ is given by

$$P_{\nu_\alpha \to \nu_\beta} = |\langle \nu_\beta^d | e^{-iHL} | \nu_\alpha^s \rangle|^2, \tag{13}$$

where $|\nu_\alpha^s\rangle \equiv |\nu_\alpha\rangle + \varepsilon_{\alpha\beta}^s|\nu_\beta\rangle$ and $\langle\nu_\beta^d| \equiv \langle\nu_\beta| + \varepsilon_{\alpha\beta}^d\langle\nu_\alpha|$ refer to a neutrino that starts in the flavor α in the source and is

TABLE II. Current experimental limits of the nonunitarity of the light neutrino mixing matrix [38]. All limits are given at a 90% C.L.

Constraint on	Current bound
α_{ee}	0.02
$\alpha_{\mu\mu}$	0.01
$\alpha_{\tau\tau}$	0.07
$\lvert\alpha_{\mu e}\rvert$	0.010
$\lvert\alpha_{\tau e}\rvert$	0.042
$\lvert\alpha_{\tau\mu}\rvert$	0.0098

detected in the flavor β in the detector after the traversing distance L. In long baseline experiments L is set by the baseline of the experiment and E_ν by the energy of the neutrino beam. The matrices ε^s and ε^d contain dimensionless elements, which slightly alter the neutrino production and detection interactions in the source and detector, respectively. They originate from CC NSI parameters $\varepsilon^{ff'C}_{\alpha\beta}$ in Eq. (8), and their current experimental bounds are reported in Ref. [20].

It is possible that a part of the experimental signal presumed to originate from the matter NSI effects is actually caused by the nonunitarity of the light neutrino mixing matrix (see, e.g., [37,38]). We shall evaluate in our numerical analysis how large this contribution could possibly be in the triplet model, Eq. (1). In the case of nonunitarity, the light neutrino mixing matrix U in Eq. (12) must be replaced with a nonunitary matrix, which we denote by N. The matrix N can be parametrized as $N = N^{\rm NP}U$, where the nonunitarity is contained in a specific 3×3 triangle matrix [24]

$$N^{\rm NP} = \begin{pmatrix} 1-\alpha_{ee} & 0 & 0 \\ -\alpha_{\mu e} & 1-\alpha_{\mu\mu} & 0 \\ -\alpha_{\tau e} & -\alpha_{\tau\mu} & 1-\alpha_{\tau\tau} \end{pmatrix}, \tag{14}$$

where $\alpha_{\ell\ell'} \ll 1$, $\ell,\ell' = e,\mu,\tau$. The current experimental bounds on nonunitarity parameters $\alpha_{\ell\ell'}$ are presented in Table II.[1]

In the leading order, the matter NSI and nonunitarity parametrizations can be related through the equations [24],

$$\begin{aligned} &\varepsilon^m_{ee} = -\alpha_{ee} \qquad \varepsilon^m_{\mu\mu} = \alpha_{\mu\mu} \qquad \varepsilon^m_{\tau\tau} = \alpha_{\tau\tau} \\ &\varepsilon^m_{e\mu} = \frac{1}{2}\alpha^*_{\mu e} \qquad \varepsilon^m_{e\tau} = \frac{1}{2}\alpha^*_{\tau e} \qquad \varepsilon^m_{\mu\tau} = \frac{1}{2}\alpha^*_{\tau\mu}, \end{aligned} \tag{15}$$

where $\alpha_{\ell\ell'}, \varepsilon^m_{\ell\ell'} \ll 1$ for $\ell,\ell' = e,\mu,\tau$. One should note that the two low energy parametrizations are not equivalent, and Eq. (15) is only relevant in the context of neutrino oscillations at long baselines.

[1]The bounds reported in Table II are based on the neutrino oscillation data from CHORUS, NOMAD, and NuTeV to constrain the nonunitarity parameters. See, e.g., Ref. [39] for a detailed discussion on tighter bounds based on precision measurements of several SM observables.

IV. NUMERICAL STUDIES

We shall study what information DUNE could provide us on the parameters M_Δ and λ_ϕ through probing the NSI effects on neutrino propagation. Since Δ is leptophilic, only electron-type matter participates in the NSI effects related to triplet Higgs bosons. In what follows, we will use the notation $\varepsilon^m_{\alpha\beta} \equiv \varepsilon^{ee}_{\alpha\beta}$. First, we remark that there are limits for both the individual NSI parameters and for their differences

$$\begin{aligned} &\varepsilon^{\rho\sigma}_{\alpha\beta} - \varepsilon^{\rho'\sigma'}_{\alpha'\beta'} \\ &\quad = -\frac{M^2_\Delta}{8\sqrt{2}G_F v^4\lambda^2_\phi}\left((m_\nu)_{\sigma\beta}(m^\dagger_\nu)_{\alpha\rho} - (m_\nu)_{\sigma'\beta'}(m^\dagger_\nu)_{\alpha'\rho'}\right). \end{aligned} \tag{16}$$

To continue, we consider only matter NSI and rewrite Eqs. (7) and (16) in the following forms:

$$\frac{M^2_\Delta}{\lambda^2_\phi} = -\frac{8\sqrt{2}G_F v^4\varepsilon^m_{\alpha\beta}}{(m_\nu)_{e\beta}(m^\dagger_\nu)_{\alpha e}}, \tag{17}$$

$$\frac{M^2_\Delta}{\lambda^2_\phi} = -\frac{8\sqrt{2}G_F v^4(\varepsilon^m_{\alpha\beta} - \varepsilon^m_{\alpha'\beta'})}{(m_\nu)_{e\beta}(m^\dagger_\nu)_{\alpha e} - (m_\nu)_{e\beta'}(m^\dagger_\nu)_{\alpha' e}}. \tag{18}$$

From this expression, it is apparent that the upper limits for $|\varepsilon^m_{\alpha\beta}|$ and $|\varepsilon^m_{\alpha\beta} - \varepsilon^m_{\alpha'\beta'}|$ translate to upper limits of $M^2_\Delta/\lambda^2_\phi$. The elements of the light neutrino mass matrix m_ν are obtained from the equation

$$\begin{aligned} (m_\nu)^2 = U\begin{pmatrix} m_1^2 & 0 & 0 \\ 0 & m_2^2 & 0 \\ 0 & 0 & m_3^2 \end{pmatrix}U^\dagger \\ + A\begin{pmatrix} 1+\varepsilon^m_{ee}-\varepsilon^m_{\mu\mu} & \varepsilon^m_{e\mu} & \varepsilon^m_{e\tau} \\ \varepsilon^{m*}_{e\mu} & 0 & \varepsilon^m_{\mu\tau} \\ \varepsilon^{m*}_{e\tau} & \varepsilon^{m*}_{\mu\tau} & \varepsilon^m_{\tau\tau}-\varepsilon^m_{\mu\mu} \end{pmatrix}. \end{aligned} \tag{19}$$

Note that compared to Eq. (11), we have shifted the $\varepsilon^m_{\mu\mu}$ element, akin to [20]. Next, we define a dimensionless quantity,

$$C_{\alpha\beta} \equiv \begin{cases} -\dfrac{8\sqrt{2}G_F v^4\varepsilon^m_{\alpha\beta}}{(m_\nu)_{e\beta}(m^\dagger_\nu)_{\alpha e}}, & \alpha \neq \beta, \\ -\dfrac{8\sqrt{2}G_F v^4(\varepsilon^m_{\alpha\beta} - \varepsilon^m_{\mu\mu})}{(m_\nu)_{e\beta}(m^\dagger_\nu)_{\alpha e} - (m_\nu)_{e\mu}(m^\dagger_\nu)_{\mu e}}, & \alpha = \beta. \end{cases} \tag{20}$$

This allows us to present the limits in a compact form,

TABLE III. Current experimental upper limits of the matter NSI parameters [28] and expected upper bounds after the first run with DUNE [20]. All limits are at a 90% C.L.

Constraint on	Global bound	DUNE bound
$\lvert\varepsilon^m_{ee}-\varepsilon^m_{\mu\mu}\rvert$	4.2	0.9
$\lvert\varepsilon^m_{e\mu}\rvert$	0.3	0.074
$\lvert\varepsilon^m_{e\tau}\rvert$	3.0	0.19
$\lvert\varepsilon^m_{\mu\tau}\rvert$	0.04	0.038
$\lvert\varepsilon^m_{\tau\tau}-\varepsilon^m_{\mu\mu}\rvert$	0.15	0.08

$$\frac{M_\Delta^2}{\lambda_\phi^2} \leq C_{\alpha\beta}. \tag{21}$$

Considering the scales for G_F, v, and neutrino masses, we expect $C_{\alpha\beta} \gg 1$ and $\lambda_\phi \ll M_\Delta$.

The upper bounds for $M_\Delta/|\lambda_\phi|$ are calculated as follows. Using Eq. (19), we maximize the denominators in Eq. (20) by varying all relevant oscillation parameters within their experimental bounds. In long baseline neutrino experiments, the electron number density N_e depends on the matter density ρ, which is approximately 2700 kg/m^3. We take the average beam energy in DUNE to be $E_\nu \approx 2$ GeV. Assuming the normal neutrino mass hierarchy, the active neutrino masses m_2 and m_3 are given by $m_2 = \sqrt{m_1^2 + \Delta m_{21}^2}$ and $m_3 = \sqrt{m_1^2 + \Delta m_{31}^2}$, where $m_1 = 0\ldots0.2$ eV, $\Delta m_{21}^2 = 7.50^{+0.19}_{-0.17} \times 10^{-5}$ eV^2, and $\Delta m_{31}^2 = 2.524^{+0.039}_{-0.040} \times 10^{-3}$ eV^2 (for inverted hierarchy $\Delta m_{32}^2 = -2.514^{+0.038}_{-0.041} \times 10^{-3}$ eV^2). The standard oscillation parameters are varied within their 90% confidence level (C.L.) error limits (see [20] for the projected DUNE limits) to obtain the upper limits of the denominators of $C_{\alpha\beta}$. We then take the DUNE 90% C.L. upper bounds for the $\varepsilon^m_{\alpha\beta}$ parameters and their differences, and insert the largest possible value of the denominator and the upper limit of $\varepsilon^m_{\alpha\beta}$ into Eq. (17). This procedure is repeated for the current experimental 90% C.L. upper bounds for matter NSI. The current experimental bounds and the simulated DUNE bounds of these parameters are given in Table III. Comparing these bounds will elucidate the performance and feasability of DUNE as a probe for the triplet Higgs model.

We calculated the expected upper bounds $|C_{ee}|$, $|C_{e\mu}|$, $|C_{e\tau}|$, $|C_{\mu\tau}|$, and $|C_{\tau\tau}|$, for $M_\Delta^2/\lambda_\phi^2$ as function of m_1 using the 90% C.L. upper bounds for $|\varepsilon^m_{ee}-\varepsilon^m_{\mu\mu}|$, $|\varepsilon^m_{e\mu}|$, $|\varepsilon^m_{e\tau}|$, $|\varepsilon^m_{\mu\tau}|$, and $|\varepsilon^m_{\tau\tau}-\varepsilon^m_{\mu\mu}|$, respectively. Thus, we obtain five $M_\Delta^2/\lambda_\phi^2$ curves as a function of m_1 and construct the strictest possible upper limit for $M_\Delta^2/\lambda_\phi^2$, namely $C_{\min}(m_1) \equiv \min(C_{ee}, C_{e\mu}, C_{e\tau}, C_{\mu\tau}, C_{\tau\tau})$. We present this piecewise combined curve in Fig. 2, which was found to be

$$C^{\mathrm{NH}}_{\min}(m_1) = \begin{cases} C_{\mu\tau}, & m_1 \lesssim 0.01 \text{ eV}, \\ C_{e\mu}, & m_1 \gtrsim 0.01 \text{ eV}, \end{cases} \tag{22}$$

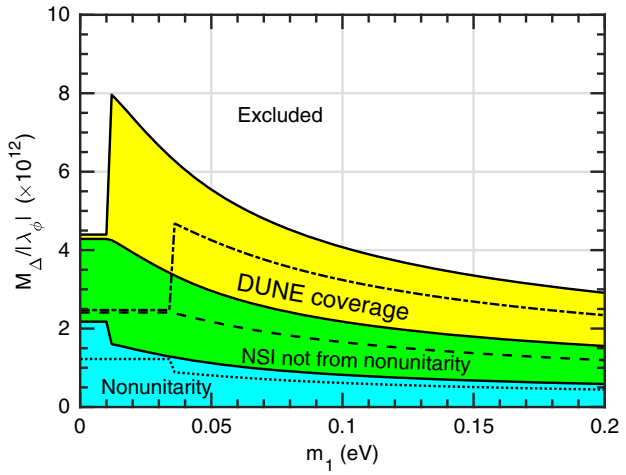

FIG. 2. The allowed values of $M_\Delta/|\lambda_\phi|$ as a function of the absolute neutrino mass scale when normal hierarchy is assumed. The white region shows the values of $M_\Delta/|\lambda_\phi|$ which are experimentally excluded at 90% C.L. when m_1 is the value of the lightest neutrino mass. The yellow region shows the values which are sensitive to DUNE. The green region shows the allowed values which cannot be constrained by DUNE but which are distinguishable from nonunitarity effects. The blue region shows the allowed values where nonunitarity could in principle be misinterpreted as a matter NSI effect. The dashed lines show where these 90% C.L. contours for nonunitarity bounds would be, if inverted hierarchy was assumed.

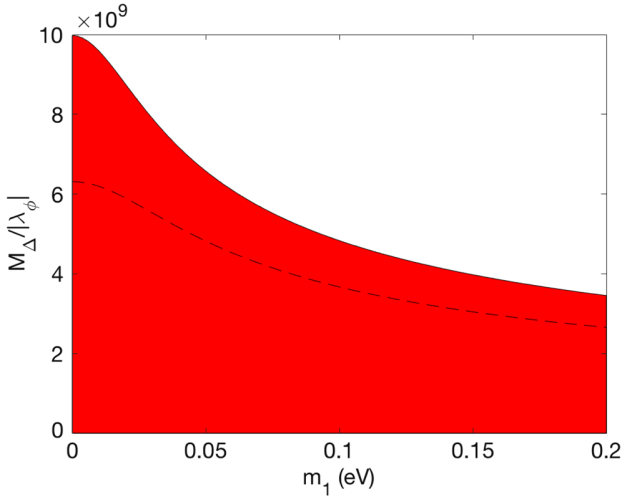

FIG. 3. The allowed values of $M_\Delta/|\lambda_\phi|$ as a function of m_1 when bounds on the source and detector NSI from CLFV experiments are considered. The white region shows the values of $M_\Delta/|\lambda_\phi|$ which are excluded at 90% C.L., whereas the values in the colored region are still allowed. The dashed line shows the 90% C.L. contour in inverted hierarchy.

$$C_{\min}^{\mathrm{IH}}(m_3) = \begin{cases} C_{\mu\tau}, & m_3 \lesssim 0.04 \text{ eV}, \\ C_{e\mu}, & m_3 \gtrsim 0.04 \text{ eV}. \end{cases} \quad (23)$$

As was pointed out, the nonunitarity effects could be mistaken as matter NSI effects. To estimate how large a part these could constitute of the signal, we transpose the current experimental bounds for the nonunitarity parameters $\alpha_{ll'}$ given in Table II into bounds for the NSI parameters $\varepsilon^m_{\alpha\beta}$ using the relations given in Eq. (15). From these bounds, we obtained the 90% C.L. bound for $M_\Delta/|\lambda_\phi|$ shown in Fig. 2.

Similarly, we derive the upper bounds for $M_\Delta/|\lambda_\phi|$ using the CLFV bounds from Table I. The resulting curve for 90% C.L. upper bound for $M_\Delta/|\lambda_\phi|$ is shown in Fig. 3. One

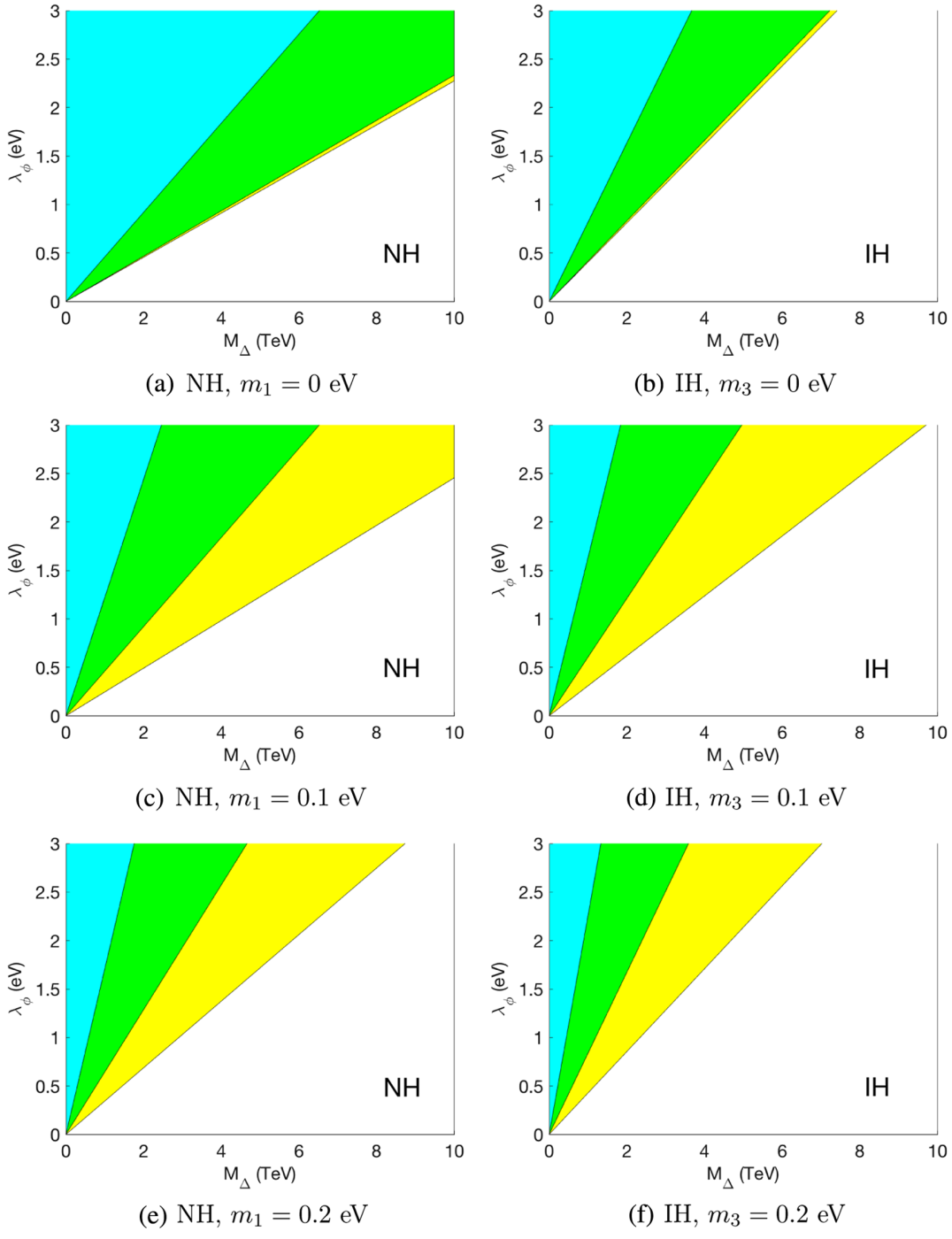

(a) NH, $m_1 = 0$ eV (b) IH, $m_3 = 0$ eV

(c) NH, $m_1 = 0.1$ eV (d) IH, $m_3 = 0.1$ eV

(e) NH, $m_1 = 0.2$ eV (f) IH, $m_3 = 0.2$ eV

FIG. 4. The allowed values of M_Δ and λ_ϕ in (M_Δ, λ_ϕ) plane, considering both mass hierarchies and different masses for the lightest neutrino. The colors are chosen as in Fig. 2.

immediately notes that the CLFV constraints are much stricter than the bounds we obtained from the matter NSI presented in Fig. 2.

In addition, we present λ_ϕ as a function of M_Δ with the constant lightest neutrino mass. We solve (17) for λ_ϕ and determine the allowed parameter space in (M_Δ, λ_ϕ) plane using the aforementioned bounds for matter NSI parameters, considering only bounds arising from current and future long baseline neutrino oscillation experiments. The bounds translate to the conditions

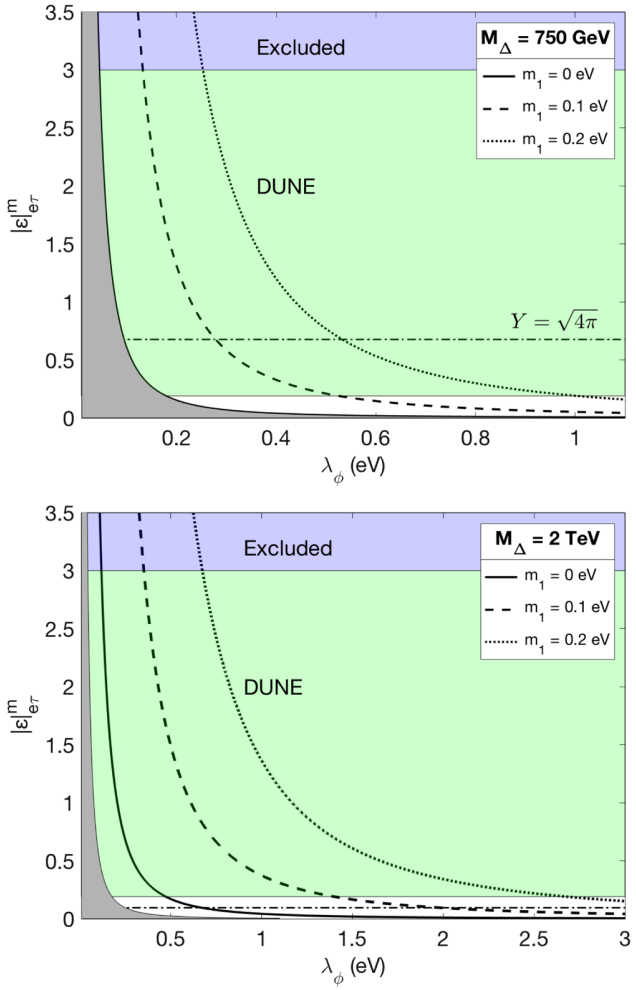

FIG. 5. The allowed values of $|\varepsilon^m_{e\tau}|$ and λ_ϕ in $(\lambda_\phi, |\varepsilon^m_{e\tau}|)$ plane, assuming a normal mass hierarchy. Blue region is excluded by experiments at 90% C.L. Green region shows the values which are sensitive to DUNE. Gray region is excluded by Higgs searches at LHC by the CMS Collaboration [40]. With a lower limit on the degenerate triplet Higgs mass M_Δ and a fixed lightest neutrino mass, everything below a m_1 contour is excluded. This gives us the lowest possible value for λ_ϕ for every $m_1 = 0$, 0.1, 0.2 eV. At the massless limit, we get the absolute limit for λ_ϕ, which may be moderately constrained by DUNE. The Yukawa couplings corresponding to $\varepsilon^m_{e\tau}$ are $< \sqrt{4\pi}$ below the dot-dashed line. In the upper subfigure, the m_1 limits are deduced from the assumption $M_\Delta = 750$ GeV and in the lower subfigure, 2 TeV.

$$\lambda_\phi \geq \frac{M_\Delta}{\sqrt{|C_{\alpha\beta}|}}, \tag{24}$$

where we again consider the bounds given by $|C_{ee}|$, $|C_{e\mu}|$, $|C_{e\tau}|$, $|C_{\mu\tau}|$, and $|C_{\tau\tau}|$. We pick the tightest constraint, given by $C_{\min}$ from Eqs. (22), and (23). The 90% C.L. bound is presented in Fig. 4.

Since there are known lower limits for M_Δ [40], we may use this information to calculate an experimental lower limit for λ_ϕ. This is done by calculating $|\varepsilon^m_{ee} - \varepsilon^m_{\mu\mu}|$, $|\varepsilon^m_{e\mu}|$, $|\varepsilon^m_{e\tau}|$, $|\varepsilon^m_{\mu\tau}|$, and $|\varepsilon^m_{\tau\tau} - \varepsilon^m_{\mu\mu}|$ as a function of λ_ϕ from Eqs. (7) and (16). We consider $m_1 = 0, 0.1$, and 0.2 eV. The tightest lower bound for λ_ϕ is found using $|\varepsilon^m_{e\tau}|$. The result is illustrated in Fig. 5 and in Table IV.

In all cases and results in this section, we have found that in the case of the inverted mass hierarchy, the bounds are similar as those presented here for the normal hierarchy, just slightly stricter in all cases. The results in the anti-neutrino matter potential case are also similar, just slightly less strict in all cases.

Finally, we conclude this section with remarks on perturbativity. By requiring all the Yukawa couplings to be $\sqrt{4\pi}$ at most, we find

$$M_\Delta \lesssim \frac{617\ \text{GeV}}{\sqrt{|\varepsilon^{\rho\sigma}_{\alpha\beta}|}}, \qquad M_\Delta \lesssim \frac{872\ \text{GeV}}{\sqrt{|\varepsilon^{\rho\sigma}_{\alpha\beta} - \varepsilon^{\rho'\sigma'}_{\alpha'\beta'}|}}, \tag{25}$$

which are acquired by combining Eqs. (5) and (6). Taking into account the lower limits for M_Δ, which we assume to be approximately 750 GeV [40,41], one can estimate the maximum possible contribution to NSI by the triplet scalar. We find $|\varepsilon^{\rho\sigma}_{\alpha\beta}| \lesssim 0.677$ and $|\varepsilon^{\rho\sigma}_{\alpha\beta} - \varepsilon^{\rho'\sigma'}_{\alpha'\beta'}| \lesssim 1.355$. For CLFV experiments, these conditions are fulfilled (see Table I), but for $|\varepsilon^m_{e\tau}|$ and $|\varepsilon^m_{ee} - \varepsilon^m_{\mu\mu}|$, the experimental limits are not restricting enough (see Fig. 5). If DUNE confirms NSI with $|\varepsilon^m_{e\tau}| \gtrsim 0.677$, all of it cannot be a manifestation of triplet scalar interactions, and there must be additional new physics contribution. In other words, in the case of the confirmation of the existence of triplet scalar and large $|\varepsilon^m_{e\tau}|$, this would indicate additional NSI originating from other extensions of SM.

TABLE IV. Current experimental and expected DUNE lower bounds with 90% C.L. for λ_ϕ inferred from current oscillation parameters, current bounds for NSI, and simulated DUNE bounds for NSI. NH and IH correspond to the normal and inverse neutrino mass hierarchy, respectively.

	Global λ_ϕ (eV)		DUNE λ_ϕ (eV)	
m_1 (eV)	NH	IH	NH	IH
0.0	0.031	0.045	0.120	0.178
0.1	0.129	0.133	0.509	0.526
0.2	0.251	0.253	0.997	1.006

V. SUMMARY AND CONCLUSIONS

The triplet Higgs bosons ($\Delta = \Delta^{++}, \Delta^{+}, \Delta^{0}$) utilized in the type-II seesaw model will affect neutrino propagation in matter by mediating interactions not present in the Standard Model. We have studied in this work how the sensitivity of DUNE for NSI interactions can be utilized to derive a constraint for the quantity $M_\Delta/|\lambda_\phi|$, where M_Δ is the mass of the triplet bosons and λ_ϕ the strength of the coupling $\Delta\phi\phi$ between the triplet Higgs and the standard Higgs doublet. We found that a long baseline experiment with the specifications of the proposed DUNE can reach the upper bound $M_\Delta/|\lambda_\phi| \lesssim (2\text{–}4) \times 10^{12}$ at 90% C.L. If the ratio $M_\Delta/|\lambda_\phi|$ were above this value, the effects of the NSI neutrino-matter interactions caused by the triplet boson exchange would be seen in the DUNE oscillation data. We found the bound to be sensitive of the neutrino mass ordering (normal or inverted).

We found that in long baseline experiments the strictest bound on $M_\Delta/|\lambda_\phi|$ arises from the $|\varepsilon^m_{\mu\tau}|$ and $|\varepsilon^m_{e\mu}|$ constraints. DUNE would be able to improve the upper limits of these NSI parameters, as indicated in Table III. The sensitivity to the matter NSI parameters has been previously studied for the proposed HyperKamiokande and T2HKK experiments, and the upper limit on $|\varepsilon^m_{ee} - \varepsilon^m_{\mu\mu}|$ achievable in these experiments is estimated to be improved, see [34].

In long baseline experiments, nonunitarity of the mixing matrix of the ordinary light neutrinos might give similar effects on the oscillation probabilities than the NSI due to the triplet Higgses, which might lead to a misinterpretation of the data. We found out that the effects caused by nonunitarity depend strongly on the lightest neutrino mass m_1 and are well below the sensitivity of DUNE. Only when $m_1 \ll 1$ eV, the signals interpreted as triplet-Higgs NSI effects could actually be caused by nonunitarity of the neutrino mixing.

We also showed that the existing constraints on the various NSI parameters obtained by studying low-energy charged lepton flavor violation (CLFV) processes, such as like $\mu^- \to e^- e^+ e^-$, correspond, when interpreted in terms of the triplet Higgs model, to constraints on $M_\Delta/|\lambda_\phi|$, which are for all values of the lightest neutrino mass orders of magnitude more stringent than one would reach in DUNE.

To summarize, the study of NSI interactions in long-baseline neutrino-oscillation experiments considered in this work and at low-energy processes would give crucially central information on the triplet Higgs model and type-II seesaw model, in particular when combined with the information one can get in collider experiments for the lower limit of the triplet mass M_Δ (see, e.g., Ref. [40]). For a normal mass hierarchy and a triplet mass $M_\Delta = 750$ GeV, for example, the future DUNE data will indicate $|\lambda_\phi| \gtrsim 0.120$ eV, a clear improvement of the strictest current limit we calculated in Table IV, $|\lambda_\phi| \gtrsim 0.031$ eV.

ACKNOWLEDGMENTS

K. H. acknowledges the H2020-MSCA-RICE-2014 Grant No. 645722 (NonMinimalHiggs). T. J. K. expresses his gratitude to the Magnus Ehrnrooth foundation for financial support. S. V. thanks University of Jyväskylä for funding a research visit to Centro de Física Teórica de Partículas, University of Lisbon, where part of this work was done.

[1] T. Kajita and Y. Totsuka, Rev. Mod. Phys. **73**, 85 (2001).
[2] Q. R. Ahmad *et al.* (SNO), Phys. Rev. Lett. **87**, 071301 (2001).
[3] P. Minkowski, Phys. Lett. **67B**, 421 (1977).
[4] M. Gell-Mann, P. Ramond, and R. Slansky, Conf. Proc. **C790927**, 315 (1979).
[5] T. Yanagida, Conf. Proc. **C7902131**, 95 (1979).
[6] R. N. Mohapatra and G. Senjanović, Phys. Rev. Lett. **44**, 912 (1980).
[7] J. Schechter and J. W. F. Valle, Phys. Rev. D **22**, 2227 (1980).
[8] K. Huitu, J. Maalampi, A. Pietilä, and M. Raidal, Nucl. Phys. **B487**, 27 (1997).
[9] J. Maalampi and N. Romanenko, Phys. Lett. B **532**, 202 (2002).
[10] M. Mühlleitner and M. Spira, Phys. Rev. D **68**, 117701 (2003).
[11] A. G. Akeroyd and M. Aoki, Phys. Rev. D **72**, 035011 (2005).
[12] G. Bambhaniya, J. Chakrabortty, J. Gluza, T. Jelinski, and R. Szafron, Phys. Rev. D **92**, 015016 (2015).
[13] G. Aad *et al.* (ATLAS), J. High Energy Phys. 03 (2015) 041.
[14] J. C. Pati and A. Salam, Phys. Rev. D **10**, 275 (1974); **11**, 703(E) (1975).
[15] R. N. Mohapatra and J. C. Pati, Phys. Rev. D **11**, 2558 (1975).
[16] R. N. Mohapatra and J. C. Pati, Phys. Rev. D **11**, 566 (1975).
[17] G. Senjanović and R. N. Mohapatra, Phys. Rev. D **12**, 1502 (1975).
[18] J. F. Gunion, J. Grifols, A. Mendez, B. Kayser, and F. I. Olness, Phys. Rev. D **40**, 1546 (1989).
[19] M. Malinsky, T. Ohlsson, and H. Zhang, Phys. Rev. D **79**, 011301 (2009).
[20] M. Blennow, S. Choubey, T. Ohlsson, D. Pramanik, and S. K. Raut, J. High Energy Phys. 08 (2016) 090.

[21] Y. Grossman, Phys. Lett. B **359**, 141 (1995).
[22] C. Patrignani *et al.* (Particle Data Group), Chin. Phys. C **40**, 100001 (2016).
[23] K. Huitu, T. J. Kärkkäinen, J. Maalampi, and S. Vihonen, Phys. Rev. D **93**, 053016 (2016).
[24] M. Blennow, P. Coloma, E. Fernandez-Martinez, J. Hernandez-Garcia, and J. Lopez-Pavon, J. High Energy Phys. 04 (2017) 153.
[25] T. Ohlsson, Rep. Prog. Phys. **76**, 044201 (2013).
[26] I. Girardi, D. Meloni, and S. T. Petcov, Nucl. Phys. **B886**, 31 (2014).
[27] D. Meloni, T. Ohlsson, and H. Zhang, J. High Energy Phys. 04 (2009) 033.
[28] C. Biggio, M. Blennow, and E. Fernandez-Martinez, J. High Energy Phys. 08 (2009) 090.
[29] J. Kopp, M. Lindner, T. Ota, and J. Sato, Phys. Rev. D **77**, 013007 (2008).
[30] R. Adhikari, A. Dasgupta, and Z. Rahman, arXiv:1204.1750.
[31] P. Coloma, J. High Energy Phys. 03 (2016) 016.
[32] A. de Gouvêa and K. J. Kelly, Nucl. Phys. **B908**, 318 (2016).
[33] M. Masud, A. Chatterjee, and P. Mehta, J. Phys. G **43**, 095005 (2016).
[34] S. Fukasawa, M. Ghosh, and O. Yasuda, Phys. Rev. D **95**, 055005 (2017).
[35] S. Davidson, C. Pena-Garay, N. Rius, and A. Santamaria, J. High Energy Phys. 03 (2003) 011.
[36] S.-F. Ge, P. Pasquini, M. Tortola, and J. W. F. Valle, Phys. Rev. D **95**, 033005 (2017).
[37] F. J. Escrihuela, D. V. Forero, O. G. Miranda, M. Tortola, and J. W. F. Valle, Phys. Rev. D **92**, 053009 (2015); **93**, 119905(E) (2016).
[38] F. J. Escrihuela, D. V. Forero, O. G. Miranda, M. Tórtola, and J. W. F. Valle, New J. Phys. **19**, 093005 (2017).
[39] E. Fernandez-Martinez, J. Hernandez-Garcia, and J. Lopez-Pavon, J. High Energy Phys. 08 (2016) 033.
[40] A search for doubly-charged Higgs boson production in three and four lepton final states at $\sqrt{s} = 13$ TeV, Report No. CMS-PAS-HIG-16-036, 2017.
[41] K. S. Babu and S. Jana, Phys. Rev. D **95**, 055020 (2017).